Summer 2010

# Simulation based design for high speed sea lift with waterjets by high fidelity urans approach

Tomohiro Takai
*University of Iowa*

# SIMULATION BASED DESIGN FOR HIGH SPEED SEA LIFT WITH WATERJETS BY HIGH FIDELITY URANS APPROACH

by

Tomohiro Takai

A thesis submitted in partial fulfillment
of the requirements for the Master of
Science degree in Mechanical Engineering
in the Graduate College of
The University of Iowa

July 2010

Thesis Supervisor: Professor Frederick Stern

Graduate College
The University of Iowa
Iowa City, Iowa

CERTIFICATE OF APPROVAL

_____

MASTER'S THESIS

_____

This is to certify that the Master's thesis of

Tomohiro Takai

has been approved by the Examining Committee
for the thesis requirement for the Master of Science
degree in Mechanical Engineering at the July 2010 graduation.

Thesis Committee: _____
Frederick Stern, Thesis Supervisor

_____
Pablo M. Carrica

_____
James Buchholz

To my family

## ACKNOWLEDGMENTS

This work is sponsored by the US Office of Naval Research through research grants N00014-08-0491, under the administration of Dr. Ki-Han Kim. The simulations were performed on 4.7GHz IBM Power 6 machine '*DaVinci*' at the DoD NAVO center.

I wish to acknowledge all of those who have helped and supported me in order to complete this work. This thesis describes not only my effort but that of a collaborative effort.

First of all, I would like to thank my advisor, Prof. Frederick Stern for the opportunity and guidance to pursue my higher education about computational ship hydrodynamics and for his generous support and frequent encouragement. I would like to extend my appreciation to the members of my advisory committee, Prof. Pablo M. Carrica and Prof. James Buchholz for reading this thesis and offering many constructive comments and valuable suggestions. Their comments and questions were helpful in improving the thesis and service on my committee is appreciated.

I am extremely thankful for the opportunity to work with Dr. Manivannan Kandasamy. I am very grateful to assistance and advice I have received from him, and I am pretty certain that much of this work would not have been done without his help. I would also like to express my appreciation to Mr. Wei He for assisting me to complete this work. In addition, I would like to appreciate Dr. Yusuke Tahara who provided me the opportunity to study at IIHR and invaluable support for this work. Invaluable assistance for numerical codes was also provided by INSEAN research group, I would especially like to thank Dr. Daniele Peri and Dr. Emilio F. Campana. Finally, I would like to appreciate my family and friends. My life and study in Iowa has been greatly enriched by my friends. I would like to thank all of them for their help and support, especially, Ms. Halim Choi, Ms. Sunim Han, Mr. Masashi Yamaguchi, Mr. Yuichi Ura, and Mr. Dongwoo Ko.

## TABLE OF CONTENTS

## LIST OF TABLES

Table

## LIST OF FIGURES

Figure

# CHAPTER 1
# INTRODUCTION

## 1.1 Background

Over the past decades, a variety of mechanical propulsion systems, such as conventional screw propeller, controllable-pitch propeller, contra-rotating propeller, surface piercing propeller, and waterjets, has been proposed for marine vehicles. Nowadays, there is a growing interest in high-speed ships with waterjet propulsion system; for instance, the U.S. Navy is now interested in high-speed ship concepts for future naval combatants in littoral operations, and the waterjet is recognized as a leading propulsor candidate. The waterjet propulsion systems have a lot of benefits over other marine propulsion systems, e.g., conventional screw propellers, such as shallow draft design, smooth engine load, less vibration, lower water borne noise, no appendage drag, good maneuverability, and so on. The waterjet also have good efficiency over the required speed range because they are effective by recovering a part of the frictional drag by ingesting the low momentum boundary layer at the inlets. In addition, the cavitation can be delayed or reduced by increasing the static pressure of impeller face through diffusing the cross-sectional area of intake duct. These advantages have combined to increase the demand of waterjet propulsion systems for a variety of marine vehicles including high-speed naval sea-lift.

Recently, significant advancements in waterjet technology have been made particular in two areas: compact waterjet technology and capability of computational fluid dynamics (CFD) for design and analysis. In fact, current waterjet market is dominated mainly by the mixed-flow systems; however, the need for high-speed ships requires the use of slender hull forms and efficient propulsion systems in order to reduce the wave resistance and therefore the required installed power. Since drag (in particular

wave drag) typically increases on the order of the square or higher of the ship speed, low-drag slender hull is necessity to struggle for the high-speed ship market. However, such slender hull introduces a problem of installing the necessary machinery to achieve required speed. This is also the reason why the conventional external propeller arrangement with its exposed shaft, shaft supports, and rudder should be eliminated due to significant appendage drag for most high-speed applications. As a result, the axial-flow waterjet system, which is compact compared to the mixed-flow systems, was introduced. For the same inlet diameter and the same unit thrust, the axial-flow pump has a significant smaller transom footprint than the mixed-flow pump. In addition, recent innovations in CFD and high-performance computing have enabled faster and cost effective approach for predicting waterjet propulsive characteristics. Numerical approaches also have enabled detailed analysis of the flow inside the waterjet ducts, which would require prohibitively expensive measurements in towing tank experiments. Such detailed flow analysis is invaluable for a deeper understanding of the flow physics giving insights into further improvement of the waterjet performance characteristics.

For the improvement of waterjet propulsion system, the design of the intake duct has an important effect on the thrust produced as well as the performance of pump/rotor and overall vibrations and noises. In fact, the design of waterjet depends on the size and desired performance of the vessel; as a result, the development of reliable design methodology of waterjet is necessary for the future of ship community immediately. The complexity of the design problem with the inherent difficulty to deal with a growing number of design goals and constraints raised the interest in the use of a numerical optimization approach, so-called simulation based design (SBD). As a matter of fact, numerical optimization methods have been becoming in use as one of the practical design tools for many engineering applications at all stages of the design process in order to achieve the reduction of cost and time during product developments. One of the advantages for using such simulation design approaches is that the initial idea can be

obtained to design products which have the new concept and there are few methodologies available to be applied such as waterjet design. In the earlier research, IIHR with research collaborators have been successfully developed SBD system for new concept naval vehicles; for instance, surface combatant with a sonar dome bow and transom stern (Tahara *et al.*, 2008c), high-speed catamaran/trimaran (Tahara *et al.*, 2007 and 2008a), America's cup sailing yacht (Campana *et al.*, 2009c), and foil-assisted high-speed ferry (Kandasamy *et al.*, 2009). Therefore, SBD system can aid in the design and optimization of waterjet systems individually adapted for every ship, to improve at any given design speed.

## 1.2 Objective and approach

The main purpose of the present study is to develop and demonstrate the simulation based design optimization system for the naval vessel with waterjet propulsion. SBD system is an emerging tool for automatic design optimization to improve time-intensive industrial design application driven by numerical algorithm, with the final goal of assisting designers in exploring the design space more quickly, efficiently, and creatively. In general, SBD system for hydrodynamic designs is composed by three main components: first, an optimization method to solve the nonlinear optimization problem formed by the objective functions and constraint conditions; second, a geometry modeling method to provide a link between the design variables and a body shape; and third, a high performance CFD solver used as analysis tool to return the objective values and functional constraints.

In order to achieve the main purpose, three approaches are taken into account; development and validation of the numerical method for waterjet propelled simulation, development of the global optimization algorithm and flexible geometric modeling method for the hydrodynamic design, and demonstration of the capability of SBD method

for a practical naval vessel. A Joint High-Speed Sea-lift (JHSS), which is a very large high-speed ship concept propelled by four axial-flow waterjet systems, is selected as an initial geometry. Since one of the main focuses of the present optimization endeavor is the optimization of the waterjet inlet geometry with regards to hull interaction and stern forces, a detailed validation of the prediction capability of Unsteady Reynolds Averaged Navier Stokes (URANS) solver for high speed waterjet propelled sealifts is necessary. Notable points of the present study are as follows: 1) Detailed verification and validation (V&V) analysis of waterjet propelled simulation using high-fidelity flow URANS solver, CFDSHIP-IOWA; 2) Detailed comparison study of global optimization algorithms, i.e., Particle Swarm Optimization (PSO) and Genetic Algorithm (GA); 3) Hydrodynamic design optimization practices for both JHSS barehull bow shape and waterjet intake duct shape.

In the present study, computational setup differs from previous numerical waterjet studies in that the waterjet-hull interactions and waterjet-wake interactions are also predicted with free surface and dynamic motions. The effects of waterjet-hull interaction are highly non-linear as they include the effect of the dynamic trim on boundary layer ingestion and shape of inflow stream tube, together with the effect of the waterjet induced vertical forces on the dynamic motion. Also, the shape of the ingested boundary layer is non-uniform over the entire cross-section at the inlet and it depends on the hull form. This phenomenon affects the non-uniformity of the flow inside the duct and hence affects the inlet efficiency. The waterjet-wake interactions do not significantly affect the propulsion characteristics, but are of interest in the study of wake signatures. Self propulsion simulations are carried out at model scale with an added tow force to compensate for the extra drag due to thicker boundary layer at model scale to get thrust loading similarity. An actuator disk model is used inside the duct instead of modeling the impeller, as the latter requires significantly more computational effort and is not needed for the purpose of calculating the waterjet performance indicators such as net thrust and

system efficiency (Bulten & Van Esch, 2007). The simulations are carried out over a range of ship speed at different IVR ratios for the waterjet, and the control volume analysis used for the powering performance predictions in the towing tank test is replicated to get the net jet system thrust. Verification and validation (V&V) studies are performed using the Experimental Fluid Dynamics (EFD) data from the 1/34 scale model testing (Jessup *et al.*, 2008). The uncertainty assessment study is conducted for both JHSS barehull and waterjet propelled simulation with two degrees of freedom following the quantitative methodology and procedures proposed by Stern *et al.*, (2006a) and recently proposed factor of safety method by Xing and Stern (2010).

Typical ship design problems involve multiple objectives; for instance, the goals of the design process include resistance reduction, lower hydrodynamic noise, and the reduced amplitude of particular motions. Unfortunately, the improvement of a specific aspect of the global design usually causes the worsening of some others. Furthermore, realistic ship design problems are often nonlinear and also non-convex. Indeed, the enforcement of nonlinear constraint conditions lead to a non-convex problem; i.e., the feasible solution set might be divided into several sub-regions. As a result, the classical gradient-based local optimization scheme would have substantial difficulties to search multiple optimum solutions. In the present study, two popular global algorithms, namely PSO and GA are considered. Since these two approaches are supposed to find a solution to a given objective function but employ different strategies and computational effort, it is appropriate to compare their implementation. Thus, detailed comparison study of optimization algorithms is performed in order to select the proper approach applied to waterjet inlet shape optimization. Both single- and multi-objective optimization problems using analytical functions are solved; besides, the solutions for multi-objective problems are evaluated quantitatively.

Finally, demonstration of the present SBD framework is performed for both JHSS barehull and waterjet appended hull. Since the fluid-dynamic design of marine is

considered in the present study, the shape plays a key role and its detailed analysis requires the solution of nonlinear partial differential equations (PDE) which are particularly expensive from the computational point of view in case of a realistic three dimensional geometry. The use of numerical codes enable to solve the set of equations in SBD is allowed by the availability of high performance computing platforms. However, the cost of a simulation, i.e., an objective function evaluation, is computational time consuming. This background leads to use the sensitivity analysis prior to performing the optimizations. The sensitivity analyses are performed manually for both barehull and waterjet case individually using as small number of design parameters as possible to obtain the parametric trend toward the objective function. According to the trend of the reduction of objective function, several geometries are selected as initial blending designs; then, those designs are applied together with the morphing scheme (blending method) in optimization loop. Four different SBD environments are generated combining the different CFD solver and global optimization algorithms for different purposes. First, optimization problem is focused on JHSS bow shape design in order to investigate the capability of the SBD system. Subsequently, JHSS waterjet intake duct shape design optimization is performed.

The author would like to note that the present work is a part of international research project, closely collaborated with Instituto Nazionale per Studi ed Esperienze di Architettura Navale (INSEAN) in Italy, and National Maritime Research Institute (NMRI) in Japan.

## 1.3 Thesis outline

This thesis is organized as the following chapters: ***Chapter 2*** provides overviews of the earlier literature including both CFD based optimization method and detailed waterjet propulsion simulation. ***Chapter 3*** describes the numerical method used in the

present study; URANS flow solver, CFDSHIP-IOWA version 4 and potential solver, INSEAN WARP. ***Chapter 4*** presents the simulation designs including geometry, brief summary of experiment, test cases, grid design, and boundary conditions. ***Chapter 5*** provides the detailed verification and validation studies for both JHSS barehull and waterjet propelled simulation. Iterative and grid size convergence along with assessment of overall numerical uncertainty are verified, and validation work is done with corresponding EFD data. In addition, wave fields and flow parameters are analyzed for barehull and waterjet case, respectively. ***Chapter 6*** described optimization algorithms; four different algorithms are introduced with their mathematical expressions. In ***Chapter 7***, the performance of optimization algorithms is analyzed using single- and multi-objective analytical optimization problems. In particular, the focus is put on quantitative evaluation of multi-objective optimization problems from global optimization algorithms, i.e., PSO and RCGA. ***Chapter 8*** describes the geometry and grid manipulation techniques. Several approaches are introduced and their advantages and disadvantages in use for hydrodynamic design optimization are summarized. ***Chapter 9*** provides the demonstration of the present SBD system for the practical hydrodynamic design. First, the system is applied to the simple optimization problem for JHSS barehull. Next, the problem is extended to multi-objective problems. Finally, optimization is performed for complex geometry, i.e., waterjet intake duct shape. Both low-fidelity (potential solver) and high-fidelity (URANS solver) flow solver is employed as analysis scheme, and two global optimization algorithms are employed as an optimizer. Lastly, ***Chapter 10*** gives conclusion and future work.

# CHAPTER 2
# LITERATURE SURVEY

## 2.1 CFD based optimization method

The next generation of naval surface ship will be developed on the basis of new concepts in order to achieve particular performance objectives for each operation profile of the ship. Currently, computational fluid dynamics (CFD) has been becoming in use as an analysis tool to study alternative designs. Indeed, the use of reliable and validated CFD solvers raises the possibility of cutting down the number of experimental model testing process. Although the use of the CFD simulation is rapidly becoming a common practice in the advanced ship design process, the approach for the practical design suffers the limitation; hence, using only simulation approach is not always able to identify the global optimal design. This is the basic motivation for developing CFD based optimization tools, so called Simulation Based Design (SBD) system, for hydrodynamic ship designs wherein automatic determination of optimal shape is the part of simulation loop. In general, CFD based optimizations can be divided into two categories: manual and automatic optimization methods. The former one basically follows conventional design methods, but utilizes more information from numerical simulations. The latter one includes optimization schemes (algorithms) so that the optimal shape is automatically obtained. To develop hydrodynamic optimization methods for ship designs, three main components need to be built: first, a optimization method to solve the nonlinear optimization problem formed by the objective functions and constraint conditions; second, a geometry modeling method to provide a link between the design variables and a body shape; and third, a high- performance CFD solver used as analysis tool to return the objective values and functional constraints. Typically, these elements are developed

separately, and combined to yield the SBD framework. Figure 2-1 illustrates basic SBD components and relationships between each component.

CFD methods used for shape optimization were initially 2D Euler/Navier-Stokes (NS) solvers, which were then extended to 3D flow solvers for more practical design applications. 3D optimization problem was first solved by using potential flow methods with linear and/or non-linear free surface boundary conditions. For instance, the solution of the Neumann-Kelvin problem had been used for ship hull shape optimization for minimizing wave-making resistance. In the late 90s, increased availability of high-speed computers enabled the use of more sophisticated flow solvers such as Reynolds averaged Navier-Stokes (RANS), NS solvers, and DES solvers. Currently, 3D unsteady RANS solver is becoming available in use for optimization tool using parallel computing approach.

Tahara *et al*., (2004) demonstrated the capability of optimization method for surface combatants design. DTMB Model 5415 hull form, which has been used as one of typical examples of a complex shape optimization problem, was selected the initial geometry. The optimization module was based on Sequential Quadratic Programming (SQP: one of popular gradient methods), extended for the higher performance optimization method by introducing parallel computing architecture. Specifically, the stern optimization for minimization of transom wave field disturbance and the sonar dome shape optimization for minimization of sonar dome vortices were demonstrated. The authors concluded that the CFD based optimization method developed in the work demonstrated the capability for flow- and wave-field optimization successfully. Some future work was addressed at that time, e.g., consideration of ship dynamic motions in the running condition, introduction of an unsteady RANS solver with free surface prediction, and introduction of non-determinative optimization scheme to realize the global optimization.

Peri and Campana (2003) investigated a variable fidelity approach to speed up the optimization process using free surface RANS in a multi-objective design problem. Several optimization algorithms (Steepest descent, SQP, and Conjugate gradient method) were tested in conjunction with a CFD solver in the paper. Later, global optimization (GO) method was applied to Model 5415 by Tahara *et al.*, (2006, 2008a). The adopted scheme was based on multi-objective genetic algorithm (MOGA), which is currently one of the most popular algorithms in use for hydrodynamic optimization applications. The detailed investigation on advantages of GA over conventional gradient-based approaches, e.g., SQP was conducted in Tahara *et al*., (2003, 2006).

Tahara *et al*., (2005) and Campana *et al*., (2006a) analyzed different alternatives for the SBD fundamental elements: derivative-free and gradient-based algorithms, the concept of variable-fidelity, and the use of parallel architectures, different techniques for shape and grid manipulation (CAD-free and CAD-based). Furthermore, dedicated experimental campaigns were also carried out to assess the optimization processes and the data were successfully used in a new verification and validation procedure developed ad-hoc for optimization problem and based on the analysis of the trend of the objective problem and based on the analysis of the trend of the objective functions to be minimized. Both SBD systems developed in these researches were essentially based on local optimization algorithms.

Nowadays, CFD based global design optimization has been successfully demonstrated and validated for the capability of handling the more complex shapes, such as fast multi-hull ships (e.g., Catamaran/Trimaran) found in Campana *et al*., (2006), Tahara *et al*., (2007, 2008a, 2008b) and high-speed foil-assisted semi-planing catamaran called SPIRIT (see Kandasamy *et al*., 2009b, Peri *et al*., 2009). In Campana *et al.*, (2009a), these efforts are well summarized; both local and global hydrodynamic ship design optimization problems are addressed, defined in either a single or a multi-objective formulation framework. However, there is less reported the optimization studies

of propulsion mechanics, especially waterjet system due to the difficulty of complex 3D geometry and reliable CFD tools. This challenge forms the motivation of the present research work.

## 2.2 Waterjet powering performance analysis

### 2.2.1 ITTC waterjet performance analysis method

The momentum flux approach and the International Towing Tank Committee (ITTC) '96 method has been used worldwide for the analysis of waterjet powering performance predictions. The ITTC Waterjet Performance Prediction Specialist Committee was active in the 21st (Kruppa *et al*., 1996), 22nd (Hoyt *et al*., 1999) 23rd (Van Terwisga *et al*., 2002), and 24th (Van Terwisga *et al*., 2005. The 21st ITTC Specialist Committee on Waterjets discussed two distinct methods; i.e., "momentum flux method" and "direct thrust measurement method". The important advantages of the first method are that a suitable arbitrary pump can be used to provide the required flow rate (corresponding to required thrust), and that no complicated watertight sealing between the waterjet and the hull is needed. In addition, scale of the waterjet model can be chosen smaller in the first method, as internal scale effects do not matter. The second method also has an advantage such as the jet system performance need not be measured separately, as this is implicitly taken into account by the correct scale model. From the experience of the Committee Members with the second method, it was concluded that this method is expensive and cumbersome; thus, they have focused on the momentum flux method.

The 24th ITTC Waterjet Performance Prediction Specialist Committee has developed a model testing procedure for waterjet propulsion. The committee adopted a control volume approach balancing momentum and energy through the waterjet system to

arrive at system thrust, thrust deduction, and delivered power. According to ITTC definition, the waterjet-hull system is decomposed into a bare hull and a waterjet system, and the waterjet system can be subdivided into a pump and a ducting system. The pump is the driving heart of the waterjet, converting mechanical power (input) into hydraulic power (output). The duct leads the required flow from the exterior to the pump and through the nozzle, back into the environment. The ITTC standard locations for the flow through the waterjet are indicated in Figure 2-2. The inflow capture area is designated as Station 1(1A), one pump diameter ahead of the inlet tangency. Station 3 is located just ahead of the pump, and Station 6 is at the nozzle discharge. A suitable control volume needs to be selected for the waterjet system in order to be able to compute or determine the powering characteristics from measurements. Using the above mentioned locations, the control volume is defined by the stream-tube captured in between station 1A and 6.

Relations for delivered thrust and corresponding required power will be derived from the conservation laws of momentum and energy, respectively. A body-fitted $(X, Y, Z)$ Cartesian coordinate system is used with $X$ positive downstream, $Z$ positive upward, and $Y$ formed by following right hand side (RHS) rule. According to Newton's second law, "the change in momentum flux over a given control volume equals to the sum of the forces acting on that control volume". This law is used to derive an expression for the net thrust that is available to propel the hull. The conservation law of mass is expressed as

$$\bar{V}_{1A} A_{1A} = \bar{V}_6 A_6 \tag{2.1}$$

where, the subscripts refer to the ITTC standard locations (Figure 2-2). Then, thrust is predicted from conservation of axial momentum

$$R_X = (M_{1A} - M_6) = \dot{m}\,[c_{M\,1A}\,\bar{V}_{1A} - c_{M\,6}\,\bar{V}_6] \tag{2.2}$$

$$c_{M\,n} = \frac{1}{\sqrt{1-C_{p\,1A}}\;Q\;U_0}\int_{A_n} u^2\,dA \tag{2.3}$$

$$\bar{V}_n = \frac{1}{A_n}\int_{A_n} u\;\;dA_n \tag{2.4}$$

The determination of the inlet capture area $A_{1A}$ is potential source of error when the momentum flux method is performed. This concern is usually twofold; location of survey plane and determination of the shape and size. As pointed out in the 21st ITTC Waterjet Committee Report (Kruppa *et al.*, 1996), $A_{1A}$ is arbitrary, and the recommendation was to place this measurement station forward of the point of tangency. In an attempt to standardize the location in order to reduce bias errors, the 23rd ITTC The Specialist Committee on Validation of Waterjet Test Procedures (Van Terwisga *et al.*, 2002) recommended placing the measurement station, referred to as Station 1A, one inlet width forward of Station 1. Here, the width of the inlet was defined as the maximum width between the port and starboard transverse points of tangency. Another concern is how to determine the shape of capture area. The recommendation of the 21st ITTC was to use a rectangular shape for capture area estimation.

Figure 2-3 describes the data flow through data acquisition and data reduction phase for determination of powering characteristics from model test recommended by ITTC. There are four main processes from which the data are collected. The first process contains the derivation of relevant data from model or ship geometry. The estimation of the inlet width for capture area at Station 1 is made in this process using nozzle discharge diameter or the nozzle discharge area. In the second process, a resistance test and a wake field measurement on the model in resistance test configuration is conducted. The wake-field measurement is to be conducted with closed intakes and the boundary layer velocity profile is used as a measure for the distortion of the inflow in the capture area. The third process consists of a calibration test and the actual propulsion test. It is recommended that flow rate calibration through a force measurement (measuring momentum flux) is

preferred over direct flow rate measurement (through a flow meter). The results of the propulsion test will have to be fed into the jet system characteristics; however, to arrive at the power that needs to be delivered to the impeller and the corresponding impeller rotation rate. The determination of the jet system characteristics is depicted as the fourth process.

### 2.2.2 Literature review on waterjet research

Recently, significant advancements in waterjet technology have been made particular in two areas; compact waterjet technology and capability of computational fluid dynamics (CFD) for design and analysis. New results were reported in the development of compact, axial-flow waterjet technology for high-speed commercial and naval ship applications (Lavis *et al*., 2006a and 2006b, Brewton *et al*., 2006). The current waterjet market is dominated by the mixed-flow waterjets; however, the need for high-speed ship requires the use of slender hull forms and efficient propulsion systems in order to reduce the wave drag and, therefore, the required installed power. Therefore, the axial-flow waterjet system, which is compact propulsion system compared with mixed-flow waterjets, was introduced (for instance, Lavis *et al*., 2006a). Figure 2-4 illustrates the size comparison between the mixed-flow and axial-flow waterjets. The figure shows that the transom flanges of the axial-flow pump can be at least 33% smaller and thus allows three axial-flow pumps to occupy the space needed by two mixed-flow pumps for the same inlet diameter and thus the same unit thrust.

***Experimental study***

The powering performance analysis of waterjet appended hulls using tow tank model testing has been a recent, ongoing area of research.

Wilson *et al*., (2005) presented waterjet propulsion thrust results for a slender, high-speed hull form model propelled with four side-by-side waterjet units (Fn=0.511). It

provided experimental and numerical results for realistic estimates of model scale propulsion interaction factors and the scaling of these results to full scale. Computational studies were carried out using a free surface capable potential flow code. Jessup *et al*., (2007) conducted model tests for the Joint High Speed Ship (JHSS) powered with four compact high density axial flow waterjets. The JHSS is a very large, high speed ship concept for transport of a single Marine Brigade to overseas theaters. Tests were conducted with detailed starboard side LDV surveys at Station 1, ahead of the inlet, Station 3, just ahead of the pump, and Station 6, just downstream of the nozzle. Static wall pressure was measured at the three stations. This approach relied heavily on LDV surveys to best document the flow non-uniformities at each station, with the use of wall static taps to establish the pressure across the station planes. The benefit of compact axial flow waterjet propulsion was explored. To accurately measure jet velocity, testing incorporated all of the approaches explored by the ITTC (Van Terwisga, 2005). These include LDV surveys, bollard tests, single total head probes, and direct measure using weight scales. Also included were traditional four shaft thrust and torque measurements. The JHSS model testing data was selected as the validation test case as extensive data is available together with uncertainty assessments in the present study. More details of experiment including main particulars and lines of JHSS barehull design are shown in the Chapter.4.

Lavis *et al*., (2006a) designed an axial-flow waterjet pump for a notional high-speed sealift ship that would be propelled by four 90-inch diameter axial flow waterjets, each absorbing 57,330 hp. An extensive model-scale evaluation was performed at Carderock Division, Naval Surface Warfare Center (CDNSWC) in 2005 using the 24-inch water-tunnel facility. For the same inlet diameter and thus the same unit thrust, the axial-flow pump has a significant smaller transom footprint than the mixed-flow pump. Therefore, for a given transom area, one can install more number of axial-flow waterjets or conversely, for the same total thrust, the use of axial-flow pumps can allow for a

significantly reduced transom size and thus a significant reduction in wave drag for a high-speed ship.

***Numerical simulation –Part.1: conventional propellers***

There is a continuous trend of increased use of theoretical and computational tools to address marine propulsion hydrodynamics. Improvements in theoretical models allow the investigation of conventional and unconventional propellers in realistic working conditions. In addition, sophisticated computational codes are becoming popular as design and shape optimization tools. Recent developments in propulsor flow simulation and their impact on design are reviewed here. The emphasis is on the work performed for the impact of numerical hydrodynamic tools in design applications.

There has been much work in the area of design optimization of marine propulsor. For instance, Mishima (1996) studies the design of cavitating propeller blades using gradient-based numerical optimization method. Black (1995) developed a method for computing optimum blade sections by using a 2D interactive potential panel method and boundary layer solver in a strip-wise sense. Additionally, generic algorithm was used to perform the optimization and included such design constraints as cavitation inception prediction, lift/drag maximization, and flow separation avoidance. Coney (1989) developed a method to compute optimum radial circulation distributions for a circumferentially averaged inflow. Traditionally, this is the first step in designing a propeller. One would then use an inverse method to design the blade which would produce the given circulation distribution (Kerwin, 1973, Kerwin *et al*., 1994). In this era of researching the design method for propellers is based on the analysis of potential-based panel methods. Performing optimization on more complex geometries and reliable analysis requires solving the nonlinear unsteady RANS equations. Brewer *et al*., (2003) proposed the design method for investigating cavitation delay using unstructured RANS solver with the ability to compute sensitivity derivatives via a Complex Taylor series expansion (CTSE) method. The localized region affecting caviation inception is

parameterized and represented by using either Non-Uniform Rational B-Spline or a Bezier patch/curve. In the study, the objective is set to maximize the minimum pressure in the trailing vortex system. Takekoshi *et al*., (2005) presented the study on the design of propeller blade sections using the optimization algorithms. A vortex lattice method is used to evaluate the performance with consideration of the occurrence of cavitation in a non-uniform flow. The objectives are set to twofold; design to realize a target pressure distribution in a rotating three-dimensional flow and design to maximize the propeller efficiency. The quasi-Newton algorithm with the Broyden-Fletcher-Goldfarb-Shannon (BFGS) update is used as optimizer for unconstrained problems; whereas, SQP method is used for constrained problems. Several optimization exercises are demonstrated, and the results show the proposed approach can be used as a design tool. However, since the potential theory based simulation was carried out, the viscous effect was treated approximately. Chen *et al*., (2007) showed that it is possible to use a genetic algorithm to design a series propeller not only when considering the optimization of hydrodynamic efficiency with material strength and caviation limitations but also when considering the optimization of both efficiency and vibration, provided that the wake information of the ship is known.

***Numerical simulation –Part.2: Waterjet propulsion system***

Recent innovations in CFD and high performance computing have enabled faster and cost effective approach for predicting waterjet propulsive characteristics. This has enabled detailed analysis of the flow through the waterjet ducts, which would require prohibitively expensive Laser Doppler Velocimetry (LDV) measurements if the whole flow field has to be measured. Such detailed flow analysis is required for a deeper understanding of the flow physics giving insights into further improvement of the performance characteristics of the waterjet. However, the numerical approach has to be thoroughly validated before relying on it for performance analysis, design, and optimization.

Bulten (2006) performed a detailed investigation both experimentally and numerically on a waterjet test setup where the waterjet inlet was mounted on top of a cavitation tunnel. The mass flow rate in the tunnel was adjusted to get the desired inlet velocity ratio (IVR) values. This was modeled in the CFD using a prescribed velocity profile at the inlet of the cavitation tunnel and a constant pressure boundary condition at the outflow plane. The waterjet stator and rotor geometry was also modeled. Validation demonstrated that the standard two equation turbulence model in combination with wall functions was able to predict the non uniformities in the duct flow field with acceptable accuracy. The results showed that the main inlet flow characteristics such as cavitation inception at cutwater where the flow to the duct separates from the main flow, velocity distribution at the impeller plane, flow separation at the inlet, the shape of the inlet stream tube are related to the IVR. The author recommends that a dedicated inlet design is recommended for each ship since variations in design ship speed and power density of the installations cause the design IVR to vary. Bulten and Verbeek (2004) also use a commercial code which has been developed with a steady-state multiple frame of reference (MFR) approach and with a fully transient moving mesh method, which computed results are validated by a comparison with experimental data. The authors conclude that the developed code with an MFR approach has a very good accuracy in the computation of thrust and torque of the impeller. Moreover, the unsteady transient computation gives more insight in the pressure fluctuations.

The waterjet analysis for the use of amphibian vehicle was performed by Jang *et al*., (2004) to provide detail understanding of complicated three-dimensional viscous flow phenomena including interactions of intake duct, rotor, stator, and contracted discharge nozzle. RANS flow solver with moving, non-orthogonal multi-block grid system was used. The CFD results were compared with experimental fluid dynamics (EFD) and the complex viscous flow feature of the waterjet, such as the secondary flow inside of the intake duct, the recovery of axial flow by the action of the stator, and tip vortex were

predicted. The performance prediction of waterjet for the use of similar vehicle by diameter sizes and weights were investigated both numerically and experimentally by Kim *et al*., (2009). Numerical methods for the prediction of performance and design of the waterjet rotor and stator components were presented in some literatures. For example, Kerwin *et al.*, (2006) proposed the approach based on inviscid flow methods (vortex-lattice methods) applied on the blades of the rotor or stator, coupled with Euler equations solver for the solution of the global flow through the pump. In their study, axial flow pumps subject to uniform upstream inflow were addressed. As such literatures, many reported the analysis of waterjet but not with consideration of waterjet-hull interaction.

An extensive study was undertaken to analyze the effect of integrating RANS calculations into experimental waterjet powering prediction by Delaney *et al.*, (2009). Two different JHSS hull forms were considered; one houses axial-flow waterjet and the other houses mixed-flow waterjet. Multi-element unstructured grids and boundary layer prism elements were generated around waterjet geometry. The hull, waterjet inlets, and shafts were all modeled. The free surface was treated as a symmetry plane, and the ship was modeled at sinkage and trim prescribed by the propelled experiment. RANS simulation used experimentally determined volumetric flow rates through the pump as a condition for the thrust provided by the actuator disk model. The effects of shaft (without, with stationary, with rotating) on the flow field non-uniformity were explored. The full scale simulations (Fn=0.35, Rn=$5.3\times10^9$) were performed in order to investigate the scaling effects by comparing boundary layers. The simulations results were discussed in particular on St 1 and 3; and RANS and EFD delivered pump power predictions agreed to within one percent at model scale and within two percent at full scale. Hino *et al.* (2009) also performed RANS analyses of a free surface flow around waterjet propelled high-speed ship (Fn=1.0, Rn=$1.0\times10^6$) using in-house RANS code, SURF. Free surface location was predicted using single-phase level set approach. An actuator disk model in which waterjet duct geometry is modeled in a computational grid was used to simulate

the self-propelled condition. The nozzle shape was not modeled, and dynamic motions were not estimated. The flow fields of waterjet propelled simulations, such as free surface elevations, pressure distributions in the duct center planes, and limiting streamlines on a ship, were compared with the towed simulations; however, the detailed V&V results were not given. Brewton *et al*., (2006) presented computations of steady performance and detailed flow in the axial-flow pump designed by Lavis *et al*., (2006a) using RANS code with a mixing-plane approach. The authors show a comparison between the computations and measurements of headrise and efficiency as a function of flow rate, and the agreement between RANS computations and measurements is very good.

In the present study, computational setup differs from previous studies in that the waterjet-hull interactions and waterjet-wake interactions are also predicted with free surface and dynamic motions. URANS with the blended k-ε/k-ω turbulent model is selected as a flow solver, and free surface location is predicted using single-phase level set approach. Self propulsion simulations are carried out at model scale with an added tow force to compensate for the extra drag due to thicker boundary layer at model scale to get thrust loading similarity. A body force model is used inside the duct instead of modeling the impeller, as the latter requires significantly more computational effort and is not needed for the purpose of calculating the waterjet performance indicators such as net thrust and waterjet system efficiency (Bulten & Van Esch, 2007). The simulations are carried out over a range of ship speed at different IVR ratios for the waterjet. The control volume analysis used for the powering performance predictions in the towing tank test is replicated to get the net jet system thrust. Waterjet-hull interaction effects are highly non-linear as they include the effect of the dynamic trim on boundary layer ingestion and shape of inflow stream tube, together with the effect of the waterjet induced vertical forces on the dynamic trim. Also, the shape of the ingested boundary layer is not uniform over the entire cross-section at the inlet and depends on the hull form. This phenomenon affects the non-uniformity of the flow inside the duct and hence affects the inlet

efficiency. The waterjet-wake interactions do not significantly affect the propulsion characteristics, but are of interest in the study of wake signatures. Since one of the main focuses of the current optimization endeavor is the optimization of the waterjet inlet geometry with regards to hull interaction and stern forces, a detailed validation of the prediction capability of URANS for high speed waterjet propelled sealifts is necessary.

Another development on waterjet numerical simulation is under research at IIHR. The IIHR waterjet model is an integral force/moment model that was derived in relative-inertial coordinates to improve the accuracy of CFD predictions for performance of waterjet-propelled vessels; such as resistance, sinkage, and trim without requiring detailed modeling (Kandasamy *et al.*, 2010). It builds on the ITTC waterjet model for sinkage and trim by using an alternative control volume also appropriate for CFD and by including both horizontal and vertical forces and angular momentum. Additionally, the waterjet induced forces on the hull stern due to waterjet-hull interaction are included in the balance of forces and moments for the vessel. Experimental results for the DTMB 5594 model from Wilson *et al*., (2005) are used to provide input parameters and to validate. Also, the IIHR waterjet model, which is applied to CFDSHIP-Iowa, is compared with ITTC model for predictions of resistance, sinkage, and trim. Correlations for the waterjet flow input variables are shown to be feasible using combination of CFD and experimental data for the waterjet system for three different hulls; i.e., Delft Catamaran, JHSS, and DTMB 5594.

***Numerical design optimization on waterjet***

During last decades, a lot of researches on waterjet propulsion have been proposed by both experimentally and numerically as fore-reviewed. Numerical study on waterjet using potential-theory-based flow solver or high fidelity RANS solver is relatively new, and nevertheless, most CFD work was devoted to the intake duct only. In fact, numerical study on the design of duct and intake shape has been rarely carried out.

An automatic optimization design study for the waterjet intake duct was presented by Hu and Zangeneh, (1999). In their method, the central plane geometry of the waterjet intake duct is optimized based on 2D RANS code. The objective of the optimization was to minimize the stagnation pressure loss and the searching direction was controlled by the Simplex algorithm. After the 2D design optimization had been solved, 3D geometry of the intake duct was designed based on the optimized 2D geometry using commercial RANS code, fluent. The deformation of the geometry is made by B-Spline with control points. It was found that optimization was successful in terms of not only reduction of the loss but the suppression of separation near to the lip wall; as a result, the flow in the duct exit became more uniform.

Lavis *et al*., (2006b) developed and validated the attributes of a preferred compact waterjet propulsor suitable for high-speed sealift applications where waterjet propulsion is the only realistic choice. To design high-power density axial flow waterjets, a trade-off study to determine the best hull form and propulsion machinery arrangement were studied. Waterjet propulsion system design included pump geometry, inlet geometry, and nozzle design. TURBOdesign was used to develop the detailed geometry of the rotor blade using the meridional geometry, radial loading distribution, and blade numbers based on the diffusion factor developed using the streamline curvature method. The method is a potential-flow inverse method where the requirements for the rotor are inputs and the blade geometry is the output. For the inlet geometry design, the analytical approach was developed that would allow the inlet design to be revised and updated in a timely manner as layout requirements in the hull and CFD computational results dictated. Centerline cut through a waterjet inlet was displayed using some basic geometric parameters. After some promising designs were obtained, they conducted model testes to investigate the pump performance and cavitation tests.

Nevertheless, there is few literature reported on the optimization research for the waterjet intake design that waterjet-hull interaction is taken into account. In addition,

more sophisticated optimization algorithms, such as RCGA or PSO mentioned previous section, can be used in order to achieve more ideal design optimization. In the present study, the main objective of optimization study is to decrease powering requirement by increasing the inlet efficiency through modification of the intake duct shape. URANS flow solver is employed as a flow solver, and the global optimization algorithm is employed as optimizer so that more practical design approach for waterjet propulsion system can be built.

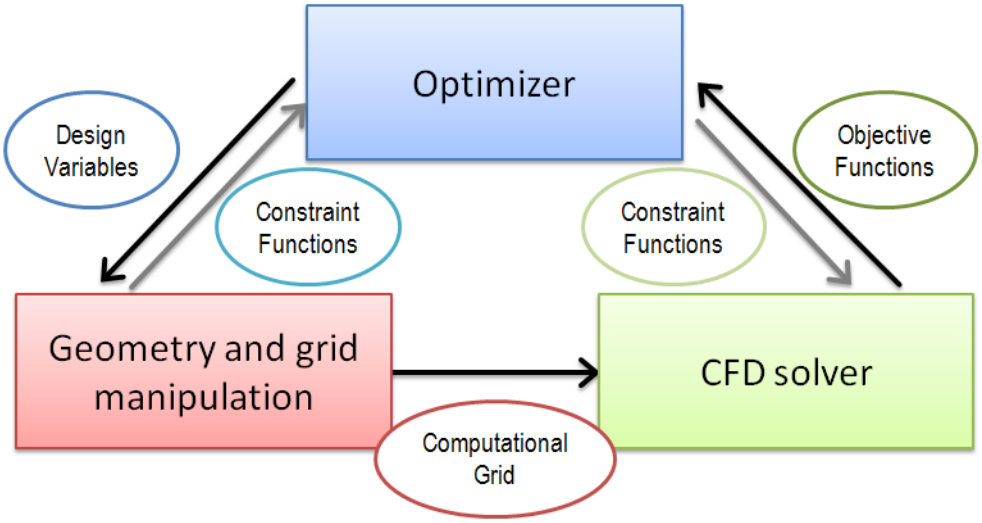


Figure 2-1 Illustration of general idea of SBD system (components and relationship)

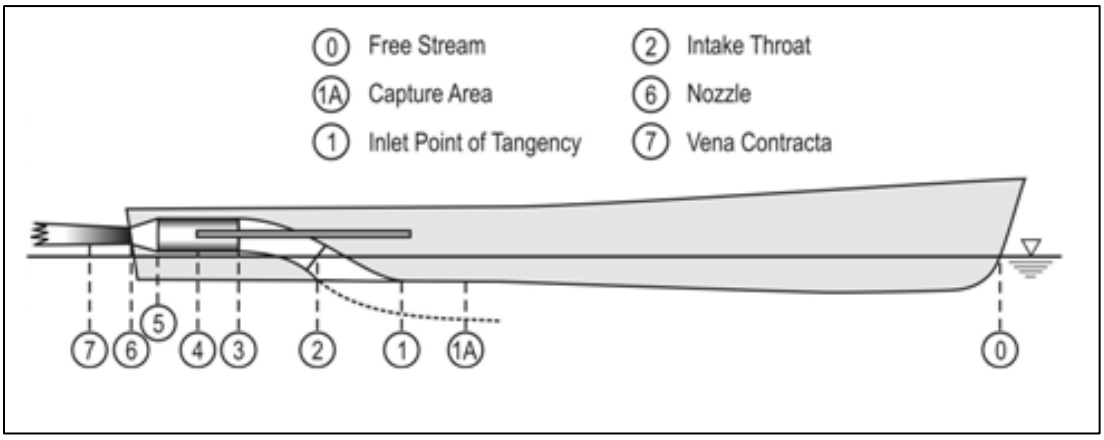


Figure 2-2 ITTC definitions of control volume analysis stations

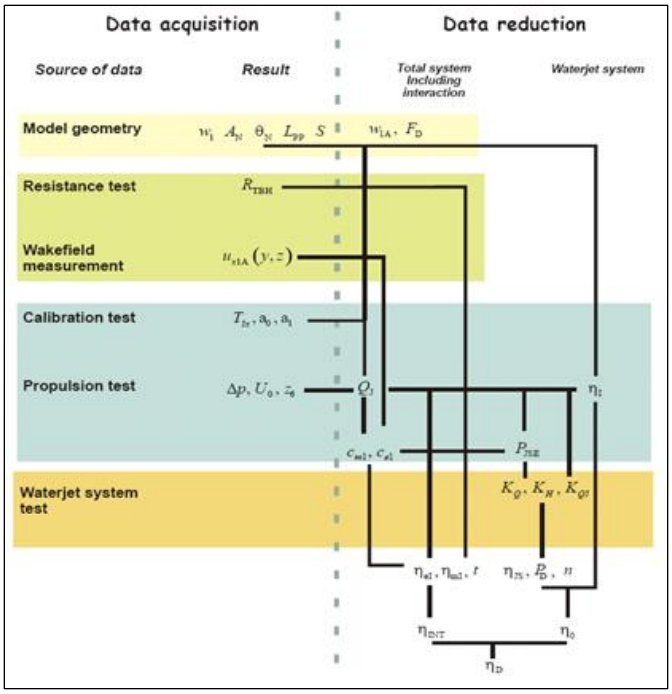


Figure 2-3 Data flow through data acquisition and data reduction phase for determination of powering characteristics from model tests recommended by ITTC

Source: Van Terwisga *et al*., (2005), "ITTC Proceedings-Volume 2: The Specialist Committee on Validation of Waterjet Test Procedures"

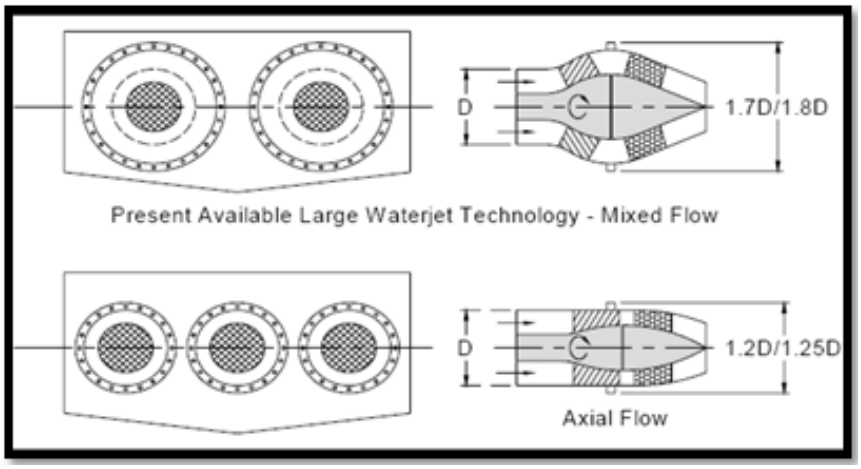


Figure 2-4 Pump size comparison between mixed-flow and axial-flow waterjet system

Source: Lavis, *et al*., (2006a), "Compact Waterjets for High-Speed Ships"

# CHAPTER 3
# COMPUTATIONAL METHOD

## 3.1 CFDSHIP IOWA: URANS/DES solver

The Unsteady Reynolds-Averaged Navier Stokes (URANS)/ Detached Eddy Simulation (DES) flow solver, CFDSHIP-IOWA has been developed at IIHR – Hydroscience & Engineering – over the past 15 years for ship hydrodynamics applications. It was originally designed to support both thesis work and project research, and it has been successfully transitioned to US Navy, University laboratories and industries. CFDSHIP-IOWA solves an incompressible 3D URANS equation with single-phase level set method as a free surface modeling, and isotropic/anisotropic k-ε/k-ω model with DES option as a turbulence modeling (Carrica *et al*., 2007a; Xing *et al*., 2008). Overset multi-block numerical grid technique is adopted to simulate dynamic ship motions and local grid refinement; in particular, the code SUGGAR (Structured, Unstructured and Generalized overset Grid Assembler, Noack, 2005) is used to obtain the overset domain connectivity between the set of overlapping grids. Message Passing Interface (MPI) based decomposition approach is used to run the code, where each decomposed block is mapped to one processor. Additionally, CFDSHIP-IOWA utilizes absolute/relative inertial earth-fixed coordinate system and non-inertial ship-fixed coordinate system to describe prescribed/predicted ship motions (Xing *et al*., 2008). Predicted ship motions are computed by the rigid-body motion equations for six degrees of freedom (6DOF); namely, surge, sway, heave, pitch, roll, and yaw (Carrica *et al*., 2007b). In addition, CFDSHIP-IOWA has interface with 3$^{rd}$ party commercial software for grid generation and boundary condition assignment by GRIDGEN© and post processing and visualization by TECPLOT 360.

In the present study, URANS with the blended k-ε/k-ω turbulent model is selected as a flow solver. The free surface location is predicted by a single-phase level-set method. A second order upwind scheme is used to discretize the convective terms of the momentum equations for URANS. A pressure-implicit split-operator (PISO) algorithm is used to enforce mass conservation on the collocated grids. The pressure Poisson equation is solved using the PETSc toolkit (Belay *et al*., 2002). All the other systems are solved using an alternating direction implicit (ADI) method. For a high performance parallel computing, a MPI-based domain decomposition approach is used, where each decomposed block is mapped to one processor. The code SUGGAR runs as a separate process from the flow solver to compute interpolation coefficients for the overset grids and communicates with a motion controller (6DOF) within CFDSHIP-Iowa at every timestep. The software USURP (Boger and Dreyer, 2006) is used to compute area and forces on the surface overlapped regions.

In addition, a simplified body force model is used for waterjet propelled simulation to prescribe axisymmetric body force with axial and tangential components (Stern *et al*., 1996). The propeller model requires thrust, torque, and advance coefficients as input and provides the torque and thrust forces. These forces appear as a body force term in the momentum equations for the fluid inside the propeller disk. The location of the propeller is defined in the static condition of the ship and moves according to the ship motions.

In the following sections, the mathematical model will be given in more detail and the numerical technique and solution strategy will be illustrated.

## 3.2 Modeling

### 3.2.1 Coordinate system

The general purpose solver CFDSHIP-IOWA solves an incompressible URANS equation in the liquid phase of a free surface flow. The coordinate system in CFDSHIP-IOWA Version.4 is shown in Figure 3-1. The governing differential equations of motions are derived and solved in the absolute inertial earth-fixed coordinate system $(X, Y, Z)$ for an arbitrary moving but non-deforming control volume and solution domain, respectively. As shown in Figure 3-1, control volume is for either the ship in black or background in gray. A non-inertial ship-fixed reference coordinates $(x, y, z)$, whose origin $o$ is located at the center of gravity (CoG) of the ship, is related to the fixed reference frame by the position vector $\underline{\mathbf{R}}$ in $(X, Y, Z)$. The linear ship translation velocity of the ship at absolute inertial earth-fixed coordinate system is;

$$\mathbf{U} = \underline{\dot{\mathbf{R}}} = \dot{\partial}\underline{R}/\partial t = u_i \mathbf{i}_0 + v_i \mathbf{j}_0 + w_i \mathbf{k}_0 \tag{3 1}$$

where $(\mathbf{i}_0, \mathbf{j}_0, \mathbf{k}_0)$ are the unit vectors of $X, Y\ and\ Z$ axes, respectively, and $U_i = (u_i, v_i, w_i)$ are the surge, sway and heave velocities in $(X, Y, Z)$. The ship rotates with angular velocity;

$$\underline{\boldsymbol{\Omega}} = \Omega_X \mathbf{i}_0 + \Omega_Y \mathbf{j}_0 + \Omega_Z \mathbf{k}_0 \tag{3 2}$$

around $(x, y, z)$ with respect to $(X, Y, Z)$ where $\boldsymbol{\Omega}_i = (\Omega_X, \Omega_Y, \Omega_Z)$ are the pitch, roll and yaw angular velocities of $(x, y, z)$ in $(X, Y, Z)$. The velocity of the control volume $\mathbf{U}_G$, in other words the grid velocity, is defined as;

$$\mathrm{U}_G = \dot{\underline{\mathrm{R}}} + \underline{\Omega} \times \underline{\mathrm{r}} \tag{3.3}$$

where $\underline{\mathbf{r}}$ is the instantaneous position vector of any point in $(x, y, z)$.

### 3.2.2 Governing equations

The continuity and momentum equations in nondimensional tensor form for the water phase can be written as;

$$\frac{\partial U_i}{\partial x_i} = 0 \tag{3.4}$$

$$\frac{\partial U_i}{\partial t} + U_j \frac{\partial U_i}{\partial x_j} = \frac{\partial \hat{p}}{\partial x_i} + \frac{1}{Re} \frac{\partial^2 U_i}{\partial x_j \partial x_j} - \frac{\partial}{\partial x_j} \overline{u_i u_j} + f_{bi}^* \tag{3.5}$$

where $U_i = (U, V, W)$ are the Reynolds-averaged velocity components, $x_i = (x, y, z)$ are the independent coordinate directions, $\hat{p} = \left(\frac{p - p_\infty}{\rho U_0^2} + {}^{z}/_{F_n^2}\right)$ is the piezometric pressure coefficient, $\overline{u_i u_j}$ are the Reynolds stresses, and $f_{bi}^*$ is non-dimensional body-force vector$\left(= f_{bi}\, L/\rho U_0^2\right)$ , where $f_{bi}$ is a force per unit volume which represents the effect of the propeller. Equations (3.4) and (3.5) are non-dimensionalized with a characteristic velocity $U_0$ (ship speed), characteristic length $L$ (ship length), fluid density $\rho$ and viscosity $\mu$. The $F_n$ and $R_n$ are defined as;

$$F_n = \frac{U_0}{\sqrt{gL}} \tag{3.6}$$

$$R_n = \frac{\rho U_0 L}{\mu} \tag{3.7}$$

Equations (3.4) and (3.5) can be transformed into the relative-inertial coordinate system $(X', Y', Z')$ translating at prescribed velocity $\mathbf{U}_C$ relative to $(X, Y, Z)$ by replacing;

$$U_j = U_j^{'} + U_{Cj} \tag{3.8}$$

$$U_{Gj} = U_{Gj}^{'} + U_{Cj} \tag{3.9}$$

where $U_j^{'}$ and $U_{Gj}^{'}$ are the fluid and grid velocities in $(X', Y', Z')$, respectively. When the computation is executed, Equations (3.4) and (3.5) are transformed from physical domain in Cartesian coordinate system to computational domain in non-orthogonal curvilinear coordinate system.

### 3.2.3 Turbulence modeling

The Reynolds stress ($-\overline{u_i u_j}$ ) are directly related to the mean rate of strain through an isotropic eddy viscosity $\nu_t$. In Cartesian coordinates, the expression is;

$$-\overline{u_i u_j} = \nu_t \left( \frac{\partial U_i}{\partial x_j} + \frac{\partial U_j}{\partial x_i} \right) - \frac{2}{3} \delta_{ij} k \tag{3.10}$$

where $\delta_{ij}$ is the Kronecker delta and $k$ is the turbulent kinetic energy (TKE). This equation can be closed by calculating the eddy viscosity.

To compute the turbulence viscosity, the blended k-ε/k-ω turbulence model is used in the present study. It is a combination of k-ω and k-ε models that keeps the advantages of both methods. In short, the k-ω model is used in viscous sub-layer because it does not involve damping functions allowing a simple Dirichlet boundary condition to be specified at solid wall, and in the log-layer for its capability in predicting adverse pressure gradient flows. Hence, it is better than other turbulent models regarding to numerical stability. In the wake region of the boundary layer and in the free shear layers, the k-ω model must be abandoned in favor of the k-ε model. The k-ω, in fact, presents some deficiencies related to the high sensitivity to the quite arbitrary free-stream,

specified for ω outside the boundary layer. On the contrary, the k-ε does not exhibit this deficiency and seems to be a fair compromise in predicting shear flows. To achieve the desired features in the different regions, a blending function is defined. The blending function is designed to be one in the viscous sub-layer and log-layer, activating the k-ω model and then gradually switches to zero in the outer wake region and free shear layers with activating the k-ε model. Detailed mathematical expression is shown in follows.

***Blended k-ε/k-ω shear stress transport (SST) model.***

The TKE and specific dissipation rate $\omega$ are computed from;

$$\frac{\partial k}{\partial t} + \left\{\left(U_j - U_{Gj}\right) - \sigma_k \nabla \nu_t\right\} \cdot \nabla k - \frac{1}{P_k} \nabla^2 k + s_k = 0 \tag{3.11}$$

$$\frac{\partial \omega}{\partial t} + \left\{\left(U_j - U_{Gj}\right) - \sigma_\omega \nabla \nu_t\right\} \cdot \nabla \omega - \frac{1}{P_\omega} \nabla^2 \omega + s_\omega = 0 \tag{3.12}$$

The $\nu_t$ and the effective Peclet numbers for $k$ ($P_k$) and $\omega$ ($P_\omega$) are defined as;

$$\nu_t = \frac{0.31k}{\max(0.31\omega, \Omega F_2)} \tag{3.13}$$

$$P_{k/\omega} = \frac{1}{\frac{1}{Re} + \sigma_{k/\omega} \nu_t} \tag{3.14}$$

where Ω in Equation (3.13) is the absolute value of the vorticity. The sources for $k$ ($S_k$) and $\omega$ ($S_\omega$) are;

$$S_k = -G + \beta^* \omega k \tag{3.15}$$

$$S_\omega = -\gamma \frac{\omega}{k} G + \beta^* \omega^2 - 2(1 - F_1)\sigma_{\omega 2} \frac{1}{\omega} \nabla k \cdot \nabla \omega \tag{3.16}$$

$$G = \tau_{ij} \frac{\partial U_i}{\partial x_j} \tag{3.17}$$

The blending functions $F_1 and\ F_2$ for blended k-ε/k-ω SST model are;

$$F_1 = tanh\left(\left\{min\left[max\left(\frac{\sqrt{k}}{0.09\omega\delta};\frac{500}{Re\,\delta^2\omega}\right);\frac{4\sigma_{\omega 2}k}{CD_{k\omega}\,\delta^2}\right]\right\}^4\right) \tag{3.18}$$

$$F_2 = tanh\left(max\left(\frac{2\sqrt{k}}{0.09\omega y};\frac{500\nu}{y^2\omega}\right)^2\right) \tag{3.19}$$

$$CD_{k\omega} = max\left(2\sigma_{\omega 2}\frac{1}{\omega}\frac{\partial k}{\partial x_j}\frac{\partial \omega}{\partial x_j};10^{-20}\right) \tag{3.20}$$

The blending function $F_1$ is designed to be unity in the viscous sub-layer and logarithmic regions of boundary layers and gradually switches to zero. The blending function $F_2$ is specifically designed for SST model where $y$ in Equation (3.19) is the nearest spacing to the wall. The model constants appeared in the equations above ($\phi$, including $\sigma_k$, $\sigma_\omega$, $\beta^*$,$\kappa\ and\ \gamma$) are calculated from the blending function;

$$\phi = F_1\phi_1 + (1 - F_1)\phi_2 \tag{3.21}$$

where $\phi_1\ and\ \phi_2$ are the constants.

### 3.2.4 Free surface modeling

Among the free surface capturing techniques, the level-set method is becoming very popular in predicting moving interfaces and can predict the evolution of complex flows including waves with large slopes, wave breaking, deforming bubbles and droplets, break up and coalescence, and so on. The free surface of ship flows is only one particular case of a more general problem involving the evolution of the interface between two or more fluids. In the classical level-set approach, equations for both fluids are solved; however, there are some fluid/fluid problems in which the interface can be considered as

a free boundary and hence the computation can be limited to the more viscous and dense fluid (single-phase level-set method). The solution of the equations involving water phase only, presents more advantages in terms of robustness in computation than in terms of computational time over the classical level set approach involving both phases. In fact, only one fluid with constant properties is solved in this case. Therefore, the classical pressure and velocity oscillations present at the interface between two fluids with high density ratios, are circumvented. Another advantage is that pressure is not solved in air and velocity and turbulence quantities follow a linear convection equation, resulting in a faster computation effort. However, this method needs the introduction of a boundary condition for pressure at the interface. As the computational grid is fixed in space and time, the detection of the free surface is necessary and this has a cost in terms of computational time.

***Single phase level set method***

In a single-phase level set method, the free surface location is identified as the zero level set of a signed distance function $\phi$, known as the level set function that is positive in water and negative in air. Since the interface is a material surface, the equation for the level set function satisfies the following equation;

$$\frac{\partial \phi}{\partial t} + \left(U_j - U_{Gj}\right)\frac{\partial \phi}{\partial x_j} = 0 \tag{3.22}$$

In the single-phase level set method, the jump condition at the free surface must be explicitly enforced since we solve the equations of motion only in water. Neglecting shear stress in the air, the jump condition at the free surface is;

$$\frac{\partial U_i}{\partial x_j} n_j \big|_{int.} = 0 \tag{3.23}$$

As a good approximation for air-water interfaces, the pressure on the air is equal to the atmospheric pressure. The dimensionless piezometric pressure at the air-water interface is then given by;

$$p_{int.} = \frac{z_{int.}}{Fr^2} \tag{3.24}$$

The solution of Equations (3.4) and (3.5) provides the appropriate transport velocity for the level set function in water. In air, Equation (3.22) guarantees that the boundary condition for velocity is satisfied and in addition provides a velocity that will keep the level set function a distance function; the velocity so obtained is called an extension velocity. Equations (3.5) and (3.22) are solved simultaneously. Since the convective transport of $\phi$ will not keep it a distance function, the level set is reinitialized periodically everywhere except at the interface by solving;

$$\mathbf{n} \cdot \nabla\phi = sign(\phi_0) \tag{3.25}$$

where $\phi_0$ is the level set function before reinitializing. The normal $\mathbf{n}$ points in this case into the fluid to be reinitialized.

### 3.2.5 Rigid body equations and 6DOF module

The governing equations of fluid motion, i.e. Equations (3.4) and (3.5) are strongly coupled with the rigid body equations of motions to solve 6DOF motions of a ship hull. The dynamic pressure force $\mathbf{F}_p$ and the hydrostatic pressure force $\mathbf{B}$ in the absolute inertial earth-fixed coordinate system for the ship are computed from;

$$\mathbf{F}_p = -\int_{Sw} p d\mathbf{a} \tag{3.26}$$

$$\mathbf{B} = \int_{Sw} \frac{z}{Fr^2} d\mathbf{a} \tag{3.27}$$

where $\mathbf{a}$ is a outward pointing area vector and $S_w$ is the wetted surface area. The friction forces $\mathbf{F}_f$ are computed using the velocity in the absolute inertial earth-fixed coordinate system as;

$$\mathbf{F}_f = \frac{1}{2Re} \int_{Sw} (\nabla \mathbf{U} + \nabla \mathbf{U}^{\mathrm{T}}) \cdot d\mathbf{a} \tag{3.28}$$

The total force $\mathbf{F}_t = \left(F_{tx}, F_{ty}, F_{tz}\right)$ is the summation of Equations. (3.26), (3.27) and (3.28) as;

$$\mathbf{F}_t = \mathbf{F}_p + \mathbf{B} + \mathbf{F}_f \tag{3.29}$$

The total moment $\mathbf{M}_t = \left(M_{tx}, M_{ty}, M_{tz}\right)$ are found from integrating the elemental forces by friction and pressure with the distance to the CoG $\mathbf{r}_{CG}$ as;

$$\mathbf{M}_t = \int_{Sw} \mathbf{r}_{CG} \times \left\{ \left[ \left( \frac{\nabla \mathbf{U} + \nabla \mathbf{U}^{\mathrm{T}}}{2Re} \right) - \left( p - \frac{z}{Fr^2} \right) \mathbf{I} \right] \cdot d\mathbf{a} \right\} \tag{3.30}$$

The $\mathbf{F}_t \; and \; \mathbf{M}_t$ are then projected into the non-inertial ship-fixed coordinate system and expressed as $\mathbf{F}_b = \left(F_{bx}, F_{by}, F_{bz}\right) \; and \; \mathbf{M}_b = \left(M_{bx}, M_{by}, M_{bz}\right)$, respectively, using Euler angle rotation matrix $\mathbf{J}_1$as;

$$\mathbf{J}_1 = \begin{bmatrix} cos\psi cos\theta & -sin\psi cos\phi + cos\psi sin\theta sin\phi & sin\psi sin\phi + cos\psi cos\phi sin\theta \\ sin\psi cos\theta & cos\psi + sin\phi sin\theta sin\psi & -cos\psi sin\phi + sin\theta sin\psi cos\phi \\ -sin\theta & cos\theta sin\phi & cos\theta cos\phi \end{bmatrix}$$

(3.31)

$$\mathbf{F}_b = \mathbf{J}_1 \mathbf{F}_t \tag{3.32}$$

$$\mathbf{M}_b = \mathbf{J}_1 \mathbf{M}_t \tag{3.33}$$

where $\sigma = (\phi, \theta, \psi)$ are the Euler angles of roll, pitch and yaw, respectively, at $(x, y, z)$. The rate of change in Euler angle $\dot{\sigma}$ is computed using $\mathbf{\Omega}_b = (\Omega_x, \Omega_y, \Omega_z)$ which is angular velocity vector with respect to$(x, y, z)$, and another transformation matrix $\mathbf{J}_2$ as;

$$\mathbf{J}_2 = \begin{bmatrix} 1 & sin\phi tan\theta & cos\phi tan\theta \\ 0 & cos\phi & -sin\phi \\ 0 & sin\phi/cos\theta & cos\phi/cos\theta \end{bmatrix} \tag{3.34}$$

$$\dot{\sigma} = \mathbf{J}_2 \mathbf{\Omega}_b \tag{3.35}$$

Finally the rigid body equations to be solved in non-inertial ship-fixed coordinate system are;

$$m\left(\frac{\partial u_b}{\partial t} - v_b\Omega_z + w_b\Omega_y\right) = F_{bx} + W_{bx} \tag{3.36}$$

$$m\left(\frac{\partial v_b}{\partial t} - w_b\Omega_z + u_b\Omega_y\right) = F_{by} + W_{by} \tag{3.37}$$

$$m\left(\frac{\partial w_b}{\partial t} - u_b\Omega_z + v_b\Omega_y\right) = F_{bz} + W_{bz} \tag{3.38}$$

$$I_x \frac{\partial \Omega_x}{\partial t} + \left(I_z - I_y\right)\Omega_y\Omega_z = M_{bx} \tag{3.39}$$

$$I_y \frac{\partial \Omega_y}{\partial t} + (I_x - I_z)\Omega_x\Omega_z = M_{by} \tag{3.40}$$

$$I_z \frac{\partial \Omega_z}{\partial t} + \left(I_y - I_x\right)\Omega_x\Omega_y = M_{bz} \tag{3.41}$$

where $\mathbf{U}_b = (u_b, v_b, w_b)$ is the linear translation velocity of the ship at non-inertial ship-fixed coordinate system, $\mathbf{I} = (I_x, I_y, I_z)$ is the moment of inertia of a ship, and $\mathbf{W}_b = (W_{bx}, W_{by}, W_{bz})$ is gravity. Integration of Equations (3.36) to (3.41) provides $\mathbf{U}_b$ and $\mathbf{\Omega}$, and then they are transformed back to the absolute inertial earth-fixed coordinate system using $\mathbf{J}_1^{-1}$ as;

$$\mathbf{U} = \dot{\mathbf{R}} = \mathbf{J}_1^{-1}\mathbf{U}_b \tag{3.42}$$

$$\mathbf{\Omega} = \mathbf{J}_1^{-1}\mathbf{\Omega}_b \tag{3.43}$$

New ship position of the ship is obtained by integrating $\mathbf{R}\ and\ \dot{\sigma}$ with respect to time. The position vectors and grid velocity are computed by;

$$\mathbf{R}_n = \mathbf{R}_{n-1} + \int_{t_{n-1}}^{t_n} \mathbf{U} dt \tag{3.44}$$

$$\boldsymbol{\eta}_n = \boldsymbol{\eta}_{n-1} + \int_{t_{n-1}}^{t_n} \dot{\boldsymbol{\eta}} dt \tag{3.45}$$

$$\mathbf{U}_G = \dot{\mathbf{R}} + \mathbf{\Omega} \times \mathbf{r} \tag{3.46}$$

### 3.2.6 Body force propulsor modeling

For waterjet self-propulsion simulation, a simplified body-force model is used to prescribe axisymmetric body force with axial and tangential components. The momentum Equation (3.5) includes a body-force term $f_{bi}$ , which may be used to model the effects of a propulsor resolving the detailed blade flow. There are numerous approaches to calculate $f_{bi}$ including simple prescribed distributions, which recover the total thrust and torque, to

more sophisticated methods which use a propeller performance code in an interactive fashion with the RANS solver to capture propeller-hull interaction and to distribute $f_{bi}$ according to the actual blade loading. The radial distribution of force is based on the Hough and Ordway circulation distribution, which has zero loading at the root and chip shown as following equation;

$$f_{bx} = A_x r^* \sqrt{1 - r^*} \tag{3.47}$$

$$f_{b\theta} = A_\theta \frac{r^* \sqrt{1 - r^*}}{(1 - R_H) r^* + R_H} \tag{3.48}$$

where

$$r^* = \frac{r/RP - RH}{1 - RH} \tag{3.49}$$

$$r = \sqrt{(y - Y\_PROP\_CENTER)^2 + (z - Z\_PROP\_CENTER)^2} \tag{3.50}$$

$$A_x = \frac{C_T}{(DXPROP)} \frac{105}{16(4+3RH)(1-RH)} \tag{3.51}$$

$$A_\theta = \frac{K_Q}{(DXPROP)\, J^2} \frac{105}{\pi(4+3RH)(1-RH)} \tag{3.52}$$

where $C_T$ and $K_Q$ are the thrust and torque coefficients, $J$ is the advance coefficient, $RP$ is the propeller radius non-dimensionalized by ship length, $RH$ is the hub radius in decimal percent of $RP$, and $DXPROP$ is the mean chord length projected into the *x*-*z* plane.

As derived, these forces are defined over an "actuator cylinder" with volume defined by $RP$, $RH$, and $DXPROP$, i.e., $\pi\left(RP^2(1 - RH^2)\right)DXPROP$. Integration of the body forces over this analytical volume exactly recovers the prescribed thrust and torque;

$$T = \rho L^2 \, U_0^2 \int_{RH}^{RP} \int_0^{2\pi} \int_{x_p}^{x_s} f_{bx} r \, dx \, d\theta \, dr \tag{3.53}$$

$$Q = \rho L^3 \, U_0^2 \int_{RH}^{RP} \int_0^{2\pi} \int_{x_p}^{x_s} f_{b\theta} \, r^2 \, dx \, d\theta \, dr \tag{3.54}$$

Integration of the body forces over this analytical volume exactly recovers the prescribed thrust and torque. During simulation, the ship accelerates until the resistance equals the prescribed thrust and added tow force and converges to the self propulsion point.

Since curvilinear non-orthogonal multi-block numerical grids are used in the present study, implementation of Equations (3.47) and (3.48) requires several issues to be addressed. A vertex-based search algorithm is used to determine which grid-point control volumes are within the actuator cylinder. The approximate volume of the cylinder by integrating the cells that lie within the cylinder be different from the prescribed volume (less than 1.5%). Given this error in volume, total thrust and torque is not recovered. Therefore, magnitude of body force in Equations (3.47) and (3.48) are uniformly scaled by the volume error such that the integrated total force is equal to that which is prescribed.

The propeller model requires the input of thrust, torque, and advance coefficients and outputs the torque and thrust force to the ship hull and the body forces for the fluid inside the propeller disk. The longitudinal and tangential forces are then projected into the ship coordinate system to result in a net force and moment to be used in the computation of the motions. The location of the propeller is defined in the static condition of the ship. When motions are involved, the propeller will move accordingly with the ship's motions and possibly will intersect different cell from different blocks as the ship evolves.

## 3.3 Numerical details and high performance computing

### 3.3.1 Discretization scheme and velocity pressure coupling

A second and third order upwind scheme is used to discretize the convective terms in the momentum equations for URANS and DES, respectively. Since only URANS is used in the present study, only the second order upwind scheme is presented here. The second order scheme is derived using a control volume cube of unit side in the computational domain. The convective terms for an arbitrary variable $\varphi$ can then be expressed as;

$$\frac{1}{J}\frac{\partial}{\partial \xi_k}\left[\hat{b}_j^k\left(u_j-\frac{\partial x_j}{\partial \tau}\right)\varphi\right]=\frac{1}{J}\left[(C_d-C_u)+(C_e-C_w)+(C_n-C_s)\right] \tag{3.55}$$

where $d, u, e, w, n,$ and $s$ stand for the down, up, east, west, north, and south faces of the control volume. At the down face, for example, we have;

$$C_d=\widetilde{U}_d\left[\alpha_d\left(a\varphi_{i+1}+b\varphi_i+c\varphi_{i-1}\right)+(1-\alpha_d)\left(d\varphi_i+e\varphi_{i+1}+f\varphi_{i+2}\right)\right] \tag{3.56}$$

The effective contra variant velocity $\widetilde{U}_d$ and $\alpha_d$ on the down face are defined as;

$$\widetilde{U}_d=\left[\hat{b}_j^1\left(u_j-\frac{\partial x_j}{\partial \tau}\right)\right]_{i+1/2} \tag{3.57}$$

$$\begin{cases}\alpha_d=1 \;\; if \;\; \widetilde{U}_d>0\\ \alpha_d=0 \;\; if \;\; \widetilde{U}_d<0\end{cases} \tag{3.58}$$

Similarly, convective terms for other directions are computed. The coefficients for the second order upwind scheme are: $a=0, b=1.5, c=-0.5, d=0, e=1.5, f=-0.5$.

Viscous terms in Equation (3.5) are discretized using a second-order central differences. Similar numerical schemes used to discretize the turbulence equations. The time derivatives for all variables are discretized using Euler second-order backward difference;

$$\frac{\partial \varphi}{\partial \tau} = \frac{1}{\Delta t}(1.5\,\varphi^{n} - 2\varphi^{n-1} + 0.5\varphi^{n-2}) \tag{3.59}$$

The Pressure Implicit Split Operator (PISO) algorithm is used to couple the momentum and continuity equations by taking the divergence of the momentum equation, using the divergence free condition, and updating the momentum and pressure equations using a predictor-corrector approach. The pressure Poisson equation is built into a sparse matrix and then solved with, a parallel solver of large algebraic systems. All the variables are defined on a collocated grid.

### 3.3.2 Dynamic overset grid

The computation of dynamic ship motion is made possible by the use of the dynamic overset grid approach. The overset-grid methodology allows the use of a set of overlapping grids to discretize the simulation domain. The typical overset grid structure in the present study is shown in Figure 3-2. This methodology is useful not only to simplify the grid generation for complex geometries but also to enable the technology for body motion simulation. Especially, it is quite reasonable technique with the case when the computational domain is composed of static and moving grids. For example, in Figure 3-2, body-fitted two blocks around the ship hull are moving and the rectangular background grid is static grid. When the dynamic overset grid is used in the simulation, the external software SUGGAR code is used to obtain the grid connectivity. Figure 3-3 shows overset grid around a sphere, overset grid arrangement of hole, interpolated and

active points, and donor cell with grid points in air and conformation to the free surface. SUGGAR runs as a separate process from the flow solver, and is called every nonlinear iteration for predicted motions, or every time step for prescribed motions to provide the interpolation information between the overset grids to the flow solver. In addition to SUGGAR, a special treatment is required to compute the area, forces and moments at no-slip surfaces where grids are overlapped, as it is the case in the present study. To avoid counting the same area in space more than once, USURP provides weights to the active points on the no-slip surfaces that result in the correct area, forces, and moments. Since the overlap at the solid surfaces does not change (i.e. the ship geometry with any appendages is fixed), USURP is used as a preprocessing step.

To couple the solution of the various grids, interpolation at appropriate points is used. In particular, any points that lie outside the domain of interest; for instance, inside of a body or behind a symmetry plane are blanked out from calculations and are termed "hole points". Points that surround the hold points become new inter-grid boundary points, which are called fringe or receptor points, and require boundary values that are provided by interpolating from a donor grid that overlaps the region. Therefore, the overset grid assembly process provides the domain connectivity information, which is the definition of which points are receptor points along with their corresponding donor members and which hare hole points. In the dynamic approach, a grid is moved new interpolation coefficients need to be computed to link the moving grids with the static grids and between each other (see Figure 3-3(b)). Note that blue grid lines indicate o-grid around sphere, green grid lines indicate box grid, red symbols shows box-grid points receiving data from sphere, and black symbols show sphere grid points receiving data from box in the figure.

### 3.3.3 Overall solution strategy and high performance computing

Figure 3-4 shows the overall solution strategy. The grids are read and the domain decomposition parallelization is accomplished using Message Passing Interface (MPI). After the initialization for all the variables, the code SUGGAR is called for the first time to obtain the initial overset interpolation information. When processing time-marching step, an inner iteration (non-linear loop) is used to converge predicted motions and/or the flow field within each time step. At the beginning of each non-linear iteration, the overset grid information is read from a binary file produced by SUGGAR, grids are moved according to the motions resulting from the 6DOF predictor/corrector steps and transformation metrics and grid velocities are computed. Thus, SUGGAR is called at the beginning of each inner iteration. Then, k-ω equations are solved implicitly followed by the level-set function transport and reinitialization. With the new location of the free surface, the pressure gradient is computed and the velocity-pressure coupling is done. Once the velocity field is obtained, the forces and moments are calculated. Then, the global residuals are evaluated. If residuals of all the variables meet the convergence criteria $10^{-3}$, inner iteration ends and goes to the next time-marching step otherwise starts another inner iteration. When the residuals of all variables drop to the criterion, motions are predicted for the next time step using a first order Euler difference approach give by the following expression for any degree of freedom. SUGGAR is called to compute the interpolation given the new location of the moving grids. If the non linear iteration is not converged for the time step, then the motion vectors are corrected using a third order approximation for time derivatives. SUGGAR is then called and a new non linear iteration is started. Two –five non linear iterations are usually required for convergence of the flow field equations within each time step. Convergence for pressure equation is reached when the residual imbalance of Poisson equation drops six orders of magnitude while convergence of all other variables is reached when residuals drop to $10^{-5}$.

## 3.4 INSEAN Potential Flow Solver (WARP)

WARP potential solver (Bassanini *et al*, 1994) is a classical Boundary Element Method (BEM) type solver which is developed by INSEAN research group originally in the late 80's and continuously improved since then. The code is routinely used at INSEAN for resistance evaluations and experiences with not only simple monohull also multihull predictions were already accumulated in the past. Rankine sources together with vortex rings are arranged on the hull geometry and on a portion of the free surface around the ship. Desingularized panels are adopted on the free surface. Derivatives of the velocity potential are obtained analytically. The set of equations are a simple impermeability condition on the body $\left(\frac{\partial \varphi}{\partial \mathbf{n}} = 0\right)$ and a unified free surface condition;

$$\varphi_{ll}\varphi_l^2 + \frac{\varphi_z}{F_n^2} = 0 \tag{3.60}$$

The quadratic term for the velocity potential $\varphi$ is updated at each iteration, together with the free surface elevation: at the end of the iterative process, the boundary condition is computed on the exact free surface, and the non-linear term is converging to the exact value. Also the wetted portion of the hull is changing according to the computed wave elevation. A different boundary condition is imposed at the transom stern if present. Simulations are not affected by the scale, since the viscous terms are not directly considered during the solution, and an accurate estimate of the wave resistance is obtained by pressure integration or by wave cut analysis. WARP also has dynamic heave and trim capabilities. Vorticity shed into the fluid from lifting surfaces is simulated via straight trailing vortices that are assumed leaving the foils (both trailing edge and tip) at unknown angle. The hull position is obtained by the equilibrium of the forces on the hull. This BEM potential solver has been used by INSEAN and IIHR research group, e.g., Peri *et al*., (2009) and Kandasamy *et al*., (2009b).

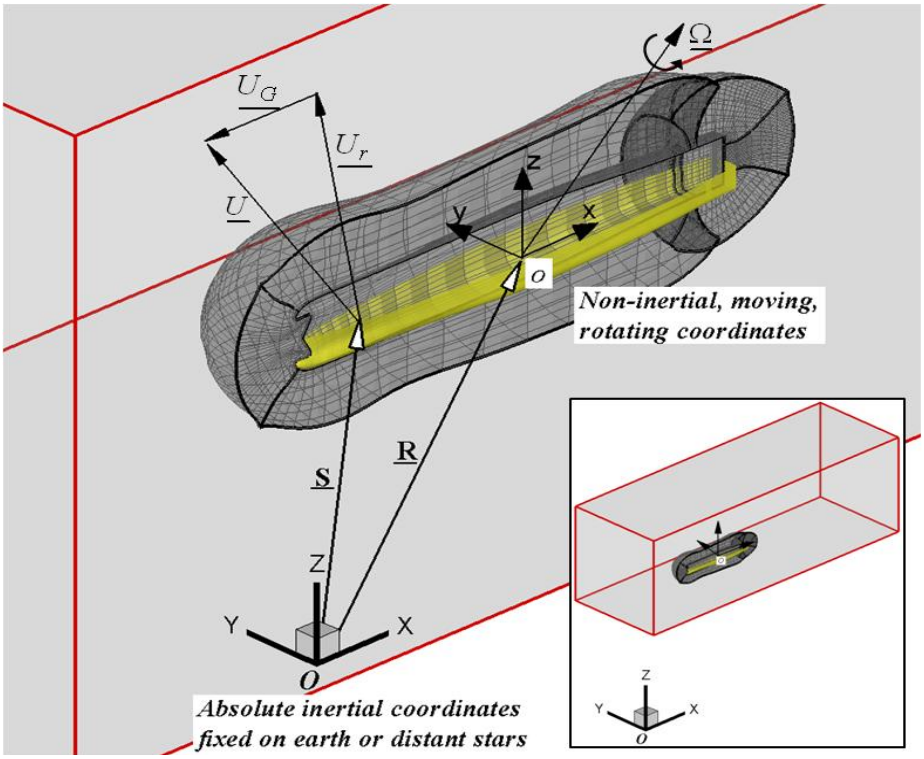


Figure 3-1 Definition of absolute inertial earth-fixed coordinate system $(X, Y, Z)$ and noninertial ship-fixed coordinate system $(x, y, z)$ used in CFD simulation

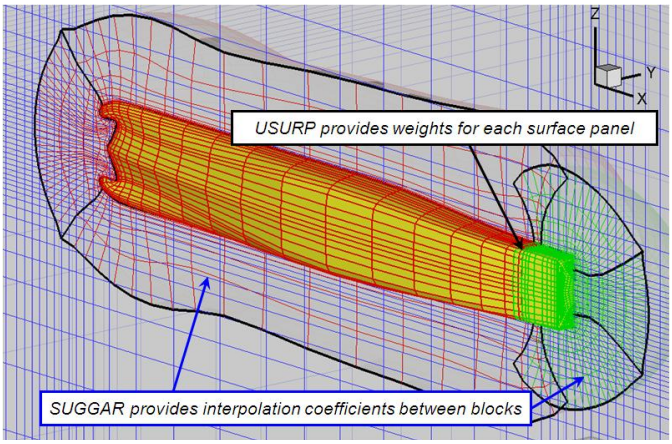


Figure 3-2 Overset grid system around JHSS barehull design (3 blocks)

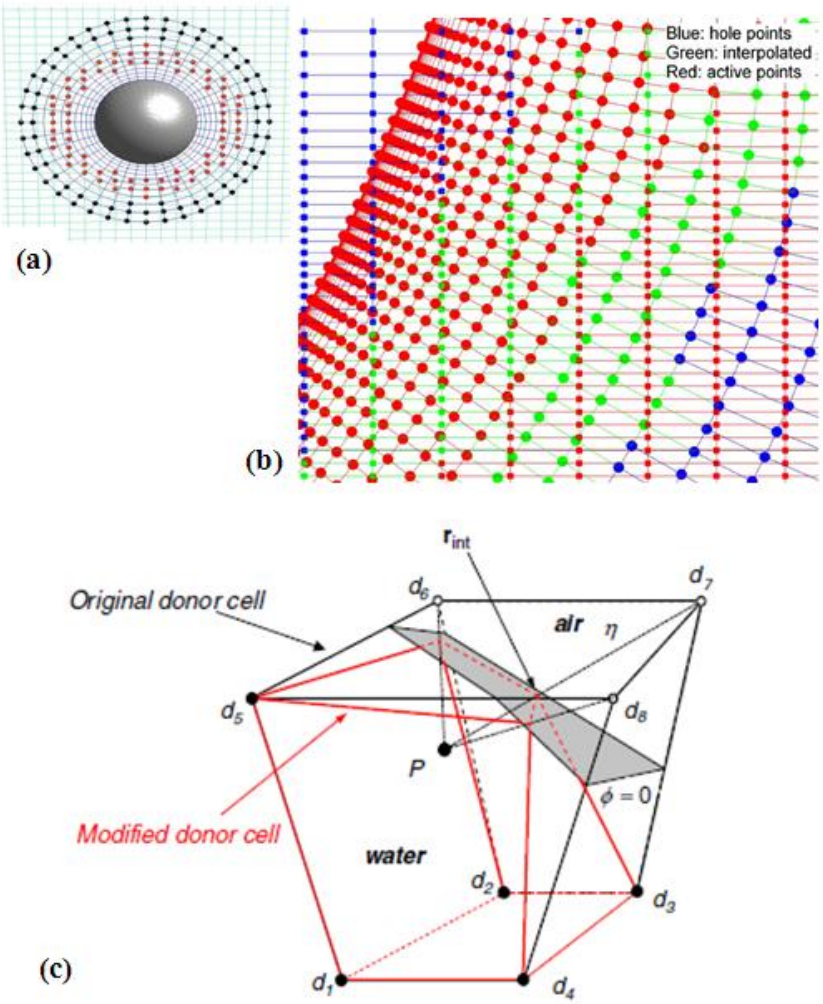


Figure 3-3 Overset grid technology: (a) overset grid generated around a sphere, (b) overset grid arrangements of hole, interpolated, and active points, (c) donor cell with grid points in air and conformation to free surface

---

Source (b) and (c): Carrica, P. M., *et al.*, 2007, "Ship motions using single-phase level set with dynamic overset grids"

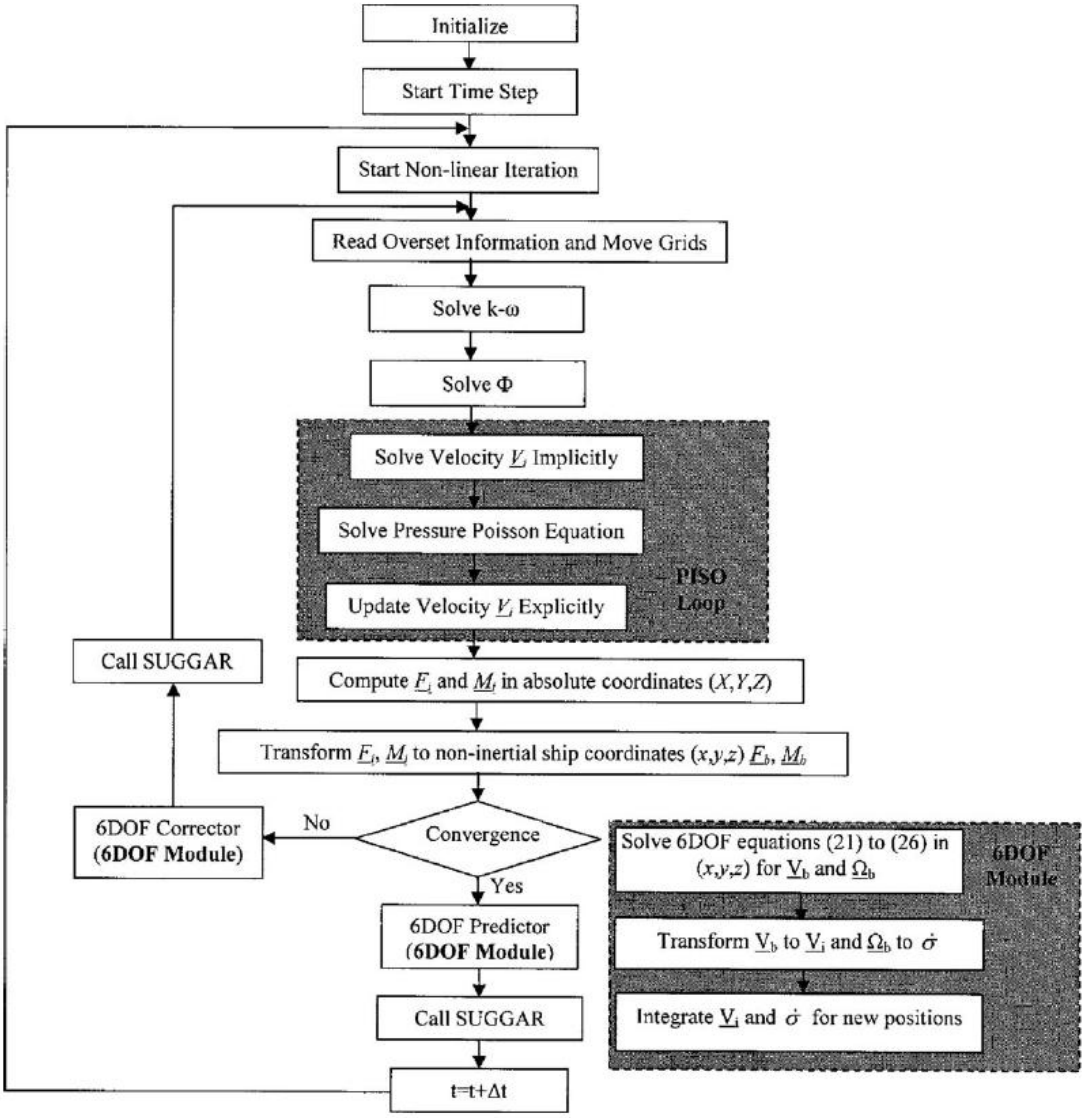


Figure 3-4 Overall solution procedure of CFDSHIP-IOWA V.4
using absolute inertia earth-fixed coordinate system

Source: Xing, T., *et al.*, 2008, "Computational towing tank procedures for single run curves of resistance and propulsion"

# CHAPTER 4
# SIMULATION DESIGN

## 4.1 Geometry

The geometry selected for the present study is the Joint High-Speed Sea-lift (JHSS), which is a very large (approximately 980ft long with beam of 105ft on full-scale), high speed vessel concept operating at a transit speed of at least 36 knots using four axial-flow waterjet propulsion system. The JHSS is concept ship for a transport of a single Marine Brigade to overseas theaters. Figure 4-1 shows the lines drawing and the main particulars of the JHSS barehull model used in experiment (same dimension is used in CFD as well). EFD data from 1/34 scale model testing (detail can be found in next section) includes resistance, dynamic sinkage and trim for both barehull and waterjet appended hull. Additional data for the waterjet propelled hull includes thrust-deduction, self-propulsion thrust, waterjet inlet boundary layer measurements, waterjet volume rate, and velocity measurements at different stations inside the duct. The waterjet appended hull model used in the present study does not include a shaft, rotor, and blade due to the complexity of numerical grid design; in contrast, EFD included these components.

## 4.2 Brief summary of experiment condition

Towing tank model testing was carried out at Naval Surface Warfare Center, Carderock Division (NSWCCD) in 2007 (Jessup *et al*., 2008) on an advanced hull form with the twin shaft axial-flow waterjet below discharge waterjet configuration. Models with various propulsor configurations were tested. The baseline model (Figure 4-2), which has a scale ratio of 34.121 (multiplying scale ratio times the model length gives full-scale vessel length), was tested for resistance and powering characteristics in both calm water and in waves. The nozzles of four axial-flow waterjet system were mounted

in line across the model's stern. The "gooseneck" bow, shown in Figure 4-2(a), was used for the model tests, which actually emerges above the free surface when the model is at rest. At all surveyed speeds, the bulb was immersed below the free surface. The waterjet hull models did not include bilge keels or a docking skeg.

Waterjets were designed for installation into the JHSS hull to represent typical mixed-flow and reduced diameter axial-flow pump units. In the present study, only axial-flow waterjet system is considered. Clearances between pump flanges and the hull bottom were specified to be typical, as shown in Figure 4-3, and pump characteristics is shown in Table 4-1. Water flow through the waterjets was measured by Laser Doppler Velocimetry (LDV). Tests were conducted with detailed starboard side LDV surveys at Station 1, ahead of the inlet, Station 3, just ahead of the pump and Station 6, just downstream of the nozzle (refer Figure 2-2). Static wall pressure was measured at three stations, with Pitot-static tubes also at Station 1 and 6 as reference and single point field pressure measurements. The tests were conducted at seven speeds, corresponding to full-scale approximately 15, 20, 25, 30, 36, 39, and 42 knots. This speed range corresponds to a Froude number range from 0.143 to 0.401. All the data used for comparison with simulation in the present study are summarized in Table 4-2 and 4-3.

This approach relied heavily on LDV surveys to best document the flow non-uniformities at each station, with the use of wall static taps to establish the pressure across the station planes. To accurately measure jet velocity, testing incorporated all of the approaches explored by the ITTC. These included LDV surveys, bollard tests, single total head probes, and direct measure using weight scales. The overall experimental uncertainty levels were estimated by 5.79%D, 3.84%D, and 0.12%D at Fn=0.34 for delivered horse power, thrust deduction, and ship speed respectively. A Monte Carlo method was used to determine both the sensitivity and uncertainty levels.

## 4.3 Simulation test case

The simulations are carried out on 1/34 model scale model for the 970 ft long JHSS ship, replicating the experimental model testing. Two cases are of interest: barehull design and waterjet appended design. Both cases are subjected free to heave and pitch. For barehull resistance computations, the ship is initially static on calm water (shown in Figure 4-4). The ship is then allowed to pitch and heave under a constant inlet fluid velocity until a steady state is reached. Ship-fixed coordinate system is used, which means that there is no surge motion allowed for the ship and the background grid. The Center of Gravity (CoG) is set to $(x, y, z) = (0.523, 0, 0.0187)$ for all the cases; and Center of Rotation (CoR) is set to $(x, y, z) = (0.523, 0, 0.0267)$ for all the cases. Note that the coordinate variables of CoG and CoR locations listed above have been non-dimensionalized by $L_{pp}$, and are identical to the values in the experiment whose details are shown above section.

For waterjet propelled simulation, a simplified body-force model is used to prescribe axisymmetric body force with axial and tangential components .The radial distribution of force is based on the Hough and Ordway circulation distribution, which has zero loading at the root and chip. Integration of the body forces over this analytical volume exactly recovers the prescribed thrust and torque. During simulations, the ship accelerates until the resistance equals the prescribed thrust and added tow force and converges to the self propulsion point. 2-5 nonlinear iterations are required for convergence of the flow field equations within each time step. Convergence of the pressure equation is reached when the residual imbalance of the Poisson equation drops six orders of magnitude. All other variables are assumed convergence when the residuals drop to $10^{-3}$. Details are presented in Chapter 3.

Detailed verification and validation (V&V) studies are conducted for both JHSS barehull and waterjet appended design with two degree of freedom (pitch and heave) at

the design cruise speed (Fn=0.34). Two sets of triplet grid systems (1,2,3 and 2,3,4) are generated by systematically refined from coarse grid using refinement ratio $r_G = \sqrt{2}$ for barehull resistance simulation cases; whereas, one set of triplet grid systems (1W,2W,3W) are prepared for waterjet cases. The grid information is presented in next section. For both cases, the time step is set to $\Delta t = 0.010\, L/U_0$ and the inner iterative is set to 3. For the verification study, systematically refined inner iterative with refinement ratio $r_I = \sqrt{2}$ are used in addition to grid size study, resulting in that the numbers of inner iteration are set to 3, 4, and 5. The number of inner iteration is studied only for barehull simulation case using the grid #3. For the waterjet simulations, two conditions are used; e.g., towed simulation and self-propelled simulation. Since the self-propulsion is time consuming simulation and it is difficult to get converged, towed waterjet simulation is carried out for some cases using same grids (Grid 1W-3W).

Furthermore, both barehull and waterjet simulations are performed over the speed range of Fn=0.19 to 0.40 and corresponding Rn at model scale (details can be found in Chapter 5) to investigate the resistance and motions curves whether they are agreed with EFD data. Additionally, the flow fields are investigated.

## 4.4 Computational overset grid and domain size

The commercial software GRIDGEN© with hyperbolic extrusion method for the curvilinear grids are used to generate all the computational grids. At the solid surfaces, the first grid point is set at $y^+ < 1$ for fine grid, as required by the blended k-ε/k-ω turbulence model. Body-fitted "O" type grids are generated around ship hull geometry; in contrast, a rectangular background grid is used with clustered grid near the free surface to resolve the wave field. The details of the grid topologies and domain size are described in Table 4-5 and Figure 4-5 for barehull case and Table 4-6 and Figure 4-6 for waterjet case.

In the present study, there are two different concepts on the design of computational grids; namely, barehull simulation grid (Grid1-4), and waterjet simulation grid (Grid W1-W3). All the grids are generated only for starboard side taking advantage of symmetry condition. Four grids are created for barehull case in order to carry out the V&V study (details are found in Chapter 5); whereas, three grids are prepared for waterjet case. The barehull grid consists of three blocks; namely, fore-hull, aft-hull, and background block. A rectangular background grid is used with clustered grid near the free surface to resolve the wave field. The fore-hull and aft-hull blocks are overlapped on the hull geometry; thus, we need to avoid counting the same area in space more than once. The code USURP (Boger and Dreyer, 2006) is used to calculate the correct area, forces, and moments. In addition, the waterjet grid makes extensive use of overset grids, and consists of 18 blocks in order to accurately express the complicated 3-D waterjet geometry. In the present study, the shaft and the downstream rotor are not included in order to avoid the complexity of the grid design since the main objective of the present study is shape optimization. Increase in the number of blocks introduces more computational loads. Hence, too large grid size is not applicable, and too complicated grid design is not preferable. For self propulsion simulation, a total of 13 million grid points (Grid W1) is split into 120 blocks with an average of 120K grid points/block for the MPI based domain decomposition.

The common domain size is used for all the grid systems; that is, in longitudinal and vertical directions are extended from $-0.5L \leq x \leq 2.5L$ and $-0.7L \leq z \leq 0.7L$, respectively. The distance from the ship hull to the side boundary is set to $1.3L$. The total number of grid for finest grid (Grid1) is approximately 28 million grid points, and it is split into 190 blocks with an average of 160K grid points/block for the MPI based domain decomposition.

## 4.5 Boundary conditions

Figures 4-5(a) and 4-6(a) show the boundary conditions applied to barehull and waterjet grid, respectively. Table 4-7 presents the mathematical description of boundary conditions. The major difference in boundary condition arose from the coordinate system appears in the velocity of inlet and no-slip conditions explained as follows.

***Relative inertial coordinate system***

Relative inertial coordinate system is adopted for barehull and waterjet towed simulation. In this coordinate system, the surge motion is not imposed to the ship; thus, the velocity components at inlet boundary are $(U, V, W) = (1,0,0)$. For all the simulations, no motions are prescribed; thus, the velocity boundary conditions at no-slip surface are $(U, V, W) = (0,0,0)$.

***Absolute inertial earth-fixed coordinate system***

Absolute inertial earth-fixed coordinate system is adopted for the waterjet self-propelled simulation. During the simulation the ship location is prescribed with a constant time interval *t* as

$$x = -Rsin\psi \tag{4.1}$$

$$y = R(1 - cos\psi) \tag{4.2}$$

$$\psi = \frac{t}{R} \tag{4.3}$$

where $R$ is the non-dimensional length of rotating arm and $\psi$ is the yaw angle relative to the advancing direction. The 1st derivatives of Equations (4-1), (4-2), and (4-3) provide the x- and y-components of linear velocity; i.e. the no-slip condition on the hull

surface, and z-component of angular velocity of the ship at non-inertial ship-fixed coordinate system as

$$u_b = \dot{x} = -cos\psi \tag{4.4}$$

$$v_b = \dot{y} = sin\psi \tag{4.5}$$

$$\Omega_z = \frac{1}{R} \tag{4.6}$$

Since the ship moves with the prescribed velocity, the velocity components at the inlet boundary are all zero.

Table 4-1 Waterjet pump characteristics in EFD

| | Pump diameter | Nozzle diameter |
|---|---|---|
| Model Scale | 3.517″(8.93cm) | 2.200″(5.58cm) |
| Full Scale | 120″(304.8cm) | 75.06″(190.7cm) |

Table 4-2 EFD resistance and motion data of JHSS barehull

| Full Scale $V_s$ (knots) | Fn | Model Scale $V_m$ (knots) | Resistance (N) | Sinkage (m) | Trim (deg) |
|---|---|---|---|---|---|
| 20.00 | 0.1902 | 3.42 | 43.99292 | -0.00602 | -0.052 |
| 25.10 | 0.2386 | 4.30 | 68.27987 | -0.00804 | -0.076 |
| 30.10 | 0.2862 | 5.15 | 91.70409 | -0.01162 | -0.103 |
| 36.11 | 0.3434 | 6.18 | 134.1444 | -0.01787 | -0.195 |
| 42.02 | 0.3996 | 7.19 | 228.1304 | -0.02502 | -0.020 |

Table 4-3 EFD waterjet related parameters of waterjet propelled JHSS

| Fn | Delivered Thrust (N) | WJ model Efficiency | Supplied Thrust (N) | Added tow Force (N) | Total thrust at Self-propulsion (N) |
|---|---|---|---|---|---|
| 0.2386 | 72.31 | 0.560 | 129.13 | 25.105 | 154.235 |
| 0.2862 | 91.70 | 0.550 | 161.67 | 35.185 | 196.855 |
| 0.3434 | 131.90 | 0.570 | 231.46 | 48.312 | 279.772 |
| 0.3996 | 264.37 | 0.575 | 459.77 | 63.756 | 523.526 |

Table 4-4 Summary of numerical condition in the present study

| CFDSHIP-IOWA V.4 | |
|---|---|
| Governing Equation | Unsteady RANS |
| Spatial discretization | $2^{nd}$ order upwind FDM |
| Level-set convection | $2^{nd}$ order hybrid scheme |
| Non-linear inner iterative | 3,4,5 |
| Time step | 0.001 |
| Froude number (Design Speed) | 0.3434 |
| Reynolds number (Design Speed) | $2.78 \times 10^7$ |
| P-V coupling | PISO |
| Turbulence model | blended k-ε/k-ω model |
| 6DOF | Pitch and Heave |
| 6DOF solver | $2^{nd}$ order implicit |

Table 4-5 Description of numerical overset grids for JHSS barehull design

| Block # | Description | Block Type | Grid #/ Grid points | | | |
|---|---|---|---|---|---|---|
| | | | 1:Finer | 2:Fine | 3:Medium | 4:Coarse |
| 1 | Fore-hull | Body-fitted | 6.65M | 2.32M | 0.84M | 0.29M |
| 2 | Aft-hull | Body-fitted | 7.80M | 2.74M | 0.99M | 0.35M |
| 3 | Back ground | Orthogonal | 14.21M | 5.08M | 1.80M | 0.64M |
| Total Grid Points | | | 28.66M | 10.15M | 3.62M | 1.28M |
| y+ | | | 0.75 | 1.13 | 1.65 | 2.53 |

Table 4-6 Description of numerical overset grids for JHSS waterjet design

| Block # | Description | Block Type | Grid #/ Grid points | | |
|---|---|---|---|---|---|
| | | | 1W:Fine | 2W:Medium | 3W:Coarse |
| 1 | Fore-hull | Body-fitted | 2.32M | 0.84M | 0.29M |
| 2 | Aft-hull | Body-fitted | 2.74M | 0.99M | 0.35M |
| 3 | WJ-inlet | Body-fitted | 0.09M | 0.09M | 0.09M |
| 4 | WJ-inlet | Body-fitted | 0.13M | 0.13M | 0.13M |
| 5 | WJ-inlet | Body-fitted | 0.07M | 0.07M | 0.07M |
| 6 | Inside WJ geo | Body-fitted | 0.21M | 0.21M | 0.21M |
| 7 | Inside WJ geo | Body-fitted | 0.21M | 0.21M | 0.21M |
| 8 | Inside WJ geo | Body-fitted | 0.19M | 0.19M | 0.19M |
| 9 | Inside WJ geo | Body-fitted | 0.20M | 0.20M | 0.20M |
| 10 | Inside WJ geo | Body-fitted | 0.20M | 0.20M | 0.20M |
| 11 | Outside WJ geo | Body-fitted | 0.21M | 0.21M | 0.21M |
| 12 | Outside WJ geo | Body-fitted | 0.21M | 0.21M | 0.21M |
| 13 | Outside WJ geo | Body-fitted | 0.19M | 0.19M | 0.19M |
| 14 | Outside WJ geo | Body-fitted | 0.20M | 0.20M | 0.20M |
| 15 | Outside WJ geo | Body-fitted | 0.20M | 0.20M | 0.20M |
| 16 | Inside WJ outlet nozzle | Body-fitted | 0.31M | 0.31M | 0.31M |
| 17 | Outside WJ outlet nozzle | Body-fitted | 0.31M | 0.31M | 0.31M |
| 18 | Background | Orthogonal | 5.08M | 1.80M | 0.64M |
| | Total Grid Points | | 13.08M | 6.55M | 4.21M |
| | y+ | | 1.13 | 1.65 | 2.53 |

Table 4-7 Description of boundary conditions

| *Description* | | $\phi$ | $p$ | $k$ | $\omega$ | $U$ | $V$ | $W$ |
|---|---|---|---|---|---|---|---|---|
| Inlet | Resistance | $\phi = -z$ | $\frac{\partial p}{\partial n} = 0$ | $k_{fs} = 10^{-7}$ | $\omega_{fs} = 9$ | $U = 1$ | $V = 0$ | $W = 0$ |
| | Self-propelled | $\phi = -z$ | $\frac{\partial p}{\partial n} = 0$ | $k_{fs} = 10^{-7}$ | $\omega_{fs} = 9$ | $U = 0$ | $V = 0$ | $W = 0$ |
| Exit | | $\frac{\partial \phi}{\partial n} = 0$ | $\frac{\partial p}{\partial n} = 0$ | $\frac{\partial k}{\partial n} = 0$ | $\frac{\partial \omega}{\partial n} = 0$ | $\frac{\partial^2 U}{\partial n^2} = 0$ | $\frac{\partial^2 V}{\partial n^2} = 0$ | $\frac{\partial^2 W}{\partial n^2} = 0$ |
| Far-field #1 | | $\frac{\partial \phi}{\partial n} = 0$ | 0 | $\frac{\partial k}{\partial n} = 0$ | $\frac{\partial \omega}{\partial n} = 0$ | $U = 1$ | $V = 0$ | $W = 0$ |
| Far-field #2 | | $\frac{\partial \phi}{\partial n} = 0$ | $\frac{\partial p}{\partial n} = 0$ | $\frac{\partial k}{\partial n} = 0$ | $\frac{\partial \omega}{\partial n} = 0$ | $U = 1$ | $V = 0$ | $W = 0$ |
| Symmetry | | $\frac{\partial \phi}{\partial n} = 0$ | $\frac{\partial p}{\partial n} = 0$ | $\frac{\partial k}{\partial n} = 0$ | $\frac{\partial \omega}{\partial n} = 0$ | $\frac{\partial U}{\partial n} = 0$ | $V = 0$ | $\frac{\partial W}{\partial n} = 0$ |
| No slip (ship hull) | | $\frac{\partial \phi}{\partial n} = 0$ | – | $k = 0$ | $\omega = \frac{60}{\beta Re \Delta y_1^2}$ | $\frac{\partial U}{\partial n} = 0$ | $V = 0$ | $W = 0$ |

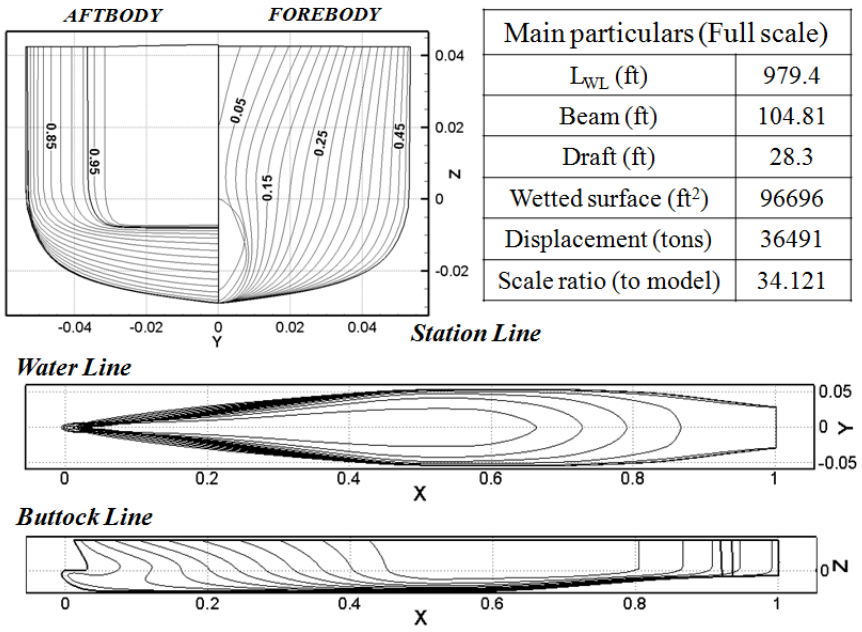


| Main particulars (Full scale) | |
|---|---|
| $L_{WL}$ (ft) | 979.4 |
| Beam (ft) | 104.81 |
| Draft (ft) | 28.3 |
| Wetted surface ($ft^2$) | 96696 |
| Displacement (tons) | 36491 |
| Scale ratio (to model) | 34.121 |

Figure 4-1 Lines and main particulars of JHSS barehull

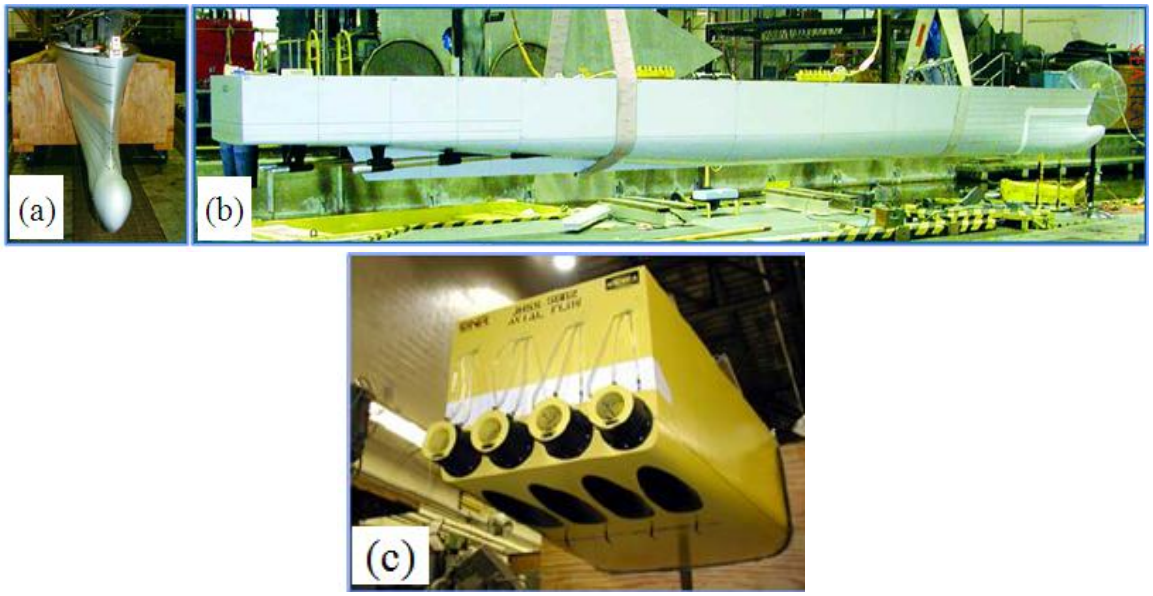


Figure 4-2 EFD JHSS model: (a) a snapshot of gooseneck bulbous bow (frontal view), (b) baseline model hull form, (c) waterjet appended design

Source: SEAFRAME 2008 Vol.4 Issue.1, Carderock Division Publication

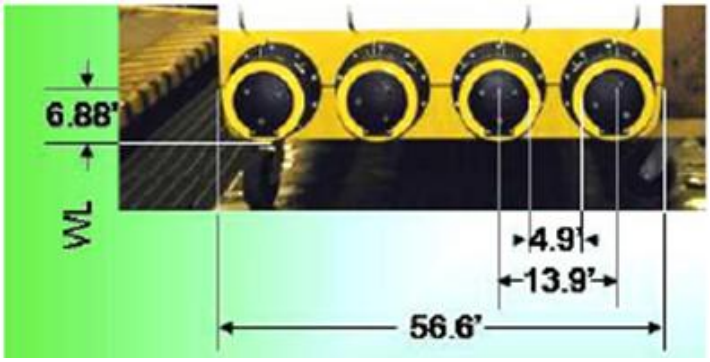


Figure 4-3 EFD waterjet transom layout for the axial-flow pump in full scale dimensions

Source: Jessup, S., *et al.*, 2008, "Performance Analysis of a Four Waterjet Propulsion System for a Large Sealift Ship"

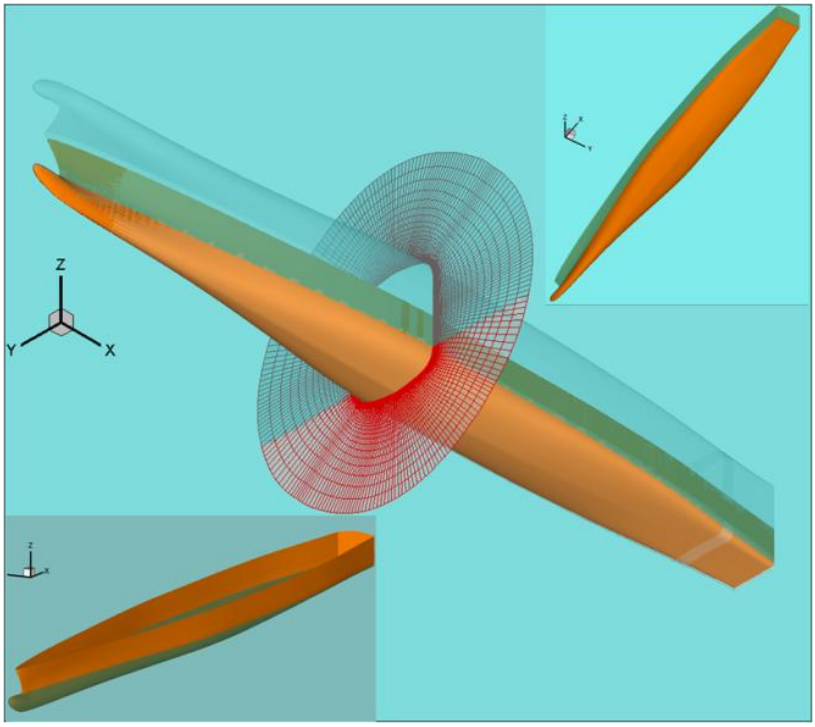


Figure 4-4 Initial static state shown with free surface and center cut of boundary grid for JHSS barehull

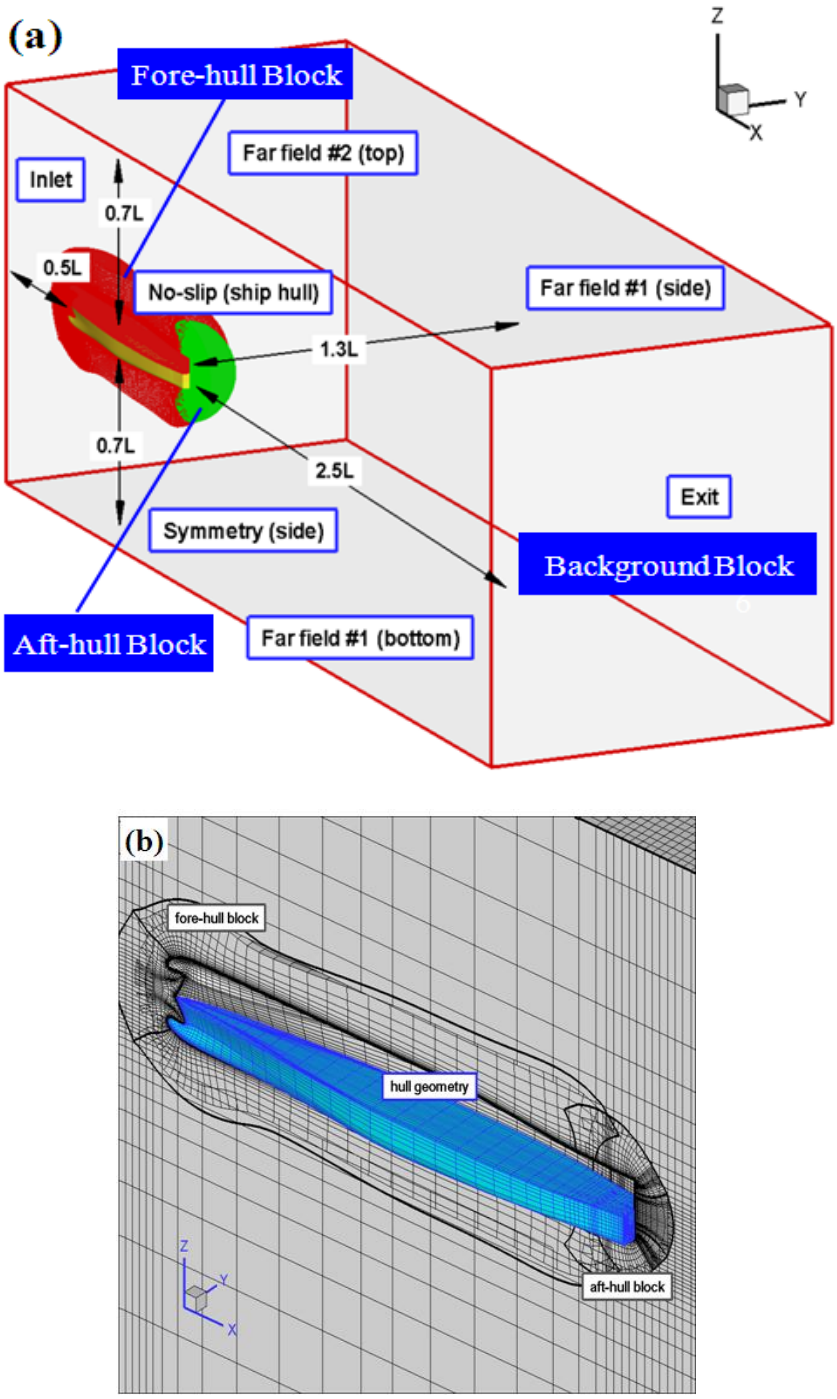


Figure 4-5 Grid topology and domain for JHSS barehull: (a) boundary conditions and domain size for barehull grid, (b) barehull grid system (total 3 blocks)

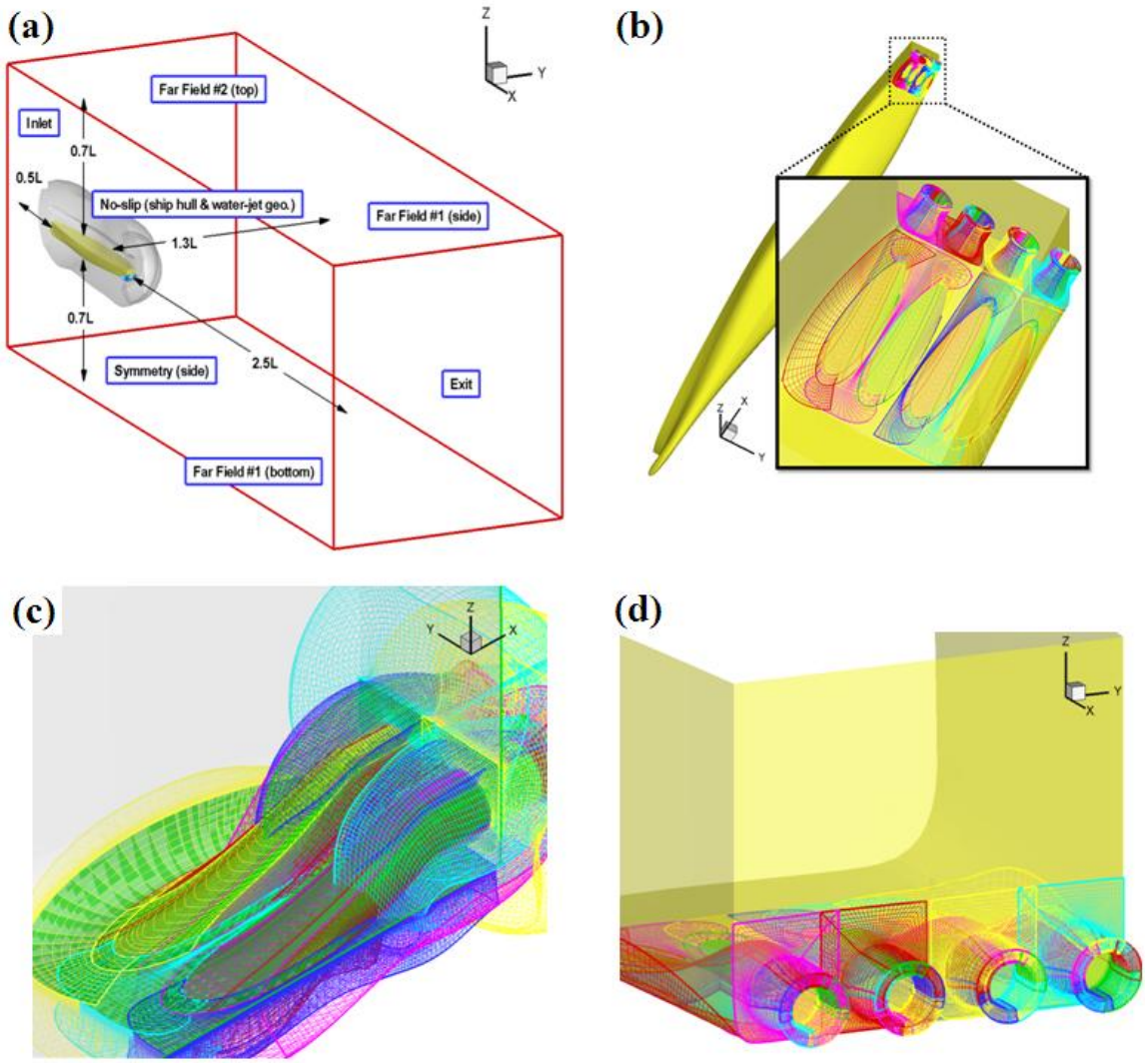


Figure 4-6 Grid topology and domain for waterjet appended JHSS design:
(a) boundary conditions and domain size for waterjet grid (total 18 blocks),
(b) perspective view of waterjet grid arrangement from bottom of the hull,
(c) volume grids around the waterjet geometry (15 blocks),
(d) surface meshes around waterjet geometry

# CHAPTER 5
# UNCERTAINTY ANALYSIS

## 5.1 Introduction

In this chapter, uncertainty analysis for both JHSS barehull and waterjet simulations is presented. Preliminary results were submitted to 10th International Conference on Fast Sea Transportation (FAST2009) by IIHR research group (Kandasamy *et al.*, 2009a), to Journal of Marine Science and Technology (JMST) by Takai *et al.*, (2010), and to some others (Wilson *et al.*, 2009 and 2010).

The influence of grid resolution and numerical accuracy on the solution of the governing equations of fluid flow is quite important for any simulation methods. Prediction errors indeed can be attributed to turbulence modeling and other modeling approximations including detailed waterjet modeling if a careful and competent handling of the computation process is assured. The use of a good verification and validation methodology will enable us to quantify the modeling uncertainties and the solutions can be validated using corresponding EFD data. It is imperative to have complementary EFD data to validate the accuracy of the modeling. The use of concurrent and complementary CFD, EFD, and uncertainty assessment has attracted a lot of attention and is gaining in popularity. The purpose of the verification and validation study of CFD simulation is to estimate the quantitative metrics; i.e., intervals of uncertainty at a specified confidence level of solutions.

In the present study, uncertainty analysis is performed based on the Verification and Validation (V&V) method proposed by Stern *et al.,* (2005) with recently proposed Factor of Safety (FS) method by Xing and Stern (2010). As mentioned in earlier chapter, EFD data (Jessup *et al.*, 2008) is used to validate the accuracy of numerical method. EFD data includes resistance, sinkage, trim, self-propulsion thrust, waterjet inlet boundary

layer measurements, waterjet volume flow rate, and velocity measurements at the different stations inside the duct. In the following sections, the methodology and procedures are given in more details.

## 5.2 Verification and Validation methodology and procedure

In this section, V&V method and improved error and uncertainty estimates used in the present study are described. In the V&V method, quantitative numerical error estimates for grid size and time convergence are based on Richardson extrapolation (RE), i.e., the error is expanded in a power series with integer powers of grid spacing/time-step as a finite summation. It is a common practice to retain only the 1$^{st}$ term of the series assuming the solutions are in the asymptotic range (AR), which leads to a grid triplet study. However, there are several issues of using RE method as shown in Stern *et al.*, (1999). One of the issues is that it is difficult to improve the accuracy by retaining more terms in the power series. For instance, solution of both the first- and second-order terms will require 5 grid solutions, which significantly increase the computational effort and additionally require that all the solutions are close to the AR, i.e., within about 6% of the theoretical order of accuracy of the numerical scheme $p_{th}$. When solutions are not in the AR, multiple grid triplet studies often show non-smooth convergence. Xing *et al.*, (2010) considered this issue and developed a Factor of Safety (FS) method for solution verification that removes some deficiencies observed in other methods.

Simulation error $\delta_S$ is defined as the difference between a simulation result $S$ and the truth $T$. It decomposes into two parts: modeling errors $\delta_{SM}$ and numerical errors $\delta_{SN}$; thus, the simulation error is expressed by $\delta_S = S - T = \delta_{SM} + \delta_{SN}$. Modeling errors are due to the mathematical physics problem formulation in terms of a continuous initial boundary value problem and numerical errors are due to numerical solution of the

discrete the problem. Simulation modeling and numerical errors are assumed additive such that simulation uncertainties root sum square (RSS).

Verification is a process for estimating the most important numerical error sources such as iterative error $\delta_I$, grid size error $\delta_G$ and time-step error $\delta_T$, and provides error and uncertainty estimates of numerical uncertainty $U_{SN}$. Validation methodology and procedures use benchmark experimental data $D$ and properly take into account both $U_{SN}$ and experimental uncertainty $U_D$ in estimating modeling errors and validation uncertainty $U_V$. The $U_{SN}$ is estimated based on graphical methods for iterative uncertainty $U_I$ and generalized Richardson extrapolation for grid uncertainty $U_G$ and time-step uncertainty $U_T$, and is expressed as

$$U_{SN}^2 = U_I^2 + U_G^2 + U_T^2 \tag{5.1}$$

***<u>Uncertainty estimates</u>***

The uncertainty estimates for Grid/time-step convergence studies are conducted with multiple solutions using systematically refined grid sizes or time steps with constant refinement ratio. First, refinement ratio $r$ for grid/time is selected. As an example, taking 3, 2, and 1 represent coarse, medium, and fine grids with grid spacing $\Delta x_3$, $\Delta x_2$, and $\Delta x_1$ respectively. Here, the refinement ratio between these solutions are defined as follows,

$$r = \frac{\Delta x_2}{\Delta x_1} = \frac{\Delta x_3}{\Delta x_2} \tag{5.2}$$

In the above Equation (5.2), the constant $r$ is not required but simplifies the analysis and thus it is recommended to use. Solution change $\varepsilon$ for medium – fine and coarse – medium solutions and the convergence ratio $R$ are defined by

$$\varepsilon_{21} = S_2 - S_1 \tag{5.3}$$

$$\varepsilon_{32} = S_3 - S_2 \tag{5.4}$$

$$R = {}^{\varepsilon_{21}}/_{\varepsilon_{32}} \tag{5.5}$$

where, $S_1$ represents the solution from fine grid, $S_2$ from medium, and $S_3$ from coarse grid.

Here, convergence types are defined by following four conditions based on $R$,

(1) Monotonic Convergence (MC): $0 < R < 1$

(2) Oscillatory Convergence (OC): $R < 0 \ and \ |R| < 1$

(3) Divergence (MD): $R > 1$

(4) Oscillatory Divergence (OD): $R < 0 \ and \ |R| > 1$

***<u>Uncertainty estimates for monotonic convergence type</u>***

When the solutions achieved monotonically convergence based on the above criterion, generalized Richardson extrapolation can be used to estimated order-of-accuracy $p_{RE}$, the error $\delta_{RE}$ and numerical benchmark $S_C$ as following equations

$$p_{RE} = \frac{ln\left({}^{\varepsilon_{32}}/_{\varepsilon_{21}}\right)}{ln(r)} \tag{5.6}$$

$$\delta_{RE} = \frac{\varepsilon_{23}}{r^{P_{RE}} - 1} \tag{5.7}$$

$$S_C = S_1 - \frac{r^{P_{RE}} - 1}{r^{P_{th}} - 1}\delta_{RE} \tag{5.8}$$

When solutions are in the AR, $p_{RE} = p_{th}$; however, in many circumstances especially for coarse girds and industrial applications, solutions are far away from the AR such that $p_{RE}$ is greater or smaller than $p_{th}$. Therefore, a metric is needed to quantify the distance of solutions to the AR. Stern *et al.*, (2001a) used Correction Factor (CF) based

on the fact that CF$\delta_{RE}$ is a better error estimate than $\delta_{RE}$ for 1D wave and 2D Laplace equations:

$$CF = \frac{r^{p_{RE}} - 1}{r^{p_{th}} - 1} \tag{5.9}$$

The deficiency of using CF as the distance metric is that CF is also a function of $r$; therefore, even for the same $p_{RE}$ and $p_{th}$, CF could be different. Herein, the ratio of $p_{RE}$ to $p_{th}$ is used to show the distance from the asymptotic range which is:

$$P = \frac{P_{RE}}{P_{th}} \tag{5.10}$$

where, $p_{th}$ is the theoretical order of accuracy of the numerical solver used as aforementioned, i.e, $p_{th} = 2$ in the present research since the order of accuracy is 2nd order. As shown in Xing *et al.*, (2010), P$\delta_{RE}$ is a better error estimate than CF$\delta_{RE}$ and useful for statistical analysis, for which analytical benchmark and numerical benchmark data can be organized according to the same P values.

The procedure of constructing numerical uncertainty $U_{SN}$ is builds on the CF method but with significant improvements: (1) P instead of CF is used as the distance metric to the AR; (2) an improved error estimate P$\delta_{RE}$ is used; and (3) three FS coefficients are used. As a result, the numerical uncertainty $U_{SN}$ is estimated using the following equation.

$$U_{SN} = \begin{cases} \{C_1 P + C_0(1-P)\}|\delta_{RE}| & 0 < P \leq 1 \\ \{C_1 P + C_2(P-1)\}|\delta_{RE}| & 1 < P \end{cases} \tag{5.11}$$

$C_0$, $C_1$, and $C_2$ are determined by statistical analysis so that the minimum values of those parameters are selected when the two criteria are met, i.e. lower confidence limit

>1.2 and at least 95% confidence that U>E for all P ranges, which shows following values of coefficients . Detail about these coefficients can be found in Xing *et al.*, (2010).

$$C_0 = 2.45, \quad C_1 = 1.60, \quad C_2 = 14.8 \tag{5.12}$$

***Validation***

The comparison error $|E|$ is defined by the difference between $D$ and simulation values $S_1$ in percentage based on the CFD fine grid as

$$|E| = \left|\frac{D - S_1}{D}\right| \tag{5.13}$$

The $U_V$(uncertainty of the EFD data $D$) is defined as

$$U_V = \sqrt{U_{SN}^2 + U_D^2} \tag{5.14}$$

When the error $|E|$ is within $\pm U_V$, solutions are validated at the levels of $U_V$.

In the present study, extensive verification and validation studies are conducted for JHSS with two degrees of freedom (pitch and heave) at the design cruise speed (Fn=0.34, Rn=$2.78\times10^7$). As summarized in Chapter 4, two sets of triplet grid systems (1,2,3 and 2,3,4) are generated by systematically refined from coarse grid using refinement ratio $r_G = \sqrt{2}$ for barehull case, and one set of triplet grid systems (1W,2W,3W) are prepared for waterjet case. The total number of grid points of finest grid for barehull case (Grid 1) is about 28M, and for waterjet case (Grid W1) is about 13M. All simulations for grid-size convergence study are performed using time step size $\Delta t = 0.010\ L/U_0$. In the present CFD simulation, friction and pressure stresses in the axial direction are integrated over the surface area of the JHSS and summed to yield the total resistance coefficient. The integration is performed in post processing using a

second-order accurate method based on the trapezoidal rule. Verification variables are the integral quantities; total drag coefficient ($C_t$), frictional drag coefficient ($C_f$), pressure drag coefficient ($C_p$), total resistance ($R_t$), dynamic area, dynamic sinkage, and dynamic trim. Herein, total resistance is dimensional value obtained using the dynamic area. For the towed waterjet simulations, same verification variables are selected to evaluate. However, for the self propulsion simulations, the ship accelerates until the resistance equals the prescribed thrust and added tow force and converges to the self propulsion point (SPP); therefore, force coefficients investigated for towed simulations become prescribed constant variables. As a result, verification study is done on SPP and dynamic motions including area for self propulsion case. In the following sections, the detailed solutions and corresponding discussions are presented for JHSS barehull, waterjet self propelled simulation, and waterjet towed simulation.

## 5.3 V&V study for JHSS barehull simulation at design speed

### 5.3.1 Inner iteration convergence

#### 5.3.1.1 Solution dependency on inner iteration number

Parametric studies on the nonlinear iterations for each time step ensure iterative convergence at each time step. The simulation of JHSS barehull free to pitch and heave is selected to study $\delta_{I0}$ depending on the number of inner iterations. The error is evaluated by performing three simulations using constant parameters which are grid (Grid 2) and time step ($\Delta t_3$=0.0100). The number of inner iterations is changed from 3 to 4 to 5.

Table 5-1 shows the summary of errors for force coefficients and dynamic motions. In the table, errors are shown in the percentage of the finest inner iteration, and it shows that all the components are converged; thus, $0 < R = {\varepsilon_{21}}/{\varepsilon_{32}} < 1$ . Note that the

highest errors (about 2%) are shown in motions, i.e., dynamic sinkage and trim. Indeed, these absolute values are small; thus, it is explainable that relative percentage gets bigger than other variables. Errors for force coefficients vary about 0.002% to 0.1%. Table 5-2 shows the iterative number uncertainty $U_{I_0}$ for all the variables shown in percentage of S; where S is the solution on finest inner iteration. Uncertainty intervals show negligibly small values (average of 0.003%S). These errors and uncertainties are at least one order smaller than the $U_I$, which is discussed in next section. Therefore, the iterative error depending on the number of inner iteration can be considered to negligibly small. The number of iteration 3 is used for the rest of cases.

#### 5.3.1.2 Solution iterative convergence

Figure 5-1 shows the typical residual history of forces coefficients and ship motions for the JHSS barehull towed simulation. Resistance is decomposed into two components; frictional and pressure component and the values shown in the figure are their coefficients multiplied by dynamic area. As seen in the figure, the solutions look fully converged; however, the solutions usually have small fluctuations even after the simulations reach steady state. This is due to non-linear inner iterations to converge predicted motions and the flow field within each time step. Therefore, it is important to analyze the statistical convergence. Root mean square (RMS) and running mean (RM) are usually used to study it. In the present study, $U_I$ is defined as $\frac{1}{2}(RM_{max} + RM_{min})$ which is the convergence of half running mean ($1/2\,\Delta$RM). Solution changes for force coefficients and motions are presented in Table 5-1 and uncertainty quantities are presented in %mean value for four grid systems in Table 5-2. As seen in the table, $U_I$ average value of all four solutions is less than 0.6%M for all the variables. Eventually, it is found that $U_I$ for $C_p$ is biggest with the finest grid (~0.9%M). It is typical that bigger $U_I$ are obtained for motions than for forces, which would indicate that it needs more flow times to get converged for the motions. Due to the grid density, the case with finest grid

shows relatively slow convergence than the others, but still these $U_I$ values can be considered small enough (average of 0.2%M).

### 5.3.2 Grid size convergence

The grid convergence study is conducted using a grid refinement ratio $r_G = \sqrt{2}$, and Table 5-3 summarizes the solutions of grid size convergence verification for resistance coefficients and ship motions obtained from barehull resistance computations with experimental uncertainties. As shown in Table 5-2, $U_I$ (Grid 1 solutions) is negligibly small, average uncertainty of 0.23%S. Corresponding $U_I/\varepsilon_{12_G}$ values for grids (1,2,3) are 0.5, 0.3, and 0.01 for $C_t$, sinkage, and trim, respectively. These small values (< 1) indicate that the $U_G$ is not affected by $U_I$. The convergence ratios ($R_G$) show the predicted convergence type (Equation 5.5). All force coefficients; namely, $C_t$, $C_f$, and $C_p$, show monotonic convergence with average of $R_G$=0.65. So is for $R_t$ with average of $R_G$=0.64. Dynamic trim show monotonic convergence for both grid sets; whereas, the sinkage with grids (2,3,4) shows divergence. Dynamic area shows oscillatory convergence and divergence for grid (1,2,3) and (2,3,4), respectively. One of the possible reasons why stable convergence type is not obtained for area is that there are not big differences in dynamic area from each simulation compared to other variables (see Table 5-1).

Overall, mostly monotonic convergence is obtained for the verification variables for barehull simulation. The order of accuracy ($P_G = p_{RE_G}/p_{th}$) differ 0.4 to 1.4. Almost all the $P_G$ show the range of 0.5-0.8. Most importantly, both grid-triplet studies achieve monotonic convergence for the total resistance coefficient ($C_t$) at the reasonable grid uncertainties (~3.7%S). For the sinkage, the solution from grid (1,2,3) achieves monotonic convergence with $U_G$=0.9%S; however, the ones from grids (2,3,4) show divergence such that $U_G$ cannot be estimated. For trim, $U_G$ is assessed at the average

intervals of 23.8%S which is relatively large uncertainty interval. The possible reason why the trim uncertainties get large is the fact that the absolute values are quite small (closer to zero) in this particular simulation case; and it is typical that motions are more difficult to converge in grid compared to resistance (Xing *et al.*, 2008a). Overall, $U_G$ for all the verification variables on grids (1,2,3) show smaller quantities than ones on grids (2,3,4) which is reasonable in consideration of the overall number of grid points. Figure 5-2 summarizes all the values for force coefficients and ship motions obtained from current V&V study.

### 5.3.3 Validation study

Since steady-state simulations are performed for the present study, the time step convergence study is not performed. The simulation numerical uncertainty $U_{SN}$, experimental data uncertainty $U_D$, validation uncertainty $U_V$, and comparison error $|E| = |D - S|$ are included in Table 5-3. Here, uncertainty due to the use of previous data is not considered; therefore, the validation uncertainty is given by $U_V = \sqrt{U_{SN}^2 + U_D^2}$. Eventually, $E$ is bigger with the higher resolution grid set (for $C_t$) than the lower; however, both values are of acceptable accuracy (~2.5%D). For grids (1,2,3), $E < U_V$ such that $C_t$ is validated at the interval of $U_V$=6.5%D. Reducing intervals of validation uncertainty for $C_t$ primarily requires reduction in experimental uncertainties since $U_D$=5.8%D > $U_{SN}$=3.6%D. Due to the lack of experimental data for the motions, $U_{SN}$ is used as the validation uncertainty. Dynamic trim is validated on finer grid set for which $E$=13.8%D < $U_{SN}$=21.2%D; whereas the sinkage is not validated since $E$=11.6%D > $U_{SN}$=0.7%D. Trim is validated but at the larger validation uncertainty interval due to larger $U_G$.

### 5.3.4 Analysis of flow fields and verification of point variables

The flow fields are investigated on four (or three) solutions. First, verification study of point variables is conducted for mean wave profiles. The computed wave height at the intersection of the free surface and no-slip surfaces from $0 \leq {}^{x}/_{L} \leq 1$ defines the wave profile. The wave profiles on four different grid systems are compared in Figure 5-3. To facilitate the comparisons, all four grids on the distribution for the data are interpolated.

***Verification of point variables (mean wave profiles)***

Evaluation of convergence ratio $R_G$, order of accuracy $p_G$, and correction factor $C_G$ for point variables can be problematic when solution changes $\varepsilon_{G21}$ and $\varepsilon_{G32}$ both go to zero so that their ratio is ill-defined. To overcome this issue, separate L2 norms of $\varepsilon_{G21}$ and $\varepsilon_{G32}$ are used to define ratios for $R_G$ and $p_G$, i.e.,

$$\langle R_G \rangle = {\|\varepsilon_{G21}\|_2}\Big/{\|\varepsilon_{G32}\|_2} \tag{5.15}$$

$$\langle p_G \rangle = \frac{\ln\left({\|\varepsilon_{G21}\|_2}\Big/{\|\varepsilon_{G32}\|_2}\right)}{\ln(r_G)} \tag{5.16}$$

where $\langle \quad \rangle$ and $\| \quad \|_2$ are used to denote a profile-averaged quantity (with ratio of solution changes based on L2 norms) and L2 norm, respectively.

For verification of the uncorrected solution, Equation (5.11) estimates distributions of $U_G$ at each point from the local solution change $\varepsilon_{G21}$, where Equation (5.16) estimates $p_G$. An L2 norm of point distributions of errors and uncertainties assess verification levels and judges if global validation happens. Iteration errors and

uncertainties are found to be negligible in comparison to the grid errors and uncertainties for all solutions, i.e., $U_I \ll U_G$ such that $U_{SN} = U_G$.

Table 5-4 tablets the investigated grid, profile-averaged convergence ratio, Richardson Extrapolation error, convergence type, order of accuracy (factor of safety), and global grid uncertainty. There are two verification studies for wave profile; namely, using Grid 1,2,3 and Grid 2,3,4. Figure 5-4 shows $\varepsilon_{G21}$, $\varepsilon_{G21}$, and $\varepsilon_{G21}$ over the investigated range ($0 \leq {}^{x}/_{L} \leq 1$). For both cases, monotonic convergence is obtained, but with $\langle p_G \rangle$ less than $P_{th}$. Noteworthy, $\langle U_{G123} \rangle = 1.94\%S \leq \langle U_{G234} \rangle = 2.57\%S$ is obtained, which means the convergence is achieved corresponding grid refinement. EFD data did not give the information for wave profiles; hence, the validation study is not conducted.

The comparison of free surface wave patterns (wave elevations) and hull surface pressure distributions is shown in Figure 5-5 and 5-6, respectively. As seen in Figure 5-5, CFD results have the symmetric wave pattern at bow, shoulder, and stern regions; and, the wave angle which gets steeper with the grid resolution. The Kelvin wave pattern obtained from the Grid 1 matches well to the theoretical estimation; e.g., transverse wavelength $\lambda_T = 2\pi \times Fn^2 = 0.7406$, diverging wavelength $\lambda_d \cong {}^{\lambda_T}/_{1.49} = 0.4970$, and wave envelope half angle $\vartheta_0 \cong 19.28^{\circ}$. Wave envelop half angle is the angle between the x-axis and enclosing the wave system. With the grid resolution is decreased, the enclosing angle gets steeper; estimated enclosing angles are $19.15^{\circ}$, $18.54^{\circ}$, $17.65^{\circ}$, and $16.39^{\circ}$ on the finer, fine, medium, and coarse solutions, respectively. It shows that the difference between solution from Grid 1 and 2 is smaller than the one between Grid 2 and 3, which means they also show the grid convergence from the view of flow fields. Hull surface pressures are compared in Figure 5-6 for three cases. Since the solution from Grid 1 has huge data set, the post processor (TECPLOT) cannot create the detailed figure due to the machine memory problem. As seen in the figure, the pressure distributions have similar trend; however, there are differences in detail near bow.

Comparison of boundary layer distributions among three grid systems is shown in Figure 5-7. The planes are cut at $x/L = 0.95$ through $0.15$ with $0.10$ distance, from upper to bottom in the figure. It is difficult to find the differences of boundary layer distribution between the three in Figure 5-7(a). To make the difference clear, the comparison of boundary layer profiles among three grid systems is given in Figure 5-7(b). Here, the investigated planes are set to near stern, namely $x/L = 0.95, 0.90$, and $0.85$. As shown in the figure, the solution from Grid 3 agrees well with the one from Grid 2; in contrast, there are differences for each profile between the solution from Grid 4 and the other two.

## 5.4 V&V study for JHSS waterjet simulation at design speed

The waterjet propelled simulations are conducted using added tow force to match the full-scale thrust identity. Waterjet thrusts are prescribed using actuator cylinder body-force model without including swirl and shaft rotation. First, towed simulation with body-force model is carried out using body-fitted coordinate system before the analysis of self-propelled cases (with earth-fixed coordinate system) is performed. Both towed simulation and waterjet propelled simulation are conducted with single speed (Fn=0.34) to estimate the error and numerical uncertainty. Three grid systems are prepared by continuously refined from coarse (4.2M) to fine grid (13.1M) with the refinement ratio of $\sqrt{2}$. Uncertainty assessment studies are performed on iterative convergence and grid convergence. Force coefficients and ship motions, same as barehull case, are evaluated for towed simulation; on the other hand, the ship speed, motions, and waterjet flow parameters are evaluated for self propelled simulation.

### 5.4.1 Towed waterjet simulation

#### 5.4.1.1 Inner iteration convergence

The towed simulations of JHSS waterjet model free to pitch and heave is selected to study $\delta_I$. Herein, only study of solution iterative convergence is presented since the inner iteration number affects relatively small as discussed in section 5.3.1. The RM value from the last 100 data is used to get $U_I$. Uncertainty quantities are presented in %mean value for four grid systems in Table 5-5. $U_I$ is estimated less than 1.6%M for all the variables except Grid 1W solution. $U_I$ for Grid 1W shows bigger values; in particular, for force coefficients.

As seen in the Table 5-5, $U_I$ average values of all three solutions are bigger than the ones for barehull simulations. In particular, $U_I$ for force coefficients are estimated large values due to the large uncertainty of Grid 1W solution. Due to the grid density, the case with finest grid shows relatively slow convergence than the others as seen in barehull case.

#### 5.4.1.2 Grid convergence

The grid convergence study is conducted using a grid refinement ratio $r_G = \sqrt{2}$, and errors for force coefficients and ship motions are presented in Table 5-6. For the force coefficients, error for pressure component ($C_p$) is seen larger than friction component ($C_f$). Since $\Delta C_p$ between Grid 1W and 3W solutions is large, $\Delta C_t$ and $\Delta Rt$ gets larger (about 6%M). For the motions, errors show bigger values than the ones for forces.

Table 5-7 summarizes the grid convergence uncertainty study for the force coefficients and ship motions obtained from waterjet towed computations. As summarized in Table 5-5, $U_I$ (Grid 1W solutions) is not negligibly small, average of 3.0%S. Corresponding $U_I/\varepsilon_{12_G}$ values for grids (1,2,3) are 3.5, 1.1, and 2.2 for $C_t$,

sinkage, and trim, respectively. These values are not small enough and indicate that the $U_G$ is affected by $U_I$. All force coefficients and motions; namely, $C_t$, $C_f$, $C_p$, $R_t$, $Area$, $Sinkage$, $Trim$ achieve convergence (monotonic or oscillatory). The order of accuracy ($P_G$) differ 0.3 to 4.1. Most importantly, the grid-triplet study achieves monotonic convergence for the total resistance coefficient ($C_t$) at the very reasonable uncertainties (~1.0%S). For the dynamic motions, both sinkage and trim show the monotonic convergence with reasonable uncertainty intervals, 0.5 and 0.3%S for sinkage and trim, respectively. Although it is typical that motions are more difficult to converge in grids compared to forces, reasonable uncertainty intervals are estimated in this particular study. Overall, $U_G$ for all the verification variables on grids (1W,2W,3W) show small uncertainty intervals with monotonic or oscillatory convergence type.

#### 5.4.1.3 Validation study

The simulation numerical uncertainty $U_{SN}$, experimental data uncertainty $U_D$, validation uncertainty $U_V$, and comparison error $|E|$ for waterjet towed simulations are presented in Table 5-7. As discussed in section 5.3.4, uncertainty due to the use of previous data is not considered in the present study; therefore, the validation uncertainty is given by $U_V = \sqrt{U_{SN}^2 + U_D^2}$. $U_{SN}$ is estimated at the reasonable intervals for $C_t$, about 3.6%S, and about 6.0%S for both $C_f$ and $C_p$. Although $U_I$ shows relatively large uncertainty interval, $U_{SN}$ for force coefficients are more reasonable intervals compared to barehull case. However, $U_{SN}$ for sinkage is estimated large (25%S) so is for trim (18%S).

$C_t$ is validated at the interval of $U_V$=6.9%D since $E < U_V$. Reducing interval of validation uncertainty for $C_t$ primarily requires reduction in experimental uncertainties since $U_D$=5.8%D > $U_{SN}$=3.6%D. As well as the barehull case, due to the lack of experimental data for the motions, $U_{SN}$ is used as the validation uncertainty. Dynamic sinkage is validated for which $E$=10.8%D < $U_{SN}$=25.8%D; whereas the trim is not validated since $E$=23.3%D > $U_{SN}$=17.7%D. Sinkage is validated but at the larger

validation uncertainty interval due to larger $U_G$. Interestingly, the result for motions is different from the barehull case where the opposite variable is validated and the other is not.

### 5.4.2 Self propelled waterjet simulation

For self-propelled waterjet simulation, the ship accelerates until the resistance equals the prescribed thrust and added tow force and converges to the self propulsion point (SPP); therefore, force coefficients investigated for barehull case become prescribed constant variables as mentioned before. As a result, verification study is done on SPP and dynamic motions for waterjet case.

#### 5.4.2.1 Inner iteration convergence

Table 5-8 shows the solution iterative uncertainties on three grids. Again, as discussed in section 5.3.1, it is found that the inner iteration number affects relatively small; thus, it is not performed. Uncertainty quantities are presented in %mean value, and are estimated at average intervals of 2.1%M on Grid 1W, which is larger than the ones for barehull case. $U_I$ on Grid 1W shows bigger values than on other grids as well as seen in the previous section. However, $U_I$ for dynamic area and self-propulsion point (SPP) are estimated at reasonable intervals. From these uncertainty intervals, it is seen that the motions need more flow time to converge compared to the area and speed for self-propelled simulation case.

#### 5.4.2.2 Grid convergence

The grid convergence study is conducted using a grid refinement ratio $r_G = \sqrt{2}$, and errors for dynamic area, ship motions, and SPP are presented in Table 5-9. For the motions, errors show bigger values than the ones for the other variables as the same trend

obtained for iterative convergence. Table 5-10 summarizes the V&V analysis for waterjet propelled computations. All the necessary information is shown with same manner as earlier simulation cases. As discussed earlier, $U_I$ show bigger values (average of 2.1%S on Grid 1W) than ones for barehull case (average of 0.2%S on Grid 1), and these $U_I$ are not negligible for this case. It would indicate that waterjet simulations need longer iterations to get converged than barehull case due to flow complexity and the residual history has bigger oscillations for waterjet cases. As a result, corresponding $U_I/\varepsilon_{12_G}$ values show relatively big values for motions. $U_I/\varepsilon_{12_G}$ for SPP and area show more than 1. The reason why $U_I/\varepsilon_{12_G}$ for SPP and area gets bigger is that $\varepsilon_{12_G}$ is relatively small (about 0.14%S and 0.10%S, respectively). According to $R_G$ values, all the investigated variables achieve the convergence (monotonic or oscillatory type). Oscillatory convergence is predicted for SPP, which is not strong convergence type; in contrast, dynamic motions and area achieve monotonic convergence. The order of accuracy ($P_G = p_{RE_G}/p_{th}$) for motions is average of 0.7 and $P_G = 0.2$ for area. $U_G$ for motions show relatively large uncertainties ($U_G$ >14%S); on the other hand, $U_G$ for SPP and area show reasonable uncertainties, $U_G$~1.1%S and 1.6%S, respectively. All the solutions for both barehull and waterjet grids with EFD values are presented in Figure 5-2. The grid convergence is clearly seen from the figure as well.

#### 5.4.2.3 Validation study

The simulation numerical uncertainty $U_{SN}$, experimental data uncertainty $U_D$, validation uncertainty $U_V$, and comparison error $|E|$ for waterjet simulations are also shown in Table 5-10. Note that the errors for dynamic sinkage and trim shown in the table are obtained at different speed; thus, the compared EFD values are obtained by interpolating the original data set. For the SPP, $E < U_V$ such that SPP is validated at the $U_V$=1.1%D interval but with oscillatory convergence condition. Dynamic trim and sinkage are validated for which $E$=10.3%D < $U_{SN}$=14.4%D and $E$=27.4%D <

$U_{SN}$=28.5%D, respectively. These are relatively large than the ones for barehull simulation and it would indicate that it is difficult to get stable convergences for the self-propulsion simulations due to the complexity of waterjet flow with dynamic motions.

#### 5.4.2.4 Analysis of flow fields for self-propelled simulations

The accurate prediction of waterjet propulsion using CFD is of interest in the standpoint of performance analysis as well as flow investigation inside the waterjets. Some flow features on waterjet are presented in this section and compared with EFD data if available.

The inlet (St. 1) and the streamlines for the CFD control volume are shown in Figure 5-9 for Fn=0.34 simulation case. Each capture area at St. 1 represents the portion of the flow that is ingested downstream into the respective waterjets. In experiments, the captures areas at St.1 are assumed to be trapezoids which are sized initially by pump diameter at St.3 only. The trapezoid is then scaled by a constant factor until the volumetric flow rate through the operating pump. However, URANS calculations solve for the entire flow field. Thus, streamlines are tracked upstream from the waterjet pumps to produce stream tubes of the flow that is ingested into the waterjets. Figure 5-10 shows more detailed streamlines tracked upstream from the waterjet inlets intersecting with the incoming boundary layer at St.1 for starboard side waterjet. The stream tubes are traced around at the desired location to determine more realistic capture areas (shapes). Actually, the shapes, hence, the areas are different for inward and outward waterjet as seen in the figure. Experimental studies approximate the capture area at St.1 with a trapezoid shape, and it is assumed that capture area sizes have dimensions that are a function of waterjet pump diameter and volumetric flow rate at St. 3. URANS calculations suggest that St. 1 capture area sizes are also dependent on other factors such as inlet spacing on the hull.

The jet interface with the wake is well captured by URANS (Figure 5-11). The outboard nozzle discharge quickly buries into the flow around the transom creating the characteristic “W” shape in both EFD and CFD clearly. All cases have circumferential variation in pressure, both before and after the nozzle even without swirl as an effect of intake geometry. Figure 5-12 compares the boundary layer and free surface elevation between the self-propelled case and the barehull towed simulations. The free surface wake just past the transom is slightly altered due to the jet discharge.

URANS computations are compared to experimental LDV measurements at a model scale. Figure 5-13 shows the comparison of the flux parameters at St. 3 and 6 for the Fn=0.34 case. Flux parameters are defined by $U_x/\bar{V}_{3,6}$. The non-uniformity of the flow is captured well at St. 3 which shows a higher mass flux at the lower half compared with the top region. EFD shows a significant swirl effects in not only St. 3 but also St. 6 due to the blade and shaft inside the duct which are not modeled in CFD; however, simulation captures the lower mass flux at the center and higher one near the circumference. The boundary layer thicknesses at St. 1 are presented at both inlet open and closed situations at Fn=0.34 (Figure 5-14). The bulges in the boundary layer at St. 1 seem both in CFD and EFD causes difference in intake between the inner and outer waterjet. CFD results show no variation of streamwise velocity along the hull width; on the other hand, EFD indicate that the boundary layer thickness changes in the vicinity of the ship centerline (Y=0). In fact, there is a small recirculation region at the corner of bottom with the Hough & Ordway circulation distribution as shown in Figure 5-15. This unrealistic recirculation flow can be fixed by using uniform loading distribution. The comparison of the flux parameters shows that they have similar distribution on St.3.

The wall pressure contours on starboard side waterjet are presented in Figure 5-16. In order to investigate the pressure change near the lip and St.3, the contour levels are changed. It is seen that the pressure distributions on outward and inward waterjet are similar. Large pressure change can be observed on lip of the inlet and also the bottom

edge of the inlet just past the lip. Also, it is seen that there is pressure variation on the upper curvature gradually. Figure 5-17 shows the pressure distributions in the duct center plane for self-propelled simulation at Fn=0.34. Contours are plotted on both inward and outward waterjet. It is seen that the pressure distribution on the outward waterjet is basically similar as the one on inward; however, there is a difference near the lip. In common, high pressure on the lip of the duct inlet and the low pressure on the fore edge of the inlet can be observed in both plots. Pressure is significantly increased near the St.3 where the body force model is mounted.

Comparison of boundary layer distributions between towed barehull and waterjet self-propelled simulation is presented in Figure 5-18(a). The planes in the figure are cut at $x/L = 0.95$ through $0.15$ with $0.10$ distance, from upper to bottom. The comparison of boundary layer profiles between two simulations is given in Figure 5-18(b). Here, the investigated planes are set near stern, namely $x/L = 0.95, 0.90$, and $0.85$. As shown in the figure, estimated boundary profiles for waterjet case differ from the ones for barehull case, in particular, ahead of the inlet tangency from the inlet. It is seen that the boundary layer is thinner for waterjet case than barehull case, and it is also observed in Figure 5-14.

Flow fields on three grid systems are compared in Figure 5-19. Free surface elevations, waterjet outlet jet flows, and boundary layers are presented in order to investigate the grid convergence. Similar difference as barehull free surface elevations can be seen in the first figure; namely, the finer solution capture the Kelvin wave well and the enclosing angle gets steeper with the grid resolution is decreased. For the jet outflows, the shape of outflow gets smooth with grid resolution, and also it is seen that the high pressure distributions are different. For boundary layer, again it is difficult to see the difference from the figure as discussed earlier for barehull case. Figure 5-20 shows the comparison of wall pressure distributions on the starboard waterjet. A little change can be seen but not significant. Lastly, the flow parameters obtained from three grid systems are compared in Figure 5-21. The figure includes comparison of dynamic

motions including self propulsion point (SPP), volume flow rate (VFR), momentum flux at St.1 and 6, net jet thrust, and energy and inlet efficiency. The VFR obtained by integration of the velocity field at St. 6. The momentum flux at St. 1 and 6 are shown together with net jet thrust which is the difference of momentum flux from St. 1 to 6. The explanation of these parameters can be found later. As seen in the figure, the different speed is obtained depending on the grid density.

## 5.5 Analysis of barehull and waterjet simulations over the speed range of 18-42 knots

After the V&V study at the single speed is conducted, both barehull resistance simulations and waterjet propelled simulations are performed over a speed range of 18-42knots. Table 5-11 summarizes the test matrix, includes ship speed $U_S$, model speed $U_M$, Froude number $F_n$, and Reynolds number $R_n$. Six speeds are selected for waterjet propelled simulations; whereas, four ones are selected for barehull simulations. All the simulations are performed based on Fn and corresponding Rn. The results are discussed as follows.

### 5.5.1 Forces and dynamic motions over the speed range

The CFD results of resistance, dynamic trim, and sinkage over a speed range of 18-42 knots are shown with EFD data and uncertainties $U_D$ in Figure 5-22. Total resistance ($R_t$) curve and corresponding thrust deduction ($R_{t_{BH}}/R_{t_{WJ}}$) are presented in Figure 5-22(a). EFD resistance increases with the speed and it does not yet reach hump within the available data for both barehull and waterjet designs. Predictions of CFD computations capture the general trend, and show reasonable agreement with EFD within the average errors of 1.8%D and 8.0%D over the speed range for barehull and waterjet

case, respectively. In particular, the errors from EFD are 0.12%D(BH) and 6.9%D(WJ) at the design cruise speed. EFD thrust deduction differs 0.88 to 0.96, and there is slight change in speed except lower speed case. CFD captures the trend of thrust deduction change; however, it overestimated with the average of 8.5%D. At the design speed, the error is overestimated by 7.5%D; this is due to the underpredicted waterjet resistance and overpredicted barehull resistance. In addition, CFD thrust deduction shows over 1.0 over the speed range, which means that the predicted resistances for waterjet case are smaller than ones for barehull case. One of the possible reasons is that there are a lot of interpolations done by SUGGAR inside the duct because about 10 overlapped blocks are used along the duct surface. Indeed, mass is not fully converged between St.1 and St.6 due to the interpolating among the overlapping grids. Therefore, CFD gives lower resistances for waterjet simulation in the present study.

Dynamic motions for pitch and heave are predicted in running conditions and the curves over speed range are shown in Figure 5-22(b). EFD sinkage increases constantly with Fn, and waterjet induced effect is seen quite small. The dynamic trim shows a bow down trend which reaches a minimum value at 36 knots for both cases, and then follows a bow up trend. Waterjet induced effect is seen on trim; but it seems constant in speed. CFD computations capture the trend of EFD trim and sinkage over the speed range with reasonable accuracy for barehull case. For waterjet simulations, CFD trim captures the trend qualitatively; however, it underpredicted quantitatively with the average of 21%D. Since trim show closer to zero for some speeds, the comparison error is taken by the dynamic range of EFD data, which is 0.175 and 0.260 for barehull and waterjet case, respectively. The prediction of CFD sinkage agrees properly with EFD qualitatively but overpredicted about 12%D.

The errors from EFD for total resistance depending on the grid size are presented in Table 5-12. It is not always that the error on finer grid is the smallest in the four solutions; however, the average error shows 0.4%D which is quite reasonable. From the

table, the grid convergence at other speed can be seen. It is not always that the monotonic convergence is obtained; for instance, monotonic convergence is obtained at Fn=0.3996 such that $|R| = \left|{\varepsilon_{21}}/{\varepsilon_{32}}\right| < 1$ but $R < 0$. Overall, the error is within the experimental uncertainty for almost all the cases.

The errors for total resistance for both barehull and waterjet case and thrust deduction are summarized in Table 5-13. In the table, the finest grid solutions are used for both barehull and waterjet cases. As seen in the table, the errors for barehull case are almost constant at the average of 0.4%D; on the other hand, the errors for waterjet case are not constant and largest error is estimated at lowest speed. Due to the errors of waterjet case, the errors for thrust deduction differ from 7%D to 20%D. The largest error is occurred at Fn=0.24, which is lowest speed. Average errors for $R_T$, sinkage, trim, thrust deduction, etc are summarized in Table 5-14.

### 5.5.2 Barehull simulations over the speed range

Figure 5-23 summarizes the comparison of total resistance given by following Equation (5.17) between the solutions from four grid systems and experimental data. EFD data is shown with the $U_D = 5.79\%$.

$$R_T = \frac{1}{2} C_T \rho U_M^2 L_{WL}^2 \tag{5.17}$$

where $C_T$ is total resistance coefficient, $\rho$ is water density, $U_M$ is model ship speed, and $L_{WL}$ is length of the model ship at Waterline. Predictions of the resistance for this speed range agree very well with the EFD data. Errors from EFD data are shown in Table 5-12. At the design speed, the error is within 6.5%D from EFD data.

As the resistance of a full-scale ship cannot be measured directly, our knowledge about the resistance of ships comes from model tests. The measured calm water

resistance is usually decomposed into various components, although all these components usually interact and most of them cannot be measured individually during the model testing. The total resistance of a ship hull can be decomposed into two components: residual resistance $R_R$ and skin friction resistance $R_{F0}$. Besides, the resistance forces are usually expressed as non-dimensional coefficient forms. Since the frictional drag is not able to be measured directly in model tests, numerical friction lines are generally used for estimated value at different Reynolds numbers. According to ITTC 2008 report (Steen *et al.*, 2008), some particular numerical friction lines are used in most of the organizations. Here, popular friction lines are shown as follows.

1) The Schoenherr correlation line [Schoenherr, (1932)]

$$\frac{0.242}{\sqrt{C_f}} = \log\left(Rn \cdot C_f\right) \tag{5.18}$$

2) ITTC '57 friction line [ITTC report, (1957)]

$$C_f = \frac{0.075}{(\log_{10} Rn - 2.0)^2} \tag{5.19}$$

3) The proposal of Grigson, (1999)

$$C_f = 10^A \tag{5.20}$$

$$with \begin{cases} A = 2.98651 - 10.8843 \cdot B + 5.15283 \cdot B^2 & : 2 \times 10^5 \le Rn \le 10^7 \\ A = -95.7459 + 26.6084 \cdot B - 30.8285 \cdot B^2 + 10.8914 \cdot B^3 & : 10^7 \le Rn \le 6 \times 10^9 \\ B = \log_{10}(\log_{10} Rn) \end{cases}$$

4) The line derived by Katsui *et al.*, (2005)

$$C_f = \frac{0.0066577}{(\log_{10}(Rn) - 4.3762)^{\alpha}} \; for \;\; 1 \times 10^6 \leq Rn \leq 7 \times 10^9 \tag{5.21}$$

$$with \;\; \alpha = 0.042612 \log_{10}(Rn) + 0.56725$$

Grigson's and Katsui's line are obtained by the numerical integration of local friction in the boundary layer, and have no analytical forms. Grigson's line was approximated by Equation (5.20) and Katsui's line is approximated by Equation (5.21). The comparison of all lines is shown in Figure 5-24 from $R_n = 1.0 \times 10^7$ to $5.0 \times 10^7$. All lines give almost same values of $C_{F0}$. In the present study, ITTC '57 line and Schoenherr correlation line are selected as a reference value for frictional resistance since they are reported as the most popular lines in ITTC report (Steen *et al.*, 2008).

Figure 5-25(a) shows the comparison of frictional resistance coefficients with above two numerical lines. As shown in the figure, predictions of CFD computations give overestimated value of frictional drag; however, the trend of Fn change match with numerical friction lines. Figure 5-25(b) shows the comparison of pressure resistance coefficients. EFD resistance data is used here after subtraction of frictional component. Again, predictions of CFD computations agree the trend of Fn change with EFD data well. The CFD and EFD barehull sinkage and trim are shown in Figure 5-26. The dynamic sinkage increases constantly with Fn. The dynamic trim shows a bow down trend which reaches a minimum value of -0.19 at Fn=0.34(36 knots), which is the given design cruise speed, and then follows a bow up trend. The numerical prediction captures this bow moving trend very well corresponding Fn change.

The wave fields at different speeds are also investigated. The wave profiles and free surface elevations are compared in Figure 5-27 and 5-28, respectively. As shown in both figures, the number of waves along the hull is increased with the speed increases.

Also, the angle of bow wave becomes larger with the ship speed increases. It is known that these phenomena are common from the view of ship hydrodynamics, and we can see same trend on EFD. Figure 5-29 shows all the flow features seen in the result at Fn=0.239 using Grid 1. Detailed flow features such as bow wave system, stern wave system, and turbulent wake are clearly shown in the figure.

### 5.5.3 Waterjet self-propulsion simulations over the speed range

The waterjet propelled simulations are conducted over a range of prescribed thrust, obtained using shaft dynamometers in the EFD, and the speed is predicted. The error in predicted speed is less than 8%D over the range of prescribed thrust with Grid #2W. The prescribed shaft thrust is not an indication of the net jet thrust, which is calculated using the ITTC control volume approach. The inlet capture area (St. 1), the streamlines, and St.6 for the CFD control volume are shown in Figure 5-30 for Fn=0.34 simulation case. The velocity profiles at the inflow capture area and the exit on different speeds are shown in Figure 5-30. The width of the capture area varies with speed and has the highest width and therefore highest boundary layer ingestion at 35 knots. The dynamic trim shown in Figure 5-32(a) correlates with Figure 5-30; minimum trim occurs at 35 knots, indicating that the boundary layer ingestion is related to the trim.

The volume flow rate (VFR) obtained by integration of the velocity field at St. 6 shows a good agreement with EFD with an average error of 5.6%D over the speed range (Figure 5-32(b)). The inlet wake fraction (IWF) calculated at St. 1 is also compared with EFD in Figure 5-32(b). The lowest wake fraction occurs at speed corresponding to the highest boundary layer ingestion and lowest trim. URANS simulation captures general trend of IWF as well as VFR. The average error of IWF over the speed range is 2.7%D. Note that the EFD assumes a trapezoidal capture area of the same width but differing heights for calculations of the inlet wake fraction. This difference of definition

contributes to the error since the momentum flux method greatly depends on the shape and size of the capture area (St. 1). URANS can be a useful tool in estimating more realistic capture area by tracing back streamlines entering the rotor to an upstream slice plane, which is also discussed in Delaney *et al.*, (2009).

The net jet thrust is obtained by the momentum flux approach recommended by ITTC. The momentum and energy at St. 1, 3 and 6 are integrated at any station *N* using Equations (5.22) to (5.24).

$$M_N = \rho \bar{V}_N^2 \int_{A_N} \left(\frac{V_{Ex}}{\bar{V}}\right)_N \times \left(\frac{u_x}{\bar{V}}\right)_N \times dA_N \tag{5.22}$$

$$E_N = \rho \bar{V}_N^3 \int_{A_N} \left(\frac{V_{Ex}}{\bar{V}}\right)_N^2 \times \left(\frac{u_x}{\bar{V}}\right)_N \times dA_N \tag{5.23}$$

where the energy velocity $V_E$ includes the static pressure and velocity terms

$$\frac{1}{2}\rho(V_E)^2 = \left(\frac{1}{2}\rho u^2 + p\right) \tag{5.24}$$

The momentum flux at St. 1 and 6 are shown in Figure 5-33(a) together with net jet thrust which is the difference of momentum flux from St. 1 to 6. The average error of net jet thrust is 6.5%D. The inlet efficiency is a measure of losses incurred from flow entering the waterjet inlet, and it is obtained by calculating the energy at St. 1 and 3 (Figure 5-33(b)). The error in the inlet efficiency is mainly due to the difference in the energy calculations between CFD and EFD at St. 3. EFD uses 4 pressure taps at the circumference of the duct in the energy calculations, whereas the CFD averages the pressure over the whole cross section. The average error of inlet efficiency over the speed range is 7.4%D. CFD results show underestimated value of inlet efficiency as well as energies at St. 1 and 3.

EFD inlet efficiency shows significant losses (>15%) over the speed range; frictional drag and pressure losses through the duct are combined together to make losses bigger. Herein, the opportunity of design optimization for intake duct shape can be identified; that is, to maximize the inlet efficiency by geometrical modification. Improving inlet efficiency can be paraphrased to reduction of powering requirement. Furthermore, the self-propelled speed at a given thrust can be used to gauge the powering performance; the shaft thrust requirements are obtained from speed-thrust relations, and it is detected that ~1% increase in speed requires ~4% increase in shaft thrust at the design speed in the present study.

## 5.6 Summary of V&V study

The present V&V work demonstrates the feasibility of using URANS for performance analysis of hull-integrated waterjet propelled ship with free surface and dynamic motions. A verification study is conducted for barehull simulations by four systematically refined grids ranging from $1.2\times10^6$ to $28\times10^6$ grid points, which allows two sets of grid studies; on the other hands, it is done for waterjet case by three systematically refined grids. Uncertainty intervals of iterative/grid size convergences are assessed, and the solutions are validated at the design speed (36knots). Ultimately, total resistance coefficient ($C_t$) for barehull is validated at the average interval of 7.0%D and ship speed for self-propulsion simulation is validated at the uncertainty interval of 1.1%D. In addition, predictions of CFD computations capture the general trend of resistance over the speed range of 18-42knots, and show reasonable agreement with EFD within the average errors of 1.8%D and 8.0%D for barehull and waterjet case, respectively. CFD computations capture trends of EFD motions over the speed range with reasonable accuracy. For barehull simulation, the verification of point variables for wave profiles is also performed, and the grid uncertainty shows reasonable intervals

(average of 2.3%S). Overall, the validation is achieved at reasonable uncertainty intervals and URANS captures the important trends of force and motions properly; thus, the current V&V work has proved that the present URANS approach is an accurate tool to predict the resistance of both JHSS barehull resistance and waterjet computations.

Detailed flow parameters for waterjet propelled simulations are also investigated. Overall, the main performance parameters; namely, net jet thrust, inlet efficiency are predicted reasonably well with an accuracy of ~10%. The simulation using URANS with simplified body force model captures jet wake interference structures well, and warrants more studies into the jets effect on ship wake signatures. Certain issues need to be addressed further to improve validation of the detailed flow features within the duct; both the shaft and the downstream rotor induce some swirl at the inlet St. 3 and 6, which has been neglected. The actuator disk model provides a pressure jump in the axial direction; however, it does not account for the swirl effects due to the blade-rotating. It might cause the increase in error with increase in loading for the shaft thrust. The effects of blades and shafts are needed to be investigated numerically. Additionally, detailed CFD waterjet modeling of geometry including blade-rotating needs to be considered to achieve more realistic simulation.

This work paves way for waterjet inlet optimization opportunity. The main objective of the optimization is identified as reduction of powering requirements by increasing the inlet efficiency through modification of intake duct shape, which currently shows significant losses (> 15%) over the speed range. Detailed flow diagnostics of pressure variations, secondary cross flows, and turbulence flows inside the duct would uncover the mechanisms of energy loss and guide shape optimization. The arrangement of the intake ducts could also be optimized. Initial optimization would focus on modification of intake duct shape to maximize inlet efficiency at 36knots, followed by optimization for modification of whole hull with multiple speeds. Additionally, the bow shape can be optimized since the unique “gooseneck” bow is selected for JHSS model.

Table 5-1 Summary of solution changes for inner iteration and grid size for barehull simulations

| **Inner iteration** | # inner iteration | ΔFS (%inner iteration=5) | | | | | | |
|---|---|---|---|---|---|---|---|---|
| | | $\Delta C_t$ | $\Delta C_f$ | $\Delta C_p$ | $\Delta Area$ | $\Delta Sink$ | $\Delta Trim$ | $\Delta Rt$ |
| | 3 | -0.006 | 0.021 | -0.086 | 0.001 | -2.044 | -1.883 | -0.006 |
| ***Grid 3*** | 4 | 0.005 | 0.002 | 0.013 | 0.001 | 0.004 | -0.004 | 0.005 |
| | 5 | - | - | - | - | - | - | - |
| **Grid size** | # grid points | ΔFS (%$S_1$) | | | | | | |
| | | $\Delta C_t$ | $\Delta C_f$ | $\Delta C_p$ | $\Delta Area$ | $\Delta Sink$ | $\Delta Trim$ | $\Delta Rt$ |
| | 3.6M | 2.145 | -3.235 | 20.55 | -0.033 | -1.031 | -8.848 | 2.111 |
| ***Grid 1,2,3*** | 10.2M | 0.866 | -1.174 | 7.792 | -0.066 | -0.359 | -3.741 | 0.800 |
| | 28.7M | - | - | - | - | - | - | - |
| **Grid size** | # grid points | ΔFS (%$S_2$) | | | | | | |
| | | $\Delta C_t$ | $\Delta C_f$ | $\Delta C_p$ | $\Delta Area$ | $\Delta Sink$ | $\Delta Trim$ | $\Delta Rt$ |
| | 1.3M | 3.352 | -4.758 | 28.671 | -0.118 | -0.267 | -19.35 | 3.230 |
| ***Grid 2,3,4*** | 3.6M | 1.268 | -2.085 | 11.835 | 0.033 | -0.674 | -5.306 | 1.301 |
| | 10.2M | - | - | - | - | - | - | - |

Table 5-2 Summary of iteration uncertainties for barehull simulations

| | Grid # | $C_t$ | $C_f$ | $C_p$ | $Area$ | $Sink$ | $Trim$ | $R_t$ |
|---|---|---|---|---|---|---|---|---|
| $\boldsymbol{U_{I_0}}$ (%) | 2 | 0.0087 | 0.0007 | 0.0043 | 0.0001 | 0.0001 | 0.0001 | 0.0085 |
| | 1 | 0.1672 | 0.1274 | 0.8321 | 0.0104 | 0.2141 | 0.0509 | 0.1782 |
| | 2 | 0.1106 | 0.0507 | 0.4803 | 0.0066 | 0.1369 | 0.0958 | 0.1211 |
| $\boldsymbol{U_I}$ (%) | 3 | 0.0630 | 0.0523 | 0.3435 | 0.0005 | 0.2391 | 0.1274 | 0.0639 |
| | 4 | 0.2065 | 0.1867 | 0.5877 | 0.0169 | 0.9908 | 0.4245 | 0.2072 |
| | Ave. | 0.1368 | 0.1043 | 0.5609 | 0.0086 | 0.3952 | 0.1747 | 0.1426 |

Table 5-3 Summary of grid convergence uncertainty study and validation study for barehull simulations

| | *Grid Set* | $U_I$ † | $U_I/\varepsilon_{12G}$ | $R_G$ | *Conv. Type* | $P_G$ | $U_G$ † | $U_{SN}$ † | $U_D$ † | $U_V$ † | $E$ † |
|---|---|---|---|---|---|---|---|---|---|---|---|
| *Ct* | 1,2,3 | 0.167 | 0.482 | 0.678 | MC | 0.561 | 3.595 | 3.599 | 5.79 | 6.817 | 2.267 |
| | 2,3,4 | 0.111 | 0.128 | 0.608 | MC | 0.717 | 3.622 | 3.624 | 5.79 | 6.830 | 0.897 |
| *Cf* | 1,2,3 | 0.127 | 0.062 | 0.570 | MC | 0.811 | 2.740 | 2.743 | - | - | - |
| | 2,3,4 | 0.051 | 0.041 | 0.717 | MC | 0.358 | 15.87 | 15.87 | - | - | - |
| *Cp* | 1,2,3 | 0.832 | 0.070 | 0.611 | MC | 0.711 | 22.57 | 22.59 | - | - | - |
| | 2,3,4 | 0.480 | 0.062 | 0.703 | MC | 0.509 | 56.50 | 56.50 | - | - | - |
| *Rt* | 1,2,3 | 0.178 | 0.137 | 0.674 | MC | 0.568 | 5.298 | 5.301 | 5.79 | 7.850 | 2.339 |
| | 2,3,4 | 0.178 | 0.152 | 0.610 | MC | 0.713 | 2.308 | 2.315 | 5.79 | 6.236 | 0.987 |
| *Area* | 1,2,3 | 0.010 | 0.305 | -0.218 | OC | - | 0.075 | 0.076 | - | - | - |
| | 2,3,4 | 0.010 | 0.223 | -2.012 | OD | - | - | - | - | - | - |
| *Sinkage* | 1,2,3 | 0.214 | 0.317 | 0.535 | MC | 0.903 | 0.696 | 0.728 | - | - | 11.61 |
| | 2,3,4 | 0.137 | 0.381 | -1.654 | OD | - | - | - | - | - | 11.80 |
| *Trim* | 1,2,3 | 0.051 | 0.010 | 0.732 | MC | 0.449 | 21.17 | 21.17 | - | - | 13.76 |
| | 2,3,4 | 0.096 | 0.026 | 0.378 | MC | 1.404 | 26.52 | 26.52 | - | - | 4.904 |

†Note: $U_D$, $U_V$, and $E$ are *%D* and others are %$S_1$ or *%*$S_2$

Table 5-4 Profile averaged verification results for barehull wave profiles

| Grid # | $R_G$ $(\varepsilon_{G21}/\varepsilon_{G32})$ $(\varepsilon_{G32}/\varepsilon_{G43})$ | δRE | Conv. Type | P $(p_G/p_{th})$ | $U_G$ $(\%S_1$ and $S_2)$ |
|---|---|---|---|---|---|
| 1,2,3 | 0.5356 | 0.00017 | MC | 0.9008 | 1.9424 |
| 2,3,4 | 0.5881 | 0.00040 | MC | 0.7658 | 2.5691 |

Table 5-5 Summary of iteration uncertainties for waterjet towed simulations

| | Grid | $C_t$ | $C_f$ | $C_p$ | $Area$ | $Sink$ | $Trim$ | $Rt$ |
|---|---|---|---|---|---|---|---|---|
| **Towed $U_I$ (%)** | 1W | 3.490 | 5.711 | 4.583 | 0.073 | 1.084 | 2.243 | 3.529 |
| | 2W | 1.154 | 1.014 | 1.539 | 0.029 | 0.119 | 0.305 | 1.159 |
| | 3W | 0.636 | 0.350 | 0.636 | 0.013 | 0.023 | 0.234 | 0.388 |
| | Average | 1.678 | 2.358 | 2.253 | 0.038 | 0.409 | 0.927 | 1.692 |

Table 5-6 Summary of solution changes for grid size for waterjet towed simulations

| Self-propelled | # Grid points | ΔFS $(\%S_{1W})$ | | | | | | |
|---|---|---|---|---|---|---|---|---|
| | | $\Delta C_t$ | $\Delta C_f$ | $\Delta C_p$ | $\Delta Area$ | $\Delta Sink$ | $\Delta Trim$ | $\Delta Rt$ |
| ***Grid 1W,2W,3W*** | 4.2M | 6.259 | 0.589 | 12.439 | -0.171 | -6.013 | -27.831 | 6.078 |
| | 6.6M | -0.398 | -0.780 | 0.542 | -0.069 | -2.697 | -7.602 | -0.467 |
| | 13M | - | - | - | - | - | - | - |

Table 5-7 Summary of grid convergence uncertainty study and validation study for JHSS waterjet towed simulations

| | *Grids* | $U_I$ † | $U_I/\varepsilon_{12G}$ | $R_G$ | *Conv. Type* | $P_G$ | $U_G$ † | $U_{SN}$ † | $U_D$ † | $U_V$ † | $E$ † |
|---|---|---|---|---|---|---|---|---|---|---|---|
| *Ct* | 1W, 2W, 3W | 3.490 | 8.776 | 0.060 | MC | 4.065 | 0.982 | 3.626 | 5.79 | 6.831 | 0.645 |
| *Cf* | | 5.711 | 6.729 | -0.670 | OC | - | 0.633 | 5.746 | - | - | - |
| *Cp* | | 4.583 | 7.183 | -0.069 | OC | - | 4.634 | 6.518 | - | - | - |
| *Rt* | | 3.529 | 7.563 | -0.071 | OC | - | 3.272 | 4.812 | 5.79 | 7.529 | 5.779 |
| *Area* | | 0.073 | 1.055 | 0.683 | MC | 0.551 | 0.295 | 0.304 | - | - | - |
| *Sinkage* | | 1.084 | 0.402 | 0.813 | MC | 0.299 | 25.76 | 25.78 | - | - | 10.84 |
| *Trim* | | 2.243 | 0.295 | 0.376 | MC | 1.412 | 17.57 | 17.71 | - | - | 23.32 |

†Note: $U_D$, $U_V$, and $E$ are $\%D$ and others are $\%S_{1W}$

Table 5-8 Summary of iteration uncertainties for waterjet propelled simulations

| | Grid | $Area$ | $Sink$ | $Trim$ | $SPP$ |
|---|---|---|---|---|---|
| **Self-propelled** $\boldsymbol{U_I}$ (%) | 1W | 0.146 | 2.696 | 5.413 | 0.188 |
| | 2W | 0.019 | 0.033 | 0.095 | 0.009 |
| | 3W | 0.013 | 0.022 | 0.276 | 0.023 |
| | Average | 0.059 | 0.917 | 1.928 | 0.073 |

Table 5-9 Summary of solution changes for grid size for waterjet propelled simulations

| Self-propelled | # Grid points | ΔFS (%$S_{1W}$) | | | |
|---|---|---|---|---|---|
| | | $\Delta Area$ | $\Delta Sink$ | $\Delta Trim$ | $\Delta SPP$ |
| ***Grid 1W,2W,3W*** | 4.2M | -0.207 | -10.873 | -27.647 | -1.989 |
| | 6.6M | -0.097 | -4.232 | -10.346 | 0.140 |
| | 13M | - | - | - | - |

Table 5-10 Summary of grid convergence uncertainty study and validation study for JHSS waterjet propelled simulations

| | *Grids* | $U_I$ † | $U_I/\varepsilon_{12G}$ | $R_G$ | *Conv. Type* | $P_G$ | $U_G$ † | $U_{SN}$ † | $U_D$ † | $U_V$ † | $E$ † |
|---|---|---|---|---|---|---|---|---|---|---|---|
| *SPP* | 1W, 2W, 3W | 0.188 | 1.337 | -0.066 | OC | - | 1.065 | 1.081 | 0.12 | 1.088 | 0.195 |
| *Sinkage* | | 2.696 | 0.637 | 0.637 | MC | 0.650 | 14.10 | 14.36 | - | - | 10.27 |
| *Trim* | | 5.413 | 0.523 | 0.598 | MC | 0.742 | 28.01 | 28.53 | - | - | 27.43 |
| *Area* | | 0.146 | 1.511 | 0.880 | MC | 0.185 | 1.621 | 1.628 | - | - | - |

†Note: $U_D$, $U_V$, and $E$ are *%D* and others are $\%S_{1W}$

Table 5-11 Test matrix of speeds selected for the URANS simulations of JHSS

| Ship Speed ($U_S$) | | Model Speed ($U_M$) | | Froude # | Reynolds # |
|---|---|---|---|---|---|
| (knots) | (ft/sec) | (knots) | (ft/sec) | | ($\times 10^6$) |
| 20.00 | 33.76 | 3.42 | 5.78 | 0.1902 | 15.411 |
| 25.10 | 42.37 | 4.30 | 7.25 | 0.2386 | 19.341 |
| 30.10 | 50.80 | 5.15 | 8.70 | 0.2862 | 23.192 |
| 36.11† | 60.96 | 6.18 | 10.44 | 0.3434 | 27.830 |
| 39.00 | 65.82 | 6.68 | 11.27 | 0.3708 | 30.051 |
| 42.02 | 70.93 | 7.19 | 12.14 | 0.3996 | 32.381 |

†Note: This speed is selected for design cruise speed

Table 5-12 Summary of errors of total resistance from EFD on four grids shown in %D for JHSS barehull simulations

| | *Finer (Grid1)* | *Fine (Grid2)* | *Medium (Grid3)* | *Coarse (Grid4)* |
|---|---|---|---|---|
| *Fn=0.2387* | -0.170 %D | 1.042 %D | 2.096 %D | -0.094 %D |
| *Fn=0.2862* | -0.114 %D | -0.040 %D | 0.936 %D | 0.401 %D |
| *Fn=0.3434* | 0.122 %D | 1.304 %D | 3.403 %D | 6.465 %D |
| *Fn=0.3996* | -2.036 %D | -2.130 %D | -0.664 %D | -0.864 %D |
| *Average* | -0.406 %D | 0.044 %D | 1.443 %D | 1.477 %D |

Table 5-13 Summary of errors of total resistance and thrust deduction from EFD on finest grids shown in %D for JHSS barehull and waterjet simulations

| | *Barehull (Finer)* | *Waterjet (Fine)* | *Thrust deduction* |
|---|---|---|---|
| *Fn=0.2387* | -0.170 %D | -16.236 %D | 19.18 %D |
| *Fn=0.2862* | -0.114 %D | -7.425 %D | 7.897 %D |
| *Fn=0.3434* | 0.122 %D | -6.870 %D | 7.508 %D |
| *Fn=0.3708* | -0.240 %D | -8.575 %D | 9.117 %D |
| *Fn=0.3996* | -2.036 %D | -8.816 %D | 7.435 %D |
| *Average* | -0.406 %D | -7.987 %D | 8.523 %D |

Table 5-14 Average errors over the speed range between CFD and EFD (%D)

| | *Rt* | *Sinkage* | *Trim*† | *Thrust deduction* | *Volume flow rate* | *Inlet wake fraction* | *Gross jet thrust* | *Inlet efficiency* |
|---|---|---|---|---|---|---|---|---|
| BH | 1.759 | 11.641 | 9.293 | - | - | - | - | - |
| WJ | 7.987 | 13.857 | 21.431 | 8.523 | 5.662 | 2.714 | 6.506 | 7.394 |

Note: † EFD Trim is dynamic range since some of them are close to zero

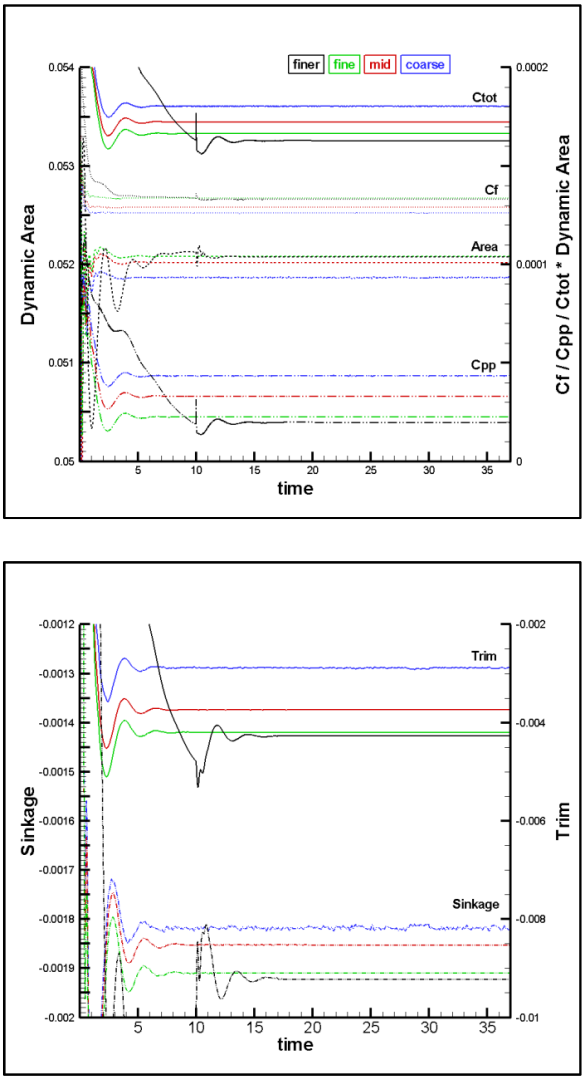


Figure 5-1 Residual history for (Top) force coefficients including dynamic area and (Bottom) dynamic motions

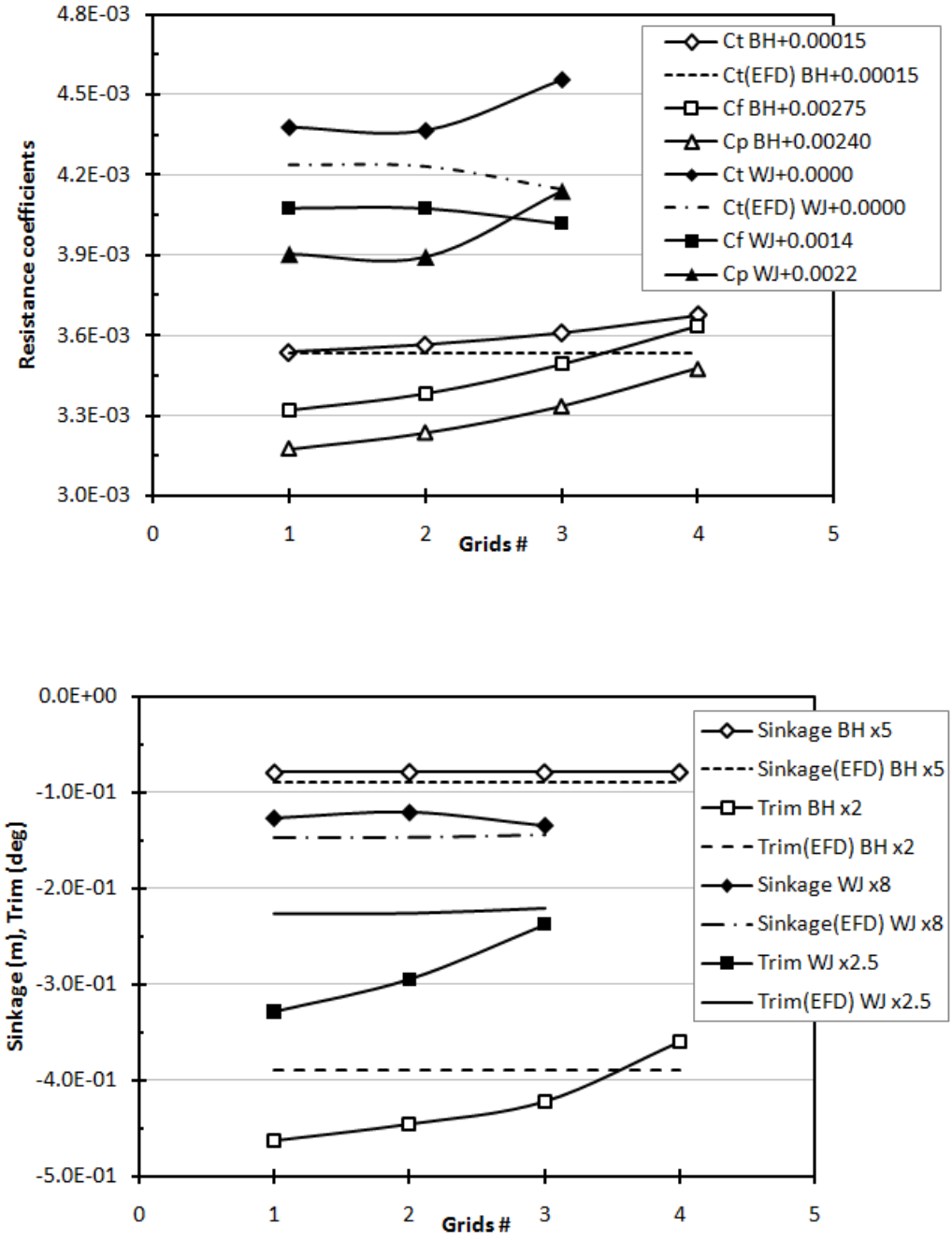


Figure 5-2 Solutions of verification variables of (Top) force coefficients and (Bottom) dynamic motions at Fn=0.34

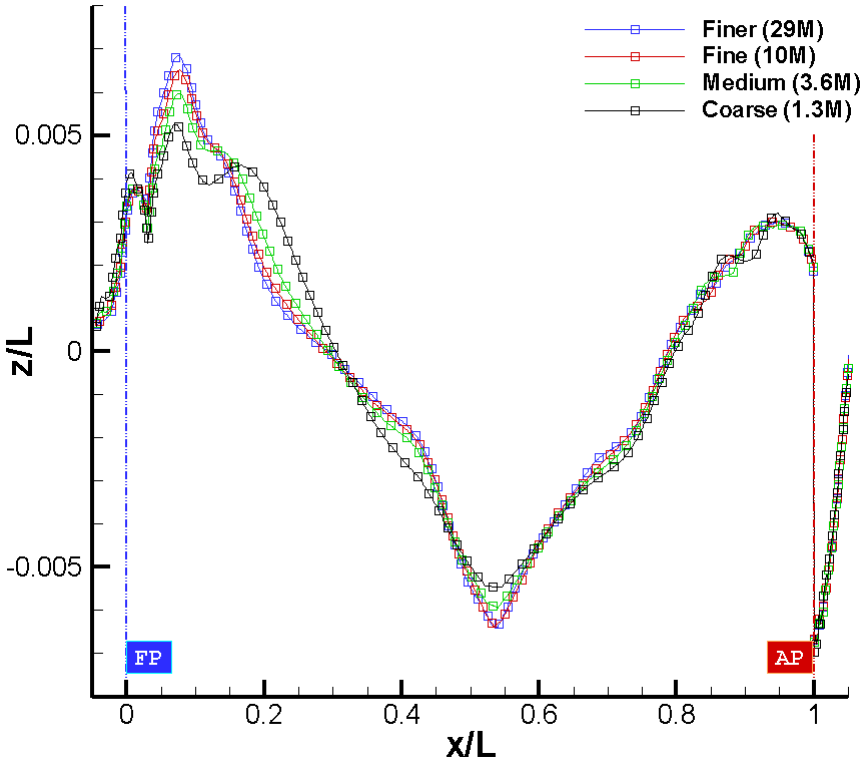


Figure 5-3 Comparison of wave profiles on four grid systems for barehull simulations

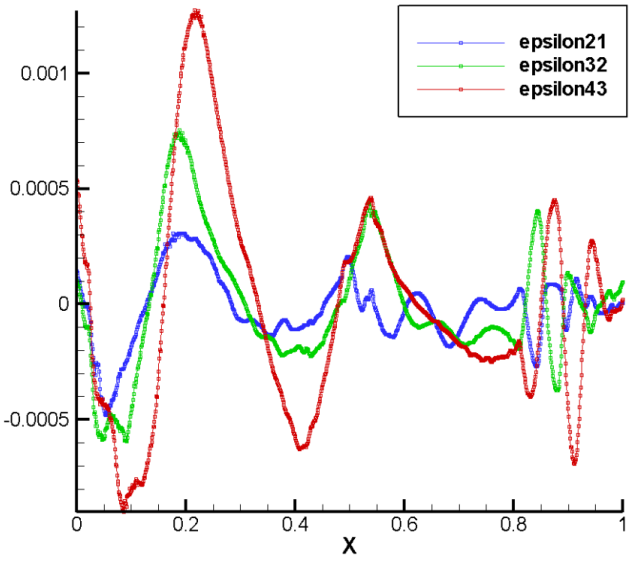


Figure 5-4 Plots of wave profile errors between solutions on four different grids

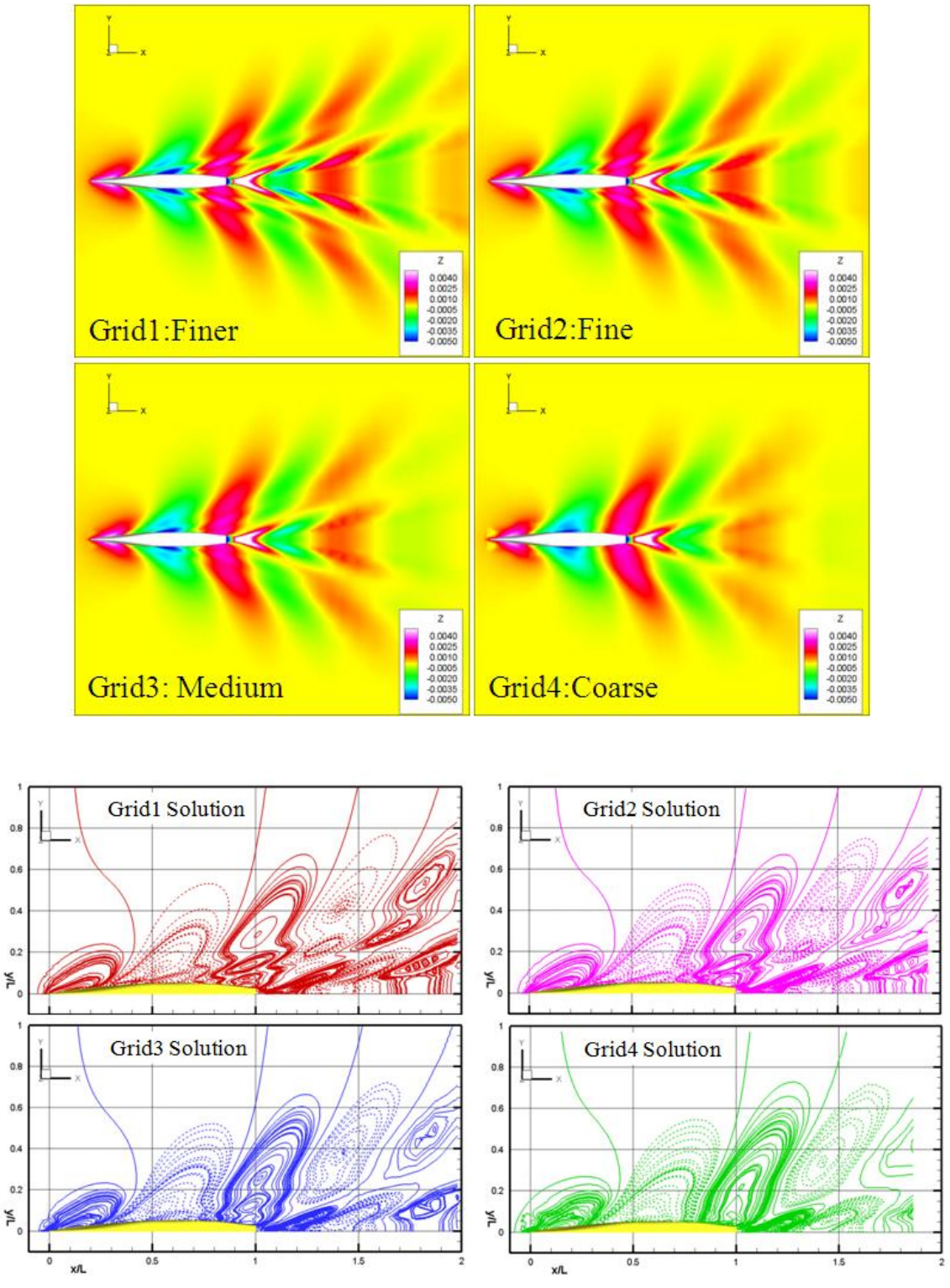


Figure 5-5 Comparison of free surface elevations around barehull on four grid systems

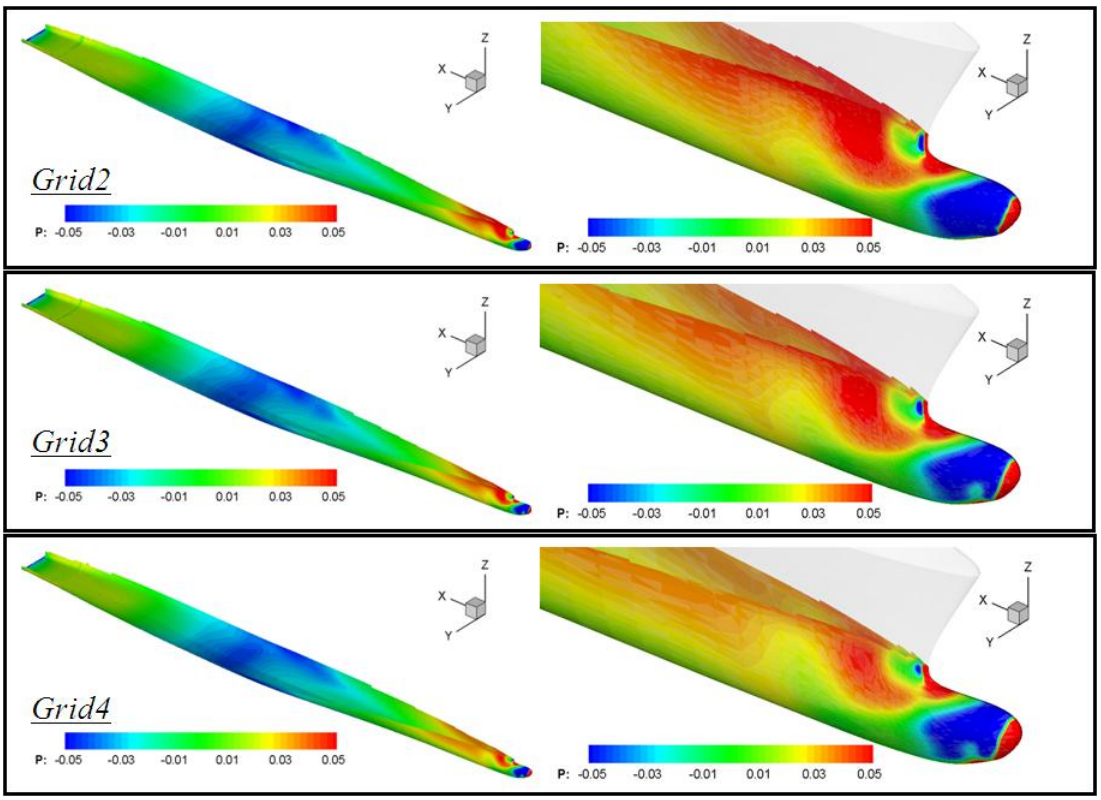


Figure 5-6 Comparison of hull surface pressure contours under the free surface on three grid systems

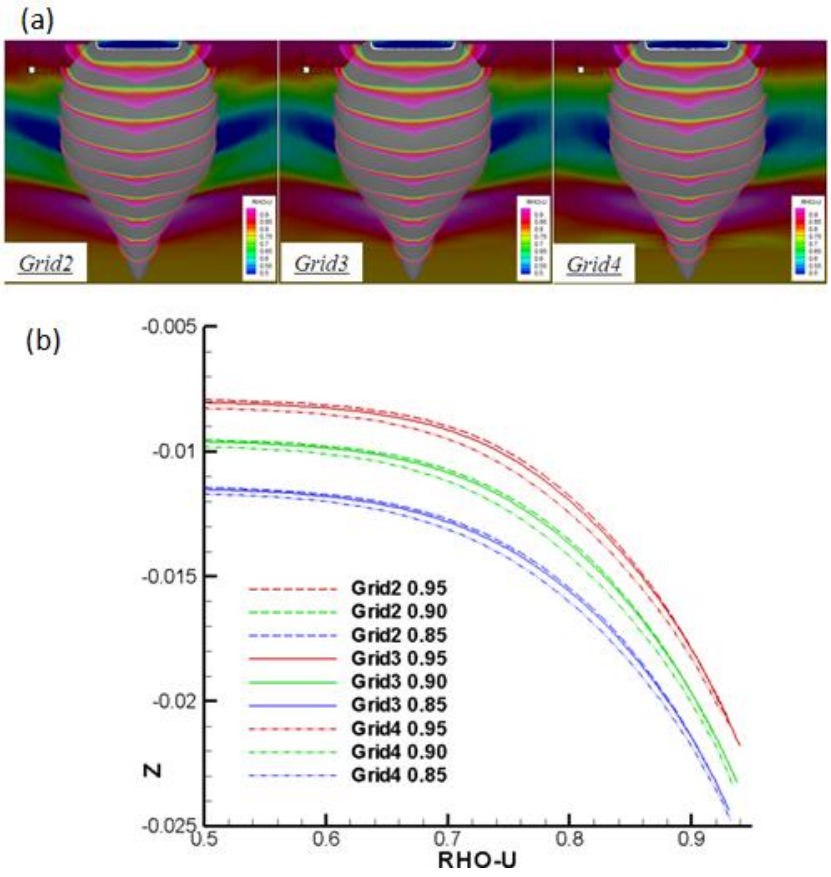


Figure 5-7 Comparison of boundary layers for barehull on three grid systems: (a) boundary layer distributions, (b) boundary layer profiles

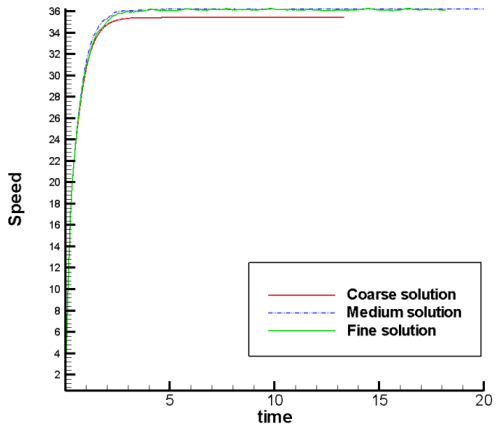


Figure 5-8 Residual history of speed for self-propulsion simulations compared on three grid systems

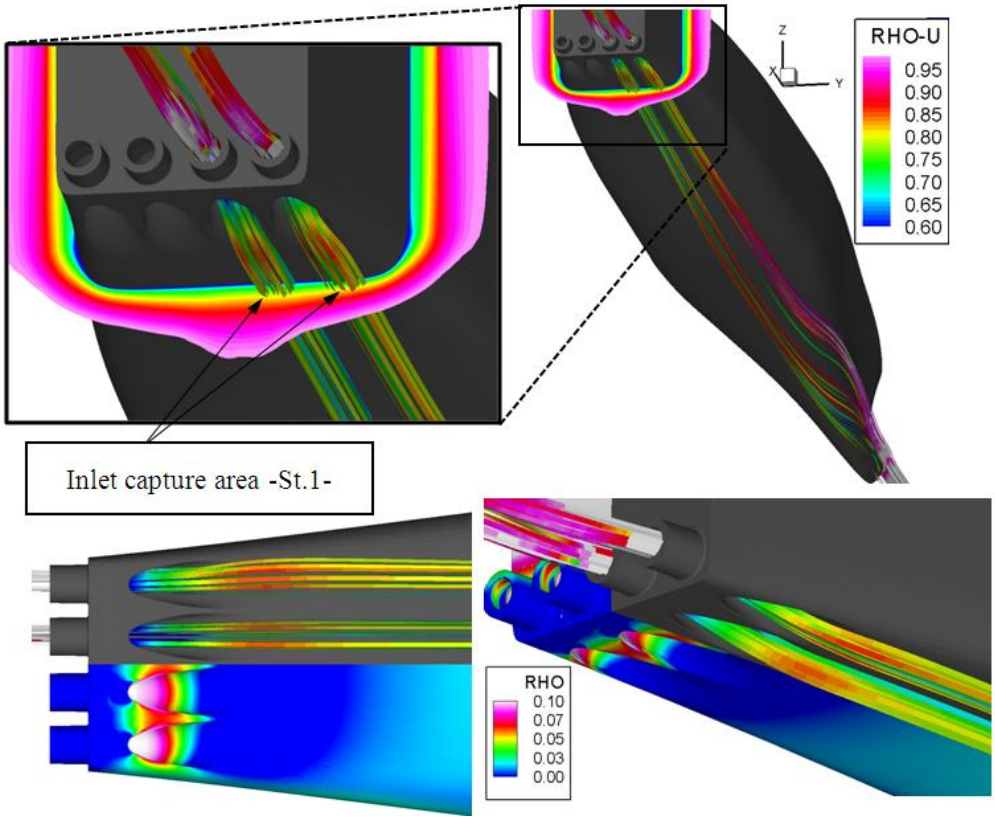


Figure 5-9 Illustration of inlet stream tube and stream line through the waterjet at Fn=0.34

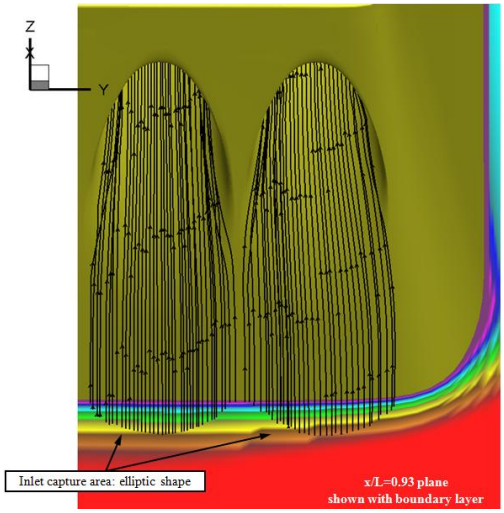


Figure 5-10 Limiting streamlines on a ship bottom shown with boundary layer at St.1

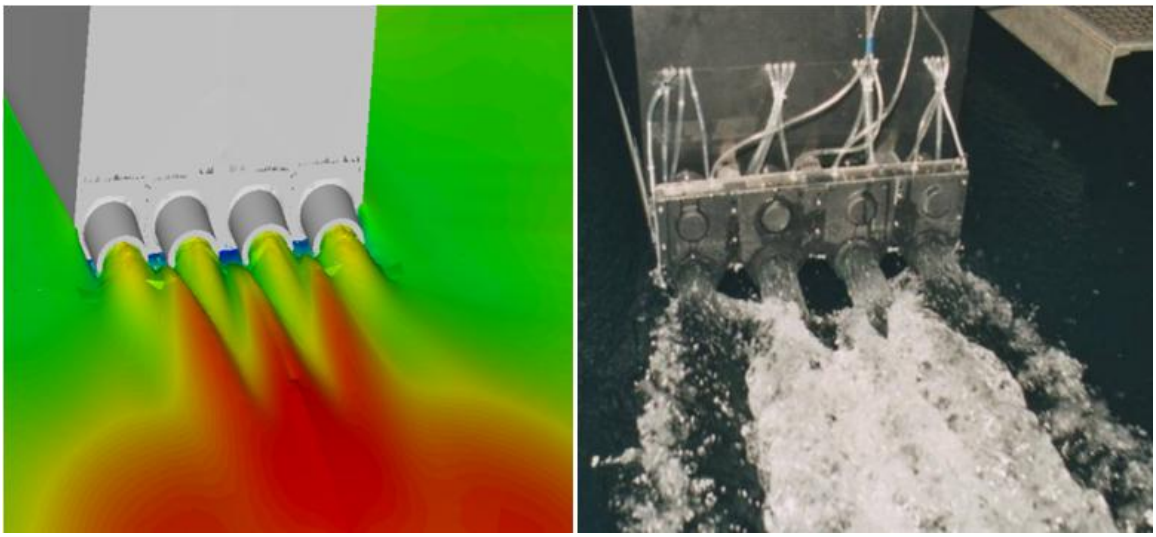

Figure 5-11 Comparison of jet wake interface at Fn=0.34: (Left) CFD, (Right) EFD

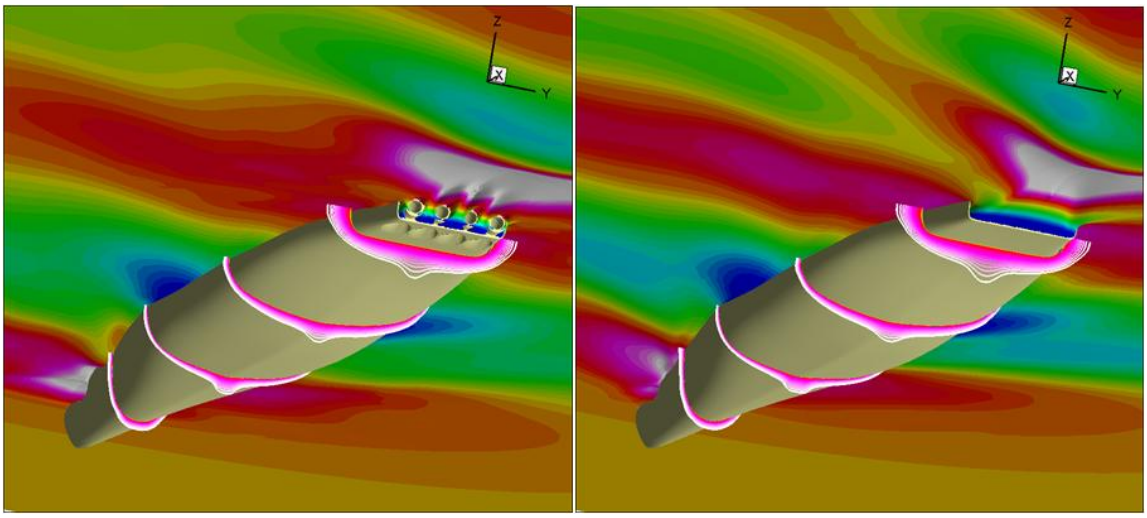


Figure 5-12 Boundary layer and free-surface predictions at Fn=0.34:
(Left) self propelled, (Right) barehull simulations

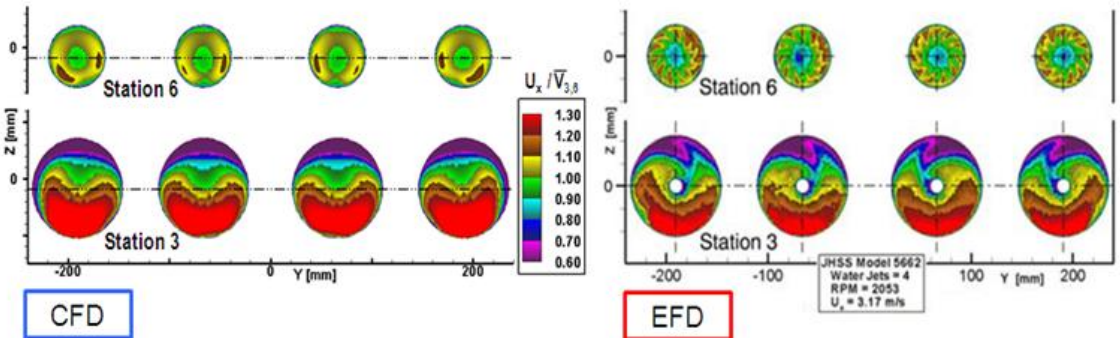


Figure 5-13 Flux parameters at St. 3 and 6 compared with EFD data at Fn=0.34

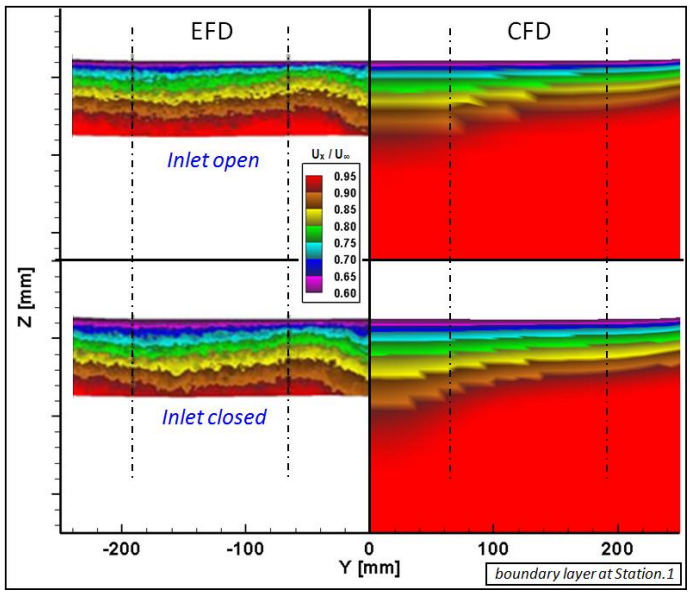


Figure 5-14 Comparison of boundary layers at St. 1 between (Left) EFD and (Right) CFD at (Top) inlet open, (Bottom) inlet closed condition at Fn=0.34

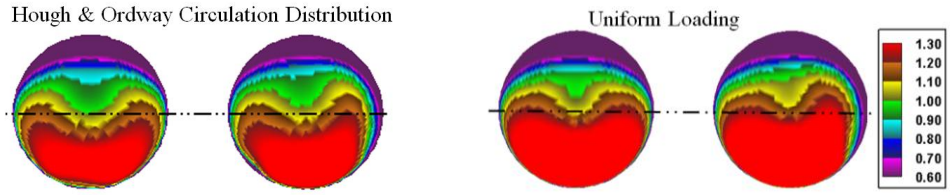


Figure 5-15 Comparison of the flux parameter at St. 3 between two different circulation distribution methods: (Left) Hough& Ordway, (Right) Uniform

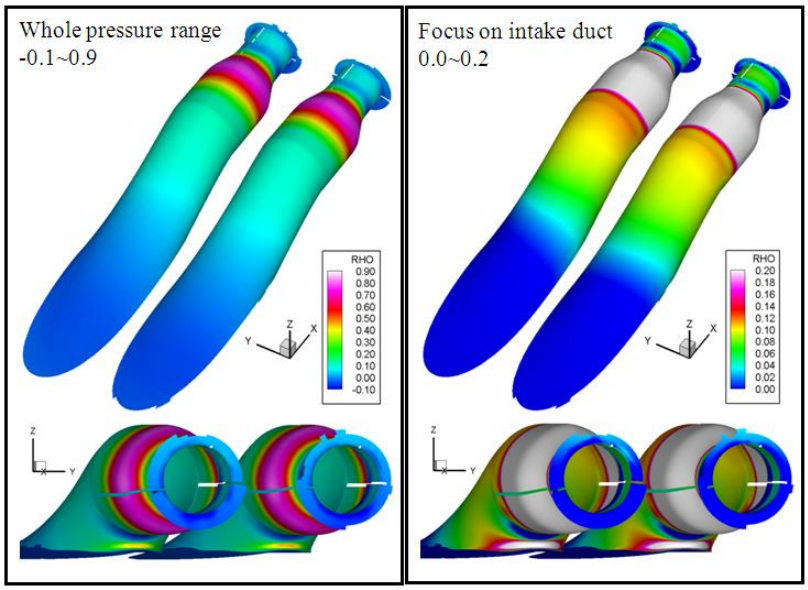


Figure 5-16 Wall pressure contours on starboard side waterjet with different scales

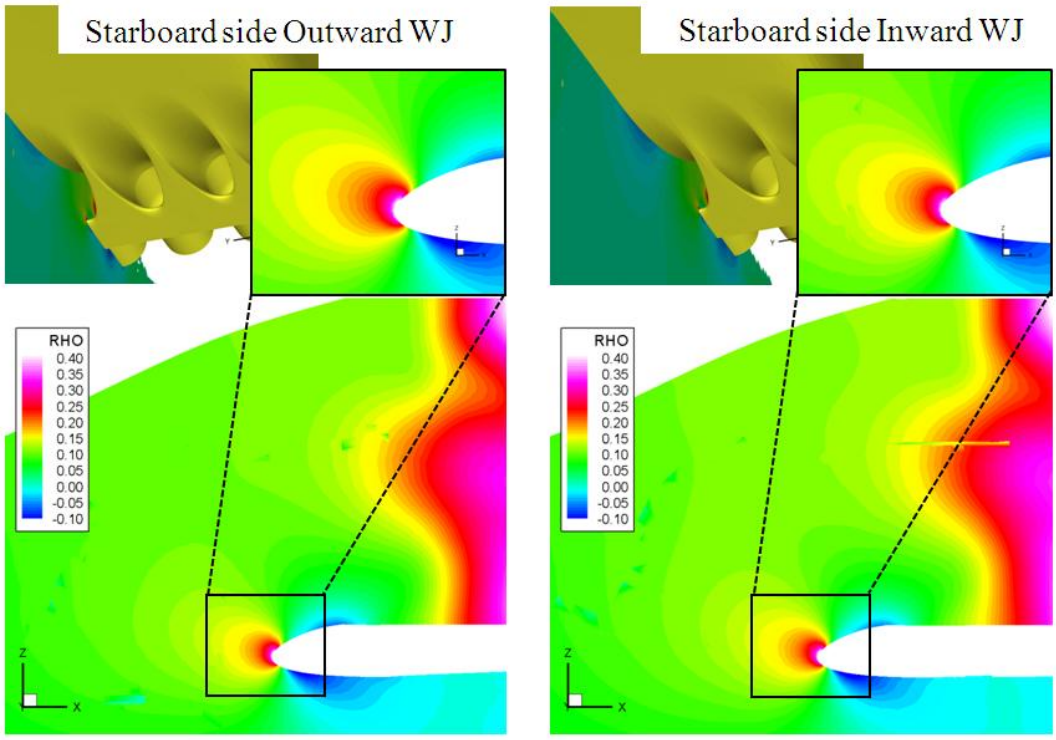


Figure 5-17 Plots of pressure contours inside the duct cutting at the center of waterjet: (Left) outward, (Right) inward waterjet

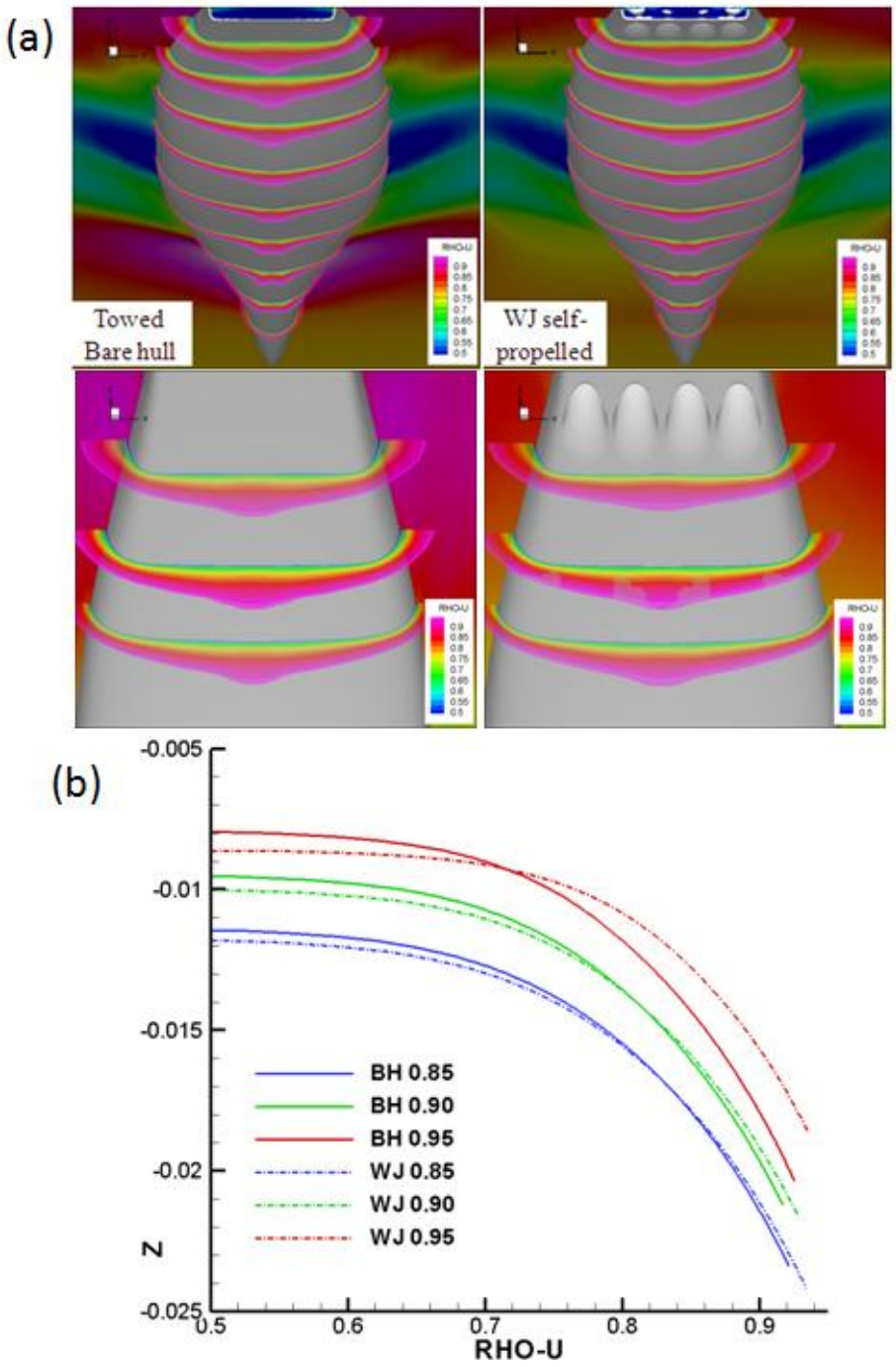


Figure 5-18 Comparison of boundary layers for waterjet simulations: (a) boundary layer distributions for (Left) towed barehull, (Right) waterjet self-propelled simulation, (b) boundary layer profiles

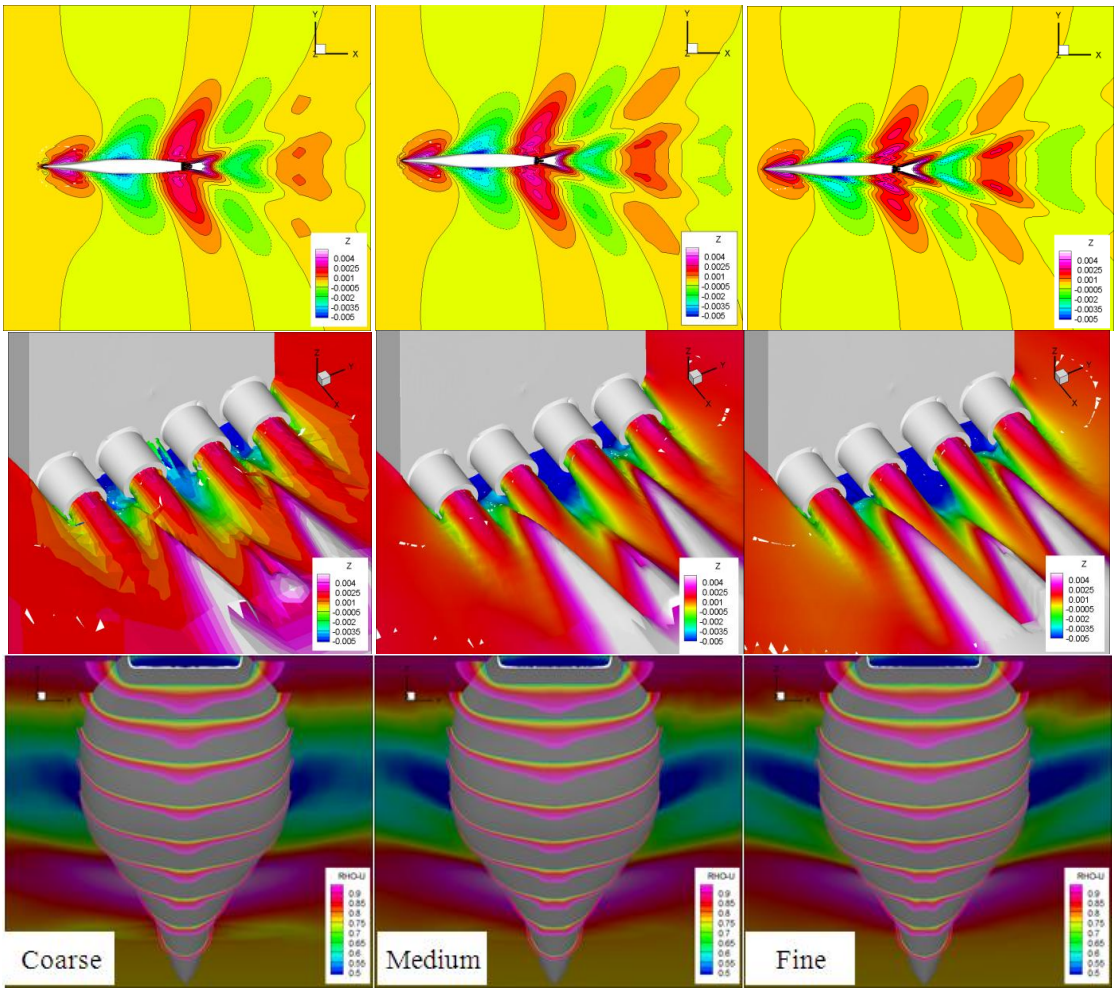


Figure 5-19 Comparison of flow fields on three grid systems: (Top) free surface elevations, (Middle) waterjet outlet jet flows, (Bottom) boundary layer distributions

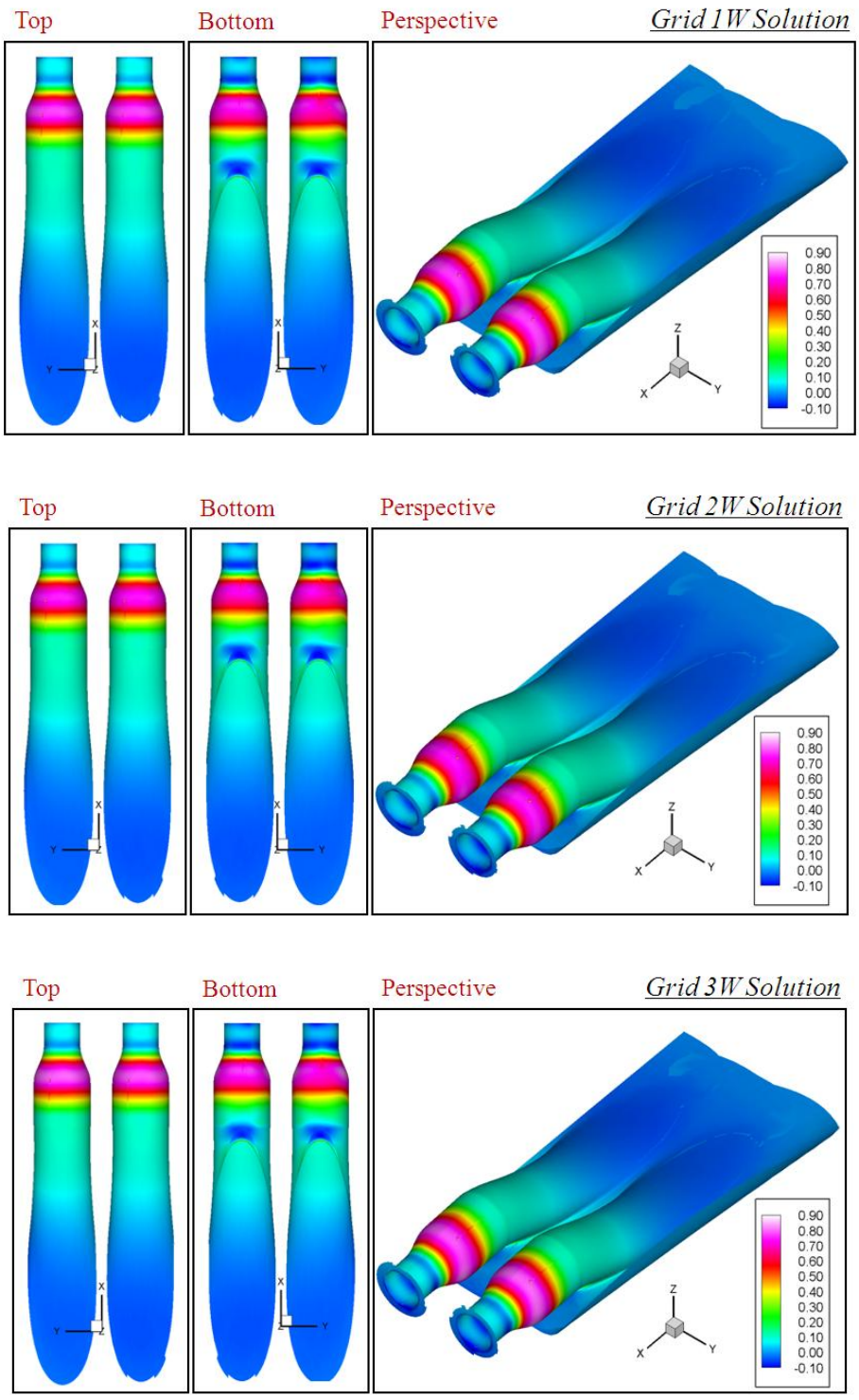


Figure 5-20 Comparison of wall pressure distributions on the starboard waterjet on three grid systems

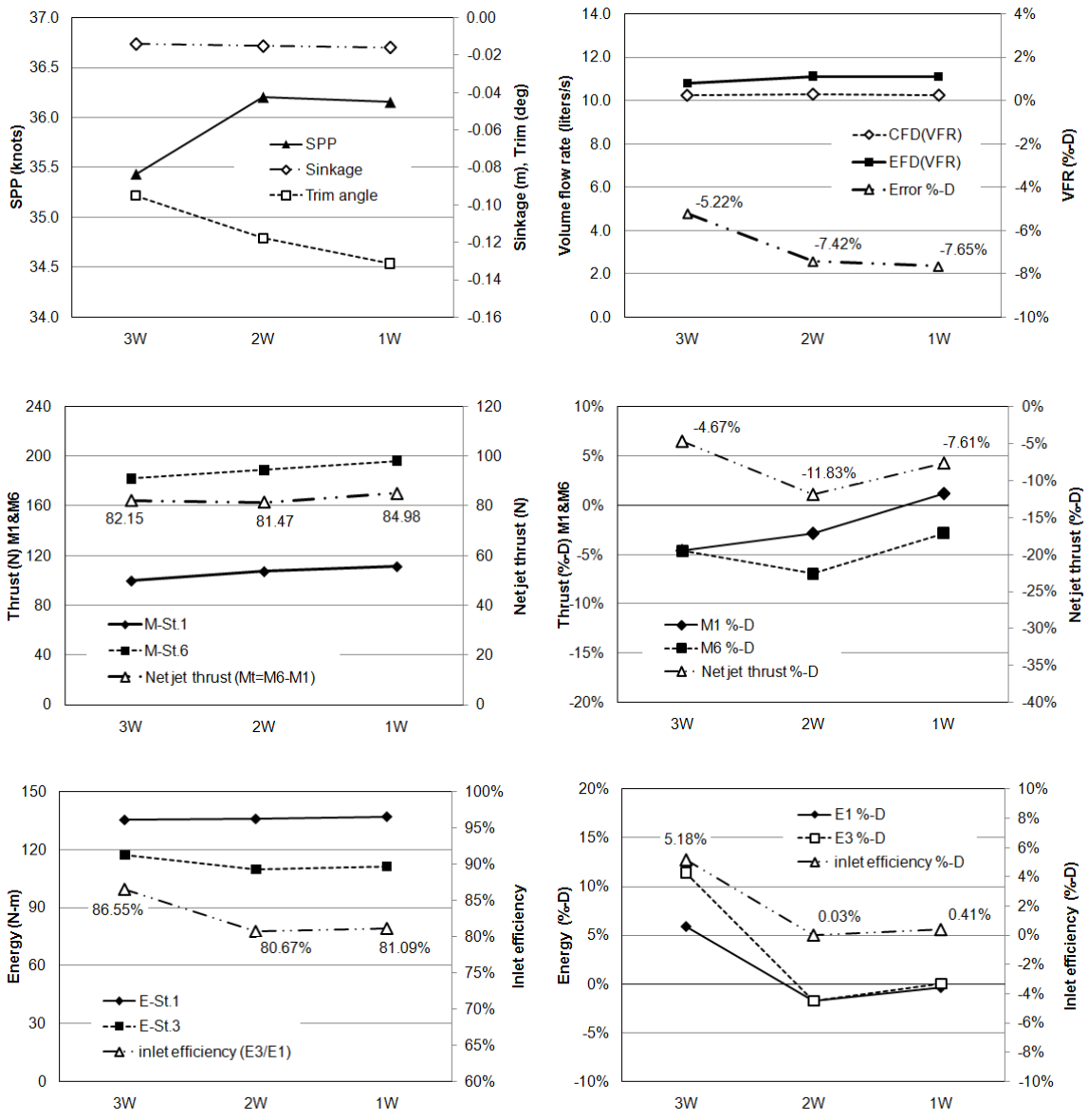


Figure 5-21 Comparison of flow parameters at Fn=0.34 on three grid systems, (Top) Left: SPP, sinkage, and trim angle, Right: VFR compared with EFD data, (Middle) Left: thrust at St. 1, 6, and NJT, Right: comparison of thrust with EFD, (Bottom) Left, energy at St. 1, 3, and IE, Right: comparison of energy with EFD

(a)

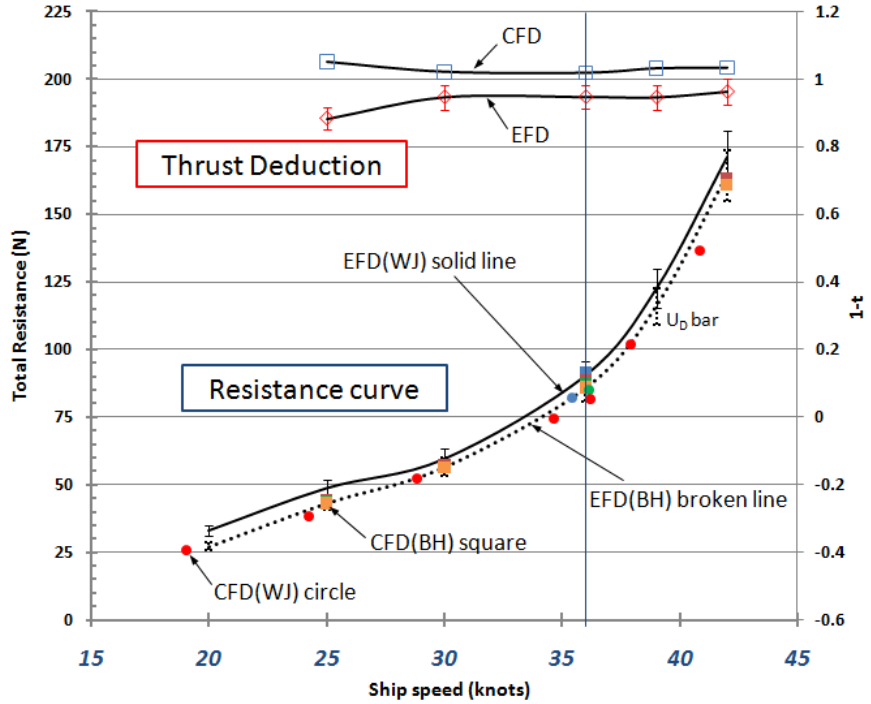


(b)

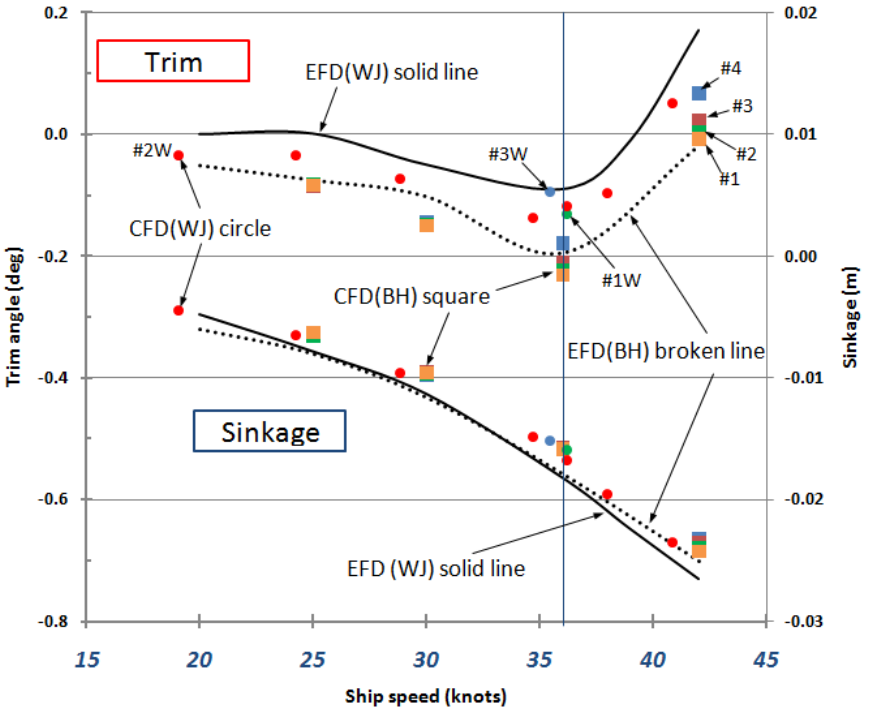


Figure 5-22 Comparison of forces and motions over the speed range with EFD data: (a) total resistance and thrust deduction, (b) dynamic trim and sinkage

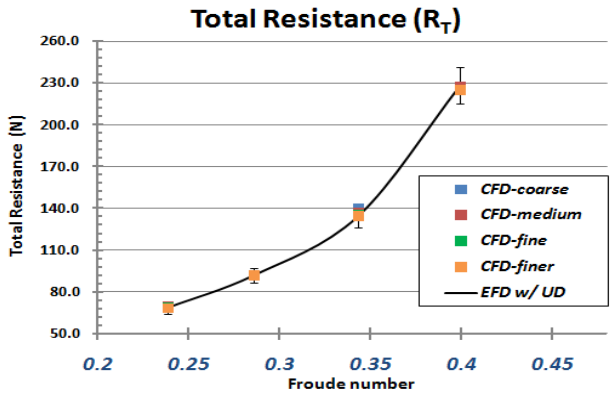


Figure 5-23 Comparison of total resistance with EFD data over the speed range of Fn=0.24~0.40 for barehull design

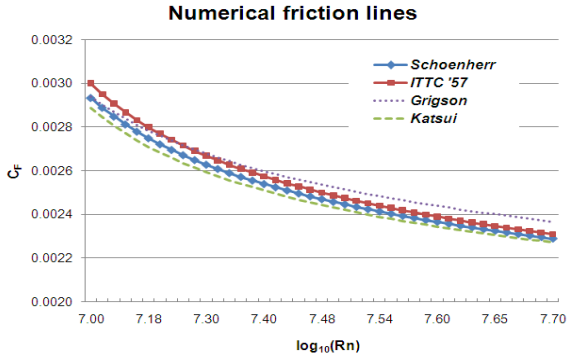


Figure 5-24 Comparison of numerical friction lines from $Rn = 1.0 \times 10^7$ to $5.0 \times 10^7$

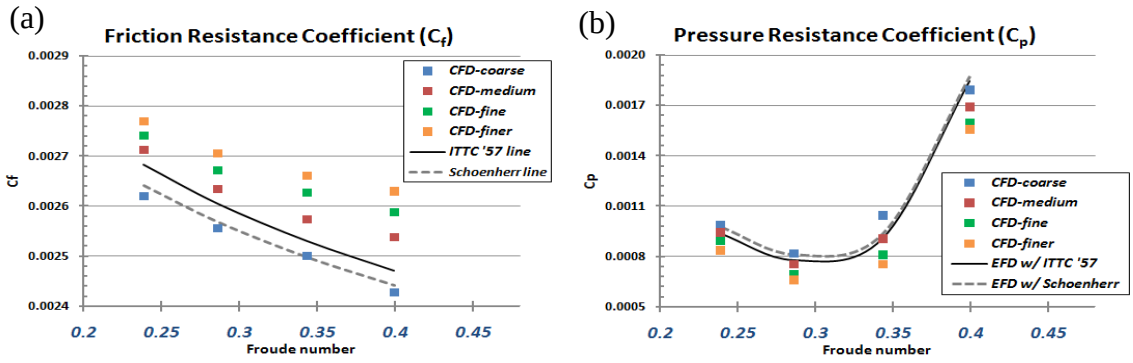


Figure 5-25 Comparison of force coefficients with numerical line over the speed range for barehull design: (a) frictional, (b) pressure resistance coefficient

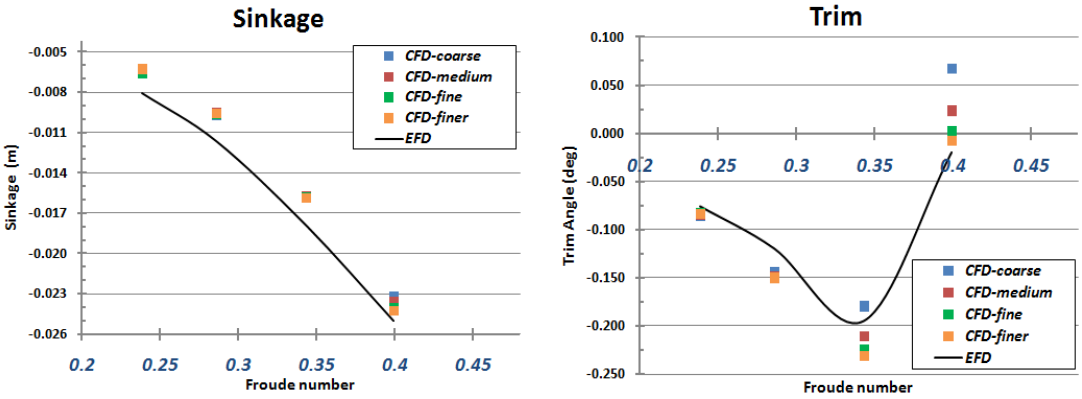


Figure 5-26 Comparison of dynamic motions with EFD over the speed range for barehull design: (Left) sinkage, (Right) trim

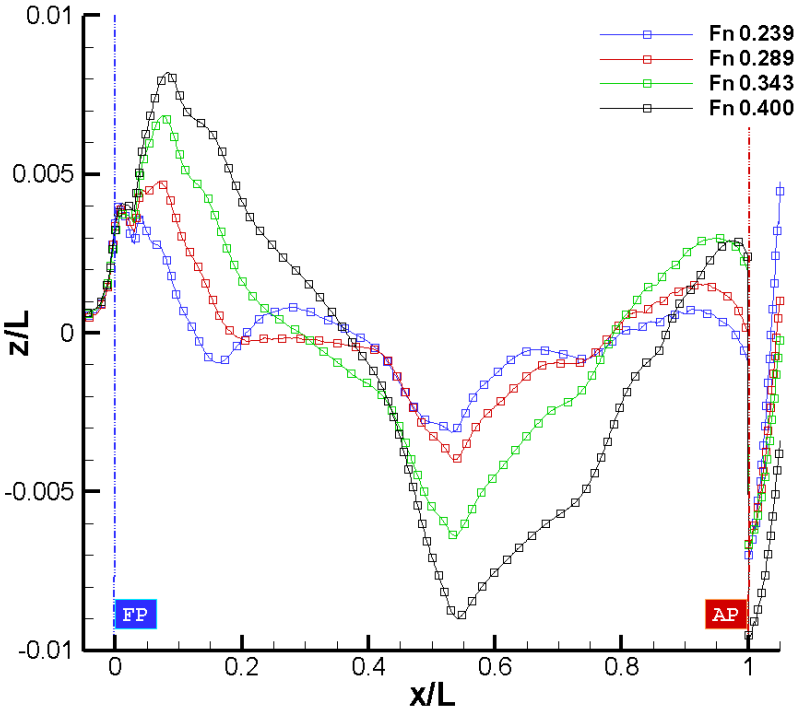


Figure 5-27 Comparison of wave profiles of barehull simulations at four different speeds

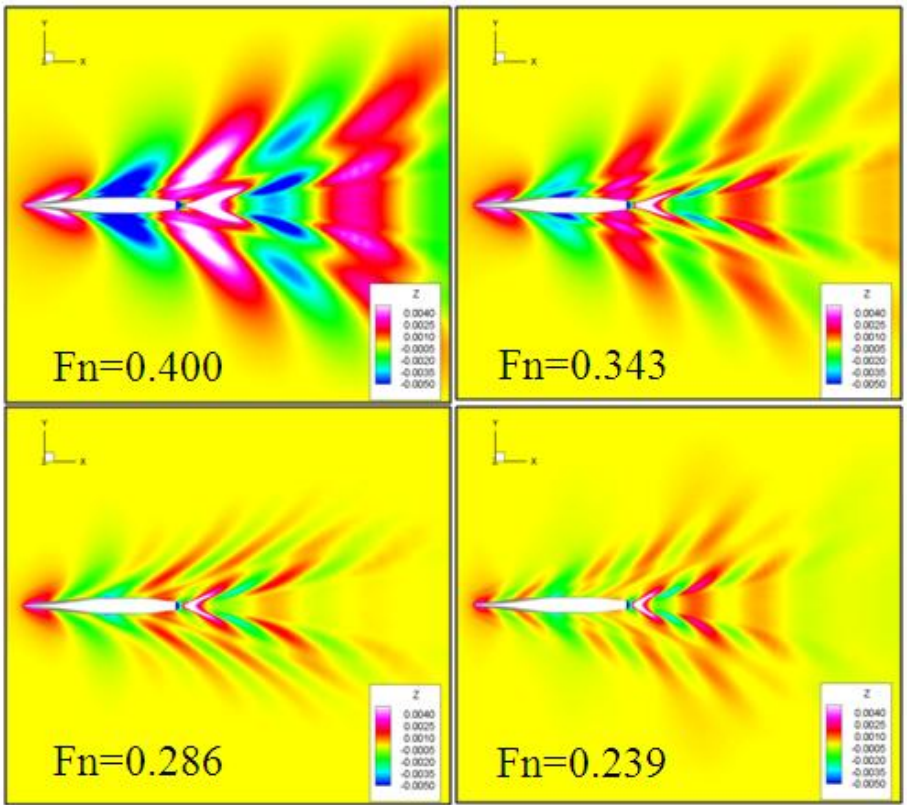


Figure 5-28 Comparison of free surface elevations of barehull simulations at four different speeds

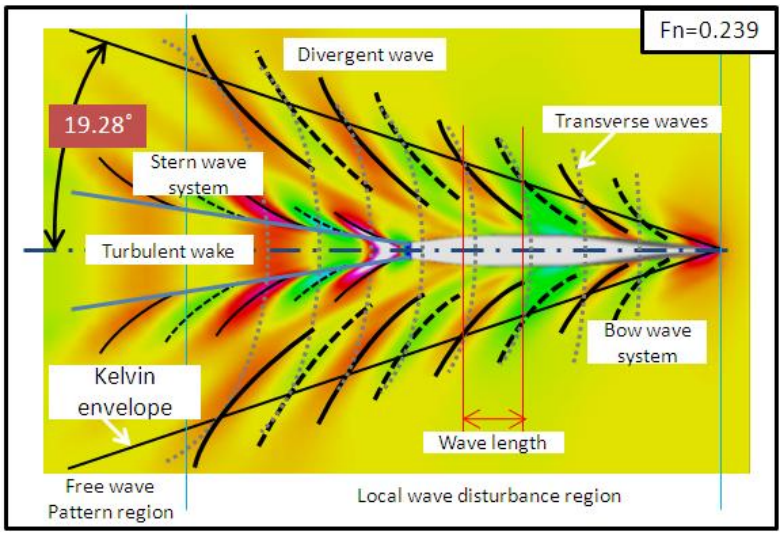


Figure 5-29 Illustration of free surface elevation at Fn=0.239 with detailed wave information

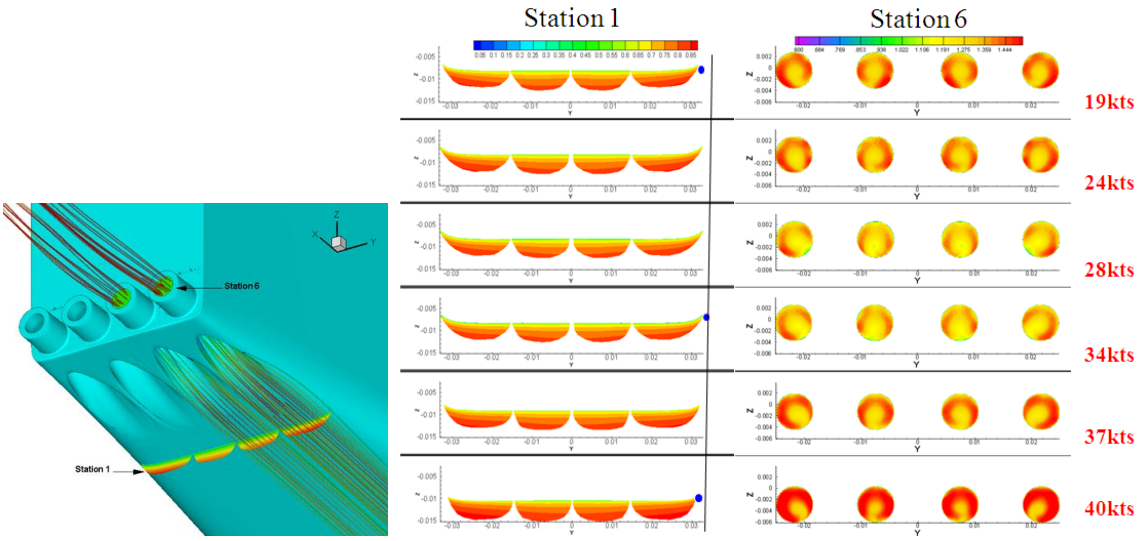


Figure 5-30 CFD control volume: (Left) illustration of inlet streamline tube, (Right) comparison of velocity profiles at St. 1 and 6 at six different speeds

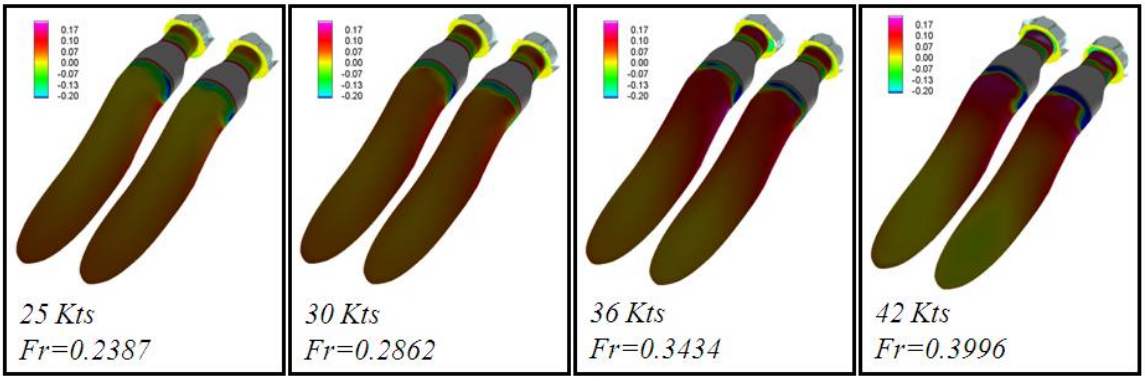


Figure 5-31 Comparison of starboard side waterjet wall pressure contours at four different speeds

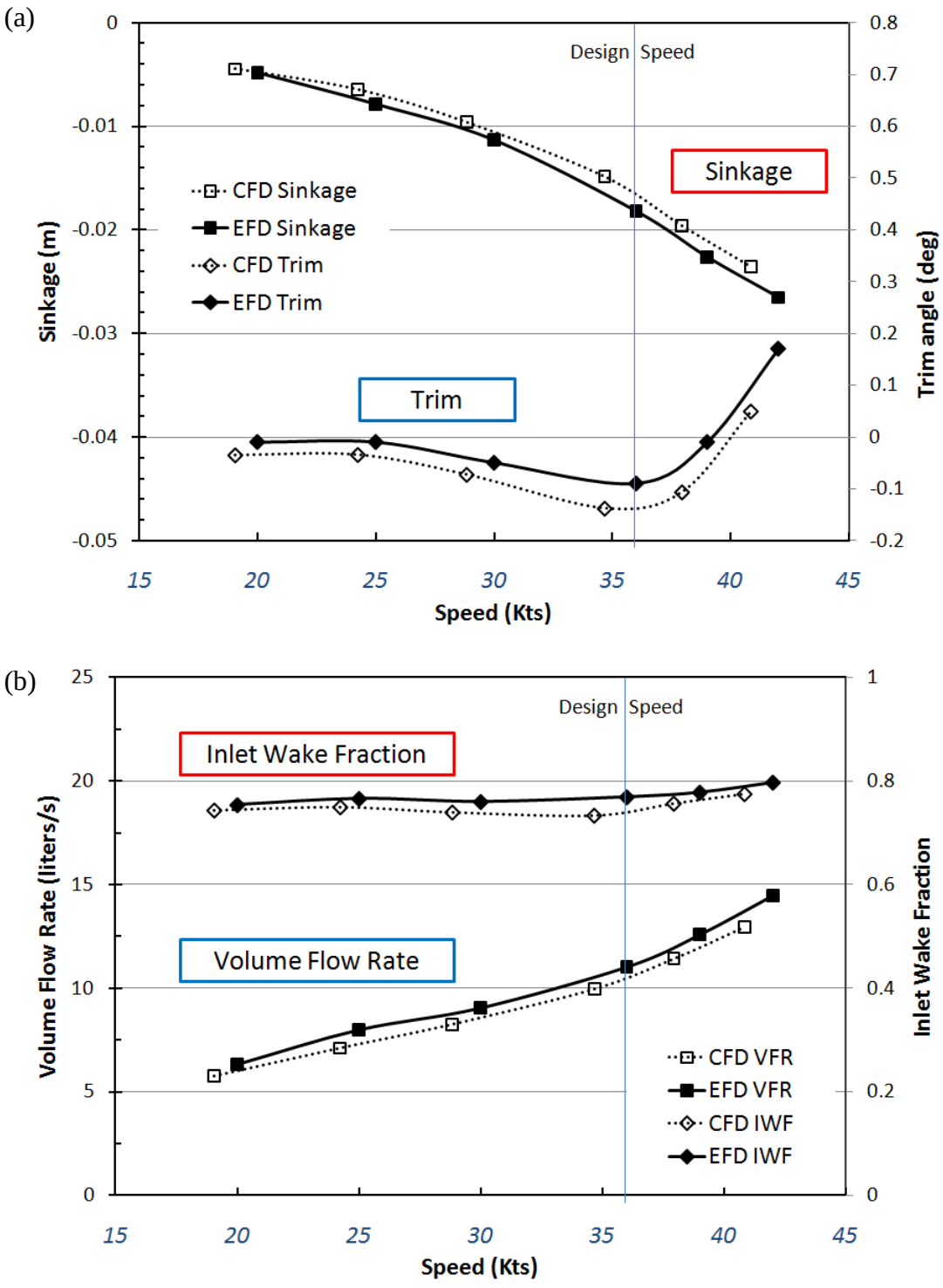


Figure 5-32 Comparison of motions and performance parameters with EFD:
(a) dynamic sinkage and trim for waterjet appended design,
(b) volume flow rate at St.6 and inlet wake fraction at St.1

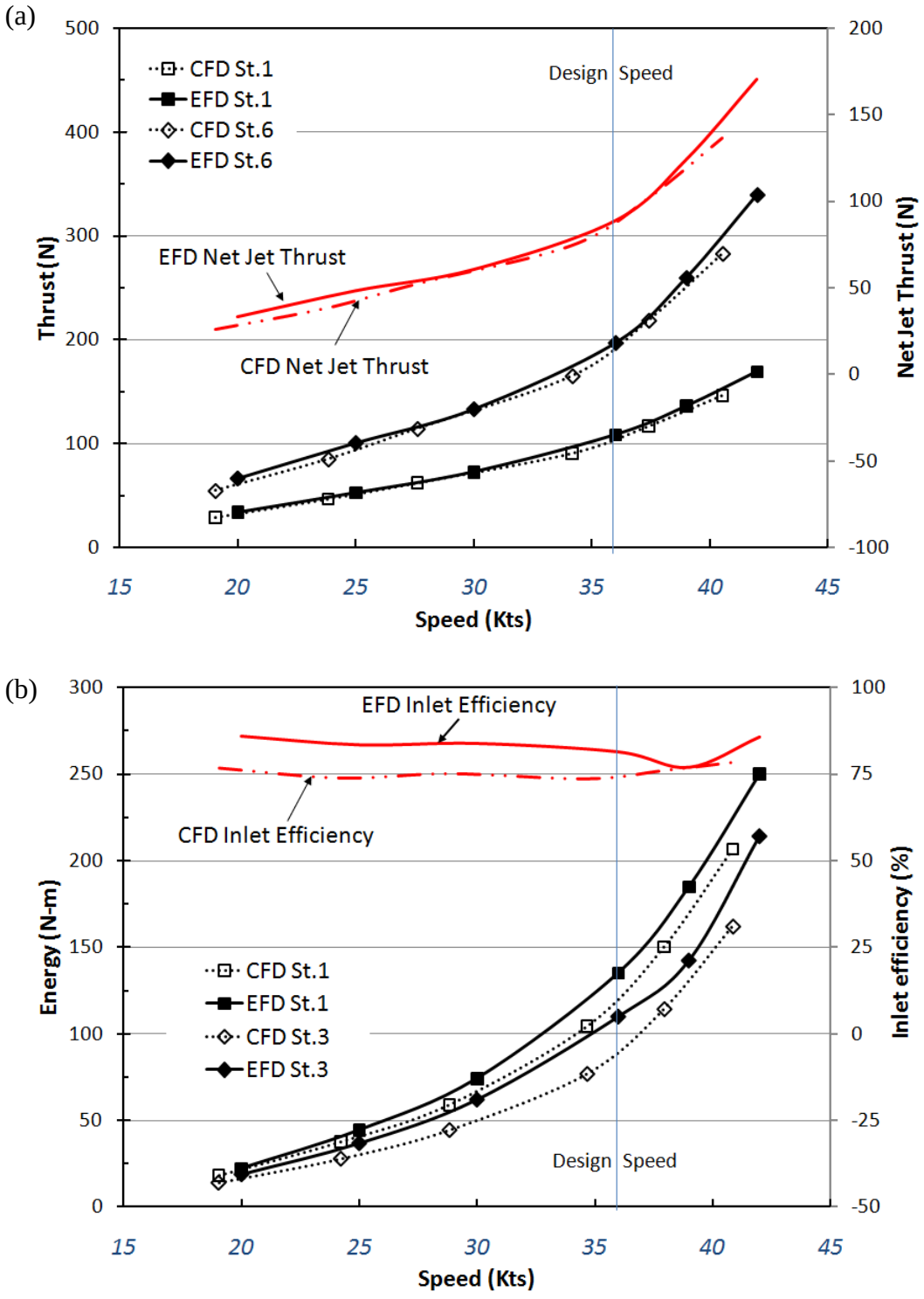


Figure 5-33 Comparison of performance parameters with EFD data:
(a) momentum flux at St.1 and 6 and net jet thrust,
(b) energy at St.1 and 3 and inlet efficiency

# CHAPTER 6
# OPTIMIZATION ALGORITHMS FOR HYDRODYNAMIC DESIGN

## 6.1 Nonlinear optimization problem in hydrodynamic design

A general expression of hydrodynamic design optimization problem with $N$-objective functions is defined as follows;

$$\text{Min:} \quad \begin{cases} \left[F_1\left(\vec{\beta};\ R_n, F_n\right)\right]_{R_n,F_n} \\ \left[F_2\left(\vec{\beta};\ R_n, F_n\right)\right]_{R_n,F_n} \\ \vdots \\ \left[F_N\left(\vec{\beta};\ R_n, F_n\right)\right]_{R_n,F_n} \end{cases} \tag{6.1}$$

$$\text{Subject to:} \quad g_i\left(\vec{\beta}\right) = 0 \quad (i = 1,2,\dots,p) \tag{6.2}$$

$$\text{Subject to:} \quad h_i\left(\vec{\beta}\right) \leq 0 \quad (i = 1,2,\dots,q) \tag{6.3}$$

where $\vec{\beta} = (\beta_1, \beta_2, \dots, \beta_k)$ is the design variables, $F_i$ is the objective functions to be minimized, $R_n$ and $F_n$ are Reynolds number and Froude number respectively, which are beaded on characteristic fluid speed and length of body. Subjected conditions $g_i$ and $h_i$ are equality and inequality constraint functions, respectively. When $N$ is equal to 1, the problem becomes a single-objective problem (SO). In contrast, if any of the constraint and objective functions is nonlinear, the resulting problem becomes a nonlinear multi-objective problem (MO); and for this case, classical method is not generally applicable (shown later). If all constraint and objective functions are linear functions, the problem is called a multi-objective linear program (MOLP) and may have theoretical properties. Unfortunately, most of the practical optimization problems in engineering are nonlinear

and often have multi-objective functions. Hence, appropriate solution scheme must be introduce to solve the problem. In other words, some algorithms cannot search the reasonable solutions.

Generally, “classical optimization methods” has been recognized as two distinct groups: direct methods and gradient-based method. In direct search methods, only the objective function and the constraint values are used to guide the search strategy; whereas gradient-based methods use the first- and/or second-order derivatives of the objective function and/or constraints to guide the search process. These methods were shown capable for many applications especially for problems where objective functions are in relatively simple form. However, there are some common difficulties as follows: (a) The convergence to an optimal solution depends on the chosen initial solution; (b) Most algorithms tend to get trapped to a suboptimal solution (so-called local optimal point); (c) An algorithm efficient in solving one optimization problem may not be efficient in solving a different optimization problem (problem dependent); (d) Algorithms are not efficient in handling problems having a discrete search space (discontinuity problems); and (e) Algorithms cannot be efficiently used on parallel machines. As a result, classical optimization methods have inherent limitation to overcome the issues (a) through (e).

In the present study, main focus is put particularly on the necessity of nonlinear and multi-objective optimization problem. Since optimization problem in industrial applications are mostly governed by nonlinear functions, advancement of optimization methods has been mostly associated with development and application of nonlinear programming (NLP). Besides, the optimizations are usually carried out with not only single objective but also multiple objectives. A common way to solve multi-objective optimization problems using classical optimization method is to follow the preference-based approach where a relative preference vector is used to scalarize multiple objectives. This yields the fact that traditional optimization schemes are able to find only a single optimal solution in a single simulation run. On the other hand, evolutionary algorithms

(EAs), which mimic some natural phenomenon, uses a population of solutions in the each iteration; and the outcome of the scheme is a population of solutions. If the multi-objective problem has a single optimal point, the EA schemes are expected to yield a population of solutions which converges to the single position; on the other hand, if the multi-objective problem has multiple optimal solutions, the EA schemes will be able to reach multiple better points (there is usually no best solution). In the latter case, the solutions from EA schemes give us a lot of choices that the designers can choose depending on own demands. The advantages and recent development of EA methods for the general multi-objective problems are well described in Deb (2001).

In general, major difference between single-objective and multi-objective optimization is that in the latter the objective functions constitute a multi-dimensional space, in addition to the usual design variable space; therefore, the multi-objective optimization is sometimes referred to as vector optimization. In Figure 6-1, the area describes a feasible region where solutions satisfy all constraint conditions. Ship designs often encounter the situation that feasible regions are divided into several sub regions not only for design space ($x_1 - x_2$ space for the case with two design variables) but for objective function space ($F_1 - F_2$ space for the case with two objective functions) due to the complexities in constraints, and feasible regions might have different shapes as shown in the figure. Hence, it is clear that a classical gradient-based optimization scheme, which starts from incorrectly given initial point, will have substantial difficulties to search multiple optimum solutions. Due to fore-mentioned limitation of classical derivative algorithms, non-gradient based probabilistic search algorithms (thus, EAs) have attracted much attention. Although most general-purpose optimization software used in industrial applications still make use of gradient-based algorithms mainly due to their computational efficiency, EAs are getting to be replaced as practical optimization schemes because of their capabilities to search global optimal point and to be applied for multi-objective non-linear optimization problems.

It is widely known that there are two popular developed EA approaches; namely, Genetic Algorithms (GA) and Particle Swarm Optimization (PSO), both of which are used in single- and multi- objective optimization applications. GA algorithm models the evolutions of a species based on Darwin's principle of survival of the fitness; whereas, PSO algorithm is based on the idea of collaborative behavior and swarming in biological populations. PSO is a relatively recent heuristic search method and has similar characteristics to the GA in the sense that they are both population based search approaches. Additionally, they both depend on information sharing among their population members to enhance their search processes using a combination of deterministic and probabilistic rules. Since the two approaches are supposed to find a solution to a given objective function but employ different strategies and computational effort, it is appropriate to compare their implementation. Furthermore, it would be preferable if the quantitative metrics are estimated (details can be found in next chapter).

Now, let us consider the particular optimization cases, namely hydrodynamic vehicle shape optimization problems. For that particular aim, the objectives are often set to the powering performance which requires the solution of nonlinear partial differential equations (PDE), namely the Navier-Stokes equations. Hence, the most of the case of design optimization problem fall into the nonlinear optimization problems. Therefore, it is necessary for the SBD system to have the proper nonlinear optimization algorithm to obtain promising results. In addition, for a given set of ship design and operational criteria, there usually exists a trade-off between parameters. For the typical case of ship shape design, powering performance and its seakeeping performance usually have a trade-off relationship. Hence, the improvement of a specific aspect of the global design usually causes worsening of some others. It is usually not possible to achieve the global optimization for both of such kinds of a pair of objectives at the same time because of the competition between these parameters and also the design constraints. As a result, the best approach is not to combine all the objectives into a single one but to keep the multi-

criteria nature of the problem and to rely on the Pareto optimality concept (Pareto, 1906). Pareto optimal front, which is shown in Figure 6-2, is a diverse set of solutions yield a good set of trade-off solutions among the objectives. Thus, important aims of multi-objective optimization scheme are following; (1) to find a set of solutions as close as possible to the Pareto-optimal front; (2) to find as many choices which are on the Pareto front as possible; (3) to find a set of solutions as diverse as possible. Therefore, the evaluation of the algorithms for multi-objective problems can be summarized to analyze (1) size of dominated space, (2) number of particles reach to Pareto, and (3) non-uniformity (diversity) of Pareto front. The comparison study of optimization algorithms including both gradient and non-gradient based approaches are performed and described in the next chapter. In the following sections, more details of both the local and global optimization algorithms are given.

## 6.2 Gradient-based, local optimization method

The interest in gradient-based, local optimization methods, for which rigorous convergence proofs exist (under some assumptions regarding the objective function), is due to fast convergence offered by first- and second-order methods, based on the knowledge of the gradient and/or Hessian (or approximate Hessian) of the objective function. Using local information about the objective function, gradient-based method is able to search a local minimum efficiently; hence, the closest minimum with respect to the given starting point.

### 6.2.1 Sequential Quadratic Programming (SQP)

Sequential Quadratic Programming (SQP) is one of the most popular methods for numerical solution for NLP. The method is based on solving a series of sub-problems

designed to minimize a quadratic model of the objective subject to a linearization of the constraints. Let us consider that a general expression of the single-objective optimization problem is defined as follows;

$$Min \quad F(\boldsymbol{\beta}) \tag{6.4}$$

$$subject\ to \quad H_i(\boldsymbol{\beta}) \leq 0 \quad (i = 1,2, \dots, q)$$

where $\boldsymbol{\beta} = (\beta_1, \beta_2, \dots, \beta_k)$ are design variables, $F$ is the objective function to be minimized, and $H_i$ are inequality constraint functions. In SQP scheme, the objective and constraint functions are approximated in quadratic form such that;

$$Min \quad \left[\nabla F(\boldsymbol{\beta})^T \boldsymbol{d} + \frac{1}{2}\boldsymbol{d}^T B \boldsymbol{d}\right] \tag{6.5}$$

$$subject\ to \quad H_i(\boldsymbol{\beta}) + \nabla H_i(\boldsymbol{\beta})^T \boldsymbol{d} = 0 \quad (i = 1,2, \dots, q)$$

where $\boldsymbol{d} = (d_1, d_2, \dots, d_k)$ is the direction vector, and $B$ is the approximate Hessian matrix of the Lagrangian. In each optimization iteration $(n)$, optimum $\boldsymbol{d}$ is obtained so as to minimize $F$, and $\boldsymbol{\beta}$ is updated by $\boldsymbol{\beta}^{n+1} = \boldsymbol{\beta}^n + \boldsymbol{d}$.

In other words, the basic idea of SQP is to model NLP at a given approximate solution, say $\boldsymbol{\beta}^n$, by a quadratic programming sub-problem, and then to use the solution to this sub-problem to construct a better approximation $\boldsymbol{\beta}^{n+1}$. This process is iterated to create a sequence of approximations that will converge to a solution $\boldsymbol{\beta}^*$. The key to understand the performance and theory of SQP is that the method can be viewed as the natural extension of Newton and quasi-Newton methods to the constrained optimization setting. Thus, SQP shares the characteristics of Newton-like methods, namely, rapid

convergence when the iterations are close to the solution but possible erratic behavior that needs to be carefully controlled when the iterations are far from a solution.

In the present study, the derivative terms in the above equations are evaluated by a second-order central difference scheme. There are some literatures which performed hull form optimization with SQP algorithm, for instance Tahara *et al*., (2004) and (2006a). Tahara *et al.*, (2004) also shows advantage of SQP over SLP (successive linear programming) for hydrodynamic design optimization.

### 6.3 Derivative-free, global optimization method

The ship design is often a nonlinear multi-objective optimization problem as in the majority of engineering problems. For example, the goals of the design process include resistance reduction, lower hydrodynamic noise, minimal bow wave height, and the reduced amplitude and acceleration of particular motions. In addition, ship designers may also be interested in enhancing certain quantities related to the maintenance costs. Indeed, the enforcement of nonlinear constraints generally leads to a non-convex optimization problem, i.e., the feasible solution set might be a non-convex set, often composed of the sum of disconnected non-convex subsets (see Figure 6-1). Therefore, the possibility of using local optimization algorithms is excluded for this type of problems. Instead, a correct solution approach must adopt a global optimization scheme (e.g., EAs) since a local optimization algorithm cannot jump across the gaps created by the nonlinear constraints to reach more promising feasible regions of the design space. On the other hand, EAs also have disadvantage; namely, its relatively slow speed for simple optimization problems and much expensive computationally. However, these issues are getting gradually less important with the rapidly increasing speed of computers and introduction of parallel computing technique. Moreover, its global searching capability that leads to robust results is sometimes considered more important in complicated

application problem. For these reasons, the main focus in the present study is put on the development of global multi-objective optimization procedures for ship design. Two popular evolutional algorithms (EAs), namely PSO and GA, are considered in the present study. Mathematical description is presented as follows.

### 6.3.1 Particle Swarm Optimization (PSO)

The Particle Swarm Optimization (PSO) algorithm is a global optimization technique introduced by Kennedy and Eberhart, (1995). Since it was originally proposed, the PSO algorithm has been studied by many researchers, and successfully applied to solve several engineering problem including ship design problems; for instance, for instance, Eberhart and Shi, (2001), Venter and Sobieszczanski-Sobieski, (2004), Pinto *et al.*, (2007) and Campana *et al.*, (2009a).

***Original PSO algorithm***

The implicit rules followed by the members of fish schools and bird flocks, that allow them to undertake synchronized movement, without colliding, has been studied. There is a general belief that social sharing of information among individuals of a population, may provide an evolutionary advantage, and there are numerous examples coming from nature to support this idea. This was the core idea behind the development of PSO. The swarm strategy simulates the social behavior of a set of individuals (particles) which share information among them while exploring the design variables space. In PSO method, each particle has its own memory to remember the best places that it has visited, whereas the swarm has a global memory to remember the best place ever visited. Furthermore, each particle has an adaptable velocity to move itself in the design space. According to these principles, each particle investigates the search space analyzing its own flying experience and that of the other members of the swarm. The basic PSO

algorithm was defined for unconstrained optimization problems. Its fundamental steps are flowing five:

Step 0 (Initialization) Distribute a set of particles inside the design space with random distribution and random initial velocities. These particles will constitute the swarm. Set $n = 0$.

Step1 (Analysis) Set $n = n + 1$. For each particle of the swarm, evaluate the objective function. Identify (1) the minimum value in the swarm (and record its location as $p_b^n$) and (2) the minimum value encountered by the single particle in its own history by comparing the current value with all the previous ones (and record its location as $p_i^n$).

Step2 (Compute velocity) Calculate a velocity vector $v_i$ for each particle, using the particle's memory and the knowledge gained by the swarm according to

$$v_i^{n+1} = \chi \left[\omega^n \, v_i^n + c_1 r_1^n \frac{(p_i^n - x_i^n)}{\Delta t} + c_2 r_2^n \frac{(p_b^n - x_i^n)}{\Delta t}\right] \tag{6.6}$$

where $\chi$ is a constriction factor, $\omega$ is called inertia weight, $c_1$ and $c_2$ are positive constants, $r_1$ and $r_2$ are random numbers, $p_i^n$ is the best position found by the particle $i$, $p_b^n$ is the best position found by the swarm up to iteration $n$, and $x_i^n$ is the position of the $i$th particle at the step $n$. We can easily recognize three contributions: the first term is the inertia of the moving particles; the second term is linked to the individual memory; whereas the last term is related to the collective memory. Generally, time step $\Delta t$ is set to 1.

Step3 (Update position) Update the position of each particle, $x_i$, using the velocity vector and previous position.

$$x_i^{n+1} = x_i^n + v_i^{n+1} \Delta t \tag{6.7}$$

Step4 (Check convergence) Go to Step.1 and repeat until convergence criteria are satisfied.

Literature reports that fine tuning of the parameters in Equation (6.6) is crucial for the optimization process, and that the final solution and the calculation time are strictly linked to the parameters setting. The inertia weight $\omega$ regulates the trade-off between the global (wide-ranging) and local (nearby) exploration abilities of the swarm. A large inertia weight facilitates global exploration (searching new areas) while a small one facilitates local exploration. A suitable value for $\omega$ usually provides balance between global and local exploration abilities and consequently results in a reduction of the number of iterations required to locate the optimal solutions. Experimental results indicate that it is better to initially set the inertia to a large value, in order to promote global exploration of the design variables space and gradually decrease it to get a more refined solution (Venter and Sobieszczanski-Sobieski, 2003). For these reasons, an initial value for $\omega$ is set and the decrease rate is calculated by;

$$\omega_k = \omega_{k-1} \cdot g_w \tag{6.8}$$

where $\omega_k$ is the new value for the inertia weight, $\omega_{k-1}$ is the previous one and $g_w$ is a constant chose between 0 and 1. In Venter and Sobieszczanski-Sobieski, (2003), it is suggested to use $0.35 < \omega < 1.4$, and $g_w = 0.975$.

The constriction factor $\chi$ is used alternatively of $\omega$ to limit the maximum velocity. The major difference between the two is that while the inertia $\omega$ is employed to control the impact of the previous history of velocities on the current one, $\chi$ offers to the user the chance to select the search resolution. Quantitatively, if box constraints are given, $\chi$ takes a value equal to a fraction of the characteristic dimension of the box.

The constant $c_1$ and $c_2$ are called cognitive and social parameter, respectively. The cognitive parameter indicates how much confidence the particle has in itself, while

the social parameter indicates how much confidence it has in the swarm. Proper fine-tuning of these coefficients may result in faster convergence and alleviation of local minima. In basic PSO algorithm (Kennedy and Eberhart, 1995), the authors proposed $c_1 = c_2 = 2$, so that the mean of stochastic multipliers of Equation (6.6) becomes 1. In Venter and Sobieszczanski-Sobieski, (2003), different values for two coefficients are used. In particular, $c_1 = 1.5$ and $c_2 = 2.5$ work well in their examples. In Campana *et al.*, (2006c), a more rigorous analysis is carried out. In the paper, a generalized PSO iteration is described by means of a dynamic linear system, whose properties are analyzed. The influence of the particles' starting points and the use of deterministic or stochastic parameters are investigated and some partial convergence results are given. In particular, the PSO parameters are selected by imposing that the particles trajectories are confined in a suitable compact set. The velocity and position updates in PSO algorithm is illustrated in Figure 6-3.

***Enhancements to basic algorithm: DPSO***

The original formulation of the PSO algorithm shown above is defined only for single-objective unconstrained optimization problems. The basic method has been extended by Venter and Sobieszczanski-Sobieski, (2003) to deal with constrained problems. In order to improve the effectiveness and the efficiency of PSO, some further modifications to the basic approach is introduced briefly here, more details are found in Pinto *et al.*, (2007). The basic idea is eliminating all the random coefficients and transforming the method into a deterministic particle swarm optimization (DPSO). There are four modifications as follows.

1) Suppression of random coefficients

In the modified version of the algorithm, the particles perform a deterministic search in the N-dimensional design space. As a consequence, the two random parameters in Equation (6.6) are set to a fixed value $(r_1 = r_2 = 1)$, hence eliminating the randomness.

2) Initialization procedure

Two approaches to initialize the swarm are introduced instead of random initialization. If the problem has a small scale or the feasible space is non-convex, LP$\tau$-net distribution is adopted. On the other hand, if the problem considered is a large-scale unconstrained, a hyper-cube distribution is used.

3) Particles with violated constraints

When a constraint is violated, the inertia $\omega$ of these particles is set equal to zero, and the objective function is set to an arbitrarily large positive value until the particle returns back to a feasible region. Therefore, Step 2 is modified as follows;

Step 2' (Compute velocity) Calculate a velocity vector $v_i$ for violated particles,

$$v_i^{n+1} = \chi \left[ c_1 \frac{(p_i^n - x_i^n)}{\Delta t} + c_2 \frac{(p_b^n - x_i^n)}{\Delta t} \right] \tag{6.9}$$

4) Convergence criterion

In their original PSO formulation, Kennedy and Eberhart, (1995) did not include a convergence criterion. Here, a convergence criterion based on the idea of basin of attraction for the single-objective problem is introduced (Campana *et al.*, 2006c).

$$\begin{cases} [F(x_i^n) - F(x_i^{n-1})] \cdot [F(x_i^{n-1}) - F(x_i^{n-2})] \geq 0 \\ F(x_i^n) - F(x_i^{n-1}) < 0 \end{cases} \tag{6.10}$$

By eliminating the randomness, the algorithm is transformed into a deterministic one, allowing a more strict control on the process and avoiding the necessity of performing many repeated runs and statistical analysis to compare different solutions. The purpose of the modification here is to perform a deterministic swarm initialization using a uniform distribution and a small size swarm, with the aim of limiting as much as possible the number of objective function evaluations. Unfortunately, it is not possible to use small and uniform distribution in all the cases, e.g., in large-scale problems. In

general, it is necessary to find a good trade-off between these issues. In the code used in the present study, LP$\tau$-net (Stantnikov & Matusov, 1995) is used for small scale problem. LP$\tau$-net is known for its good sampling characteristics of a given space. It represents an approximate solution of the so-called uniform covering problem and avoids some limitations of the typical regular grid sampling. On the other hand, if we are dealing a large-scale unconstrained problem, a hyper-cube distribution is preferable (Pinto *et al.*, 2004), setting one particle at the center of each hyper-face of the design variable space.

When we are solving an optimization problem with a nonconvex feasible design space, the particles could also explore regions of the design space where the constraints are not satisfied. Particles in infeasible regions need to be attracted toward the feasible spaces. When a constraint is violated, the step 2 is modified. The velocity of the $i$th particle at the iteration $n + 1$ is modified in Equation (6.9). It is thus influenced only by the best point found so far for the $i$th particle, and the best point in the swarm. In most cases, this new velocity vector will point back to a feasible region.

For the convergence criterion, the idea of basin of attraction for the single objective problem is used. When several particles are attracted by the same basin, the average distance among them is computed, and the center of the basin is estimated. The average distance is then used to check the remaining particles. If their velocity is too slow and their position is too far from the center of the basin, they are abandoned. Convergence is assumed if the average distance among all the particles lying in the same basin of attraction is less than a predefined value.

***Extension to multi-objective optimization problems***

In multi-objective (MO) problems, more than one objective function has to be optimized at the same time. With this purpose, let us consider a system the behavior of which may be described by a set of equations (differential, algebraic, etc.) each one denoting a different and relevant performance aspect of the system under investigation. Assume that the status of the system depends on an $N$-dimensional design variable

vector $\boldsymbol{X} = (x_1, x_2, \dots, x_N)^T$. The objective functions vector $\boldsymbol{F}(\boldsymbol{X}) = [F_1(\boldsymbol{X}), F_2(\boldsymbol{X}), \dots, F_M(\boldsymbol{X})]^T$ defines the main characteristics of the system, which the designer would like to control and hopefully optimize. The optimization problem may be finally formulated as follows;

$$minimize \quad \{F_1(\boldsymbol{X}), F_2(\boldsymbol{X}), \dots, F_M(\boldsymbol{X})\} \tag{6.11}$$

$$subject\ to \quad \boldsymbol{X} \in S$$

where $\boldsymbol{F}: \Re^N \rightarrow \Re^M$.

Consider now the abovementioned MO problem with $M$ objective functions, $\boldsymbol{F}$, and $N$ design variables, $\boldsymbol{X}$. The solution of the MO problem is given by the design variable vector $\boldsymbol{X}^* = (x_1^*, x_2^*, \dots, x_N^*)^T$, which satisfies the constrain conditions; and yields the optimal values of all the objective functions. Unfortunately, this result cannot be obtained in each kind of optimization problem. In fact, the objective functions may be easily in conflict with each other. For this reason, it could be impossible to find a point satisfying the global minima of all the $\boldsymbol{M}$ objective functions for the same design variable vector $\boldsymbol{X}^*$ (Miettinen, 1999).

As a consequence, there is no unique solution that improves the original state of the system, but a set of solutions is available that satisfies the constraints. According to this, the problem boils down to finding the Pareto optimal front. In order to define the Pareto optimal set, it is necessary to introduce the concept of Pareto dominance. Therefore, let $\boldsymbol{u} = (u_1, u_2, \dots, u_k)^T$ and $\boldsymbol{v} = (v_1, v_2, \dots, v_k)^T$ be two vectors; assume that $\boldsymbol{u}$ dominates $\boldsymbol{v}$ if and only if $u_i \leq v_i, i = 1,2, \dots, k$ and there exists at least one index with $u_i^- < v_i^-$. Thus, a solution $\boldsymbol{X}^*$ of the MO problem is said to be Pareto optimal if and only if there does not exist another solution $\widetilde{\boldsymbol{X}}^*$ so that $\boldsymbol{F}(\boldsymbol{X}^*)$ is dominated by $\boldsymbol{F}(\widetilde{\boldsymbol{X}}^*)$. The

vector $\boldsymbol{X}^*$ corresponding to the solutions included in the Pareto optimal set are called non-dominated.

$$\mathcal{PF}^* = \{(F_1, F_2, \dots, F_M) | \boldsymbol{X} \in \mathcal{P}^*\} \tag{6.12}$$

The set $\mathcal{PF}^*$ is called the Pareto front, and it can be convex, concave, or partially convex and/or concave and/or discontinuous.

### 6.3.2 Genetic Algorithm (GA)

The genetic algorithm (GA) is a search heuristic that inspired by Darwin's theory about evolution. Algorithm is started with a set of solutions, which is represented by chromosomes, called population. Solutions from one population are taken and used to form a new population. This is motivated by a hope, that the new population will be better than the old one. Solutions which are selected to form new solutions are selected according to their fitness; the more suitable they are the more chances they have to reproduce. This treatment is repeated until some condition is satisfied. In GA, a population of strings (also called chromosomes), which encode candidate solutions to an optimization problem, evolves toward better individuals. Solutions are represented in binary as strings of 0s and 1s, traditionally. This is the reason why the original GA approach is called Binary-Coded GA (BCGA).

***Original strategy (Binary-Coded Genetic Algorithm: BCGA)***

Figure 6-4 shows the basic flowchart of original GA approach. In a form of mathematical model of GA, the genotype is represented as frequency. For instance, the frequency of genotype $B_i$ at generation $t + 1$, i.e, $x_i(t + 1)$ is given terms of frequency at generation $t$ as follows;

Selection: $x_i(t+1) = \frac{f_i}{\bar{f}(t)}\, x_i(t), \quad (i = 1,2,\dots,n)$ (6.13)

where $n$ is population size, $f_i$ is a fitness of $B_i$, and $\bar{f}(t)$ is the average fitness of a population. In similar manner, change in the frequency through crossover and mutation are given by;

Crossover: $x_k(t+1) = \sum_{i=1}^{n} \sum_{j=1}^{n} C(k\,|i,j)\, x_i(t)\, x_j(t)$ (6.14)

Mutation: $x_i(t+1) = \sum_{j=1}^{n} M_{ij}\ \ x_j(t)$ (6.15)

where $C$ is a crossover tensor, and $M_{ij}$ is a mutation matrix which stands for the probability of mutation from $B_j$ to $B_i$ over one generation. $C$ and $M_{ij}$ include crossover and mutation ratios, both of which are called system parameters. Evaluation of effectiveness of GA is often discussed in conjunction with schema theory; however, that will not be main objective of the present study. It is known that simulated annealing, a related probabilistic optimization technique, can also be used within a standard GA algorithm, simply by starting with a relatively high rate of mutation, which decreases over time along a given schedule. Figure 6-5 shows the illustration of crossover and mutation operations. Note that the judgment is decided by the convergence criterion and/or generally it is set to maximum number of generations.

***Extension to multi-objective optimization problems (MOGA)***

The extension of GA to multi-objective version (MOGA) is straightforward. Main goal is to detect uniformly distributed globally Pareto optimal front in solving multi objective problem. Definition of globally Pareto-optimal set is "the non-dominated set of the entire feasible search space is globally Pareto-optimal set (Deb, 2001)". In order to make the conditions of Pareto optimality mathematically rigorous, we state that a vector $\boldsymbol{x}$ is particularly less than $\boldsymbol{y}$, symbolically $\boldsymbol{x} < P\boldsymbol{y}$ when the following condition holds;

$$(\boldsymbol{x} < P\boldsymbol{y}) \Leftrightarrow (\forall i)(x_i \leq y_i) \ \wedge \ (\exists i)(x_i < y_i) \tag{6.16}$$

Under this circumstance, we say that point $\boldsymbol{x}$ dominates point $\boldsymbol{y}$. If a point is not dominated by any other, we say that it is nondominated or noninferior. The basic definition is used to find noninferior points in MOGA in association with Pareto-ranking technique and sharing method in the present study. At each generation, higher fitness $f_0$ is given to individuals of higher Pareto ranking $R_P$, and at the same time, additive fitness $f_s$ is given to individual with the best quality in one of objective functions (see Figure 6-6 for example of two-objective function case), i.e., $f_0 = 1/R_P + f_s$. The functional constraints are accounted for by using a penalty function approach, which artificially lowers the fitness if the constraints are violated and is expressed as;

$$f = f_0 - r\left[\sum_{j=1}^{M}\left|h_j(x)\right| + \sum_{j=1}^{N}\left|min\{0, g_j(x)\}\right|\right] \tag{6.17}$$

***Real-Coded Genetic Algorithm (RCGA)***

GA was originally developed with binary coding to represent chromosomes. In applications to optimization problems that have a continuous search space, some difficulties will appear (Deb, 2001), e.g., Hamming cliffs associated with certain strings, and string length and precision issues. In this aspect, Real-coded (or Real parameter) GA implementation is more suitable, since the real parameters are used without any string coding and the problems defined in real parameters are directly solved as shown in Figure 6-7. By using the real parameters to express each chromosome, phase structure of state space and gene space is matched. A concern in RCGA is implementation of crossover and mutation operations, mainly because the string length is no longer finite. A scheme named unimodel normal distribution crossover (UNDX), proposed by Ono *et al.*, (1997), is a method to perform crossover operation in RCGA (Figure 6-7(b)). The scheme was shown very promising through their test cases and those performed by others (for

instance, Tahara *et al*, 2007). The UNDX has designed to preserve the characteristic of individuals while the crossover. When optimizing function has epitasis among parameters, the UNDX generates children near the line segment connecting two parents so that the children lie on the valley where the parents locate. For the present RCGA, the mutation operation is simulated by using the "gene pool" approach. That is, a gene pool whose size is larger than $n$ is initially generated by a random manner, and genes in the pool are replaced those for the individuals with high fitness. Through this approach, new genetic information is always involved into creating new generation, which is similar manner to the mutation operation defined in BCGA. Hence, the mathematical formulation of the present RCGA is similar to that for BCGA, i.e.;

$$\text{Selection:} \qquad x_i(t+1) = \frac{f_i}{\bar{f}(t)}\, x_i(t), \quad (i = 1,2,\dots,n) \tag{6.18}$$

$$\text{Crossover:} \qquad x_l(t+1) = \sum_{i=1}^{n_0} \sum_{j=1}^{n_0} \sum_{k=1}^{n_0} C(k\,|i,j,k)\, x_i(t)\, x_j(t) x_k(t) \tag{6.19}$$

where, $n < n_0$ and $n_0$ is size of gene pool. In the present study, $n_0$ is three times larger than $n$. The present RCGA approach proceeds as following steps; (i) Generation of an initial population of individuals at random manner, (ii) Evaluation of some predefined quality criterion, referred to as the fitness, (iii) Selection of individuals based on a probability proportional to their relative fitness, (iv)Crossover operation. The steps (ii) through (iv) are repeated until the generation achieves designated number.

In the present study, the RCGA is used in forms of multi-objective optimization solver. As discussed earlier, an important feature of these global optimization schemes (including PSO) is adoptability to parallel computing in nature, which is also of great importance in implementation into high-performance optimization framework in association with expensive CFD solvers.

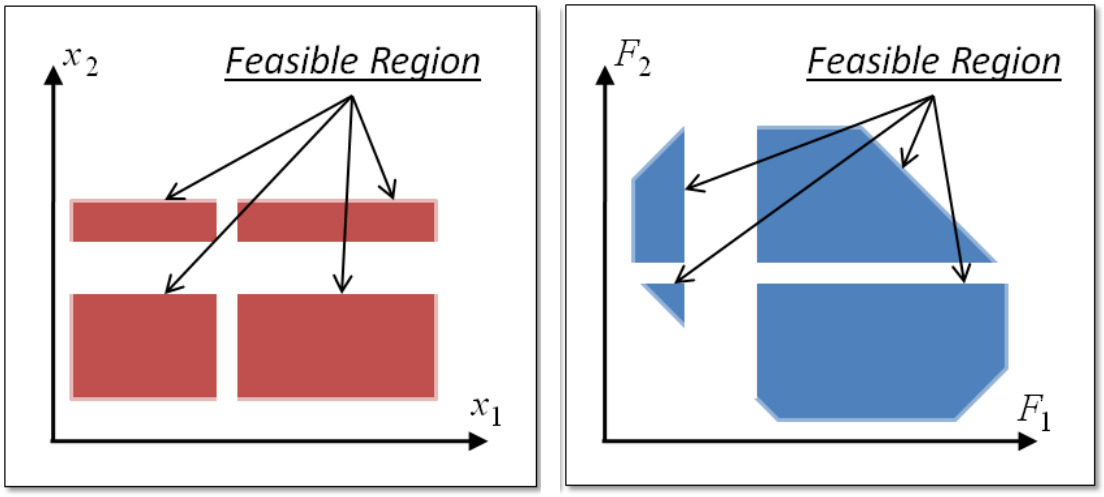


Figure 6-1 Illustration of feasible region on (Left) design space and (Right) objective space, where both $F_1$ and $F_2$ are functions of $x_1$and $x_2$

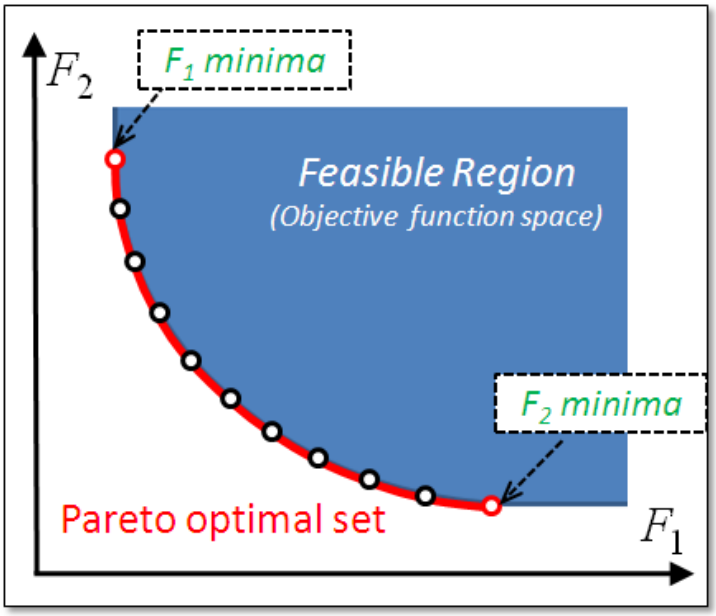


Figure 6-2 Illustration of feasible region and definition of Pareto optimal set for two-objective problem case

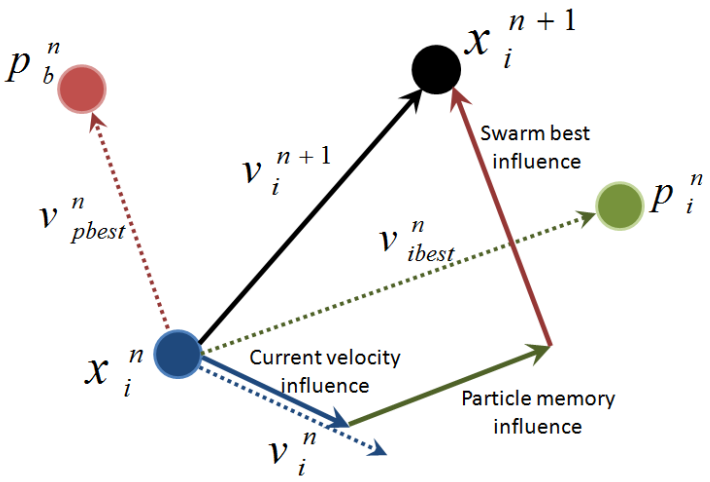


Figure 6-3 Illustration of velocity and position updates in PSO algorithm

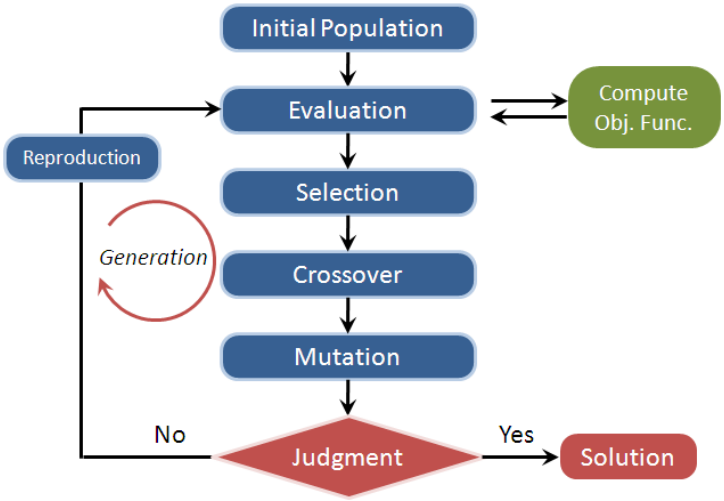


Figure 6-4 Basic flowchart of Genetic Algorithm

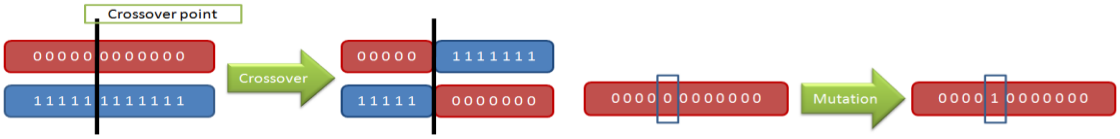


Figure 6-5 Illustration of (Left) crossover and (Right) mutation operation in BCGA

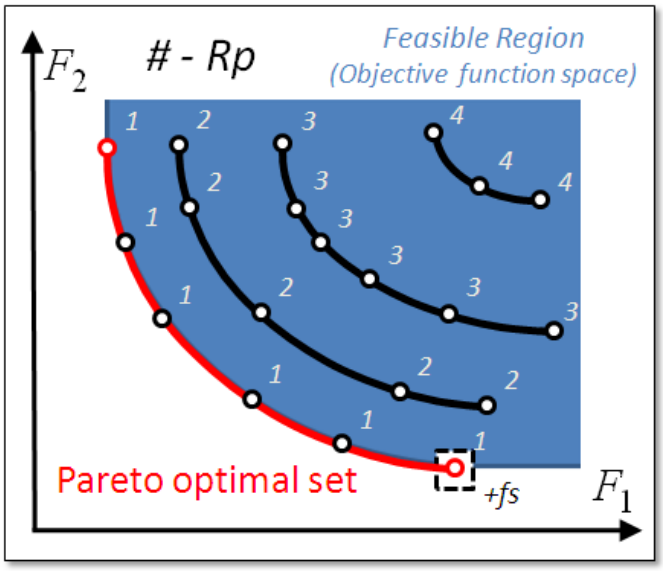


Figure 6-6 Concept of Pareto ranking (*Rp*) and sharing operation

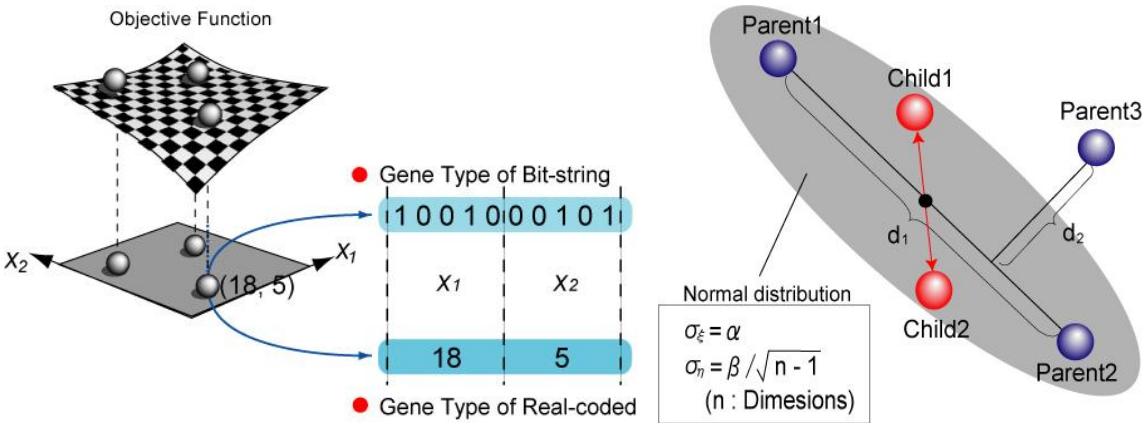


Figure 6-7 Operation in RCGA: (Left) illustration of real parameter coding, (Right) unimodel normal distribution crossover (UNDX) for 2-dimension case

# CHAPTER 7
# COMPARISON OF OPTIMIZATION ALGORITHMS

## 7.1 Introduction

This chapter deals with the comparison study of optimization algorithms. The objective of this particular study is to perform the comparison analysis among four different optimization algorithms, i.e., Particle Swarm Optimization (PSO), Binary-Coded Genetic Algorithm (BCGA), Real-Coded Genetic Algorithm (RCGA), and Sequential Quadratic Programming (SQP) in order to investigate their performance characteristics toward analytical optimization problems as a prerequisite to the hydrodynamic design optimization studies. Both single- and multi- objective problems are considered and results are discussed. Note that the population size=*n* means that *n* particles/individuals in single generation.

In order to achieve the above objective, three approaches are taken into account:

***i. Verification of PSO capability for solving simple optimization problems***

At first, the verification study is performed by PSO method for simple analytical functions. Investigated functions have only one peak on the feasible design space. For each test function, two design variables and two swarm particles are used with constant coefficient (see Table 7-1). There are six test functions are prepared as presented in Table 7-3. This task is carried out to evaluate the PSO performance with little population size toward the simple single-objective problems.

***ii. Single-objective optimization problems***

For single objective problems, eleven analytical functions are evaluated using three optimization algorithms; i.e., PSO, RCGA, and SQP. Functions have more than one peak in their design spaces. The effect of population is also studied; hence, population size is set to 2 and 8. The maximum iteration (generation) is set to 100 for all the cases

with constant system parameters (see Table 7-1 and 7-2). Test cases for complicated single-objective problems are summarized in Table 7-4. Main focuses are put on the following topics;

a) Gradient based algorithm (SQP) vs. Derivative-free algorithm (PSO)

b) Comparison of two global optimization algorithms for SO problems

c) Solution dependency on population size of PSO for complicated SO problems

First, SQP and PSO solutions are compared to investigate the difference between gradient and derivative-free approach. Initial (starting) point for PSO is randomly generated; on the other hand, one for SQP is arbitrary value. As mentioned in the previous chapter, it is widely known that the capability of SQP for searching the global optimal location is highly depending on the initial point. To carry out the reliable comparison, the initial value for SQP is set to the same value of $x_1$ (Swarm #1).

Next, solutions from three algorithms are compared. Micro Soft Excel non-linear solver is used to calculate the benchmark solutions. Quadratic estimation and central derivative options are used with Conjugate search method. The precision and tolerance are set to $10^{-10}$ in order to get reliable solutions. All the solutions from three optimization algorithms are compared with benchmark solutions, and relative errors are calculated. Furthermore, the study of RCGA capability for single objective problem is conducted. RCGA was developed for solving multi-objective problems in the present study; thus, dummy objective function is assigned to have it solve single objective problem. Therefore, all the case with single objective problems are set to $F_2=0$.

Finally, the dependency of population size is also investigated; 2, 4, 6, and 8 are selected as the population size. The solutions are also compared with benchmark values.

***iii. Multi-objective optimization problems***

For multi-objective problems, six analytical functions are evaluated with PSO and GA. Flexible numbers of design variables can be set to three functions, while only two

design variables can be applied to the other three functions. The number of design variables is set to 2 and 16 for first three functions, and the population size is set to 2 and 8. In addition, two maximum iterations (generations) are used; 30 and 100. Thus, total eight test cases are prepared (Table 7-5). Note that the constant coefficients except maximum iteration number for PSO and RCGA are fixed for all the cases in this study as summarized in Table 7-1 and 7-2.

The important aims of multi-objective optimization scheme are following; (1) to find a set of solutions as close as possible to the Pareto-optimal front; (2) to find as many choices which are on the Pareto front as possible; (3) to find a set of solutions as diverse as possible. In the present study, three evaluation methods are introduced, namely, area of dominated space, size of Pareto front, and non-uniformity of Pareto front in order to analyze the performance of optimization algorithms quantitatively.

Finally, two different coding types of genetic algorithms; which are BCGA and RCGA, are compared. Multi-objective optimization problems are subjected to solve by two GA; and the difference of solution distributions toward generation are carefully compared.

## 7.2 Verification of PSO method for simple single-objective optimization problems

In this section, the verification of PSO capability for solving single objective optimization problems is presented. The following analytical function is evaluated by PSO with the constant value of system parameters (see Table 7-1).

$$minimize \qquad f_1 = (x_1 - \alpha)^2 + (x_2 - \beta)^2 \tag{7.1}$$

$$subject\ to \qquad 0 \leq x_1, x_2 \leq 1$$

where, $f_1$, $x_1$, and $x_2$ are objective function and two design variables, respectively.

In the Equation (7.1), α and β are arbitrary numbers, and six cases are considered in the present study as presented in Table 7-3. As a result, the design spaces always have only one global minimum; for example the design space of case 1 is shown in Figure 7-1 where the minimum value is found at $x_1$=$x_2$=0.5. For each case, two swarm particles (in one generation) and 100 maximum iterations (generations) are used.

The results are plotted in Figure 7-2; x1 vs. x2 (design variables of all the generations) and generation vs. x1, x2, and F. All the detailed solutions are summarized with errors in Table 7-6. As shown in Figure 7-2 and Table 7-6, PSO shows good performance in terms of both speed and capability of searching the global optimal locations. All the solutions show less than 1.5% error (average of 0.32%) from the theoretical value, and less than 70 iterations to get converged. Besides, as shown in Figure 7-2, it is faster to reach the optimal points than iterations PSO takes; thus, optimal solution (with small fluctuation) can be obtained less than 50 generations for all the cases if the convergence criterion is changed.

## 7.3 Single-objective optimization problems

In this section, the comparison study for complicated single-objective optimization problems is presented. Eleven analytical functions are selected to evaluate the performance of three optimization algorithms, i.e., PSO, RCGA, and SQP. All the test functions have two design variables and more than one peak on the design space;

F1: $$f_1 = -0.1\sin(10x_1) + 0.2x_1 + (x_2 - 0.7)^2 + 0.1 \quad (7.2)$$

F2: $$f_1 = -0.1\sin(10x_1) - 0.2x_1 + (x_2 - 0.7)^2 + 0.1 \quad (7.3)$$

F3: $$f_1 = 0.1\cos(4\pi x_1) + 0.2x_1 + (x_2 - 0.5)^2 \quad (7.4)$$

F4: $$f_1 = -0.1\sin(15x_1) + 0.2x_1 + (x_2 - 0.7)^2 + 0.1 \quad (7.5)$$

F5: $$f_1 = -0.1\sin(15x_1) - 0.2x_1 + (x_2 - 0.7)^2 + 0.1 \quad (7.6)$$

F6: $$f_1 = 0.1\cos(6\pi x_1) + 0.2x_1 + (x_2 - 0.5)^2 \quad (7.7)$$

F7: $$f_1 = -0.1\sin(20x_1) + 0.2x_1 + (x_2 - 0.7)^2 + 0.1 \quad (7.8)$$

F8: $$f_1 = 0.1\cos(8\pi x_1) + 0.2x_1 + (x_2 - 0.5)^2 \quad (7.9)$$

F9: $$f_1 = 0.2\cos(6\pi x_1) + 0.2x_1 + 0.1\cos(4\pi x_2) + 0.2x_2 \quad (7.10)$$

F10: $$f_1 = 0.2\cos(8\pi x_1) + 0.2x_1 + 0.2\cos(6\pi x_2) + 0.2x_2 \quad (7.11)$$

F11: $$f_1 = -0.1\sin(20x_1) - 0.2x_1 + (x_2 - 0.7)^2 + 0.1 \quad (7.12)$$

### 7.3.1 Comparison study of PSO/RCGA/SQP

Table 7-4 describes the case matrixes; thus, five test cases are performed for this study. As mentioned earlier, the initial points for PSO and RCGA are randomly generated and one for SQP is set to same value of the one of swarm particle. Figure 7-3 shows solution plots from three algorithms (3-dimensional distribution of x1, x2, and F and distribution of design variables x1 vs. x2), and Table 7-7 provides the summary of solutions (from only global algorithms) compared with benchmark solutions.

As shown in Figure 7-3, SQP often tends to get trapped to the local minima or other locations; it is also true that SQP successfully search the global optimal location for some functions such as F2, F3, F5, and F7. These results indicate that the performance of SQP is highly depending on the initial given points. In contrast, PSO shows the better performance over SQP for all test functions in terms of searching global minima; however, the time (iteration) to reach the global optimal point is always longer than the one of SQP. The solutions from RCGA show highly random distribution although RCGA could reach the global optimal point for some functions eventually.

As summarized in Table 7-7, PSO with 8 particles reaches global optimal point with ~0.0005% error; however, PSO gets trapped to other locations for most cases when the smaller population size is selected. Therefore, it is assumed that performance of PSO depends on population sizes. More detailed study on the population size is presented in later section. Since particles communicate each other in the PSO algorithm, it is unsurprising result that solutions with smaller population size show worse accuracy than larger population size. In contrast, RCGA shows the random performance and sometimes it could reach the global minima even though the number of population is set to 2. Mostly RCGA solutions with larger number of populations show better results than the ones with smaller; however, it is not always true such as the F7 case. Therefore, RCGA is not affected by the population size compared to PSO.

### 7.3.2 RCGA performance analysis

In the previous sub-section, the solutions for single-objective optimization problems are presented using three different optimization algorithms. In this sub-section, the focus is put on the solutions from RCGA. As mentioned earlier, the solutions show highly random distributions. Figure 7-4 shows the solution distributions of generation vs. F and x1 vs. x2. As observed in the figure, design variables are generated by random

manner even though different functions are solved. Almost all the cases show the similar distributions of design variables. Thus, the capability of present RCGA scheme toward single-objective optimization problems is not preferable.

### 7.3.3 Dependency of population sizes in PSO

In sub-section 7.3.1, PSO is used to find the optimal locations of analytical optimization problems. As shown in Table 7-7, PSO with 8 particles shows the best performance to find solutions which agrees well with benchmark solutions; however, PSO with 2 particles shows worse accuracy. Therefore, the dependency of population size for complicated single-objective problems is investigated in more detail. The population size is set to 2, 4, 6, and 8. Four functions are evaluated with constant system parameters (Table 7-1).

The solutions are summarized in Table 7-8 where the dependency is clear to be observed. When 8 particles are used, PSO can reach the global optimal points with less than 0.001% error; however, the accuracy gets down with decreasing the population size. In addition, with smaller population sizes, PSO tends to get trapped to local optimal points as seen in the Figure 7-3. The results indicate that it is important to have enough particles in single generation to reach global optimal points unlike it is not important for GA; however, it should be remembered that the computational effort becomes double if the population size gets double.

## 7.4 Multi-objective optimization problems

The ship design is usually a nonlinear multi-objective optimization problem; for instance, the goals of the design process include resistance reduction, lower hydrodynamic noise, and the reduced amplitude of particular motions. Unfortunately, the

improvement of a specific aspect of the global design usually causes worsening of some others, and the best approach is not to combine all the objectives into a single one but to keep the multi-criteria nature of the problem and to rely on the Pareto optimality concept.

### 7.4.1 Evaluation method

In this sub-section, the evaluation method for multi-objective optimization problems is described. Three evaluation methods are proposed to obtain quantitative values in order to analyze the capability of two evolutionary algorithms, PSO and GA. The basic idea of three evaluation methods is used with the idea of Pareto optimal set. The detail procedures are described as follows.

***i. Area of dominated space***

The area of dominated space is used to evaluate how wide domain, which is closer to Pareto front, the algorithms search in the range of feasible region. In other words, how much of the objective space is weakly dominated by a given non-dominated set. Figure 7-5 illustrates the idea of the dominated space. In the figure, the shaded green space is recognized as a dominated space in the case with two objective functions problem. Herein, $F_{1Max}$ and $F_{2Max}$ are defined by $F_{1Max} = \min(F_1|_{F_2=F_{2min}})$ and $F_{2Max} = \min(F_2|_{F_1=F_{1min}})$, respectively. Since the objective of the example problem is to minimize two objective functions, a maximum value for each objective is selected to determine the size of the dominated space. With bigger area, the solution is recognized as better one. On the other hand, smaller area indicates the algorithm tends to converge on some particular locations instead of searching wider solution space. Note that the outer region of the defined dominated space is ignored when the area is calculated.

***ii. Size of Pareto front***

Next, size of Pareto front is selected as second barometer to evaluate the performance. Number of points on Pareto front is directly used as the measure. Only the

points on Pareto front are counted. Size indicates the efficiency of reaching Pareto front, and the higher size means the algorithm gives the designer more choices. Maximum value of size is equal to maximum generation multiply by population size; thus, the evaluation is carried out using the percentage of the particles which reach Pareto front out of all particles.

***iii. Non-uniformity of Pareto front***

Last measure is non-uniformity (diversity) of Pareto front. To quantitatively evaluate the non-uniformity of the distribution of a Pareto front, the quality function $D$ is introduced. The quality $D$ is given by the following equation;

$$D = \sqrt{\frac{\sum_i^{n-1}(d_i/\bar{d}-1)}{n-1}} \tag{7.13}$$

where $d_i$ is the Euclidian distance between two consecutive points along the Pareto front, $\bar{d}$ is average distance of all the points on Pareto front, and $n$ is number of points lie on Pareto.

This quality function is a standard deviation of the distances normalized by the average distance. When $D = 0$, the spacing of the points on Pareto is uniform. The higher value of this barometer, the more non-uniform spacing is obtained; in other words, the algorithm tends to search some particular locations but wider range. Therefore, a lower value of this quality function is desired in order to evaluate the quality of algorithm capability for multi-objective functions.

### 7.4.2 Comparison study of PSO and RCGA

In this sub-section, the comparison study for multi-objective optimization problems is presented. PSO and RCGA are compared, and six analytical functions (FM1 through FM6) are evaluated. FM1, 2, and 3 have H function so that the number of design

variables is controllable; on the other hand, FM4, 5, and 6 can be used with two design variables. Since the actual hydrodynamic optimization is planned to use two design variables, the test cases here is also focused on two design variables case. Three different distributions of Pareto optimal front can be seen in the test functions; namely, FM1 and FM5 have convex Pareto set, FM2 and FM4 have concave Pareto set, and FM3 and FM6 have discontinuous Pareto set. Among these test functions, FM4 has unique shape of solution space (see Figure 7-6), and it is relatively difficult to find the Pareto front because minimal point of either objective is actually maximum point of the other and Pareto front region (overlapping region in Figure 7-6) is quite small. Thus, this function could become good example to measure the capability for finding Pareto front. These functions have been used in several literatures; for instance, see Pinto *et al*., (2007), Tahara *et al*., (2007), Obayashi *et al*., (2004), and Fonseca *et al*., (1995).

FM1: $$\begin{cases} f_1 = x_1 \\ f_2 = H\left(1 - \sqrt{f_1/H}\right) \end{cases} \tag{7.14}$$

FM2: $$\begin{cases} f_1 = x_1 \\ f_2 = H(1 - (f_1/H)^2) \end{cases} \tag{7.15}$$

FM3: $$\begin{cases} f_1 = x_1 \\ f_2 = H\left(1 - \sqrt{f_1/H}\right) \pm f_1\, sin(10\pi\, f_1) \end{cases} \tag{7.16}$$

FM4: $$\begin{cases} f_1 = 1 - exp(-(8x_1 - 5)^2 - (8x_2 - 3)^2) \\ f_2 = 1 - exp(-(8x_1 - 3)^2 - (8x_2 - 5)^2) \end{cases} \tag{7.17}$$

FM5: $$\begin{cases} f_1 = (x_1^2 + x_2^2)/2 \\ f_2 = ((x_1 - 1)^2 + (x_2 - 1)^2)/2 \end{cases} \tag{7.18}$$

FM6: $$\begin{cases} f_1 = ((x_1 + 1)^2 + (x_2 + 1)^2)/4 \\ f_2 = 1 - x_1 \sin^4(4\pi x_2) \end{cases} \tag{7.19}$$

where,

$$H = 1 + \frac{9}{N-1}\sum_{i=2}^{N} x_i$$

Test matrix is presented in Table 7-5. The population size is set to 2 and 8. Besides, two maximum iterations are prepared to measure the speed to reach the Pareto front since the maximum iteration is the stopping criteria for both algorithms for multi-objective optimization problems (there should not be converged locations).

Figure 7-7 shows the solution distributions from both PSO and RCGA. As seen in the figure, larger population size can form wider region of Pareto front for all the test functions as expected. In addition, RCGA solutions have more random distribution than PSO solutions as seen in single-objective problems. Overall, both algorithms successfully detect the Pareto front more or less. Finally, the evaluation results are shown in Table 7-9 which contains the list of objective functions, algorithms used, maximum generation number, population size, area of dominated space, size/percentage of Pareto front, and diversity of Pareto front. These results are visualized by the lines and dot symbols as presented in Figure 7-8 and 7-9. Discussions on these quantitative results are presented as follows focusing on each barometer.

*Area of dominated space*

Generally, RCGA can search bigger area than PSO when smaller population size is used; on the other hand, PSO can search bigger area than RCGA when larger population size is used. This trend is almost always true except the cases with FM1 and FM5, i.e., convex Pareto front. In addition, PSO solutions show bigger area change depending on population sizes than RCGA. Therefore, it is necessary to use larger population size when PSO is selected as an optimization algorithm for multi-objective optimization problems. Dependency of maximum iteration number is relatively small for both algorithms except the case with FM4. As mentioned earlier, FM4 has complicated solution space; thus, both algorithms tend to need more time to find the Pareto front than other functions. Overall, because of the random characteristic, RCGA could search the wider range or Pareto front than PSO without the effect of population size.

*Size of Pareto front*

PSO particles can reach Pareto front more than RCGA for all the test cases except the only one case (FM4, 30 generation, and 2 particles). Besides, PSO with 30 generations solutions show over half of the particles reach the Pareto front except FM4 case. These results indicate that PSO has more efficient in terms of finding more choices on Pareto front than RCGA even though the smaller population size and generations are used.

*Non-uniformity of Pareto front*

RCGA gets smaller non-uniformity values than PSO for all the cases. The possible reason why the RCGA shows better diversity than PSO is that the populations are distributed more randomly in the design space in GA; on the other hand, particles in PSO tend to get converged to some particular locations. As a result, RCGA gives us wider space on Pareto front. Fewer iteration cases always give the less uniformity. The dependency of population size affects relatively smaller.

Ultimately, PSO has advantages over RCGA such as faster to reach Pareto optimal front, more number of particles are reached to Pareto optimal set, and smaller generation case gives efficiency. In contrast, RCGA has advantages over PSO such as getting bigger area of dominated space, getting wider choices on Pareto front, and less dependency of population numbers.

### 7.4.3 Comparison study of BCGA and RCGA

In this sub-section, the capability of finding the Pareto front for multi-objective problems are compared using BCGA and RCGA. Three functions (FM1, FM2, FM3) are assigned to be minimized. Herein, the BCGA system parameters are subjected to constant for BCGA as shown in Table 7-2.

Figure 7-10 shows the comparison of results between BCGA and RCGA for representative test cases, where theoretically defined, complex Pareto optimal set must be detected. The same system parameters are used for the two computations, except for the mutation ratio, that is not defined in the BCGA. For the two schemes, the same number of individuals is plotted in the figure. For all three test functions, both BCGA and RCGA can detect the Pareto optimal set as shown in Figure 7-10(a); however, the convergence characteristics of the solutions are significantly different as seen in Figure 7-10(d). It is seen that the distribution for RCGA is more diverse, and Pareto optimal set is more widely detected, thus, the shape of Pareto front is more accurately expressed. It is also seen that BCGA tends to get trapped toward particular locations; the plot of 3-dimensional distribution clearly shows this trend. On the other hand, RCGA tends to find the global range of solution space even the iteration goes on. Therefore, it might be true that the BCGA speed is faster than RCGA until they reach the first optimal set; however, RCGA can search wider space of Pareto set efficiency. Overall, both algorithms have particular advantage and disadvantage; thus, the optimization scheme should be selected carefully based on the problem.

## 7.5 Summary of optimization algorithm study

To sum up the present study, there are six conclusions obtained from the test results. Overall, three optimization problems are considered in this study; simple single-objective optimization problems, complicated single-objective problems, and multi-objective problems. Following summary contains several discussions: Verification of PSO performance, PSO vs. RCGA vs. SQP for single-objective optimization problems, performance analysis of RCGA for single-objective problems, dependency on population size for PSO for single-objective problems, PSO vs. RCGA for multi-objective problems, and BCGA vs. RCGA for multi-objective problems.

***Verification of PSO performance***

Figure 7-2 and Table 7-6 show the performance of PSO method to solve simple single-objective optimization problems. Optimization studies are performed using seven analytical functions which have single peak on the feasible solution space to evaluate the capability of PSO. Ultimately, the solutions indicate that PSO with two particles can search the optimal point (actually the global minima) for simple single objective problems accurately with smaller generations (~50 iterations). The average error from the theoretical value is within 0.2%.

***PSO vs. RCGA vs. SQP for single-objective optimization problems***

It is widely known that SQP is able to efficiently search optimal point if the initial point is correctly given. That is, the design and objective function space has to be known before the initial point is assigned. If the initial point is not correctly given, SQP is trapped into local minima (it is not capable to climb the hill since the algorithm is based on derivative method). In other words, SQP can be used only when the design space was known and objective function is one, or design space is only dominated by linear function and objective function is one.

On the other hand, it is proven that PSO can search the global optimal point efficiently even when the design spaces have many peaks. As shown in Figure 7-3, PSO solutions reach global optimal points for every test case; whereas, the SQP solutions trap in local minima. From these results, we can say that the PSO can be adapted as a search method for single objective optimization problems, which have multi-peak on solution space, better than SQP method. In contrast, RCGA show the capability of searching global optimal location; however, the distributions of design variables are generated by random manner for all the test cases. The more details on this randomness issue are discussed later. Therefore, the difference between population-based global optimization algorithms and gradient-based local algorithms can be seen clearly from the study, and it is proven that local algorithms are not applicable.

***Performance analysis of RCGA for single-objective problems***

As seen in the Table 7-7, RCGA have a capability to find the global minima for some functions, not all the test functions. However, as shown in Figure 7-4, the design variables generated by RCGA are quite random; in particular, the solution from less populations show almost same distribution of design variables. It means that the design variables, which should be generated by considering the minimization of objective function, are not successfully made. Eventually, some design variables get the good agreement with the benchmark solution; however, that is the case accidently happened since the distributions do not seem reasonable. As a result, RCGA is not a proper choice for the single-objective optimization problems.

***Dependency of population size for PSO for single-objective problems***

By comparing the population size (Table 7-8), it is appeared that PSO with two particles has less capability to search the global optimal point and it often traps into local optimal points. However, when the swarm number is increased, the converged solution gets closer to the benchmark analytical value. With eight swarm particles, all the cases search the global optimal point with ~0.02% uncertainty in terms of objective function.

***PSO vs. RCGA for multi-objective optimization problems***

Three evaluation methods are used to obtain the quantitative value to measure the performance of both algorithms. Here, the summary is focus on three comparisons, namely, general trend of both algorithms to evaluate the performance, dependency of population size to evaluate the efficiency, and dependency of generation numbers to evaluate the speed. Table 7-9 summarizes the all results and Figure 7-7 shows the comparisons.

***BCGA vs. RCGA for multi-objective problems***

Figure 7-10 shows the comparison of solution distributions for multi-objective problems from BCGA and RCGA. As seen in the figure, the features of each algorithm are clearly shown; i.e., the distribution for RCGA is more diverse, and Pareto optimal set

is more widely detected. It is also seen that BCGA tends to get trapped toward particular locations. On the other hand, RCGA tends to find the global range of solution space even the iteration goes on. Therefore, BCGA speed is faster than RCGA until they reach the first location on optimal set; however, RCGA can search wider space of Pareto set efficiency. Overall, both algorithms have particular advantage and disadvantage; thus, the optimization scheme should be selected carefully based on the problem. Quantitative evaluation is not presented since the characteristic of each algorithm is shown clearly in the figure.

In consequence, overall results from three algorithms show both advantages and disadvantages. For the single objective optimization problems, PSO should be the first choice over other two algorithms because of its speed and accuracy with the condition of enough population size. For the multi-objective problems, both RCGA and PSO have different advantages; thus, they should be used depending on the purpose and demands.

Table 7-1 Constant system parameters for PSO

| | |
|---|---|
| Constriction function $(\chi)$ | 1 |
| Initial inertia weight value $(w_0)$ | 0.729 |
| Decreasing coefficient for the inertia weight $(K_w)$ | 1 |
| Cognitive parameter $(c_1)$ | 1.494 |
| Social parameter $(c_2)$ | 1.494 |
| Bounds limit for the design variables | [0:1] |
| Maximum number of objective function evaluations | $100\times\#_{\text{particles}}$ |

Table 7-2 Constant system parameters for RCGA and BCGA

| RCGA | |
|---|---|
| Crossover ratio | 0.75 |
| Bounds limit for the design variables | [0:1] |
| Maximum number of objective function evaluations | $100\times\#_{\text{chromosomes}}$ |
| **BCGA** | |
| Crossover ratio | 0.75 |
| Mutation ratio | 0.30 |
| Bounds limit for the design variables | [0:1] |
| Maximum number of objective function evaluations | $100\times\#_{\text{chromosomes}}$ |

Table 7-3 Test matrix for simple single-objective optimization problems

| Case # | α | β |
|---|---|---|
| 1 | 0.5 | 0.5 |
| 2 | 0.2 | 0.2 |
| 3 | 0.2 | 0.8 |
| 4 | 0.8 | 0.2 |
| 5 | 0.1 | 0.1 |
| 6 | 0.9 | 0.9 |

Table 7-4 Test matrix for complicated single-objective optimization problems

| Case # | OPT algorithm | # objective functions | # design variables | Population size | Maximum iteration |
|---|---|---|---|---|---|
| 1 | SQP | 1 | 2 | - | 100 |
| 2 | PSO | 1 | 2 | 2 | 100 |
| 3 | RCGA | 1 | 2 | 2 | 100 |
| 4 | PSO | 1 | 2 | 8 | 100 |
| 5 | RCGA | 1 | 2 | 8 | 100 |

Table 7-5 Test matrix for multi-objective optimization problems

| Case # | OPT algorithm | # objective functions | # design variables | Population size | Maximum iteration |
|---|---|---|---|---|---|
| 1 | PSO | 2 | 2 | 2 | 30 |
| 2 | RCGA | 2 | 2 | 2 | 30 |
| 3 | PSO | 2 | 2 | 8 | 30 |
| 4 | RCGA | 2 | 2 | 8 | 30 |
| 5 | PSO | 2 | 2 | 2 | 100 |
| 6 | RCGA | 2 | 2 | 2 | 100 |
| 7 | PSO | 2 | 2 | 8 | 100 |
| 8 | RCGA | 2 | 2 | 8 | 100 |

Table 7-6 Summary of PSO solutions for simple single-objective optimization problems compared with theoretical values

| | Final values | | | | | | Analysis | | | | |
|---|---|---|---|---|---|---|---|---|---|---|---|
| | SWARM.1 | | SWARM.2 | | Optimal position | | Theoretical values | | Error(%-th) | | Iteration |
| ID# | alpha | beta | alpha | beta | alpha | beta | alpha | beta | alpha | beta | |
| 1 | 0.49984 | 0.50044 | 0.50272 | 0.50194 | 0.49984 | 0.50044 | 0.5 | 0.5 | -0.032 | 0.089 | 45 |
| 2 | 0.19839 | 0.19956 | 0.19988 | 0.19916 | 0.19988 | 0.19956 | 0.2 | 0.2 | -0.059 | -0.221 | 62 |
| 3 | 0.19856 | 0.80269 | 0.20184 | 0.79966 | 0.19856 | 0.79966 | 0.2 | 0.8 | -0.720 | -0.043 | 46 |
| 4 | 0.80118 | 0.19876 | 0.80094 | 0.19940 | 0.80094 | 0.19940 | 0.8 | 0.2 | 0.117 | -0.301 | 58 |
| 5 | 0.09880 | 0.09820 | 0.10065 | 0.09865 | 0.10065 | 0.09865 | 0.1 | 0.1 | 0.647 | -1.348 | 69 |
| 6 | 0.90060 | 0.89864 | 0.89878 | 0.89846 | 0.89878 | 0.89864 | 0.9 | 0.9 | -0.066 | -0.152 | 60 |

Table 7-7 Summary of solutions for complicated single-objective optimization problems

| Objective function | algorithm | Population size | Optimal position X1 | Optimal position X2 | objective | Error |
|---|---|---|---|---|---|---|
| **F1** | Benchmark | | 1.3694E-01 | 7.0000E-01 | 2.9409E-02 | |
| | PSO | 2 | 7.6533E-01 | 7.0004E-01 | 1.5507E-01 | 427.294% |
| | | 8 | 1.3691E-01 | 6.9987E-01 | 2.9409E-02 | 0.00007% |
| | RCGA | 2 | 1.0611E-01 | 7.3560E-01 | 3.5199E-02 | 19.687% |
| | | 8 | 1.4689E-01 | 7.1524E-01 | 3.0128E-02 | 2.4454% |
| **F2** | Benchmark | | 8.0553E-01 | 7.0000E-01 | -1.5909E-01 | |
| | PSO | 2 | 9.9299E-01 | 7.0219E-01 | -5.0204E-02 | -68.442% |
| | | 8 | 8.0551E-01 | 6.9999E-01 | -1.5909E-01 | 0.00001% |
| | RCGA | 2 | 7.8451E-01 | 7.1636E-01 | -1.5663E-01 | -1.5435% |
| | | 8 | 8.0093E-01 | 6.9297E-01 | -1.5893E-01 | -0.0966% |
| **F3** | Benchmark | | 2.3728E-01 | 5.0000E-01 | -5.1269E-02 | |
| | PSO | 2 | 2.5744E-01 | 1.0298E-01 | 1.0955E-01 | -313.681% |
| | | 8 | 2.3727E-01 | 5.0003E-01 | -5.1269E-02 | 0.00000% |
| | RCGA | 2 | 2.1576E-01 | 4.7009E-01 | -4.6839E-02 | -8.64203% |
| | | 8 | 2.4800E-01 | 5.1294E-01 | -5.0201E-02 | -2.08266% |
| **F4** | Benchmark | | 9.5804E-02 | 7.0000E-01 | 2.0054E-02 | |
| | PSO | 2 | 9.8673E-01 | 7.2484E-01 | 2.1920E-01 | 993.056% |
| | | 8 | 9.5808E-02 | 6.9999E-01 | 2.0054E-02 | 0.00001% |
| | RCGA | 2 | 9.8914E-02 | 7.0833E-01 | 2.0231E-02 | 0.88491% |
| | | 8 | 9.7093E-02 | 7.0121E-01 | 2.0074E-02 | 0.09974% |
| **F5** | Benchmark | | 9.5139E-01 | 7.0000E-01 | -1.8939E-01 | |
| | PSO | 2 | 1.0000E+00 | 6.9999E-01 | -1.6503E-01 | -12.861% |
| | | 8 | 9.5138E-01 | 6.9999E-01 | -1.8939E-01 | 0.00001% |
| | RCGA | 2 | 9.4469E-01 | 6.4796E-01 | -1.8618E-01 | -1.69532% |
| | | 8 | 9.5312E-01 | 6.8228E-01 | -1.8904E-01 | -0.18333% |
| **F6** | Benchmark | | 1.6103E-01 | 5.0000E-01 | -6.7230E-02 | |
| | PSO | 2 | 5.0033E-01 | 2.0048E-01 | 8.9781E-02 | -233.54% |
| | | 8 | 1.6103E-01 | 5.0000E-01 | -6.7230E-02 | 0.00000% |
| | RCGA | 2 | 1.7283E-01 | 5.5740E-01 | -6.1463E-02 | -8.5783% |
| | | 8 | 1.5574E-01 | 4.7312E-01 | -6.6016E-02 | -1.8057% |
| **F7** | Benchmark | | 7.3531E-02 | 7.0000E-01 | 1.5208E-02 | |
| | PSO | 2 | 1.0000E+00 | 6.9999E-01 | 2.0871E-01 | 1272.381% |
| | | 8 | 7.3522E-02 | 7.0002E-01 | 1.5208E-02 | -0.00004% |
| | RCGA | 2 | 8.1697E-02 | 6.8759E-01 | 1.6693E-02 | 9.76629% |
| | | 8 | 8.5432E-02 | 7.0391E-01 | 1.8050E-02 | 18.6918% |
| **F8** | Benchmark | | 1.2183E-01 | 5.0000E-01 | -7.5317E-02 | |
| | PSO | 2 | 6.2435E-01 | 2.6758E-01 | 7.8903E-02 | -204.761% |
| | | 8 | 1.2178E-01 | 4.9947E-01 | -7.5316E-02 | -0.00050% |
| | RCGA | 2 | 3.8931E-01 | 5.3916E-01 | -2.0450E-02 | -72.8484% |
| | | 8 | 3.7290E-01 | 5.0668E-01 | -2.2741E-02 | -69.8068% |
| **F9** | Benchmark | | 1.6385E-01 | 2.3728E-01 | -2.1822E-01 | |
| | PSO | 2 | 5.0024E-01 | 2.0009E-01 | -1.4090E-01 | -35.4298% |
| | | 8 | 1.6384E-01 | 2.3738E-01 | -2.1822E-01 | -0.00004% |
| | RCGA | 2 | 3.5192E-01 | 2.0135E-01 | -1.5147E-01 | -30.5861% |
| | | 8 | 3.7592E-01 | 2.3587E-01 | -1.7215E-01 | -21.1089% |

Table 7-7 continued

| Objective function | algorithm | Population size | Optimal position X1 | Optimal position X2 | objective | Error |
|---|---|---|---|---|---|---|
| | Benchmark | | 1.2342E-01 | 1.6385E-01 | -3.4211E-01 | |
| | PSO | 2 | 3.7496E-01 | 1.5803E-01 | -2.9076E-01 | -15.009% |
| **F10** | | 8 | 1.2339E-01 | 1.6387E-01 | -3.4211E-01 | 0.0000% |
| | RCGA | 2 | 1.1727E-01 | 1.6227E-01 | -3.3587E-01 | -1.8239% |
| | | 8 | 1.2990E-01 | 1.5200E-01 | -3.3401E-01 | -2.3675% |
| | Benchmark | | 1.0000E+00 | 7.0000E-01 | -1.9130E-01 | |
| | PSO | 2 | 1.0000E+00 | 6.9999E-01 | -1.9130E-01 | -0.00001% |
| **F11** | | 8 | 1.0000E+00 | 6.9999E-01 | -1.9130E-01 | -0.00001% |
| | RCGA | 2 | 1.0000E+00 | 8.7755E-01 | -1.5977E-01 | -16.4799% |
| | | 8 | 1.0000E+00 | 7.0665E-01 | -1.9125E-01 | -0.02308% |

Table 7-8 Solutions from four different population sizes for complicated single-objective optimization problems

| Objective function | algorithm | Population size | Optimal position X1 | Optimal position X2 | objective | Error |
|---|---|---|---|---|---|---|
| | Benchmark | | 1.3694E-01 | 7.0000E-01 | 2.9409E-02 | |
| | PSO | 2 | 7.6533E-01 | 7.0004E-01 | 1.5507E-01 | 427.294% |
| **F1** | | 4 | 7.6538E-01 | 7.0018E-01 | 1.5507E-01 | 427.294% |
| | | 6 | 7.6555E-01 | 7.0008E-01 | 1.5507E-01 | 427.294% |
| | | 8 | 1.3691E-01 | 6.9987E-01 | 2.9409E-02 | 0.00007% |
| | Benchmark | | 9.5804E-02 | 7.0000E-01 | 2.0054E-02 | |
| | PSO | 2 | 9.8673E-01 | 7.2484E-01 | 2.1920E-01 | 993.056% |
| **F4** | | 4 | 5.3415E-01 | 4.2733E-01 | 1.8243E-01 | 809.700% |
| | | 6 | 9.5834E-02 | 7.0004E-01 | 2.0054E-02 | 0.00001% |
| | | 8 | 9.5808E-02 | 6.9999E-01 | 2.0054E-02 | 0.00001% |
| | Benchmark | | 7.3531E-02 | 7.0000E-01 | 1.5208E-02 | |
| | PSO | 2 | 1.0000E+00 | 6.9999E-01 | 2.0871E-01 | 1272.38% |
| **F7** | | 4 | 7.0178E-01 | 6.9996E-01 | 1.4087E-01 | 826.325% |
| | | 6 | 3.8774E-01 | 7.0004E-01 | 7.8039E-02 | 413.162% |
| | | 8 | 7.3522E-02 | 7.0002E-01 | 1.5208E-02 | -0.00004% |
| | Benchmark | | 1.2342E-01 | 1.6385E-01 | -3.4211E-01 | |
| | PSO | 2 | 3.7496E-01 | 1.5803E-01 | -2.9076E-01 | -15.009% |
| **F10** | | 4 | 1.3995E-01 | 1.1196E-01 | -2.3842E-01 | -30.307% |
| | | 6 | 1.2335E-01 | 1.6382E-01 | -3.4211E-01 | 0.0000% |
| | | 8 | 1.2339E-01 | 1.6387E-01 | -3.4211E-01 | 0.0000% |

Table 7-9 Comparison of solutions between PSO and RCGA for multi-objective problems with two maximum generation cases

| Objective function | Algorithm | Max Gen. | Population size | Area | Size | | Diversity |
|---|---|---|---|---|---|---|---|
| FM1 | RCGA | 30 | 2 | 0.5103 | 3 | 5.000% | 0.4600 |
| | | | 8 | 0.5039 | 7 | 2.917% | 0.9022 |
| | | 100 | 2 | 0.5934 | 9 | 4.500% | 0.6454 |
| | | | 8 | 0.6325 | 38 | 4.750% | 1.2839 |
| | PSO | 30 | 2 | 0.5945 | 16 | 26.667% | 1.0390 |
| | | | 8 | 0.6592 | 223 | 92.917% | 1.8371 |
| | | 100 | 2 | 0.6113 | 87 | 43.500% | 2.8978 |
| | | | 8 | 0.6623 | 727 | 90.875% | 2.7053 |
| FM2 | RCGA | 30 | 2 | 0.2045 | 3 | 5.000% | 0.3364 |
| | | | 8 | 0.1989 | 5 | 2.083% | 0.9433 |
| | | 100 | 2 | 0.2464 | 9 | 4.500% | 0.6092 |
| | | | 8 | 0.2974 | 39 | 4.875% | 1.2507 |
| | PSO | 30 | 2 | 0.2420 | 16 | 26.667% | 1.4232 |
| | | | 8 | 0.3260 | 223 | 92.917% | 1.5532 |
| | | 100 | 2 | 0.2461 | 87 | 43.500% | 3.8946 |
| | | | 8 | 0.3291 | 727 | 90.875% | 2.3133 |
| FM3 | RCGA | 30 | 2 | 0.7256 | 2 | 3.333% | 0.0000 |
| | | | 8 | 0.8386 | 4 | 1.667% | 0.1987 |
| | | 100 | 2 | 0.7744 | 5 | 2.500% | 0.8030 |
| | | | 8 | 0.9928 | 28 | 3.500% | 1.1072 |
| | PSO | 30 | 2 | 0.5649 | 13 | 21.667% | 1.3363 |
| | | | 8 | 1.0271 | 152 | 63.333% | 2.9373 |
| | | 100 | 2 | 0.5691 | 77 | 38.500% | 4.0445 |
| | | | 8 | 1.0288 | 669 | 83.625% | 6.1712 |
| FM4 | RCGA | 30 | 2 | 0.0215 | 8 | 13.333% | 0.4312 |
| | | | 8 | 0.0452 | 16 | 6.667% | 0.6389 |
| | | 100 | 2 | 0.0435 | 21 | 10.500% | 0.7977 |
| | | | 8 | 0.0578 | 56 | 7.000% | 0.8373 |
| | PSO | 30 | 2 | 0.0001 | 7 | 11.667% | 0.8895 |
| | | | 8 | 0.0464 | 23 | 9.583% | 0.9016 |
| | | 100 | 2 | 0.0014 | 101 | 50.500% | 3.0680 |
| | | | 8 | 0.0610 | 209 | 26.125% | 1.7747 |

Table 7-9 continued

| Objective function | Algorithm | Max Gen. | Population size | Area | Size | | Diversity |
|---|---|---|---|---|---|---|---|
| FM5 | RCGA | 30 | 2 | 0.7893 | 23 | 38.333% | 0.6510 |
| | | | 8 | 0.8173 | 72 | 30.000% | 1.1777 |
| | | 100 | 2 | 0.8201 | 66 | 33.000% | 0.9483 |
| | | | 8 | 0.8290 | 219 | 27.375% | 1.1914 |
| | PSO | 30 | 2 | 0.6658 | 55 | 91.667% | 3.0234 |
| | | | 8 | 0.8058 | 131 | 54.583% | 1.8998 |
| | | 100 | 2 | 0.6658 | 150 | 75.000% | 5.1761 |
| | | | 8 | 0.8167 | 676 | 84.500% | 3.2288 |
| FM6 | RCGA | 30 | 2 | 0.8598 | 12 | 20.000% | 0.5468 |
| | | | 8 | 0.9915 | 14 | 0.5833% | 0.4786 |
| | | 100 | 2 | 0.9299 | 16 | 8.000% | 0.7129 |
| | | | 8 | 1.0208 | 35 | 4.375% | 0.8458 |
| | PSO | 30 | 2 | 0.4022 | 36 | 60.000% | 3.1428 |
| | | | 8 | 1.0037 | 139 | 17.375% | 2.9839 |
| | | 100 | 2 | 0.4022 | 132 | 66.000% | 6.3017 |
| | | | 8 | 1.0042 | 607 | 75.875% | 6.1748 |

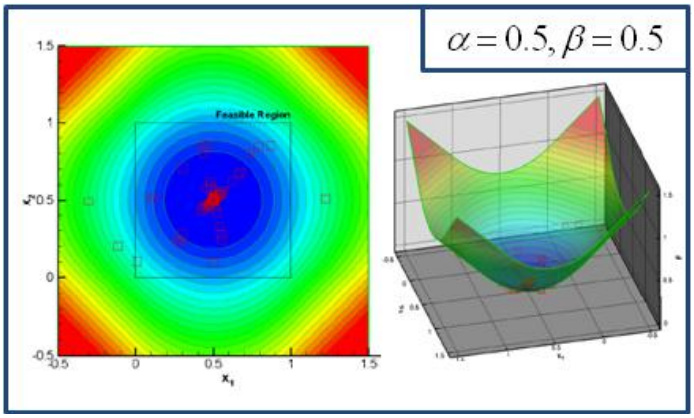


Figure 7-1 Example of design space for simple single-objective problem (case #1)

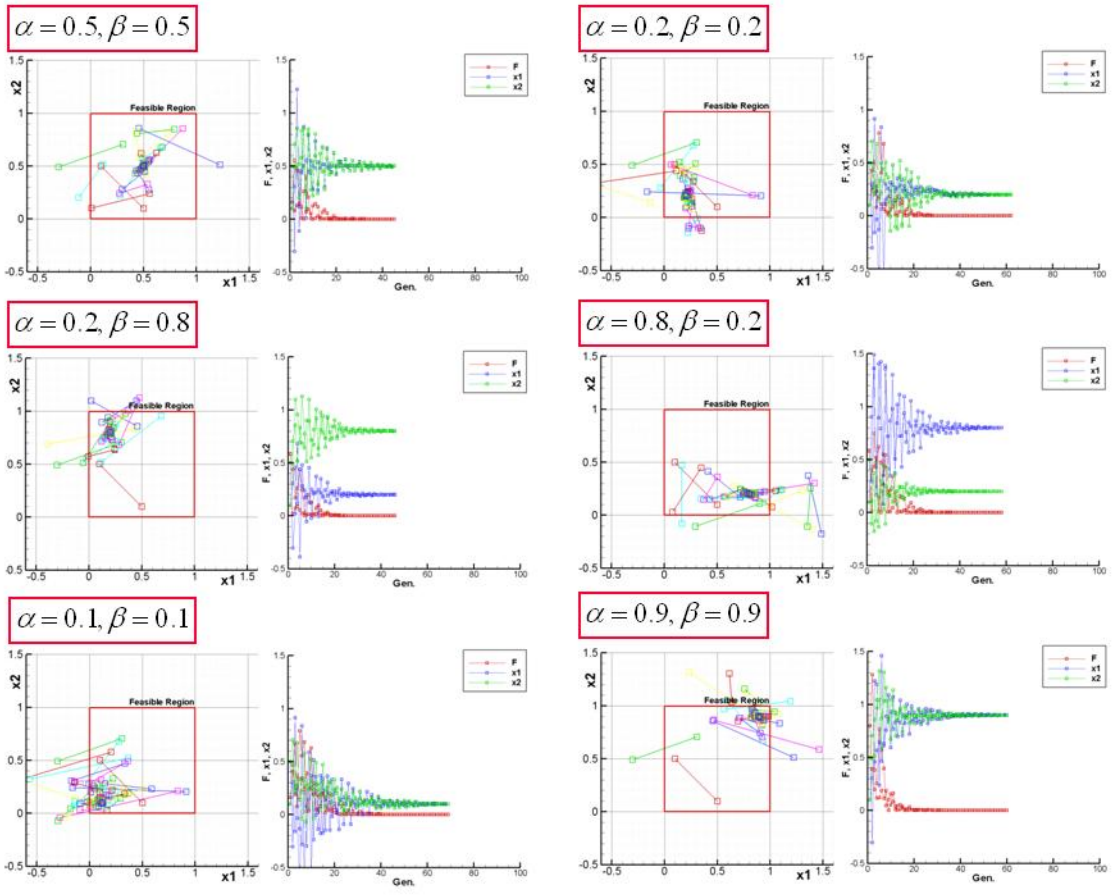


Figure 7-2 Verification of PSO using single-objective analytical functions:
(Left) $x_1$ vs. $x_2$, (Right) generation vs. F, $x_1$, $x_2$

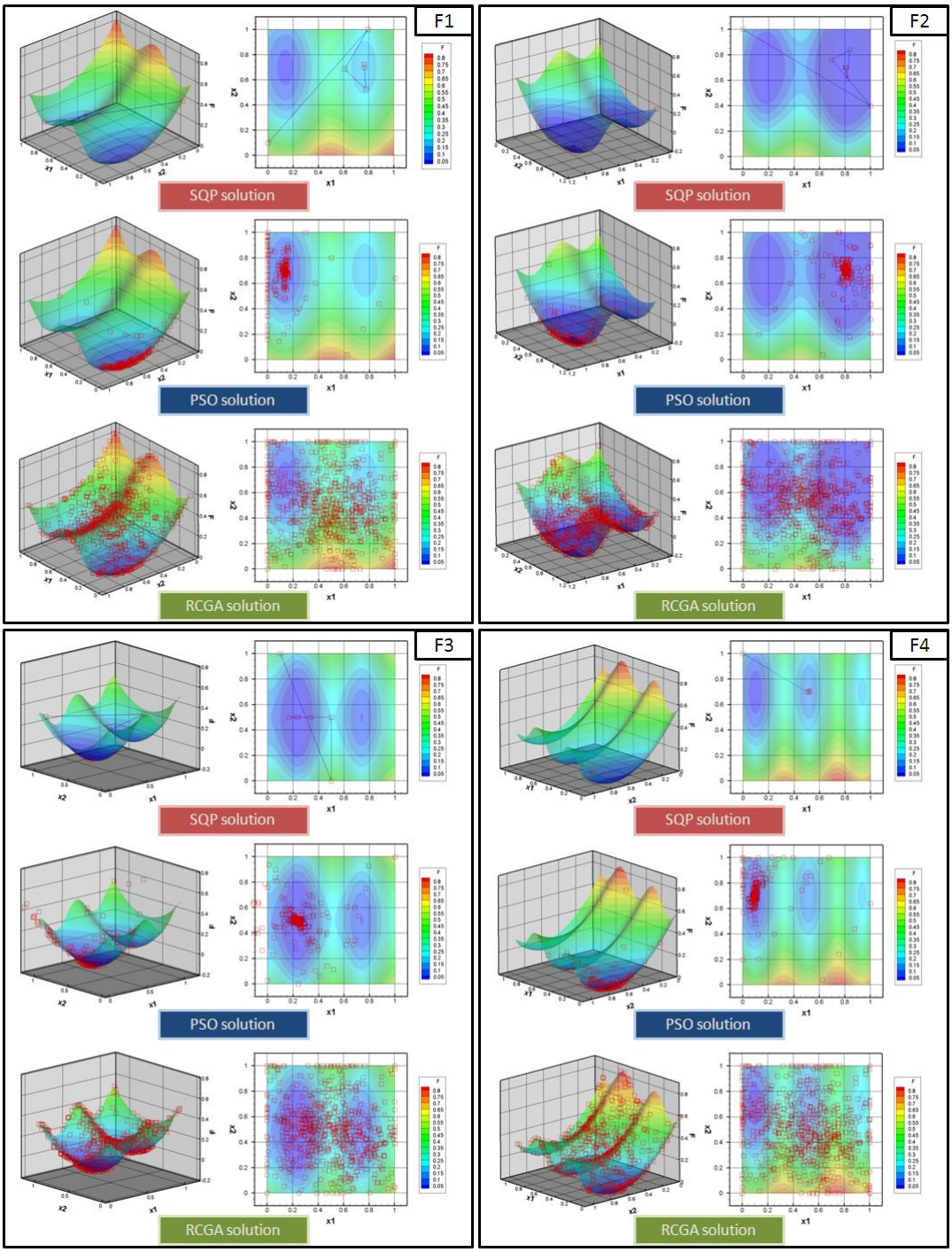


Figure 7-3 Solution distributions for single-objective functions, F1 to F11 obtained from case1 (SQP), 4 (PSO), and 5 (RCGA):
(Each box contains) Left: 3-dimensional distribution of $x_1$, $x_2$, and F, Right: $x_1$ vs. $x_2$

Figure 7-3 continued

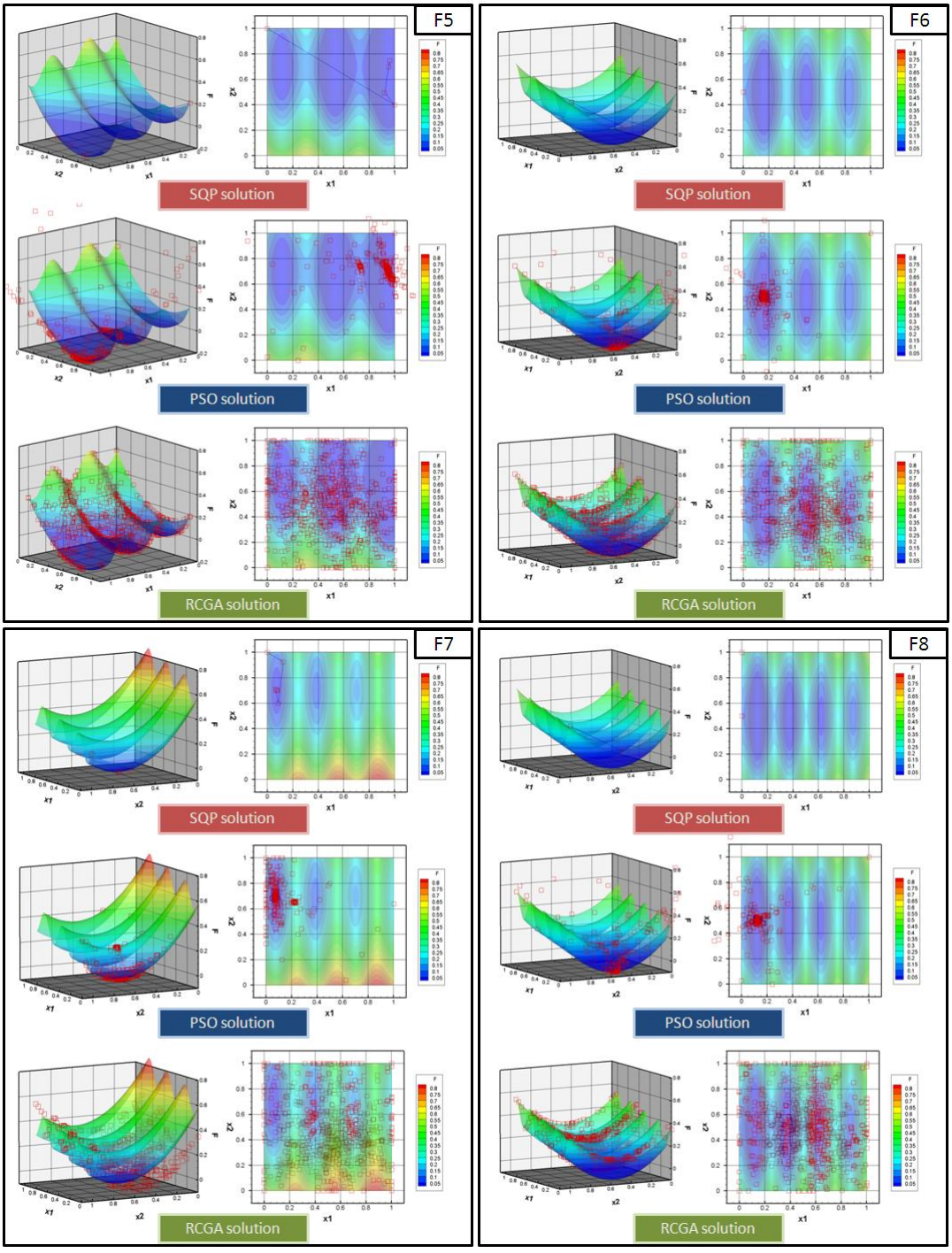

Figure 7-3 continued

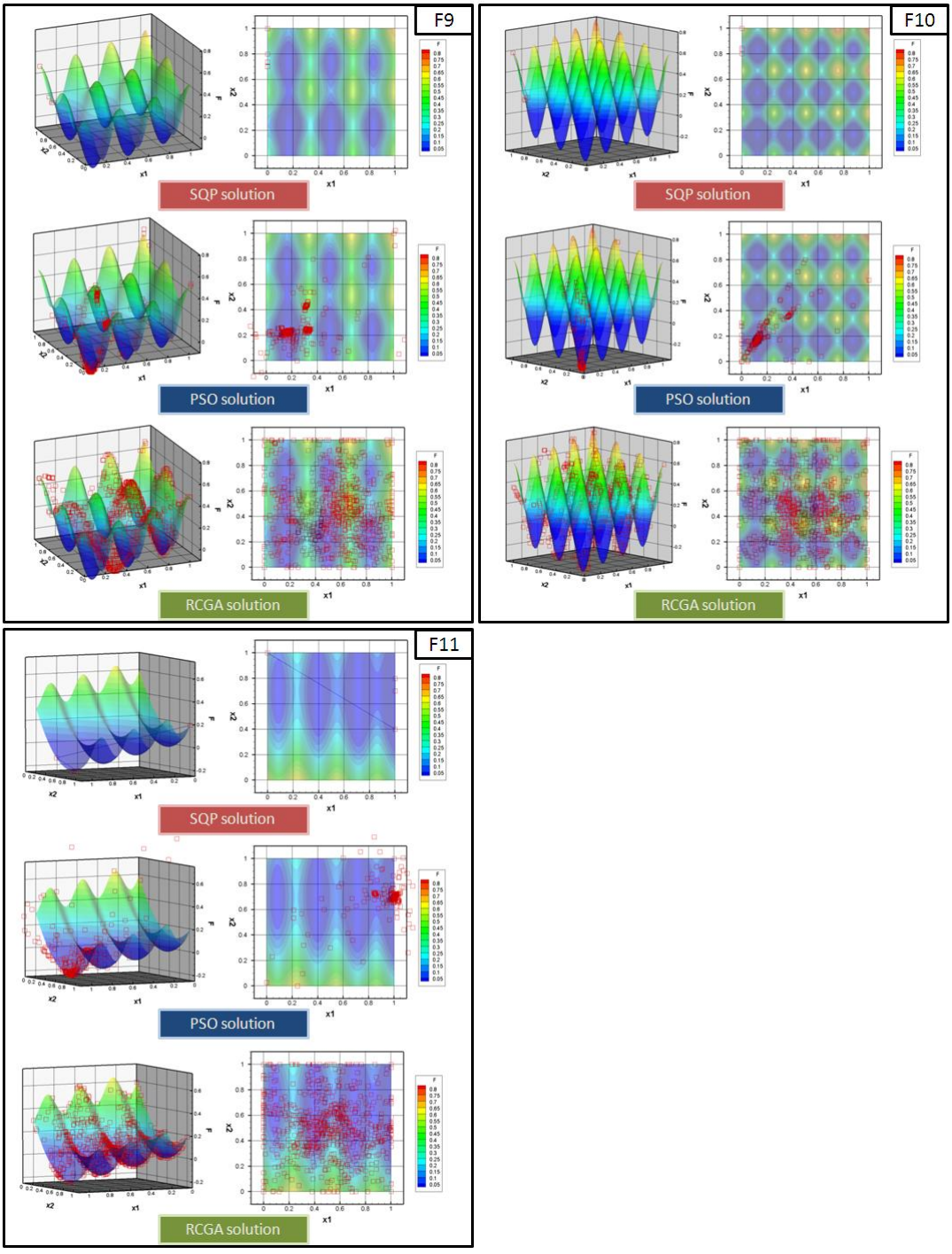

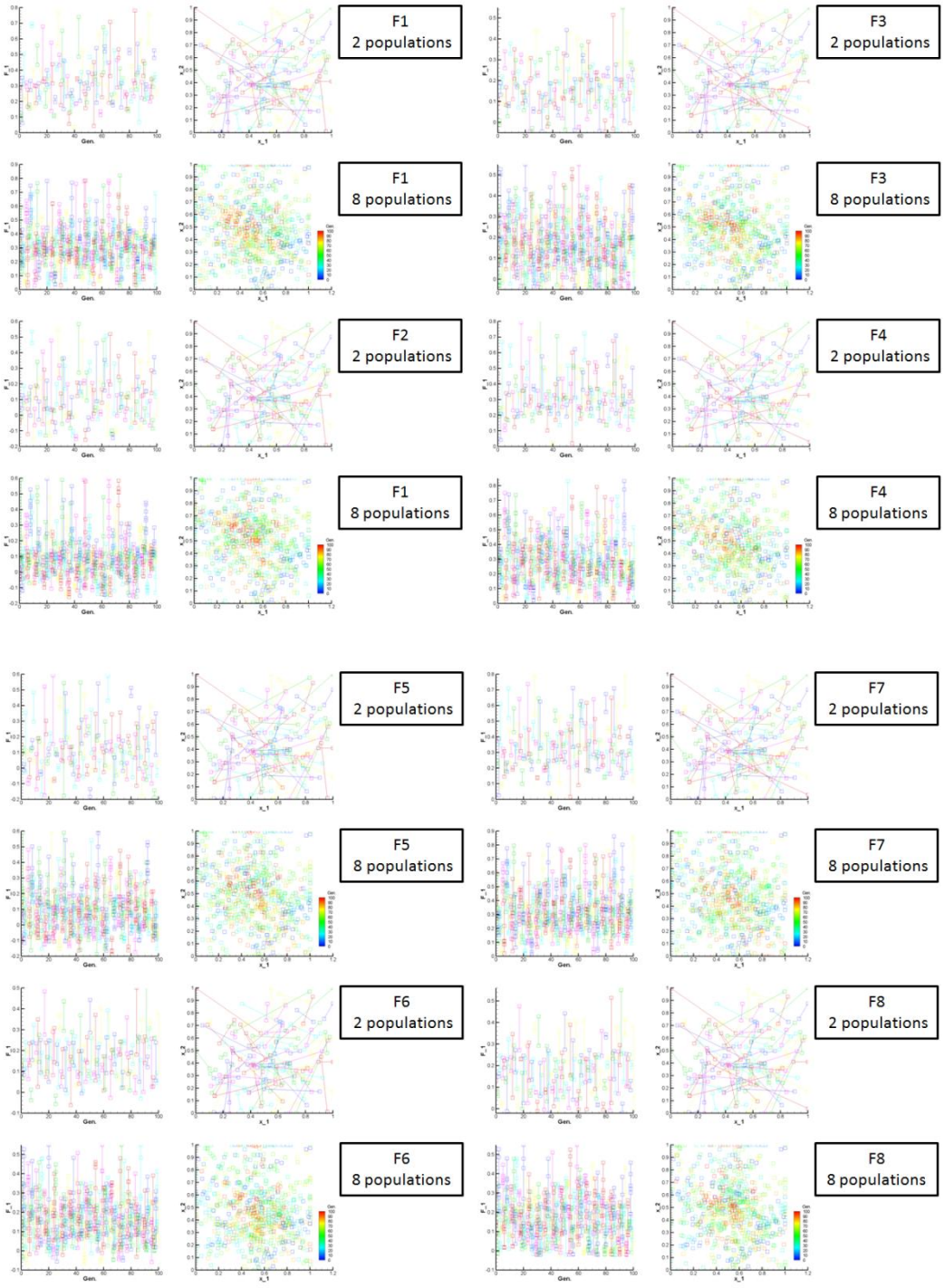


Figure 7-4 Solution distributions of RCGA for single-objective functions, F1 to F8: (Each box contains) Left: generation vs. F, Right: $x_1$ vs. $x_2$

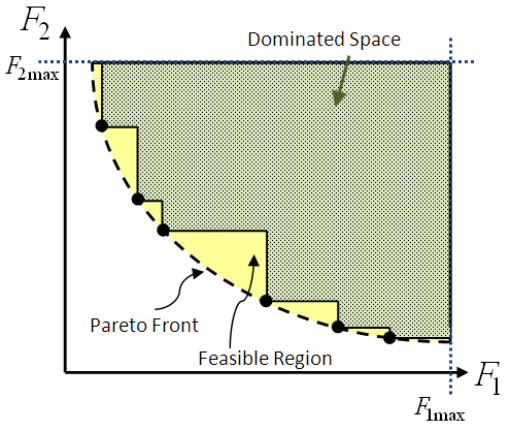


Figure 7-5 Illustration of the idea of dominated space (green area)

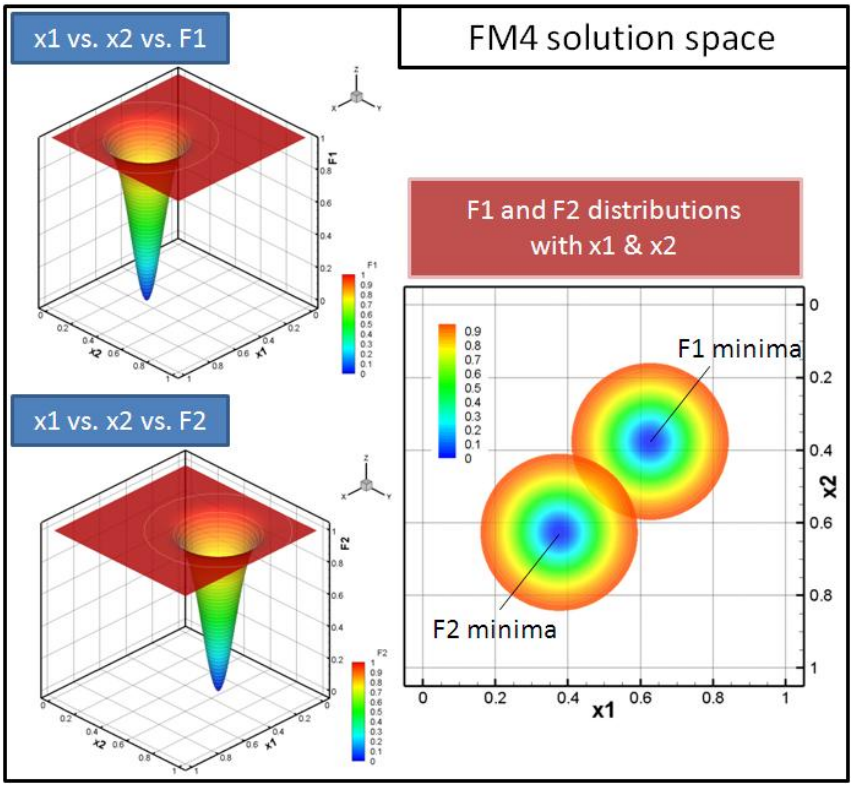


Figure 7-6 Surface plots of objective functions and solution distributions of FM4: (Left) 3-dimensional distribution (Top) $x_1$ vs. $x_2$ vs. $F_1$, (Bottom) $x_1$ vs. $x_2$ vs. $F_2$, (Right) contour plots of $F_1$ and $F_2$ distribution on design space

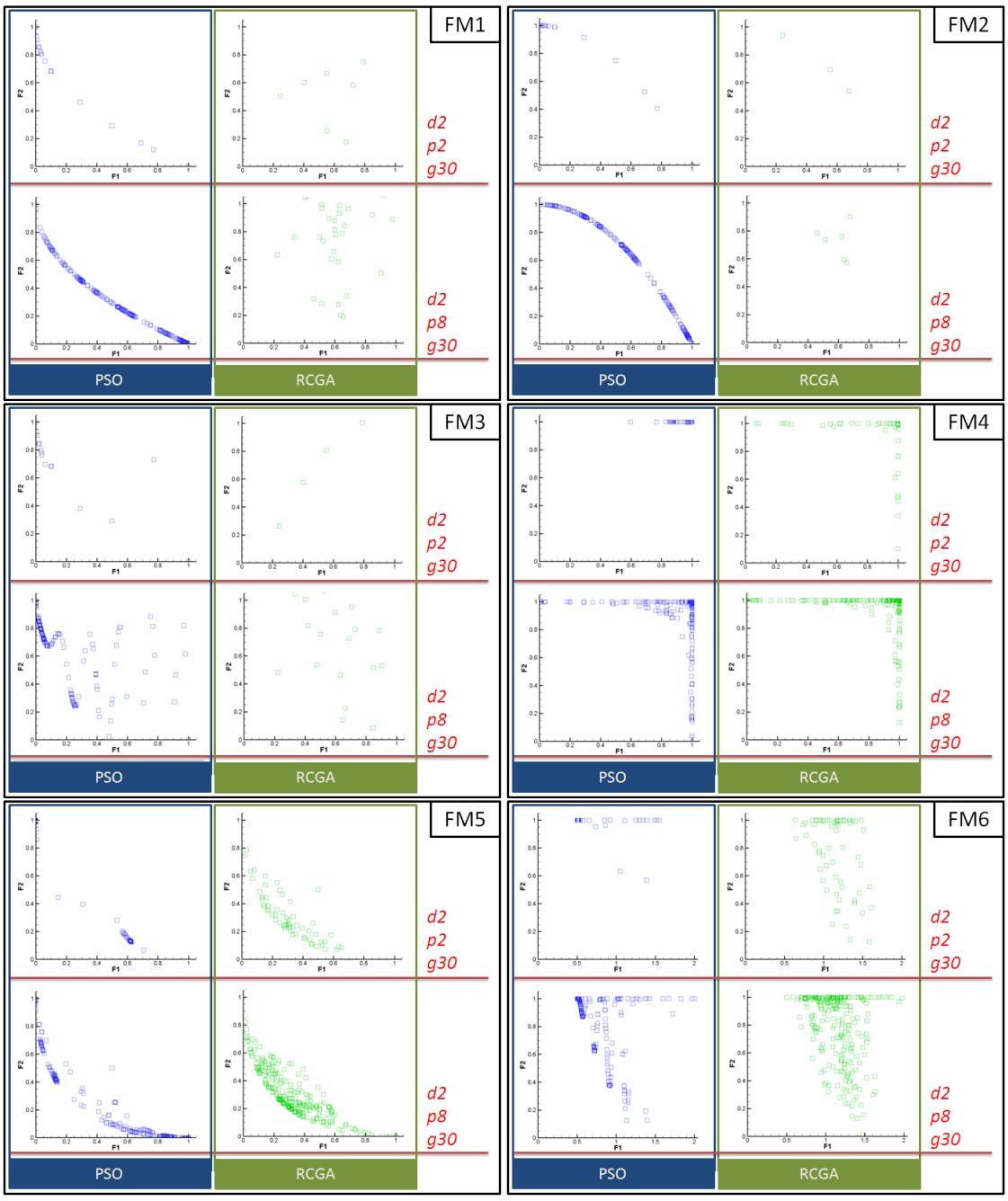


Figure 7-7 Distribution of solutions ($F_1$ vs. $F_2$) for multi-objective functions: (Each box contains) Top: fewer population sizes, Bottom: larger ones, Left: PSO solutions, Right: RCGA solutions

Figure 7-7 continued

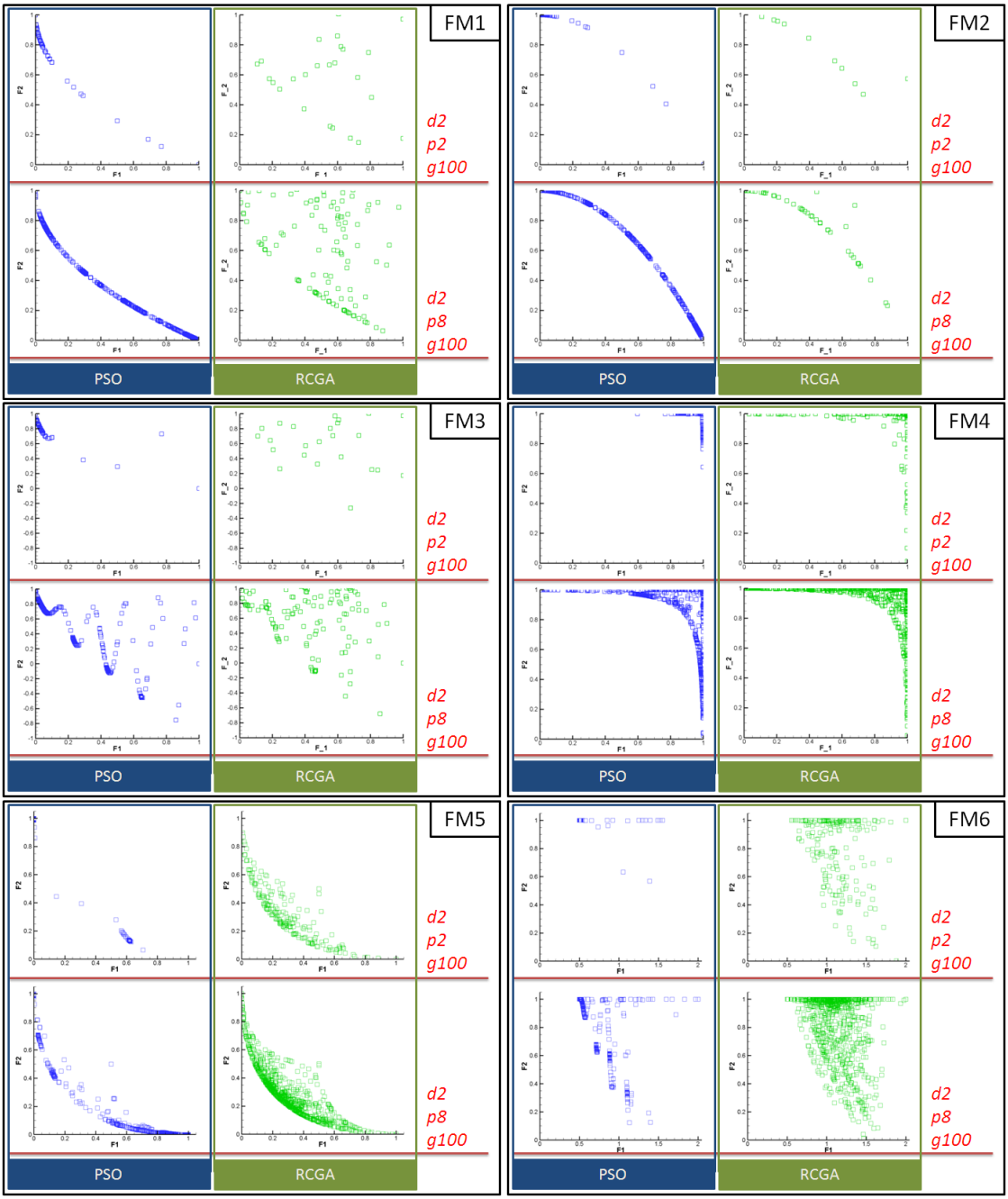

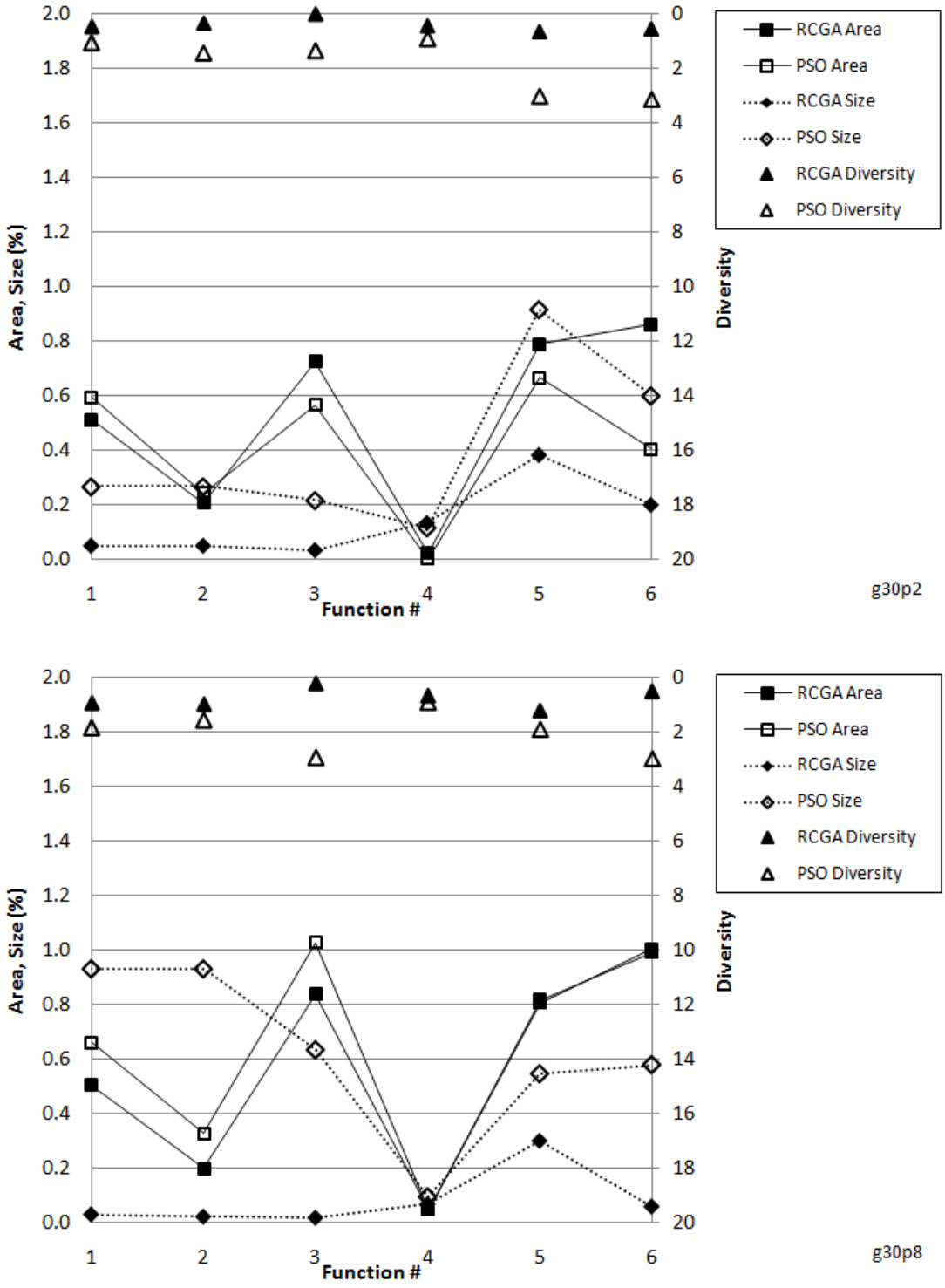


Figure 7-8 Comparison of evaluation results for smaller maximum generation cases (30): (Top) population size=2, (Bottom) population size=8

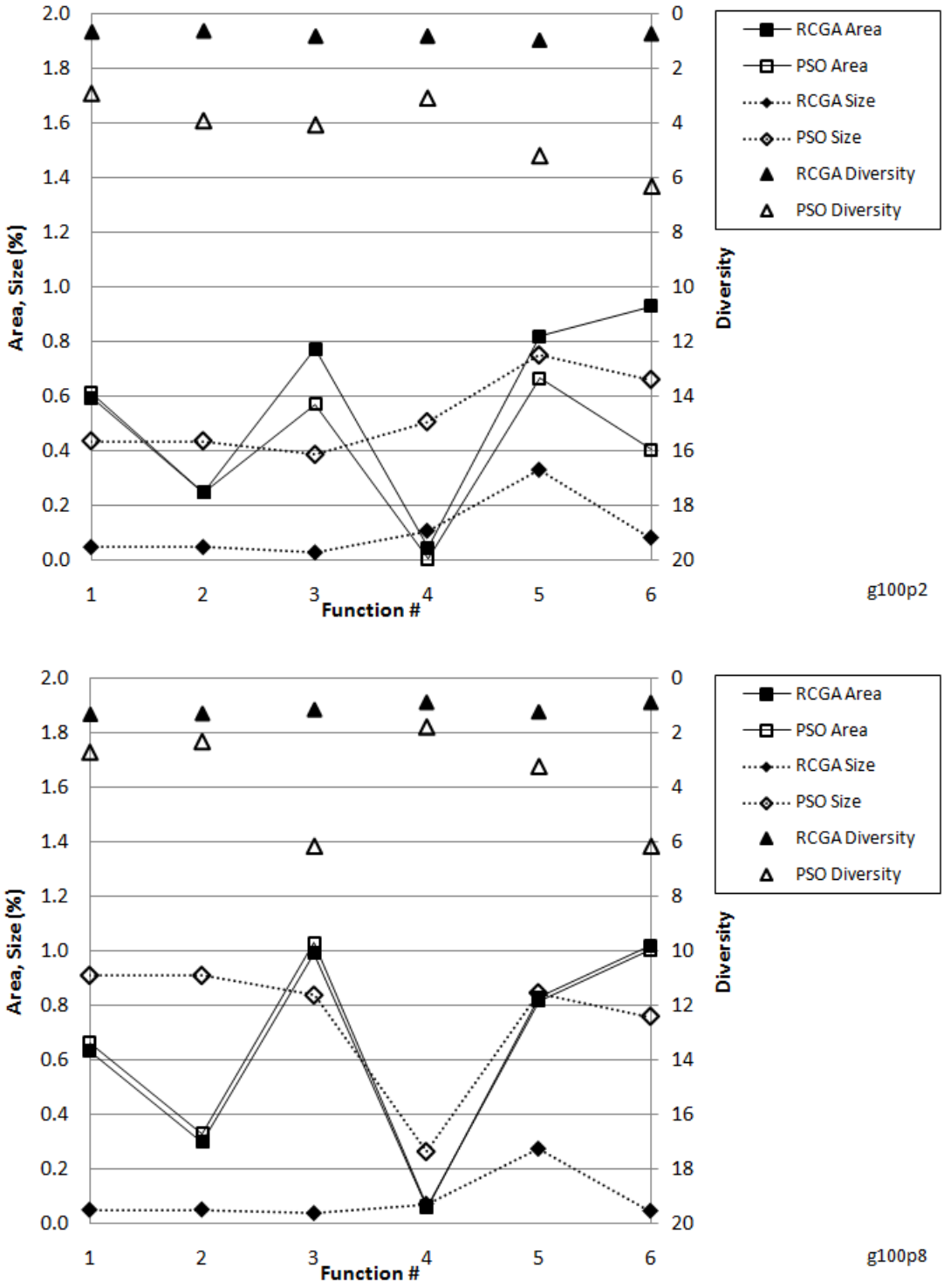


Figure 7-9 Comparison of evaluation results for larger maximum generation cases (100): (Top) population size=2, (Bottom) population size=8

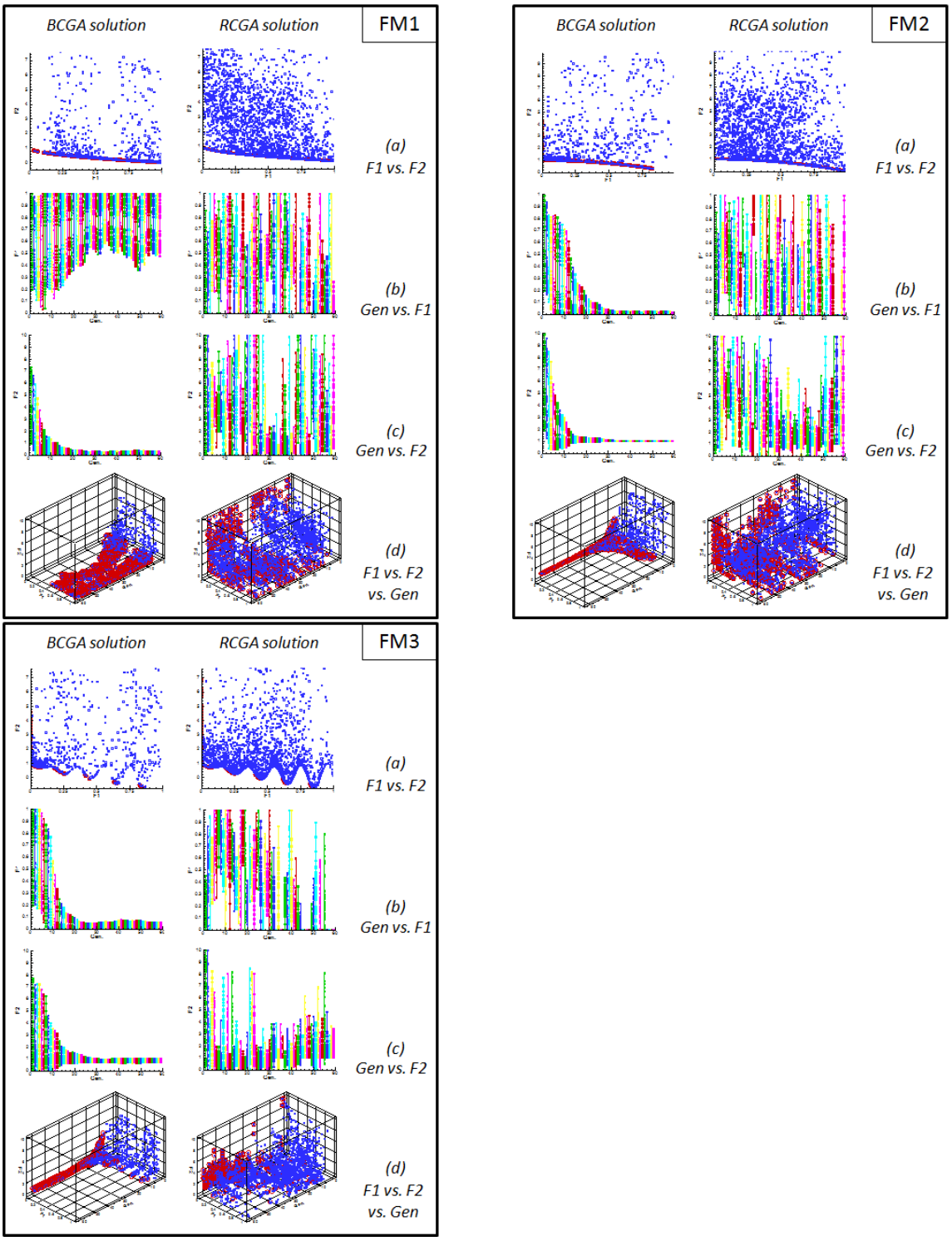


Figure 7-10 Comparison of solution distributions obtained from BCGA and RCGA for three multi-objective optimization problems, FM1-FM3: (Each box contains) (a) $F_1$ vs. $F_2$, (b) generation vs. $F_1$, (c) generation vs. $F_2$, (d) 3-Dimensional distribution

# CHAPTER 8
# GEOMERY AND GRID MANIPULATION

## 8.1 Geometry modeling method for hydrodynamic design optimization

In the design optimization spiral, new designs are created automatically based on initial design(s) using some parameters. The selection of the shape parameterization technique has major impact on the implementation of the optimization and on its flexibility. In other words, the design space is limited depending on the shape modification method; besides, it is not always true that the design space should be as big as possible especially when the considered problem has constraint conditions. Therefore, the technique of shape parameterization has to be developed carefully with consideration of the problem types. Furthermore, the design surfaces are perturbed and one has to face the problem of transferring these perturbations to the computational grid during the design optimization process. The importance of both elements on the overall performances of the SBD is gradually recognized in the literature; for instance, different techniques for geometry and grid deformation are reported in a review by Samareh, (2005).

An efficient and flexible approach to modify (deform) the geometry of the body is necessary for full investigation of the design space and successful optimization. Techniques should be enough versatile to describe a broad variety of complex 3D configurations and sufficiently compact so that it can be used as few variables as possible in the optimization loop. Among the large number of methods available in principle to generate and modify a hull form, historically, ship designers are interested in systematic variations of some general global parameter. The major benefit of this classical parametric modification approach is that the original ship geometry can be easily

deformed by direct selection of a limited number of design parameters. As a consequence, useful information about the effect of the modification in the parameters are immediately obtained, and easily visualized. At the same time, these parameters can be considered as design variables in the formulation of an optimization problem. These parameters are then varied systematically one by one, keeping constant all the others, and the ship performances are eventually evaluated with some easy tool to extract design sensitivities. Furthermore, surface smoothness is guaranteed because the modified geometry is constricted by modification functions. The main disadvantage of this type of approach is that it is not fully flexible and it allows us to obtain the modified geometry according to the defined parametric modification functions.

In the present research, two different parameterization approaches are introduced; i.e., CAD-based approach and CAD-free approach. Both hull form modification method and FFD have been demonstrated in the earlier work (for instance, see Campana *et al.*, 2006a, and Tahara *et al.*, 2008c). The CAD-based modification scheme described below is directly applied to the surface grid points. The main strategy is twofold (Figure. 8-1); e.g.,

- Type-A: Direct movement of hull surface points in particular direction
- Type-B: Hull form blending by using several basic hull designs

On the other hand, Free Form Deformation (FFD) technique is selected as a CAD-free approach. With this approach, the use of CAD or parameterization of the hull surface can be avoided and the deformation of the shape is defined and controlled using a few control points, much fewer than the number of nodes used for the discretization adopted in the flow analysis. Surface movement through the optimization loop is enforced in an explicit and simple way (Sederberg and Parry, 1986). In the following sections, the mathematical model will be given in more detail and basic strategies will be illustrated.

## 8.2 Direct expansion and reduction method using Spline function

Type-A method is direct movement of hull surface points in particular direction which also can be used by combining in multiple directions. Type-A modification is performed by using modification function to reduce number of design variables, to decrease computational load, and in practice, to ensure continuous surface gradients and curvatures at the boundary of modification region. Basic strategy of this type of hull form modification method is shown in Figure 8-1(a). In the present study, six design parameters are assigned to particular region where modification is performed. Three parameters control the locations of surface movement, and the other three do the amount of movements.

As shown in Figure 8-2, a Cartesian coordinate system is used with the origin on the water-plane, $X$ and $Y$ axes on the horizontal plane, and $Z$ axis directed vertically upward, where $X = 0.0$ and $X = 1.0$ corresponds to $AP$ and $FP$ of the hull, respectively. Hence, for example, transverse modifications are defined as follows;

$$Y(X,Z) = Y_0(X,Z) \cdot B(X,Z) \tag{8.1}$$

where $Y_0(X,Z)$ is the original hull surface defined by the longitudinal and vertical coordinates. In this form, depthwise modification of a flat bottom is not considered. $B(X,Z)$ is the modification function, which provides transverse directional expansion and a reduction ratio for a modification region in the range of $X_1 \le X \le X_2$ and $Z_1 \le Z \le Z_2$ given by;

$$B(X,Z) = \{1 - B_1(Z) \cdot sin(\pi a^3 b^3)\} \tag{8.2}$$

$$\begin{cases} a = \left(X^{B_2(Z)} - {X_1}^{B_2(Z)}\right) / \left({X_2}^{B_2(Z)} - {X_1}^{B_2(Z)}\right) \\ b = \left(X^{B_2(Z)} - {X_2}^{B_2(Z)}\right) / \left({X_2}^{B_2(Z)} - {X_1}^{B_2(Z)}\right) \end{cases} \tag{8.3}$$

$$\begin{cases} B_1(Z) = f_1(Z)\,\beta_1 + f_2(Z)\,\beta_2 + \cdots + f_m(Z)\,\beta_m \\ B_2(Z) = f_{m+1}(Z)\,\beta_{m+1} + f_{m+2}(Z)\,\beta_{m+2} + \cdots + f_n(Z)\,\beta_n \end{cases} \tag{8.4}$$

where $B_1(Z)$ and $B_2(Z)$ are depthwise and longitudinal modification functions, $\beta_1,\ \beta_2,\ \ldots,\ \beta_m,\ \ldots,\ \beta_n$ are the design parameters, and $f_1,\ f_2,\ \ldots,\ f_m,\ \ldots,\ f_n$ are the Spline interpolation functions. $B_1(Z)$ and $B_2(Z)$ are defined in the $Z$ coordinate and satisfy the following end conditions;

$$\frac{\partial B_1}{\partial Z} = \frac{\partial B_2}{\partial Z} = 0 \quad at \quad Z = Z_1 \; and \; Z_2 \tag{8.5}$$

The above modification function has continuity in the first and second-longitudinal derivatives at the boundary of definition, and the two independent 1-D functions, defined in the vertical coordinate $Z$, that is $B_1(Z)$ and $B_2(Z)$ are capable of proving continuous transverse-directional expansion and reduction ratio varying in the $X-Z$ plane. Note that $\beta_1 \sim \beta_3$ control cross-sectional modifications and $\beta_4 \sim \beta_6$ do longitudinal modifications. The present function can easily be applied to vertical hull modification by replacing $Z$ with $Y$.

This type of modification method is mainly used in the sensitivity analysis stage in the present study. Since this type of change probably affects the undesirable modification when the geometrical constraints are considered, it is difficult to apply this modification directly to the optimization process using machine-learning algorithm. One of the brief procedures of Type-A method is described in Figure 8-3. Note that there are various ways of setting up the modification besides this example. Figure 8-3 also describes the modification result using the example method mentioned above. The figure shows one of the results which is obtained from the case for original water-jet inlet duct shape modification (details can be found in next chapter). As an example modified shape shows, modification is successfully made, and the surface curvature is maintained smooth.

## 8.3 Hull form blending method

In the Type-B morphing approach, the deformation is produced starting from a number of prescribed initial hull shapes. As a consequence, we need $P$ designs for the same hull, and we need also a computational grid with the same subdivision. Mapping is adopted between the grid points of the different designs based on the grid topology. If we have a suite of grids, all subdivided into $(N \times M)$ intervals, we can pick up the generic $(i, j)$ point on the grid, thus defining;

$$\vec{P}(i,j) = \omega_1 \vec{P}_1(i,j) + \omega_2 \vec{P}_2(i,j) + \cdots + \omega_n \vec{P}_n(i,j) \tag{8.6}$$

plus the condition;

$$\sum_{i=1}^{n} \omega_i = 1 \tag{8.7}$$

Here, $\vec{P}_k(i,j)$ represents the vector of coordinates of the generic point with grid coordinates$(i,j)$ belonging to the $k$-th grid. This approach produces a linear blending among the available geometries. This obviously limits the possible shapes, implicitly defined by the initial designs provided.

Type-B has been used in author's project group; for instance (Tahara, *et al*., 2007), where advantages of the scheme are found that the simple operation is able to yield variety of modified hull forms to large extent, and successfully avoid unrealistic modification which often causes CFD breakdown. In the past research, same number of design variables was used as the number of initial designs, e.g., three parameters handle three-hull-form blending. However, number of design parameters can be reduced using mathematical technique (shown below), e.g., two parameters can handle three-hull-form blending.

$$\vec{P} = a_1\vec{P}_1 + a_2\vec{P}_2 + a_3\vec{P}_3 \tag{8.8}$$

$$with \begin{cases} a_1 = \alpha \\ a_2 = (1-\alpha)\cdot\beta \\ a_3 = (1-\alpha)\cdot(1-\beta) \end{cases} so\ that\ \ a_1 + a_2 + a_3 = 1$$

where $\vec{P}_1$ through $\vec{P}_3$ are hull surface points for three initial designs, and $\alpha$ and $\beta$ are design variables. Here, constraint conditions for these variables must be taken in account as $0 \leq \alpha \leq 1$ and $0 \leq \beta \leq 1$ in order to satisfy the $a_1 + a_2 + a_3 = 1$ condition.

Type-B modification method is used in optimization stage with machine-learning algorithm such as Particle Swarm Optimization. If the initial designs are set as same geometrical characteristics, such as displacement or overall length of the ship, the modified geometries always have same geometrical characteristic as initial designs. This is the important advantage of using this Type-B method in optimization process because there are usually geometrical constraint conditions in practical engineering optimization problems.

## 8.4 Free Form Deformation (FFD)

Free Form Deformation (FFD) technique is also considered as geometry modeling scheme. This technique is originally proposed in computer graphics for morphing images and deforming models (Sederberg and Parry, 1986) to deform the solid geometric models in a free-form manner. It is now widely known that FFD is a powerful high-level approach; a few control points are able to alter the shape significantly. This technique has the great advantage of the independence by the mesh structure defining the deforming object, since it acts on a volume. Its drawback is that the link between the FFD design variables and the “classical” global parameter of the ship is often unclear and the ship designer may have some difficulties in using the FFD information.

In FFD approach, the geometry (object) to be deformed is virtually embedded into a parallelepiped. The latter is subdivided via coordinate planes and the resulting vertices are the control points of the FFD that can move themselves along the prescribed directions. The control points can be used in many different ways to deform the shape; they can move along one or more directions, or they can be grouped together and forced to have equal movements (or opposite, or in a given proportion). The movement of the vertices induces a deformation on the parallelepiped. Bernstein polynomials of degree 3 are used to produce the changes by using the relation;

$$L(u,v,w) = \sum_{i,j,k=0}^{3} B_i(u)\, B_j(v)\, B_k(w)\, P_{ijk} \tag{8.9}$$

which maps the generic point $P$ of the original space into the deformed space point $L$ ($B$ is the generic Bernstein polynomial of degree 3).

FFD is a block surrounding the object to be deformed. If we have to deform a volume grid, we have to be careful about the external faces of the FFD block to be fixed in order not to produce jumps in the resulting volume grid. Deformation is performed only inside the block, so all the grid points outside the block are not moved; hence, if the boundaries of the FFD block are moved, a discontinuity in the resulting grid is produced. More than one block can be used in combination to idealize the more complicated deformation. For a simple example, the FFD box adopted for the bow of JHSS barehull is illustrated in Figure 8-4. Three slices are assigned to cut the box along the longitudinal axis. The external sections are typically kept fixed in order to maintain the fairness of the surface at the connections, whenever only a part of the geometry has to be modified. On the selected control points (20 in the figure), a limitation is imposed allowing only laterally displacements, i.e., along the y direction only. In this example, all the control points are linked together as a single family (block).

In the present study, FFD is actually combined to the SBD environment as a deformation scheme option; however, it is not used in the present optimization studies. Since the author is more familiar with Spline approach to deform the geometry and for trained users, it is often better to use Spline method over FFD in order to get practical hydrodynamic designs. In contrast, FFD has advantages for non-trained users of Spline approach since FFD can offer easy way to deform geometry and give more geometrical options. Indeed, FFD has been successfully used in the previous research; for instance, see Campana *et al*., (2009c), Peri *et al*., (2009), and Campana *et al*., (2006a).

## 8.5 Volume grid manipulation method

Once the hull surface grid is modified, computational volume grid around the hull should change accordingly with a simple adaptive algorithm. Note that the same grid manipulation method is used in association with above two types of modification methods. During the optimization, the volume grid is updated at every optimization cycle right after the hull form shape is modified. This is accomplished by the use of simple algebraic scheme to increase the computational efficiency and keep the computational quality. In the following, the method is described in detail.

After an initial grid is generated, the geometrical information is computed and stored in the memory as follows;

$$\begin{cases} P = S^1(\xi^1, \xi^2, \xi^3) \\ Q = S^2(\xi^1, \xi^2, \xi^3) \\ R = S^3(\xi^1, \xi^2, \xi^3) \end{cases} \tag{8.10}$$

where $P, Q, R$ are grid clustering and stretching functions defined in the $(\xi^1, \xi^2, \xi^3)$ directions, respectively. More specifically, those are normalized metric of $(\xi^1, \xi^2, \xi^3)$ coordinates, such that $0 \leq S^i \leq 1$, and $S^i = 0$ and $S^i = 1$ for $\xi^i = 1$ and

$\xi^i = \xi^i_{max}$, respectively. The grid points for the original geometry are already defined in computational coordinates, i.e.,

$$\begin{cases} x = x_0(\xi^1, \xi^2, \xi^3) \\ y = y_0(\xi^1, \xi^2, \xi^3) \\ z = z_0(\xi^1, \xi^2, \xi^3) \end{cases} \tag{8.11}$$

and the hull surface is expressed as;

$$\begin{cases} x = x_0(\xi^1, 1, \xi^3) \\ y = y_0(\xi^1, 1, \xi^3) \\ z = z_0(\xi^1, 1, \xi^3) \end{cases} \quad \text{or} \quad \begin{cases} x = x_m(\xi^1, 1, \xi^3) \\ y = y_m(\xi^1, 1, \xi^3) \\ z = z_m(\xi^1, 1, \xi^3) \end{cases} \tag{8.12}$$

where $\xi^2$ is taken to be normal direction to the surface, and values with subscript 0 and $m$ correspond to the original and modified hull surfaces. The grid points at the outer boundary is fixed and given by;

$$\begin{cases} x = x_0(\xi^1, \xi^2_{max}, \xi^3) \\ y = y_0(\xi^1, \xi^2_{max}, \xi^3) \\ z = z_0(\xi^1, \xi^2_{max}, \xi^3) \end{cases} \tag{8.13}$$

In the optimization process, the hull surface is modified but other computational boundaries. In the past work, Tahara *et al*., (2004), all grid points are relocated using $P, Q, and\ R$ when the surface is modified, and an iterative manner is used to complete the procedure. On the other hand, simpler grid relocation method can be applied of the modification is assumed to occur in local scale. That is, the method is based on only $Q$ and simply written as;

$$\begin{cases} x = x_0(\xi^1, \xi^2, \xi^3) + \left(x_m(\xi^1, 1, \xi^3) - x_0(\xi^1, 1, \xi^3)\right) \cdot \left(1 - S^2(\xi^1, \xi^2, \xi^3)\right) \\ y = y_0(\xi^1, \xi^2, \xi^3) + \left(y_m(\xi^1, 1, \xi^3) - y_0(\xi^1, 1, \xi^3)\right) \cdot \left(1 - S^2(\xi^1, \xi^2, \xi^3)\right) \\ z = z_0(\xi^1, \xi^2, \xi^3) + \left(z_m(\xi^1, 1, \xi^3) - z_0(\xi^1, 1, \xi^3)\right) \cdot \left(1 - S^2(\xi^1, \xi^2, \xi^3)\right) \end{cases} \tag{8.14}$$

Although the method is relatively simple and straightforward, it was found that it is able to keep the grid quality nearly equal to the original one. The simple expression of this method is shown in Figure 8-5.

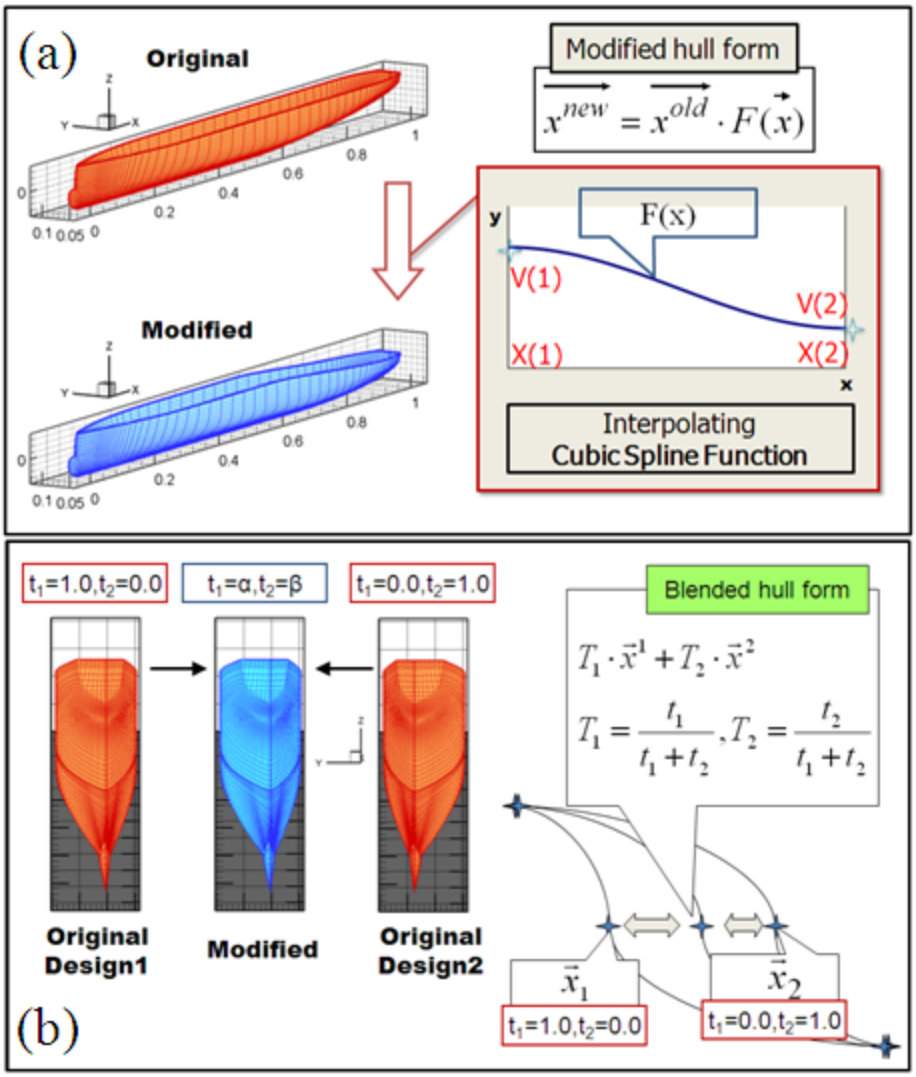


Figure 8-1 Basic Strategy of CAD-based hull modification method:
(a) Type-A: Direct expansion and reduction method,
(b) Type-B: Hull form blending method

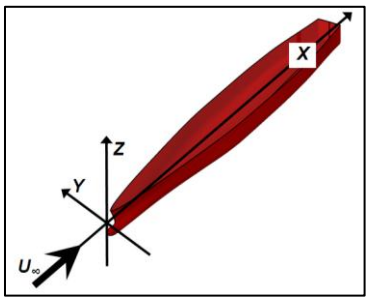


Figure 8-2 Definition of coordinate system for CAD-based hull modification method

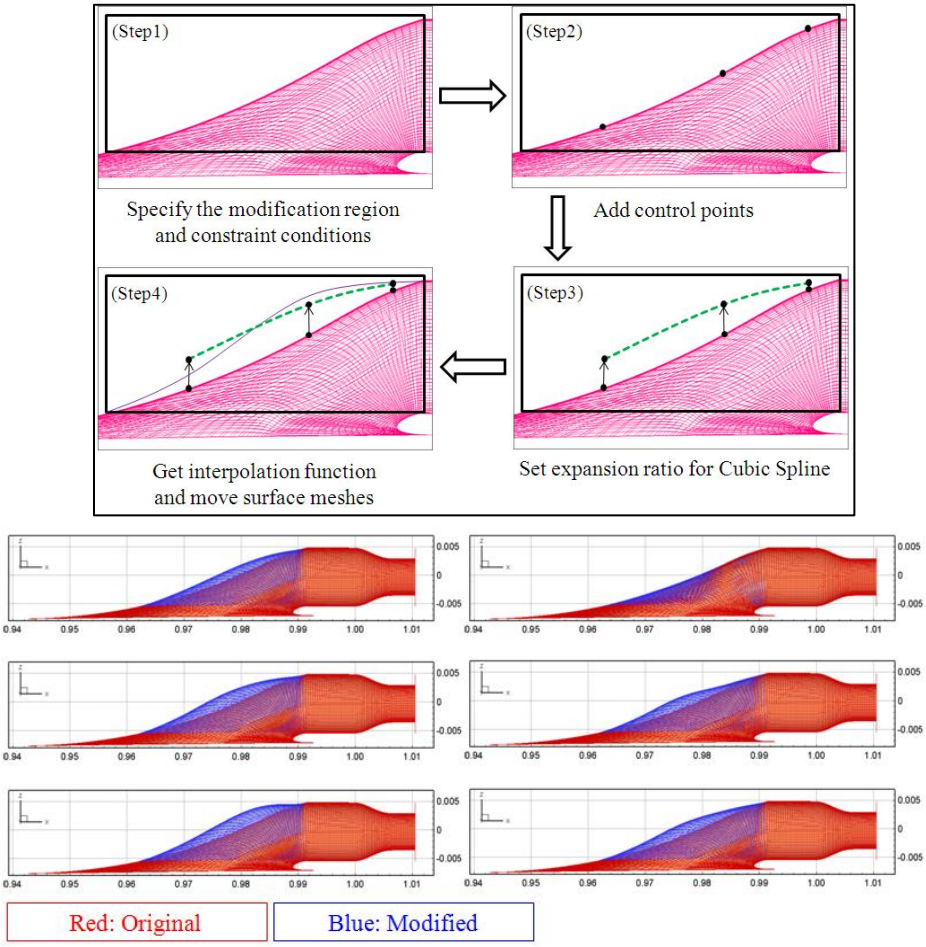


Figure 8-3 Procedure of Type-A where control points are represented by dot symbols: (Top) applied to original waterjet duct, (Bottom) examples of modified shape

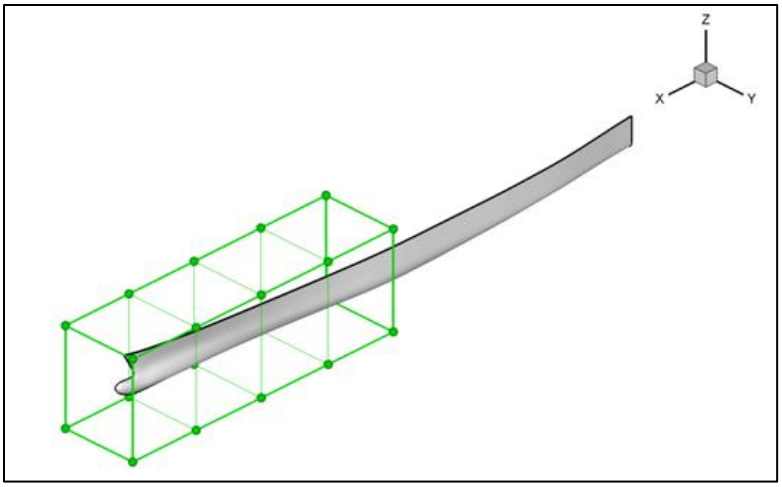


Figure 8-4 Perspective view of FFD parameterization box applied to JHSS barehull fore-body shown with control points (dot symbols)

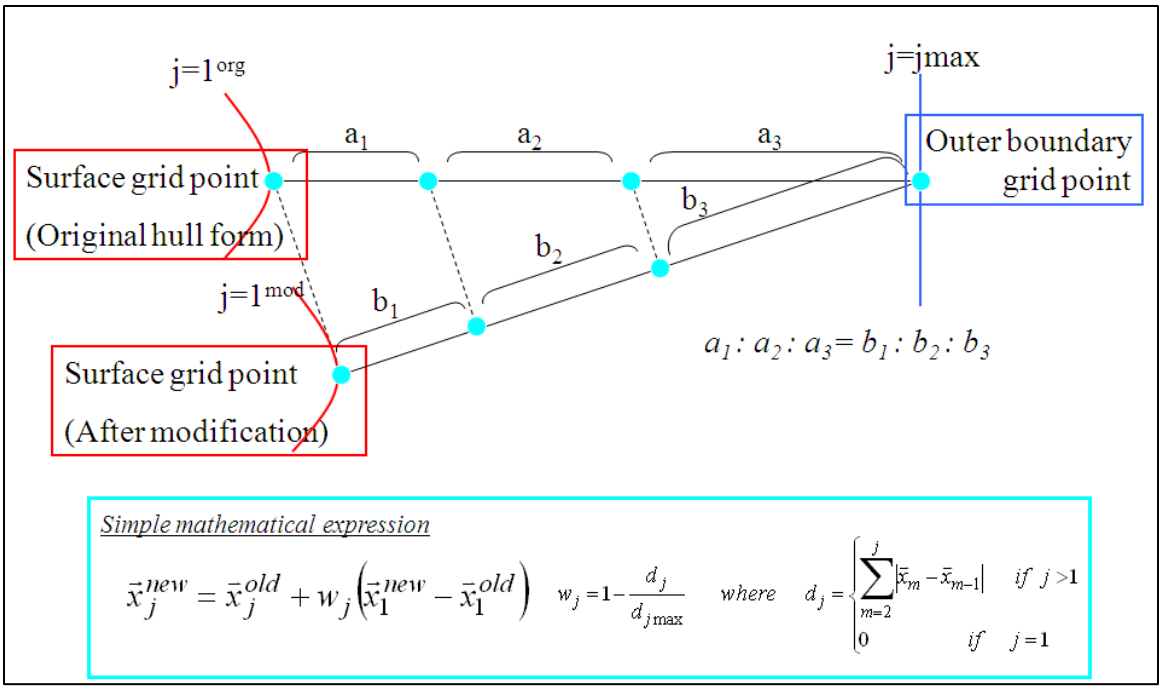


Figure 8-5 Relocation method of volume grid after modification of surface grids

# CHAPTER 9
# DESIGN OPTIMIZATION PROBLEM

## 9.1 Integration of components: SBD environment

The previous chapters described the SBD components such as URANS flow solver, potential BEM solver, non-linear global optimization algorithm, and geometry manipulation method. Those components are integrated to yield four SBD environments, i.e., SBD-A, SBD-B, SBD-C, and SBD-D system. In the following, these approaches are summarized in association with additional information regarding the environment.

***SBD-A system***

In the present version of SBD-A, PSO (Particle Swarm Optimization) in the single objective version, the CAD-based and grid manipulation method (Type-B: blending morphing scheme), and high-fidelity URANS solver CFDSHIP Iowa V.4 compose the SBD-A. The computations are performed on NAVO IBM P6, *DaVinci* (IBM Power6 4.7GHz).

***SBD-B system***

SBD-B is used for comparison of the single-objective optimization problem, and it is composed by PSO in the single objective version, the CAD-based and grid manipulation method (modified Type-B), and low-fidelity potential flow solver WARP. Since the potential solver WARP is selected as a flow solver, only panel information (not 3D numerical grid) is needed. Panel includes surface mesh and free-surface mesh. Hence, the Type-B method is modified to be able to handle the panel blending. The computations are performed on IIHR LINUX machine, *Rex* (SGI Altix 450).

***SBD-C system***

SBD-C is similar system as SBD-B; the optimizer PSO is replaced by RCGA. Thus, the system is composed by RCGA (Real-Coded Genetic Algorithm) in the single

objective version, modified Type-B geometry modeling scheme, and low-fidelity potential flow solver WARP. The computation is also conducted on *Rex*. Since the potential flow solver is selected as CFD scheme, the speed until getting converged solutions is the faster using SBD-B and C systems; hence, it is good practice to evaluate the system capability.

***SBD-D system***

SBD-D is developed for testing multi-objective problem, and it is composed by RCGA as a global optimization scheme, the CAD-based and grid manipulation method (Type-B), and high-fidelity URANS flow solver CFDSHIP-IOWA V.4 for resistance computation. The integrated system also involves the ship motion program (SMP), INSEAN FreDOM code, based on a strip theory approach (for an outline of the approach, see for instance, Newman, 1977, Nakos, *et al.*, 1990) to evaluate the response amplitude operators. The computations are performed at NMRI as a part of international collaboration project and the results are provided.

As seen in the system description above, Type-B method (blending morphing scheme) is employed as the geometry and grid manipulation method for all the systems. Advantages of the function-based hull form modification approach are: (i) to reduce the number of design variables, (ii) to decrease computational load, and (iii) to ensure continuous surface gradients and curvatures at the boundary of modification region. On the other hand, Type-A method (direct expansion and reduction scheme) allows us to make more flexible change in geometry as described in Chapter 8. However, there is no guarantee that the geometrical constraints are satisfied using this type of method; in contrast, those constraints must be satisfied using Type-B method as long as the initial (input) geometries are assured to satisfy the conditions. This is another reason why Type-B method is employed to SBD systems.

## 9.2 JHSS barehull bow shape optimization with single-objective function

First optimization study case (OPT1) is carried out for JHSS barehull bow shape design with single-objective function for improving the powering performance at the design speed. As follows, the optimization condition including objective function and constraints, the results of sensitivity analysis, and the optimization solution are presented.

### 9.2.1 Objective function and constraint conditions (OPT1)

OPT 1 is set to a relatively simple single-objective function problem. The difficulty comes from the flow complexity and the consideration of free-surface and dynamic motions in running condition as well as the complex 3D geometry such as unique bow shape and transom stern. As performed in previous work (e.g., Tahara *et al.*, 2008a), the main objective of the present study is system development and demonstration of the capability, which justifies the use of relatively simple constraints and conditions. The optimization problem for OPT1 is defined as in Table 9-1. The table includes objective function to be minimized, geometrical constraints to satisfy the requirements, variable constraints for optimization scheme, and modification region constraints to maintain the numerical grid quality.

The objective function to be minimized is the total resistance ($R_t$), which is directly computed by URANS code. Geometrical constant constraints are imposed for length perpendicular ($L_{pp}$), maximum beam (B), and total displacement ($\Delta$). Draft ($d$) is not subjected, and it is automatically adjusted in running to satisfy the displacement constraint condition. In the optimization loop, dynamic sinkage and trim in the running condition is predicted. Modification region is another constraint to maintain the numerical grid quality. The quality is investigated by examining the expansion/size ratio

(ER), aspect ratio (AR), skewness (Q), and Jacobians; i.e., the high-quality numerical grid is assured if the criteria of these are satisfied. The criteria for a high-quality grid is 0.3<ER<1.0, AR<20,000, 0<Q<0.9, and Jacobians>0. Aspect ratio is generally not limited because very large AR occurs within the boundary layers; however, too large aspect ratio may cause unphysical calculations within those cells and should be avoided. In consequence, modification region is imposed by $-0.025 \leq x/L \leq 0.05$, $0 \leq y/L \leq 0.01$, and $-0.0285 \leq z/L \leq 0.015$ and corresponding figure is presented in Figure 9-1.

### 9.2.2 Sensitivity analysis for JHSS barehull bow shape design

Simulation Based Design (SBD) for complex systems is an emerging tool to improve time-intensive industrial design which combines complex simulation codes and algorithms for numerical optimization. In particular, the fluid-dynamic design of marine is considered in the present study. For that particular aim, the shape plays a key role and its detailed analysis often requires the solution of nonlinear partial differential equations (PDE), namely the Navier-Stokes equations, which are particularly expensive from the computational point of view in case of with a realistic three dimensional geometry. The use of numerical codes unable to solve the set of equations in SBD is allowed by the availability of high performance computing platforms. However, the cost of a simulation, i.e., an objective function equation is computational time-consuming. This background leads to use the sensitivity analysis prior to the actual optimization studies. In fact, the sensitivity analysis in the present study can be categorized as one of the CFD based optimization; manual optimization.

Herein, Type A method (Direct expansion and reduction method using Spline function) is used to deform the surface geometry of bow shape. Two approaches are found to be promising to achieve the reduction of objective functions; namely, modifications are focused on bow depth (vertical $z$ direction) and width (horizontal $y$

direction). Figure 9-2 shows the examples of bow shape modification. In this stage of optimization, manually find feasible modified hull forms which decrease the objective function according to the grid quality examination mentioned earlier. Note that Grid 3 (medium: 3.6M) is used to carry out the sensitivity analysis. It is relatively large grid for optimization compared to earlier studies; however, it is important to use higher-quality grid so that the geometrical (parametrical) trend would be captured properly by the sensitivity analysis.

Figure 9-3 shows the solutions from the sensitivity analysis for both depthwise and widthwise modifications. Total resistance, dynamic area, sinkage, and trim are shown in the percentage of the error from the original shape. For the depthwise modification, six different geometries are generated and simulations are carried out using URANS. The number in the figure indicates the amount of modification; thus, for widthwise, 0.2 means 20% expansion of the bow shape; on the other hand, negative values mean reduction of the bow mass. On the other hand, positive percentage means the upward movement for depthwise modification. As shown in Figure 9-3, the results clearly show the variable sensitivity; thus, the modification should be made for downward. The total resistance is reduced by 6.7% from original shape, and it is significant amount of reduction because the shape modification is made only for bow shape (bow is geometrically only 5% of whole JHSS hull). It is noteworthy that with the amount of reduction gets bigger, dynamic motions gets bigger than original design. For widthwise modification, similar trend is obtained; negative percentages get better objective function. It indicates that the modification should be made for reduction of bow mass. As well as the depthwise modification case, with the amount of reduction of total resistance gets bigger, both motions get bigger. Hence, these sensitivity results possibly indicate that reduction of resistance is obtained only because of the change of motions.

In order to investigate the effect of motions, extra simulations are carried out by moving the center of gravity (COG) manually. By changing the location of center of

gravity, ship motions can be artificially changed. Table 9-2 summarizes the CFD solutions from five cases. When the COG moves forward to the bow by 1.0% from original location, the sinkage increases 11%O (where O indicates solution on original); moves backward to the stern by 1%, the sinkage decreases 10%O. CFD trim shows more sensitive results in changing the COG location than sinkage, and 1% forward COG shows increase of 71% in trim. Sensitivity analysis shows increases of motion indicate reduction of resistance, and the same trend is obtained in these extra simulations. However, the amounts of resistance reduction by COG effects are much less than ones by the modifications, 1.5%O by COG change and 6.7%O by modifications. On the other hand, the increases of motions by COG effects are much bigger than ones by modifications. This result indicates that the reduction of resistance is achieved not only by motion changes but also geometrical changes through the modification.

In order to explain the gain obtained by modifications, flow fields are analyzed. From the depthwise modifications, also two cases (-0.2 and -0.4 in the Figure 9-3(a)) are selected, and they are called d-2 and d-4, respectively from now on. From the widthwise modifications, two cases (-0.4 and -0.8 in the Figure 9-3(b)) are selected to be analyzed and they are called w-4 and w-8, respectively. The free surface elevations are compared with original JHSS in Figure 9-4 and 9-5. As seen in the figures, the far-field waves are not changed much due to the modification. The magnified figures for hull surface pressure and bow wave are shown in Figure 9-6 and 9-7, where the differences are clearly observed. Modifications make pressure gradient lower on hull surface near bow for both modification directions; as a result, wave heights above the bow are decreased. This effect can be better seen on the wave profiles as shown in Figure 9-8 and 9-9. From the sensitivity analysis, two initial blending designs for optimization are selected which are w-8 and d-4 in addition to original design. Figure 9-10 shows buttock lines for all three initial designs and hull surface pressures. From now on, these three initial designs are

called $P_1$ (original design), $P_2$ (widthwise modified design), and $P_3$ (depthwise modified design).

### 9.2.3 Sensitivity results on coarse grid

The present optimization study follows a similar procedure to that used in previous work, i.e., sensitivity analyses are performed on a medium grid (Grid 3), and optimizations are performed using a coarse grid (Grid 4). As shown in previous work (e.g., Tahara *et al.*, 2008c), this approach effectively reduces the computational load of CFD-based optimization using the resource-intensive RANS equation solver, as long as the correct trends are predicted for both grids. Therefore, the coarse grid solution is analyzed and results are shown in this section. Three initial designs obtained previous section are simulated using Grid 4 (coarse) again, and the solutions are compared with the Grid 3 solutions.

Figure 9-11 summarizes the solutions from both grid systems, and includes dynamic area, $R_t \cong C_t \times dynamic\ area$, sinkage, and trim. In the figure, $P_1$, $P_2$, and $P_3$ results with Grid number (hence, #3 or #4) are presented. Data labels are shown by the exact values obtained from CFDSHIP-IOWA, and the percentages are shown by $\%O_3$ or $\%O_4$. As seen in the figure, the coarse grid results (#4) follow the same trend with the medium results (#3) even though the quantitatively small changes from original are obtained with Grid #4. For instance, the reduction of total resistance show $6.7\%O_3$ and $4.5\%O_4$ for $P_2$ with Grid 3 and Grid 4, respectively; in contrast, $2.8\%O_3$ and $2.9\%O_4$ for $P_3$ with Grid 3 and Grid 4, respectively. Both grid results show that bigger gain is obtained for $P_2$ than $P_3$ design, and $P_2$ and $P_3$ show less resistance than $P_1$ (original). Other variables show same trend as resistance; thus, the Grid 4 can be used instead of Grid 3 to reduce the computational time in optimization. Figure 9-12 compares the hull surface pressures with free surface on both Grid 3 and 4. Overall, both Grid results have

same trend on hull pressure and free surface for modified ships compared to original design.

### 9.2.4 Optimization solution for OPT1 by low-fidelity approach: SBD-B and SBD-C system

JHSS barehull bow shape optimization is carried out by SBD-B and SBD-C system using Grid 4 with single-objective function. Prior to the optimization study by high-fidelity URANS approach, optimization with low-fidelity potential solver approach is conducted to avoid repeating the expensive computations. The optimization conditions are described in Table 9-1. In this section, the results are presented and discussed. The dependency of population sizes is also investigated; thus, four cases with either PSO or RCGA are performed using different sizes (2, 4, 6, and 8). The numerical meshes around JHSS barehull for WARP solver is shown in Figure 9-13. Two meshes need to be generated; one (900 panels) is for hull surface and the other (1350 panels) is for free surface. The solution topology map obtained by SBD-C system with 8 populations is shown in Figure 9-14. In the figure, x-axis indicates $x_1$ (design variable #1) and y-axis does $x_2$ (design variable #2), and the contour plots are colored by F (objective function). Blue region is lower objective function, and white (pink) is higher. As seen in the figure, solution topology map clearly show the trend; which is lower resistance in left half and higher in right half, beside, lower region tends to gather in upper half and higher in lower half. The optimal design is obtained with $x_1$=0.000, $x_2$=0.853, and the reduction of resistance is 8.167%O with 8 particles case. Thus, the optimal design is almost same design as one of the initial designs, $P_2$. The solution maps by SBD-B and SBD-C system are shown in Figure 9-15 and optimal solutions are summarized in Table 9-3. Eight optimization tests are carried out with different population sizes and global optimization algorithms. As seen in the Figure 9-15, RCGA can search the wide distribution of

topology map; on the other hand, PSO fails to detect the all design spaces especially with smaller population size. All solution maps obtained by SBD-C system have similar trend; however, the ones by SBD-B system have poor similarity. However, the solutions with largest population size show similar trend, which is higher resistance occurs in the lower right half, lower in the upper left half. Additionally, there is not only one peak (minima) in the design space as observed in Figure 9-15. The solutions with smaller population size seem to get trapped in local minima. On the other hand, RCGA works quite well since the algorithm has more random search characteristic. The solutions with largest population size are compared in Figure 9-16. Besides of solution maps, the generation histories of design variables are presented. As seen in the figure, PSO shows significantly faster convergence on $x_1$; however, the several locations are detected on $x_2$. It turns out that the detected locations have almost same objective values even though the geometrical characteristics are different. It is assumed due to fidelity of potential solver. The solution from SBD-C system, hence RCGA, show more random distribution on all generations as seen in the comparison study (Chapter 7). This randomness character helps to find the wider solution maps.

### 9.2.5 Optimization solution for OPT1 by high-fidelity approach: SBD-A system

Subsequently, JHSS barehull bow shape optimization is carried out also by SBD-A, which is integrated with high-fidelity URANS solver. The optimization condition, i.e., objective function and constraint condition, is same as described in Table 9-1 and initial designs are also same as previous case; namely, $P_1$ (original design), $P_2$ (widthwise modified design), and $P_3$ (depthwise modified design). The computation is carried out on NAVO IBM P6, *DaVinci* (IBM Power6 4.7GHz), and the converged solutions are

obtained with 250k ~ 300k computational time. The population size is set to 4 and 6 according to the previous results by SBD-B system.

The solution topology map and generation history of design variables and objective function are shown in Figure 9-17 and Figure 9-18, respectively. Since the PSO with relatively smaller population size is used for this study, the solution map is not obtained on all design spaces due to lack of data points. Also, as seen in Figure 9-18, the both solutions with different population sizes are converged to one location within 30-35 generations. The optimal solution is obtained with $x_1$=0.025, $x_2$=0.975, and the reduction of resistance is 4.5%O with 8 particles case. The reduction of objective function corresponds 6.7%O on Grid#3 (see Figure 9-11). Eventually, the optimal design is detected almost same design as one of the initial designs, $P_2$. This result is same as the one from previous optimization study. As expected, the optimized hull forms obtained by SBD-A, SBD-B, and SBD-C are not identical, but show many similarities in terms of their general trends. For these results, the important modification trends are same; hence, the modified hull is generated between $P_2$ and $P_3$ ($x_1$=0). Although the blending ratios between two hulls are not identical, three systems tend to search around the location with $x_1$=0.0, $x_2$=1.0 which generates the hull shape of $P_2$.

Overall, single-objective optimization studies for JHSS barehull bow shape design are conducted by several SBD environments in the section. As discussed earlier, both high-fidelity flow solver (HF: URANS) and low-fidelity flow solver (LF: potential) has proven the capability to search the optimal design with global optimization algorithms (PSO or RCGA). In fact, the computational load is quite different between SBD system with HF and with LF solver; and the final results are obtained eventually with similar designs. It is not always true that the final design is similar between both systems. As the present study, design engineers typically have a suite of different tools to evaluate the performance of a ship, ranging from some simple (i.e., low-fidelity) model based on some simplified theory to more complex (i.e., high-fidelity) simulation codes. Complex

physical models provide obviously high quality in the prediction, at the expense of large computational costs. Variable fidelity modeling (VFM) techniques reduce the number of expense HF analysis by taking advantage of cheap LF models. The idea of using computational models of varying fidelity has a long history in engineering design: perform most of the computations with LF model and correct these predictions by using indication coming from a HF model. VFM procedures may be obtained by changing the physics, but also by using different grid density or computational accuracy. Occasional recourse to HF models does not ensure the convergence to HF solutions. The ability of the LF model to guide the optimization process has to be monitored and its quality improved when required, while consistency constraints have to be enforced to ensure global convergence to the original HF solutions.

## 9.3 JHSS barehull bow shape optimization with multi-objective function

Second optimization study case (OPT2) is performed for JHSS barehull bow shape design with multi-objective function for improving the powering performance at the design speed and seakeeping performance. For this optimization case, same initial designs as used in OPT1 are selected for initial designs. As follows, the optimization condition including objective function and constraints, optimization solution, and comparison between original and optimal designs are presented.

### 9.3.1 Objective function and constraint conditions (OPT2)

The problem (OPT 2) presented in this section concerns the multi-objective design optimization of JHSS barehull bow shape. The definition of optimization problem for OPT2 is summarized in Table 9-4. The table includes objective function to be

minimized, geometrical constraints to satisfy the requirements, variable constraints for optimization scheme, and modification region constraints to maintain the numerical grid quality.

Objective functions are set to $F_1$=*Rt (Fn, Rn)* and $F_2$=*Seakeeping Merit Function (SMF)*, involving the RMS vertical acceleration at the bridge. Since the detailed information about the location of bridge is not provided, it is assumed to be located at $x/L = 0.3$ in the present study. Constraint conditions are subjected as follows. Geometrical constant constraints are imposed for length perpendicular ($L_{pp}$), maximum beam (B), and total displacement (Δ). Draft ($d$) is not subjected, and it is automatically adjusted in running to satisfy the displacement constraint condition. In the optimization loop, dynamic sinkage and trim in the running condition is predicted. Modification region is another constraint to maintain the numerical grid quality; however, it is automatically satisfied because the blending scheme is used for the optimization study.

### 9.3.2 Evaluation of initial designs

Since the seakeeping merit function (SMP) is selected as the second objective function, the performance analysis of initial designs is performed using INSEAN FreDOM code prior to optimization study. Figure 9-19 shows the panel arrangement around JHSS barehull for the frequency domain panel method and solutions of response amplitude operators (RAO) for heave, pitch, and $\ddot{z}_B/g$ at bridge for original JHSS ship ($P_1$). In the Figure 9-19 (b), lambda ($\lambda$) indicates the incoming wavelength. Wave number (k) can be calculated by $k = 2\pi/\lambda$. As seen in the figure, RAO shows typical response for the barehull ship; hence, heave motion converges to around 1.0 with the $\lambda/L_{pp}$ gets bigger; on the other hand, pitch motion converges to around 0.0 with the $\lambda/L_{pp}$ gets bigger. The RAO solutions for ship $P_2$, $P_3$ are shown in Figure 9-20 and these results are summarized in Figure 9-21 shown in %O. RAOs for other two ships show similar trend

as the one for original ship, but the maximum amplitude is different. As seen in Figure 9-21, $P_2$ has bigger reduction in resistance but bigger amplitude of motions; on the other hand, $P_3$ has smaller reduction in resistance but smaller amplitude of motions compared to original hull. Thus, $P_2$ is the best design for objective function #1 ($R_T$) and the worst design for objective function #2 (SMP); in contrast, $P_3$ is the best design for objective function #2 (SMP) and not the best design for objective function #1 ($R_T$). These results for both objective functions are really good from the view of optimization.

### 9.3.3 Optimization solution for OPT2 by SBD-D system

The optimization study is performed by SBD-D system; namely, high-fidelity URANS flow solver, RCGA, and blending morphing scheme in order to investigate the capability of the present SBD framework for multi-objective optimization. Figure 9-22 shows the distribution of solutions from the multi-objective optimization with resistance and the seakeeping function as the two objective functions. As abovementioned, the resistance is calculated using CFDSHIP-IOWA, and the seakeeping function is calculated using INSEAN code FreDOM. Unlike the cases for single-objective optimization, main goal of the present multi-objective optimization is to detect Pareto optimal set. As seen in Figure 9-22, all the designs surrounded by a red square form the Pareto optimal set. Indeed, these designs on the Pareto set can be candidates for design tradeoff between $F_1$ and $F_2$; thus, all the designs can be recognized as optimal design. Design constraints are rigorously satisfied, that is one of the advantages to introduce the present blending approach, i.e., if all initial designs satisfy the design constraints, the new design from the blending operation automatically satisfies the constraints. The best design for $F_1$ show 7% reduction in resistance and the other best design for $F_2$ show 4% reduction in seakeeping function. In order to investigate trend in geometry and flow, the final optimized design is set to “ID-204”, which achieves the minimum SMF.

Figure 9-23 shows comparison of buttock line between original ($P_1$) and optimal hull forms. In the figure, red and blue lines correspond to the original and optimal hull, respectively. The overall trend seen in optimal hull is such that bow volume distribution moves downward and bit inward which is not similar trend as ones obtained in single-objective optimization problems. In order to consider the RAO reduction, the shape of $P_3$ design is involved to the optimal design. The comparison of RAO between original and optimal design is shown in Figure 9-24. As seen in the figure, the RAO for both heave and pitch motions are not changed a lot; however, the maximum amount of $\ddot{z}_B/g$ at bridge is reduced. The flow fields of optimal hull design are presented in Figure 9-25 and Figure 9-26. Figure 9-25 shows the comparison of hull surface pressure and free surface elevation near the bow, where the major difference is seen for the wave above the bow, i.e., that for the optimal hull indicates considerably reduced amplitude of wave crest above the bow. In association with the significant change in wave field, the total resistance is reduced about 7%O. Figure 9-26 compares the free surface elevations with different magnifiers. Overall, the change is barely seen; however, the wave change near the bow can be seen as well as Figure 9-25.

Overall, the optimal design is obtained with better performances for both objective functions in the present study; hence, the present optimization shows the capability of developed SBD framework to solve the multi-objective hydrodynamic design optimization problem. Most importantly, the SBD system detects the Pareto optimal set which is the solution set of optimal designs so that designers can select the modified design with own demands.

## 9.4 JHSS waterjet intake duct shape optimization with single-objective function

Third optimization study case (OPT3) is performed for JHSS waterjet intake duct shape design with single-objective function for improving the inlet efficiency which currently shows significant loss. As follows, investigation of optimization expectations, the optimization condition including objective function and constraints, the results of sensitivity analysis, and the optimization solution are presented.

### 9.4.1 Investigation of optimization expectation

Figure 9-27 summarizes relationships between speed and shaft thrust and speed and jet energy obtained from EFD data. As seen in the figure, the curves of speed/thrust relationship and speed/energy relationship have different slopes, and both have higher than 2$^{nd}$ order in gradient. From these relationships, self propelled speed at a given thrust can be used to gauge the ship performance; thus, at 36knots, 1% increase in speed requires 4% increase in shaft thrust, 1% increase in speed corresponds 7% increase in jet energy. Shaft thrust directly indicates the total resistance of the ship; on the other hand, jet energy can be used as measure of inlet efficiency under the assumption of that inlet efficiency is only affected by jet energy (energy at St.6). As mentioned earlier, the objective of the waterjet inlet shape optimization is improvement of inlet efficiency which currently shows significant loss over the speed range. From the Figure 9-34, it is observed that SPP can be used as an objective function in optimization instead of inlet efficiency, and their relationship is 1% change in speed corresponds 7% change in energy at St.6 which indicates that 1% change in speed corresponds 23.5% change in inlet efficiency. Also, 1% change in $R_t$ corresponds 5.89% change in inlet efficiency.

It is found that the self-propulsion simulation is relatively unstable and it is difficult to get fully converged solution (Figure 9-28). In the Figure 9-28, the y-axis

indicates the ship speed on full-scale which is desired to be 36knots. As observed in the figure, the residual histories of ship speeds show big fluctuations although the speed curve seems converged at the fewer flow time. However, the differences can be seen clearly after the other variables satisfy the criterion for convergence, about 18 flow times in this case; hence, the modified geometries in the figure can get higher speed than original geometry. As a result, it is difficult to evaluate the single value in the optimization loop if the SPP is set as an objective function. Hence, it would be preferable that other quantities can be used instead as an objective function. As discussed earlier, relationship between speed and thrust/energy can be obtained by EFD, and it is calculated that 1% change in $R_t$ corresponds 5.89% change in inlet efficiency. Therefore, total resistance can be used as an objective function instead of inlet efficiency under the assumption that inlet efficiency is only affected by jet energy.

### 9.4.2 Objective function and constraint conditions (OPT3)

Finally, the optimization demonstration for JHSS waterjet inlet shape design is performed. The definition of the optimization conditions is described in Table 9-5. The computations are carried out with the towed waterjet condition in order to avoid the complexity of objective function evaluations in optimization loop. Because SPP needs to be used as an objective function for self-propulsion waterjet simulations, it is difficult to evaluate the correct final value from single run since SPP show relatively large fluctuation after the other parameters satisfies convergence criteria (Figure 9-28).

The objective function to be minimized is the total resistance ($R_t$), which is directly computed by URANS code. Geometrical constant constraints on hull are imposed for length perpendicular ($L_{pp}$), maximum beam (B), and total displacement (Δ). Draft ($d$) is not subjected, and it is automatically adjusted in running to satisfy the displacement constraint condition. Additionally, geometrical constant constraints on

waterjet system are imposed for the sizes of the component; pump, blade, nozzle, and inlet size are constant. These waterjet geometry constraints are satisfied by the modification region constraint conditions; this is another advantage to use the CAD-based geometry modeling method over CAD-free modeling method (such as FFD) because it is easy to control the region using CAD-based approach. In the optimization loop, dynamic sinkage and trim in the running condition is predicted.

Since the object considered here is complex three-dimensional waterjet geometry, it is necessary to identify the modification approaches prior to perform the sensitivity analysis. Rhino software is used to perform the investigation of geometrical characteristic; e.g., Gaussian curvature. Rhino is commercial available 3D CAD software, can create, edit, analyze, document, render, animate, and translate Non-Uniform Rational B-Spline (NURBS) curves, surfaces, and solids and polygon meshes. As similar manner of Type A method, control points can be assigned to the box around the geometry (Figure 9-29). Besides of the geometry modeling, analysis mode can be used in Rhino; for instance, Gaussian curvatures are shown in Figure 9-30, where the higher Gaussian curvature occurs on upper curvature and lower ones on lip shape. Figure 9-31 shows the examples of modification on these two locations using control points approach. As seen in Figure 9-31(a), the high Gaussian curvature location is reduced by the modification; however, non-smooth curves are appeared due to the manual modification. Same problems can be observed in Figure 9-31(b) as well. This is one of the reasons why Rhino is not directly used as the geometry modeling scheme in the present study; hence, it is difficult to make it parametrical change and it is almost impossible to keep the curves smooth by manual change. However, the focused locations to be modified are identified.

Modification region is another important constraint to maintain the numerical grid quality and the production requirement such as the constraint for bottom semi-elliptical shape of the inlet. In consequence, two modification regions is imposed; namely, for upper curvature modification by $0.9615 \leq x/L \leq 0.9913$, $0.0005 \leq y/L \leq 0.0285$, and

$-0.0055 \leq z/L \leq 0.005$ and for lip shape modification by $0.9860 \leq x/L \leq 0.9913$, $0.0005 \leq y/L \leq 0.0268$, and $-0.007 \leq z/L \leq 0.0055$, and corresponding figures are presented in Figure 9-32.

### 9.4.3 Sensitivity analysis for JHSS waterjet intake duct design

In order to reduce the computational load, the sensitivity study is performed for waterjet inlet shape design as well as for barehull bow shape design. As mentioned in the previous section, simulations are performed using towed condition in the optimization loop; however, self-propulsion simulation is used for the sensitivity analysis to get more reliable trends of variables. Type A method (Direct expansion and reduction method using Spline function) is used to deform the surface geometry of waterjet inlet. Two approaches are found by Gaussian curvature plot and modification using Rhino; hence, modifications are focused on upper curvature (Type1) and lip shape (Type2). Figure 9-33 illustrates the locations of control point and examples of waterjet intake duct shape modification. Three control points are assigned to the geometry boundaries, and at least one point is imposed to 0, which means the continuity in the first and second-longitudinal derivatives at the boundary of definition at the location (for instance, $r_3$ in Type1). It is necessary treatment in order to keep the geometrical constraint. In this stage of optimization, manually find feasible modified hull forms which decrease the objective function according to the grid quality examination. Note that Grid 2W (medium: 6.55M) is used to carry out the sensitivity analysis. Figure 9-34 summarizes the examples of modified shapes for two directions.

Approximately 30 designs are generated by Type A method for Type 1 (upper curvature) and 15 designs are generated for Type 2 (lip shape). It is found that the modification of waterjet intake duct geometry is really sensitive such that some cases are diverged in the middle of simulations due to the grid quality and flow complexity. Hence,

there is no large modification can be made on the waterjet geometry. Figure 9-35 to 9-37 show the sensitivity analysis results.

In general, the pressure loss in pipes and tubes is divided into major loss due to friction and minor loss due to change of velocity in bends, valves, and such. However, it is common idea that the pressure loss in pipes and tubes depends on the flow velocity, pipe/duct length, pipe/duct diameter, a friction factor based on the roughness of the pipe/duct, and Reynolds number (whether the flow is turbulent, transient, or laminar). In the present study, the pipe-like shape (intake duct) is located only within 5% of the whole hull geometry, and the length of the duct is significantly short compared to the length perpendicular of the hull. Hence, the major loss due to friction becomes similar amount as minor loss as shown in Figure 9-35. The resistance is decomposed into frictional and pressure components, and shown in single-column in the figure. As observed in the figure, both components are almost equally distributed for all the cases which have different waterjet intake shape.

Figure 9-36 shows the solutions of resistance and dynamic area from the sensitivity analysis; total 35 converged solutions including original design are shown with speed (SPP). With same applied thrust, the reached self-propulsion point is different with different waterjet geometry; thus, the speed gain is due to geometrical change. As seen in Figure 9-36(a), the modified designs with increased speed show lower pressure resistance and higher frictional resistance; however, the amount of change is different. The absolute value of slope for reduction of the pressure drag is higher than the one for increase of frictional drag. The changes of frictional drag totally correspond to the changes of dynamic area (Figure 9-36(b)). Since the major loss (friction) and minor loss (pressure etc) are almost same amount in the present case, the bigger reduction of pressure change due to curvature changes contributes the increase of speed with same applied thrust. The change of ship motions are presented in Figure 9-37. Basically, increase trends are obtained for both dynamic sinkage and trim with the speed increases;

however the amounts of changes on motions depend on the modification Type. These motion changes could affect the reduction of objective function. From these better designs, two shapes (tagged with ID#018 and #029 in Figure 9-36(a)) are selected as initial designs for subsequent optimization study. Herein, the initial designs for JHSS waterjet intake duct shape is called $P_{1W}$, $P_{2W}$, and $P_{3W}$ for original, upper curvature modified design, and lip shape modified design, respectively. The shapes of these two modified designs are presented in Figure 9-38 compared with original design.

### 9.4.4 Sensitivity results on coarse grid with towed simulation condition

Sensitivity analyses are performed on a medium grid (Grid 2W), and optimizations are performed using a coarse grid (Grid 3W). This approach effectively reduces the computational load of CFD-based optimization using the resource-intensive RANS equation solver as long as the correct trends are predicted for both grids. Therefore, the coarse grid solution is analyzed and results are shown in this section. Three initial designs obtained previous section are simulated using Grid 3W (coarse) again, and the solutions are compared with the Grid 2W solutions.

Figure 9-39 summarizes the solutions from both grid systems, and the figure includes dynamic area, SPP for self-propelled simulation, $R_t \times 200$ for towed simulations, sinkage, and trim. In the figure, $P_{1W}$ (Original), $P_{2W}$ (upper curvature modification), and $P_{3W}$ (lip shape modification) results are presented. Data is shown by the exact values obtained from CFDSHIP-IOWA, and the percentages are shown by $\%O_{2W}$ or $\%O_{3W}$. As mentioned earlier, all the force coefficients become constant value for self-propelled simulations; thus, self propulsion point (SPP) is used instead for reference value. $R_t$ is shown after it is multiplied by 200 in order to plot on same figure with SPP. SPP for $P_{2W}$ and $P_{3W}$ are increased compared to $P_{1W}$ with same applied thrust. In contrast, $R_t$ for $P_{2W}$ and $P_{3W}$ are decreased compared to $P_{1W}$ with towed conditions.

Although the quantity of reductions is different using two grid systems, same trend is obtained.

### 9.4.5 Optimization solution for OPT3 by SBD-A system

The optimization demonstration is performed by SBD-A system; namely, high-fidelity URANS flow solver, PSO, and blending morphing scheme in order to show the capability of the present SBD framework for complicated waterjet inlet shape optimization. Indeed, the optimization studies have been carried out by a lot of researchers for waterjet duct shape; however, almost all the work are focused on only the duct shape without considering waterjet-hull interaction. The complexity of problem is significantly increased by taking into account the combination of waterjet and hull.

Figure 9-40 shows the initial result obtained by SBD-A system for JHSS waterjet intake duct design optimization. The optimization is carried out with two particles because it turns out that the SBD code has limit on the number of CPU. Besides, waterjet simulations need to use relatively many computational blocks; as a result, maximum particles must be two in the present environment. The plots are colored by F on design variable space ($x_1$ vs. $x_2$) and the rectangular box shows the feasible space. Since the waterjet simulation is really sensitive and takes quite long time to get converged, the restart function is used in the optimization loop. The restart file is obtained from the simulation with original design after 510 iterations; then, the simulation is run with modified geometry for about 100 iterations. Using this approach helps to reduce computational time significantly; however, the iteration history needs to be carefully monitored. It is quite promising approach to reduce the computational load but it is just a temporary approach because the geometry is changed in the middle of simulations; as a result, the strange results are sometimes obtained. For instance in Figure 9-40, the optimal solution (with minimum objective function) is appeared at ($x_1$=0.76, $x_2$=0.08)

and the worst design is occurred at ($x_1$=0.77, $x_2$=0.12). These designs are geometrically quite similar; but the objective function shows relative difference of 7.3%. Therefore, the solutions need to be investigated more; it could be true since the object of this particular optimization demonstration is complicated 3D waterjet geometry and waterjet simulation results always show sensitive residual histories. Figure 9-41 shows the generation history of objective function. As observed in the figure, the solution is getting converged into a particular location. The final optimal design shows 2.7%O reduction in *Rt*; thus, approximately 16%O improvement in inlet efficiency.

## 9.5 Reduction of major loss: manual optimization

In the previous section, the demonstration result for waterjet intake duct design optimization is presented. As shown in the sensitivity analysis, the duct shape optimization is focused on the upper curvature and lip shape; therefore, the effort is put on reduction of minor loss (mainly pressure loss) by changing the curvature effect. In this section, the effort is put on the reduction of major loss and the initial result is presented.

As mentioned earlier, the major loss is due to friction in duct, and surface area directly affects to the frictional drag in duct. Therefore, the problem becomes how to reduce the surface area of intake duct. Since it is difficult to reduce the area from original intake duct design by developed geometry modeling scheme, drastic approach is taken in the present study; namely, merging the inlet together. In a conceptual stage, two starboard waterjets are merged together to yield the new concept inlet design as shown in Figure 9-42. The merged inlet shape is created by manual treatment using Gridgen software. As observed in the figure, the duct surface area is drastically reduced; thus, the frictional resistance in duct is reduced as well. Figure 9-43 shows the comparison of hull surface pressure between merged and original inlet design. As seen in the figure, general trend of pressure distribution is not changed a lot; however, the pressure on lip is occurred lower

for merged inlet and high pressure is appeared on the edge of the center structure between two inward waterjets. The wave field of waterjet merged inlet design is shown in Figure 9-44. Because the location of inward waterjet is moved outward, the distance between inward waterjets between port and starboard side gets bigger. As a result, the shape of jet outflow is different from one with original inlet design. These changes of flow and pressure seen in Figure 9-43 and Figure 9-44 would affect the pressure increase from original design; however, the frictional reduction is more significant. In fact, the merged inlet design shows about 1.5%O increase in speed with self-propulsion simulation condition. This gain corresponds 6%O reduction in *Rt*, and 35%O improvement in inlet efficiency. The gain obtained with the merging modification is promising; however, it is only the conceptual stage and needs to be investigated more carefully.

## 9.6 Summary of design optimization demonstrations

In this chapter, demonstrations of hydrodynamic design optimizations are presented. First, integration of optimization components is described; four different SBD systems are generated by integrating CFD solver, global optimization algorithm, and geometry modeling scheme. Optimization is carried out for both JHSS barehull bow shape and JHSS waterjet intake duct shape design, and the demonstrations are performed for three test cases. JHSS barehull design is selected as an initial design for first two demonstrations and waterjet appended design is selected for last demonstration. Sensitivity analysis is performed to reduce the computational load prior to optimization activity using SBD system. Two promising modified designs are obtained from each sensitivity analysis.

OPT1 is focused on simple problem, single-objective function optimization problem; therefore, the objective function is set to resistance reduction. Three SBD systems are used for OPT1 problem; namely, SBD-A, -B, and -C system. SBD-A system

is consisted of high-fidelity (HF) URANS solver, PSO, and blending scheme; SBD-B is consisted of low-fidelity (LF) BEM solver, PSO, and blending scheme; SBD-C is consisted of LF BEM solver, RCGA, and blending scheme. The population sizes are set to 2, 4, 6, and 8 for LF approach, whereas 4 and 6 are used for HF approach. Overall, optimal ship shows significant amount of reduction of objective function, about 8%O reduction. The solution topology maps are created and compared among solution obtained by three systems. General trend on the map obtained by HF approach is similar as ones obtained by LF approach; however, there are not multiple peaks from HF approach unlike LF approach gives multi-peak on the design space. The final optimal designs obtained from test cases have almost same geometrical characteristics.

The optimization problem is extended to multi-objective problem (OPT2). OPT2 is carried out by SBD-D system, which is consisted of HF URANS solver, RCGA, and blending scheme. Two objective functions to be minimized are considered, i.e., total resistance and seakeeping merit function. Realistic functional and geometrical constraints are enforced for preventing unfeasible results and to get a final meaningful design. First objective function is calculated by CFDSHIP-IOWA (HF URANS approach) and second one is estimated by INSEAN FreDOM solver. FreDOM is based on strip theory approach to evaluate the response amplitude operators (RAO). The amplitude of acceleration on bridge is selected as the second objective function. The goal of optimization is different between single- and multi-objective optimization problems; hence, the purpose of solving multi-objective optimization problems is to detect the Pareto optimal set. As solution distribution shows, Pareto optimal front is detected by developed SBD framework. The best design for each objective function shows 7%O in resistance reduction and 4%O in seakeeping merit function.

Final demonstration (OPT3) is focused on waterjet intake duct shape optimization. SBD-A system is used for OPT3. Realistic functional and geometrical constraints are enforced for preventing unfeasible results and to get a final meaningful

design; besides, the geometrical constraint is strictly imposed for waterjet geometry. The optimization is carried out by different approach from other demonstrations; that is, the final demonstration is performed using restart files which is obtained with original design. Several issues need to be addressed; more deep investigation on modified designs, investigation on residual history if the solutions are enough converged, and so on. In the present demonstration case, the final optimal design show 2.7%O reduction in *Rt*; thus, 16%O improvement in inlet efficiency.

The optimization demonstrations shown above are focused on reduction of minor loss in duct, which is pressure component, using numerical geometry modeling approach. Furthermore, the optimization is demonstrated for major loss which is reduction of friction component in duct by manual design. The merged inlet design is presented as an initial conceptual modification approach.

Overall, the demonstration work is concentrated on two geometries with single-/multi-objective functions; and it has proven the capability of developed SBD framework to the design tool of naval sea-lift.

Table 9-1 Definition of the nonlinear constrained optimization problem with single-objective function for JHSS barehull bow shape design (OPT1)

| Type | Definition | Note |
|---|---|---|
| *Objective function* | *Min. $F_1$= Rt (Fn,Rn)*<br>*Rt≈Ct× Dynamic Area* | *Barehull, free to pitch & heave*<br>*Fn=0.3434(Model scale), Rn=2.783×$10^7$* |
| *Geometrical constraints* | *Lpp, B(max)=constant*<br>*Total displacement=constant* | *Draft is not fixed*<br>*Displacement is automatically fixed in flow solver* |
| *Variable constraints* | *0≤α≤1, 0≤β≤1* | *Both design variables must be from 0 to 1* |
| *Modification region constraints* | *-0.025≤x≤0.05,*<br>*0≤y≤0.08,*<br>*-0.0285≤z≤0.015* | *Controlled by geometry modeling method* |

Table 9-2 Investigation results of motion effects

| Case | COG (x/L) | Sinkage (m) | | Trim (deg) | | Dynamic Area | | Resistance | |
|---|---|---|---|---|---|---|---|---|---|
| 1.0% forward | 0.5177 | -2.032E-03 | +11.00% | -0.3498 | +70.97% | 5.2152E-02 | +0.43% | 1.7844E-04 | -1.51% |
| 0.5% forward | 0.5204 | -1.928E-03 | +5.36% | -0.2755 | +34.65% | 5.2051E-02 | +0.23% | 1.7928E-04 | -1.04% |
| Original | 0.5230 | -1.830E-03 | 0.00% | -0.2046 | 0.00% | 5.1930E-02 | 0.00% | 1.8117E-04 | 0.00% |
| 0.5% backward | 0.5256 | -1.739E-03 | -4.96% | -0.1310 | -35.97% | 5.1821E-02 | -0.21% | 1.8257E-04 | 0.77% |
| 1.0% backward | 0.5282 | -1.654E-03 | -9.62% | -0.05972 | -70.81% | 5.1715E-02 | -0.41% | 1.8398E-04 | 1.55% |

Note: percentages are shown in %ORG

Table 9-3 Optimization solutions for OPT1 by (Left) SBD-B, (Right) SBD-C system

| # Particles | 2 | 4 | 6 | 8 |
|---|---|---|---|---|
| Reduction of resistance (%ORG) | 5.342 | 7.129 | 8.167 | 8.167 |
| Optimal variable location ($x_1$) | 0.000 | 0.000 | 0.000 | 0.000 |
| Optimal variable location ($x_2$) | 0.000 | 0.022 | 0.715 | 0.859 |

| # Population | 2 | 4 | 6 | 8 |
|---|---|---|---|---|
| Reduction of resistance (%ORG) | 8.167 | 8.125 | 7.805 | 8.167 |
| Optimal variable location ($x_1$) | 0.000 | 0.000 | 0.000 | 0.000 |
| Optimal variable location ($x_2$) | 0.853 | 0.645 | 0.598 | 0.853 |

Table 9-4 Definition of the nonlinear constrained optimization problem with multi-objective function for JHSS barehull bow shape design (OPT2)

| Type | Definition | Note |
|---|---|---|
| *Objective function* | *Min. $F_1$=Rt (Fn, Rn)*<br>*Min. $F_2$=Seakeeping Merit Function(SMF)*<br>*Rt≈Ct× Dynamic Area*<br>*SMF:$\frac{\ddot{z}_B}{g}$*<br>*(maximum amplitude of acceleration)* | *Barehull, free to pitch & heave*<br>*Fn=0.3434(Model scale), Rn=2.783×$10^7$*<br>*SMP is evaluated to vertical acceleration at the ship bridge* |
| *Geometrical constraints* | *Lpp, B(max) =constant*<br>*Total displacement = constant* | *Draft is not fixed*<br>*Displacement is automatically fixed in flow solver* |
| *Variable constraints* | *0≤α≤1, 0≤β≤1* | *Both design variables must be from 0 to 1* |
| *Modification region constraints* | *-0.025≤x≤0.05,*<br>*0≤y≤0.08,*<br>*-0.0285≤z≤0.015* | *Controlled by geometry modeling method* |

Table 9-5 Definition of the nonlinear constrained optimization problem with single-objective function for JHSS waterjet inlet shape design (OPT3)

| Type | Definition | Note |
|---|---|---|
| *Objective function* | *Min. $F_1$=Rt (Fn,Rn)*<br>*Rt≈Ct× Dynamic Area* | *Waterjet propelled hull,*<br>*free to pitch & heave*<br>*Fn=0.3434(Model scale), Rn=2.783×$10^7$* |
| *Geometrical constraints*<br>*(Hull & waterjet system)* | *Lpp, B(max) =constant*<br>*Total displacement= constant* | *Draft is not fixed*<br>*Displacement is automatically fixed in flow solver* |
| | *Pump, blade, nozzle, and inlet size =constant* | *Only duct shape can be modified* |
| *Variable constraints* | *0≤α≤1, 0≤β≤1* | *Both design variables must be from 0 to 1* |
| *Modification region constraints for Type 1 (upper curvature)* | *0.9615≤x≤0.9913,*<br>*0.0005≤y≤0.0285,*<br>*-0.0055≤z≤0.005* | *Controlled by geometry modeling method* |
| *Modification region constraints for Type 2 (lip shape)* | *0.9860≤x≤0.9913,*<br>*0.0005≤y≤0.0268,*<br>*-0.007≤z≤-0.0055* | *Controlled by geometry modeling method* |

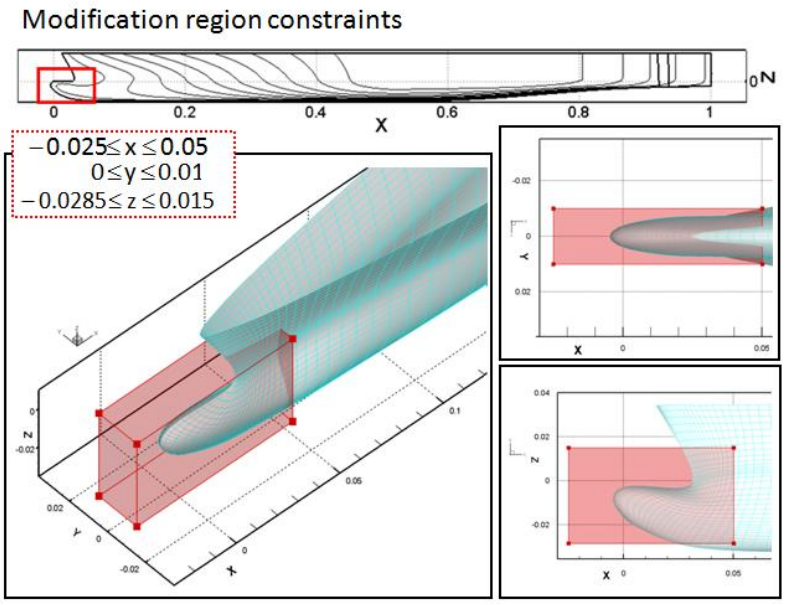


Figure 9-1 Modification region constraint condition for JHSS barehull optimization

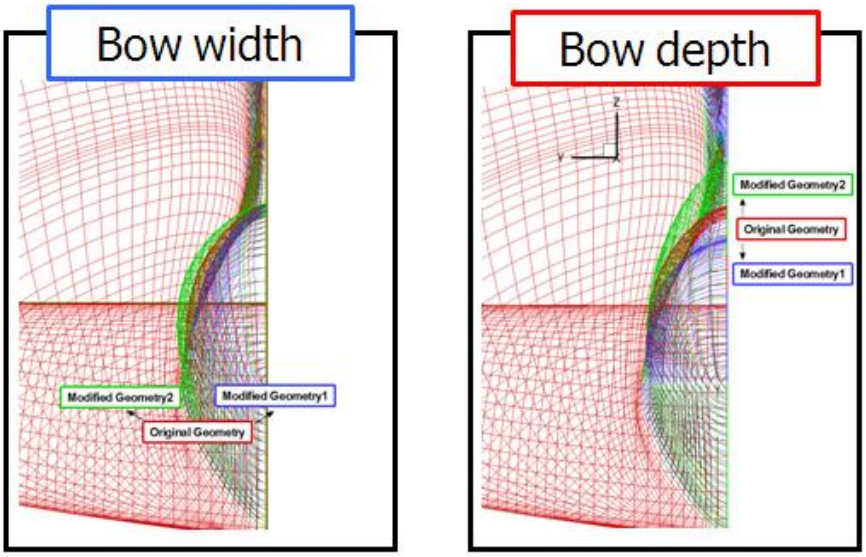


Figure 9-2 Illustrations of modified bow shapes for two directions:
(Left) widthwise, (Right) depthwise direction

(a)

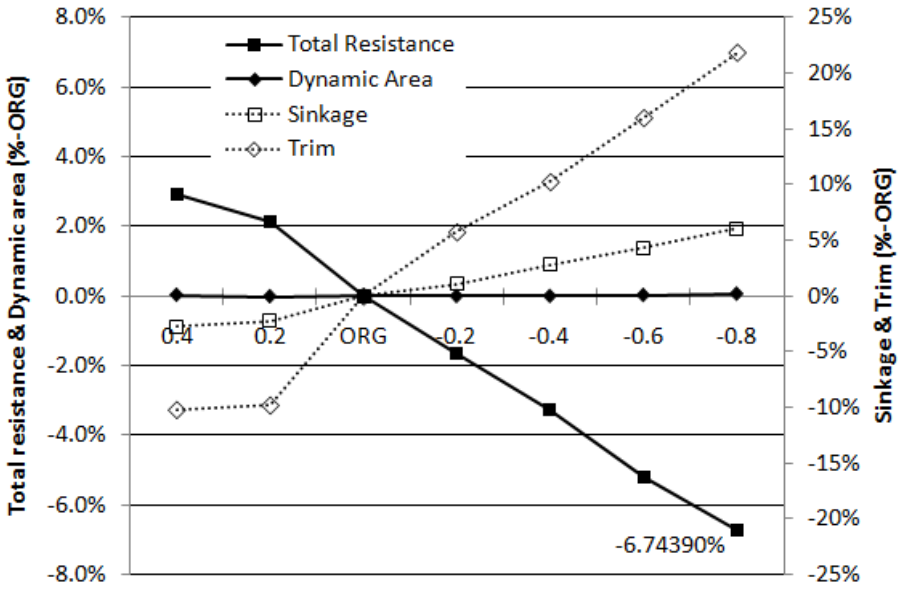


(b)

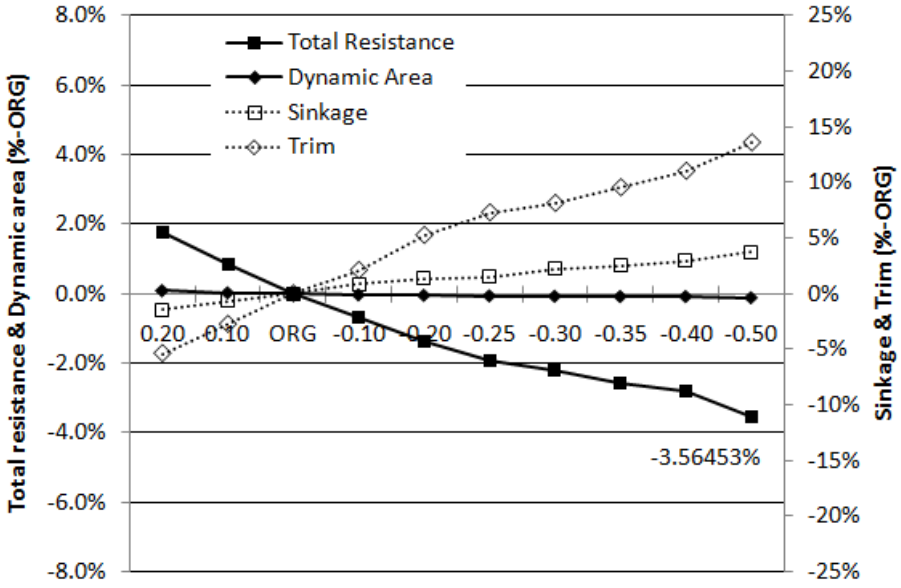


Figure 9-3 Results of force coefficients and motions for sensitivity analysis for JHSS barehull bow shape optimization:
(a) widthwise modification case,
(b) depthwise modification case

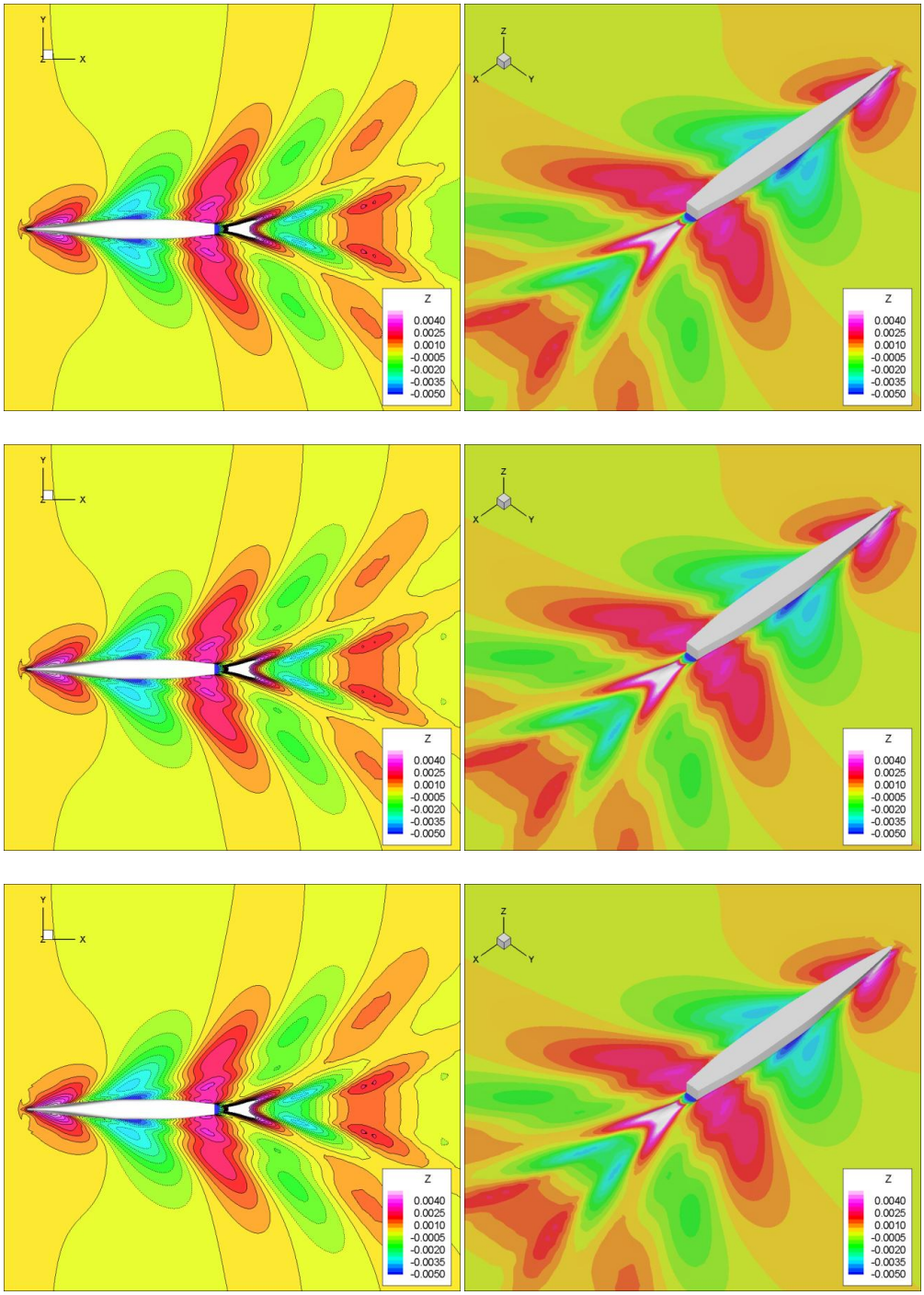


Figure 9-4 Comparison of free surface elevations: (Top) original, (Middle) w-0.4, (Bottom) w-0.8 case

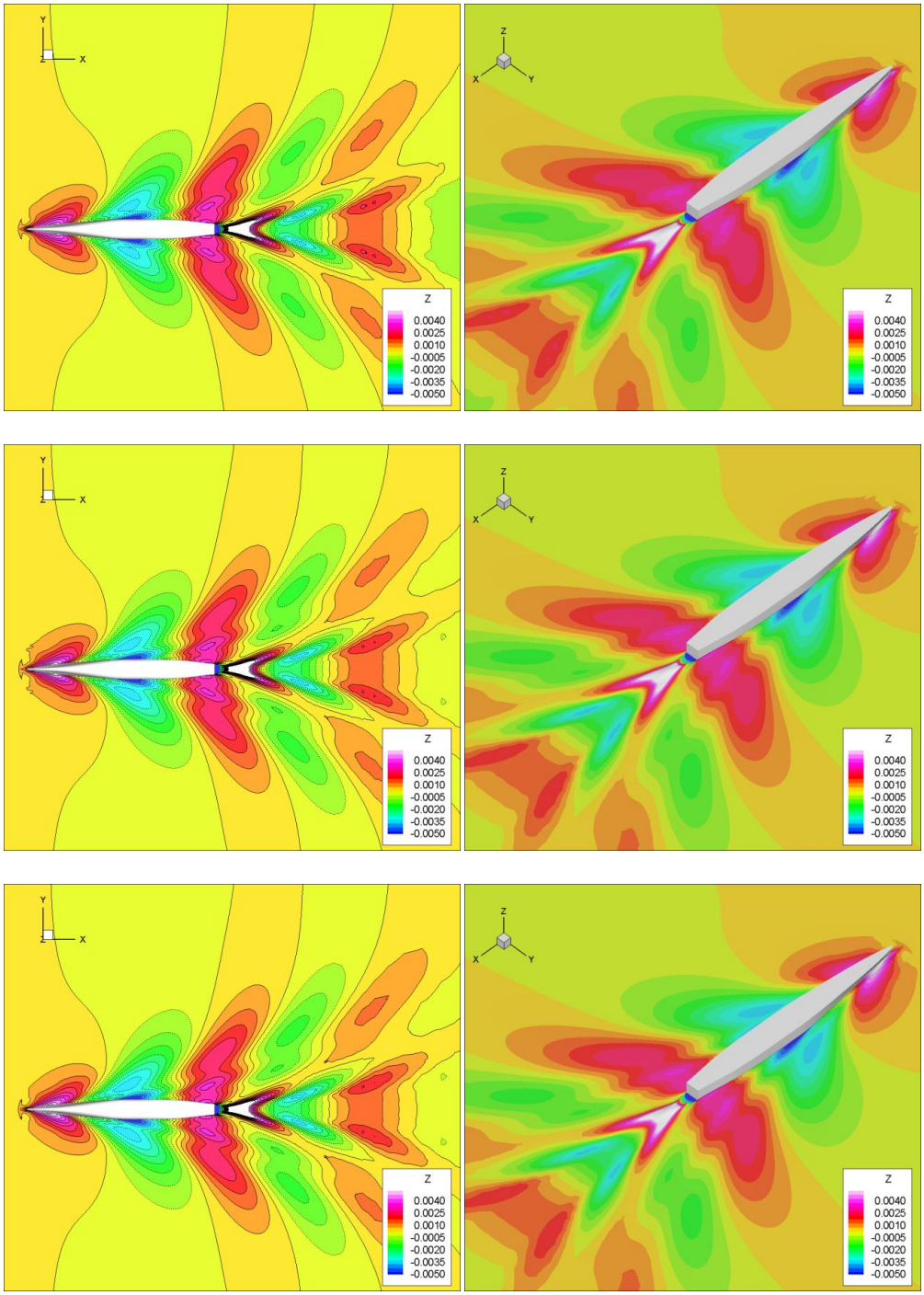


Figure 9-5 Comparison of free surface elevations: (Top) original, (Middle) d-0.2, (Bottom) d-0.4 case

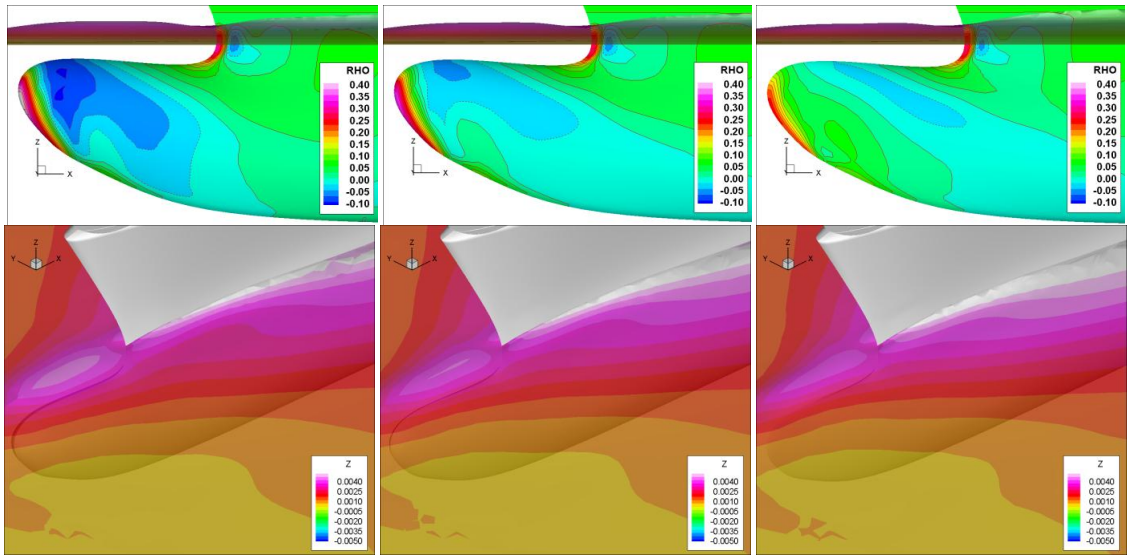


Figure 9-6 Comparison of hull surface pressures and bow waves:
(Left) original, (Center) w-0.4, (Right) w-0.8 case

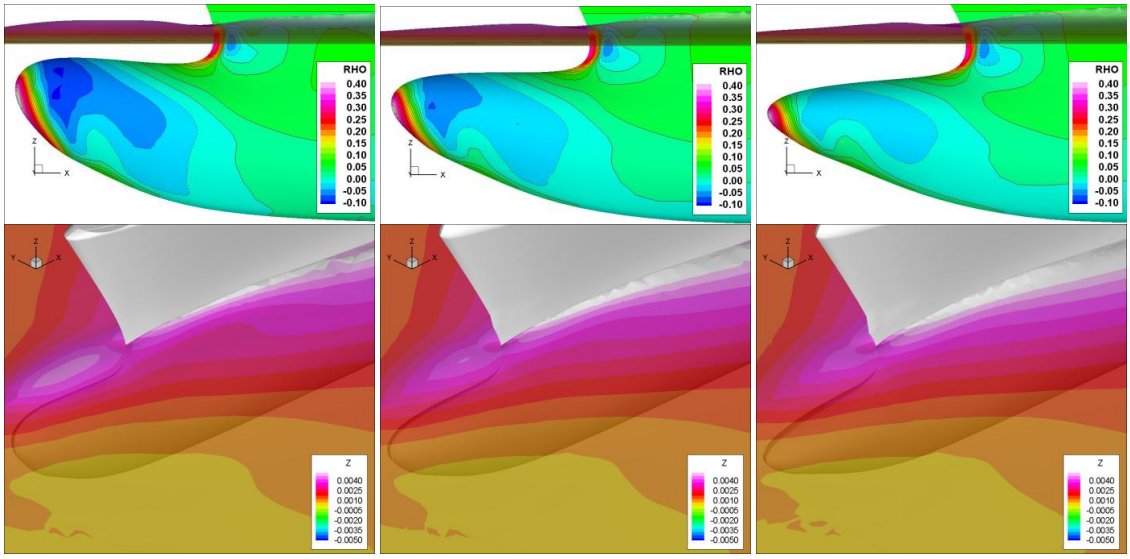


Figure 9-7 Comparison of hull surface pressures and bow waves:
(Left) original, (Center) d-0.2, (Right) d-0.4 case

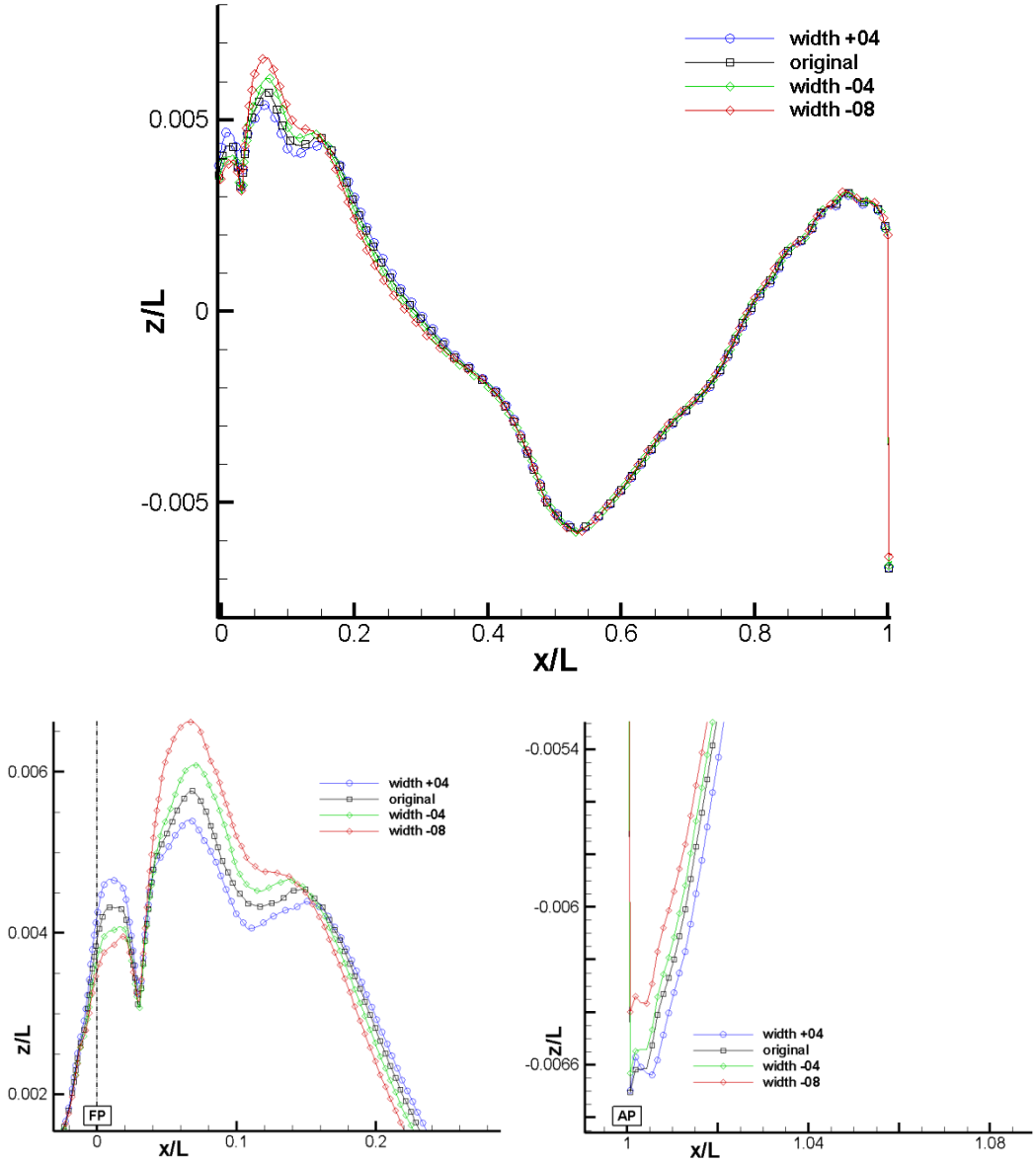


Figure 9-8 Comparison of wave profiles obtained by widthwise modifications compared with original

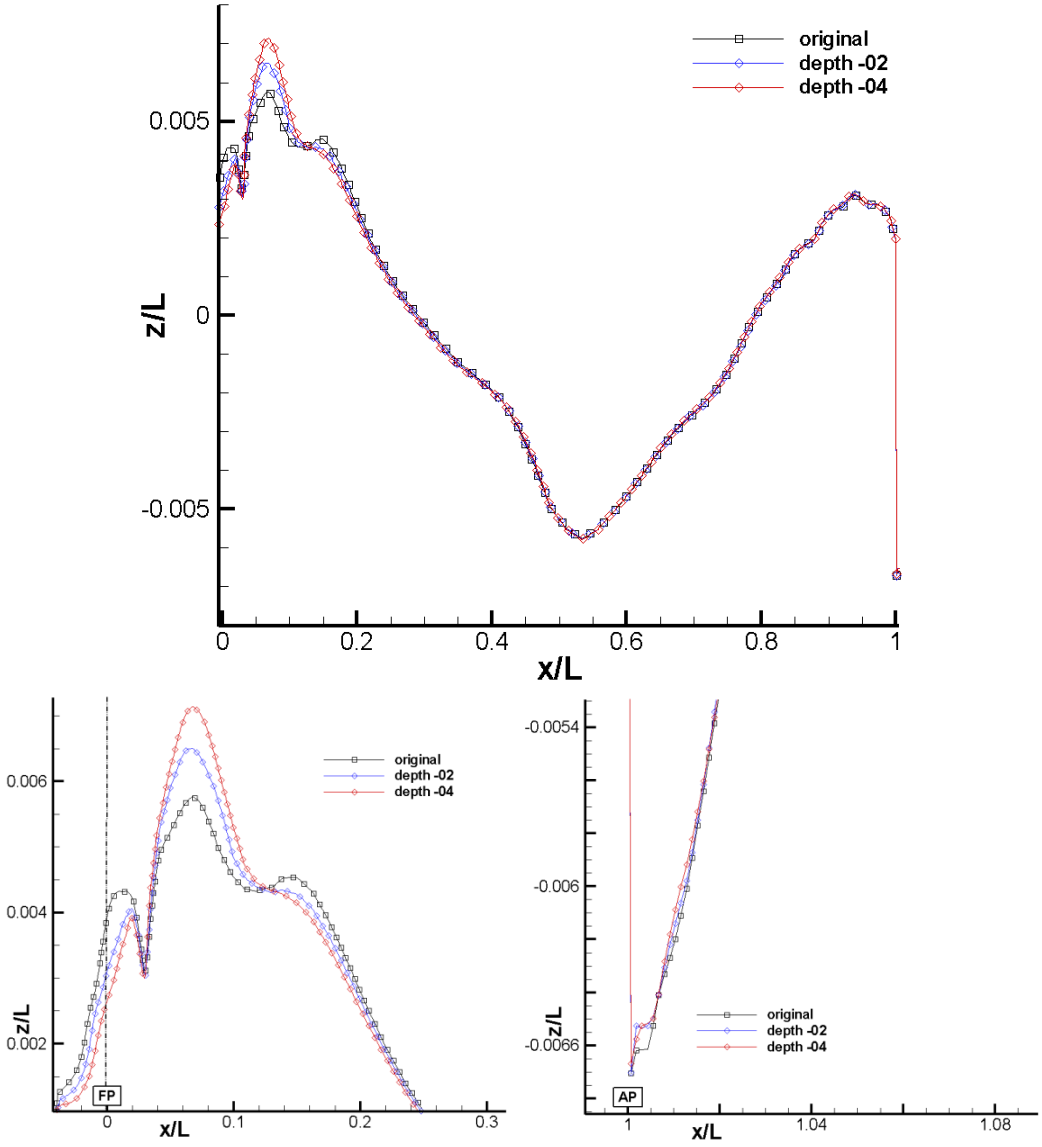


Figure 9-9 Comparison of wave profiles obtained by depthwise modification compared with original

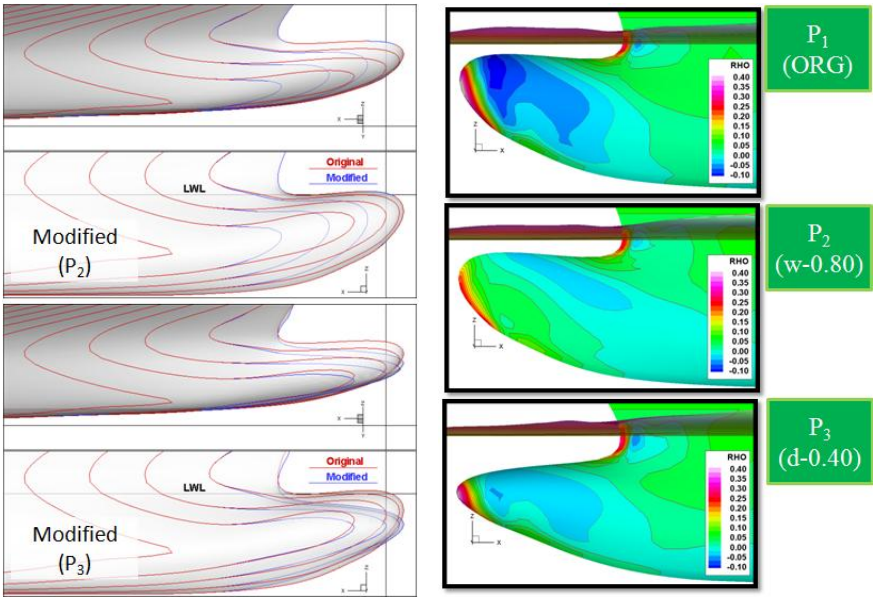


Figure 9-10 Initial designs obtained from sensitivity analysis:
(Left) buttock lines drawing compared to original,
(Right) hull surface pressures and bow waves

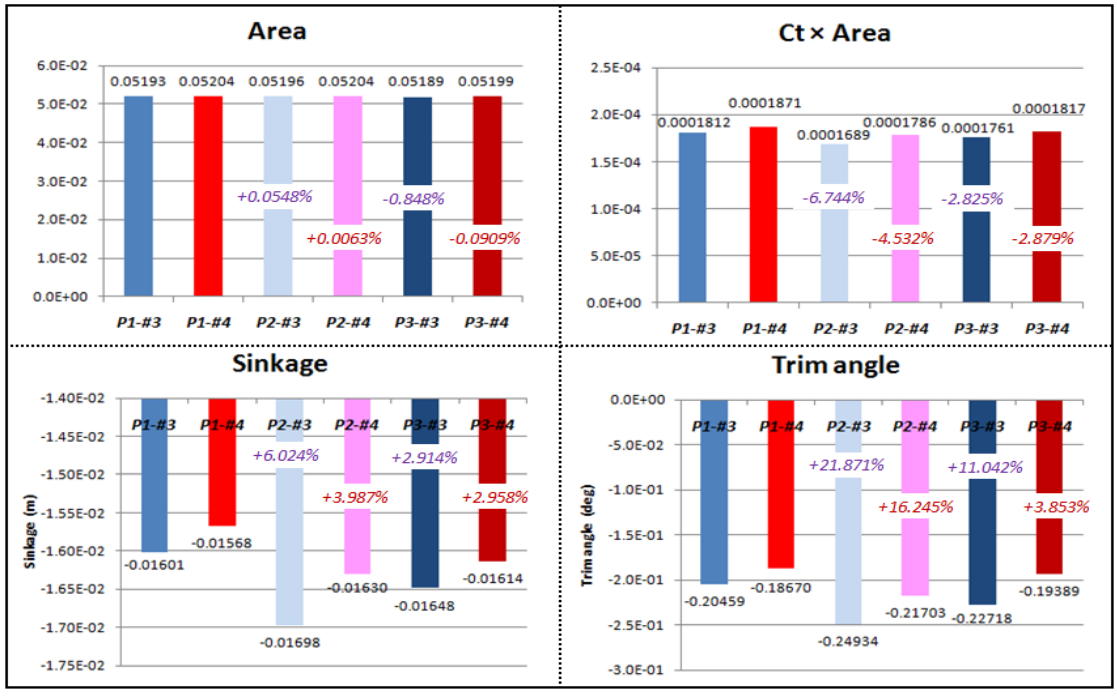


Figure 9-11 Comparison of dynamic area, Rt, sinkage, and trim among the solutions from Grid 3 and 4 for initial designs

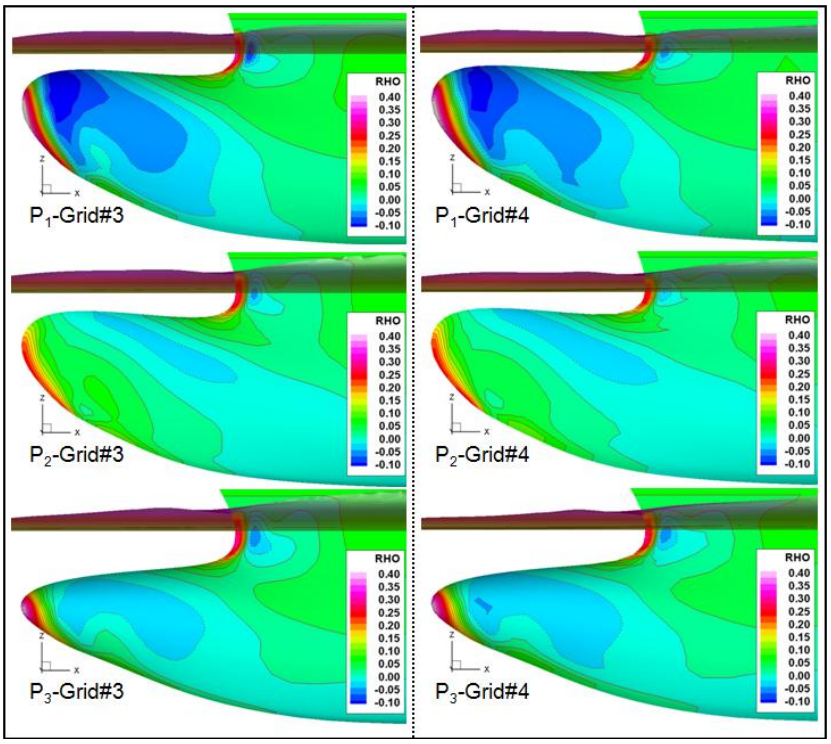


Figure 9-12 Comparison of hull surface pressures with free surface between two grid solutions (#3 and #4)

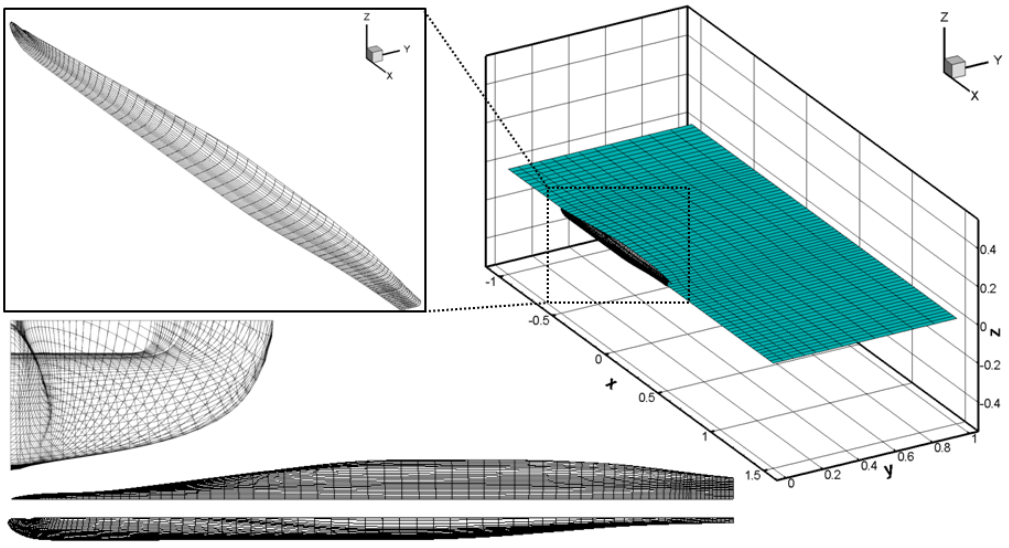


Figure 9-13 Numerical meshes around JHSS barehull and free surface for WARP solver

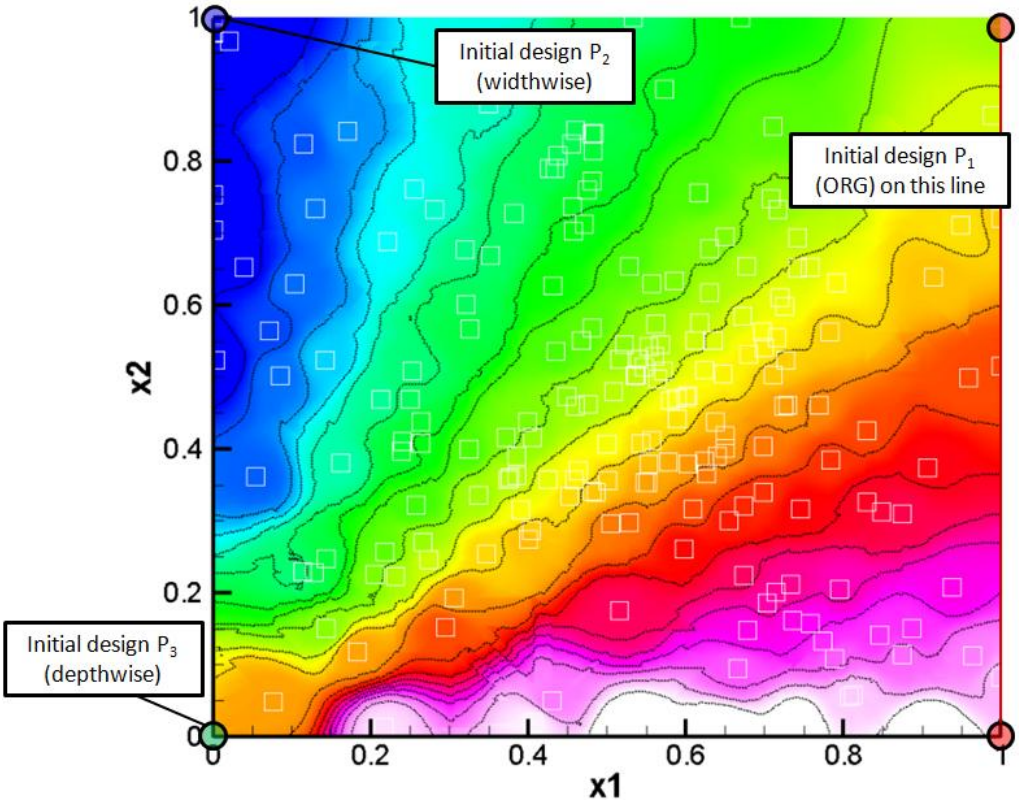


Figure 9-14 Solution topology map obtained by SBD-C system with 8 particles; design variable space ($x_1$ vs. $x_2$) colored by objective function (F)

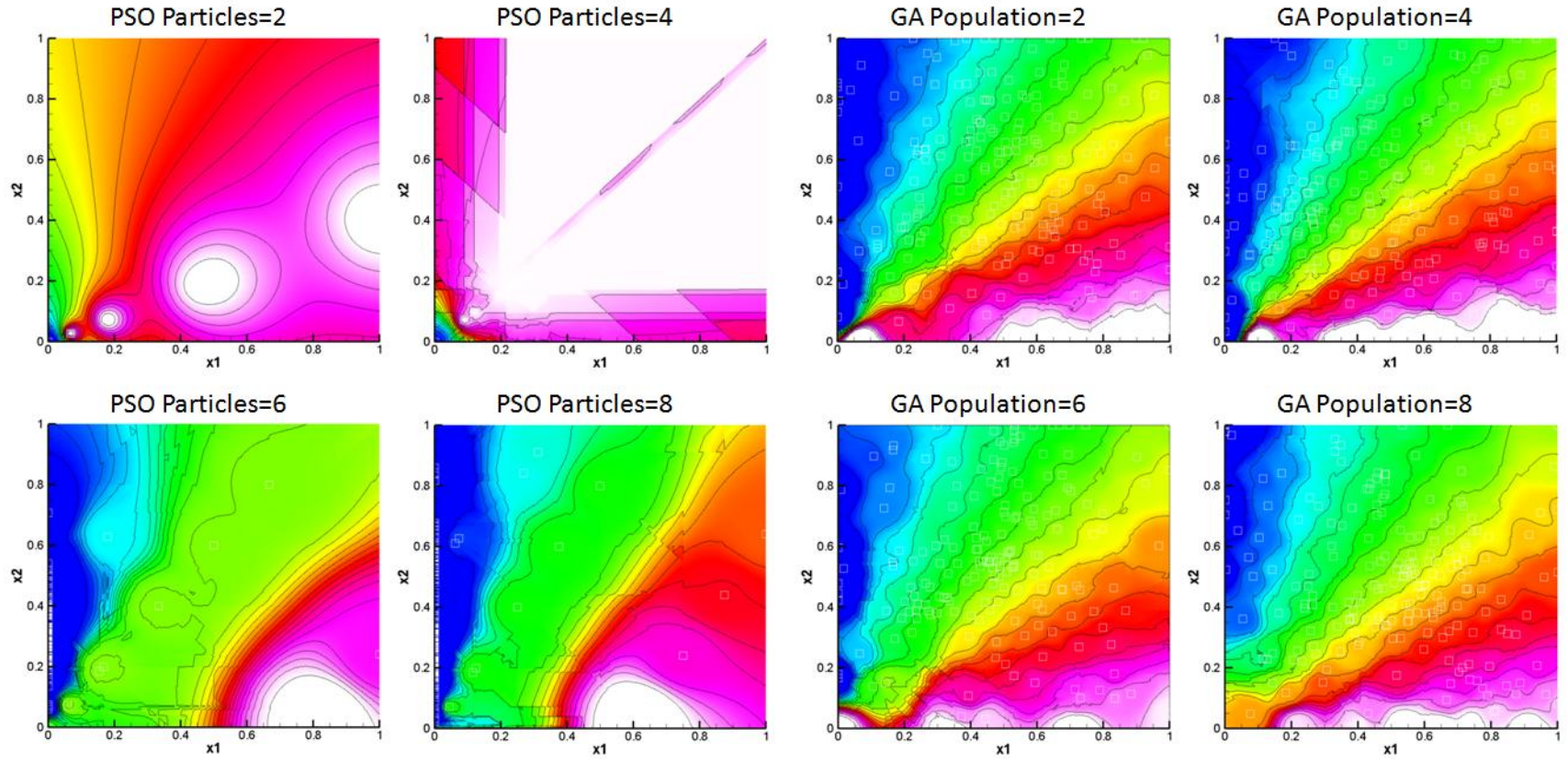


Figure 9-15 Comparison of solution topology maps obtained by SBD-B and SBD-C system with 2, 4, 6, and 8 particles/individuals

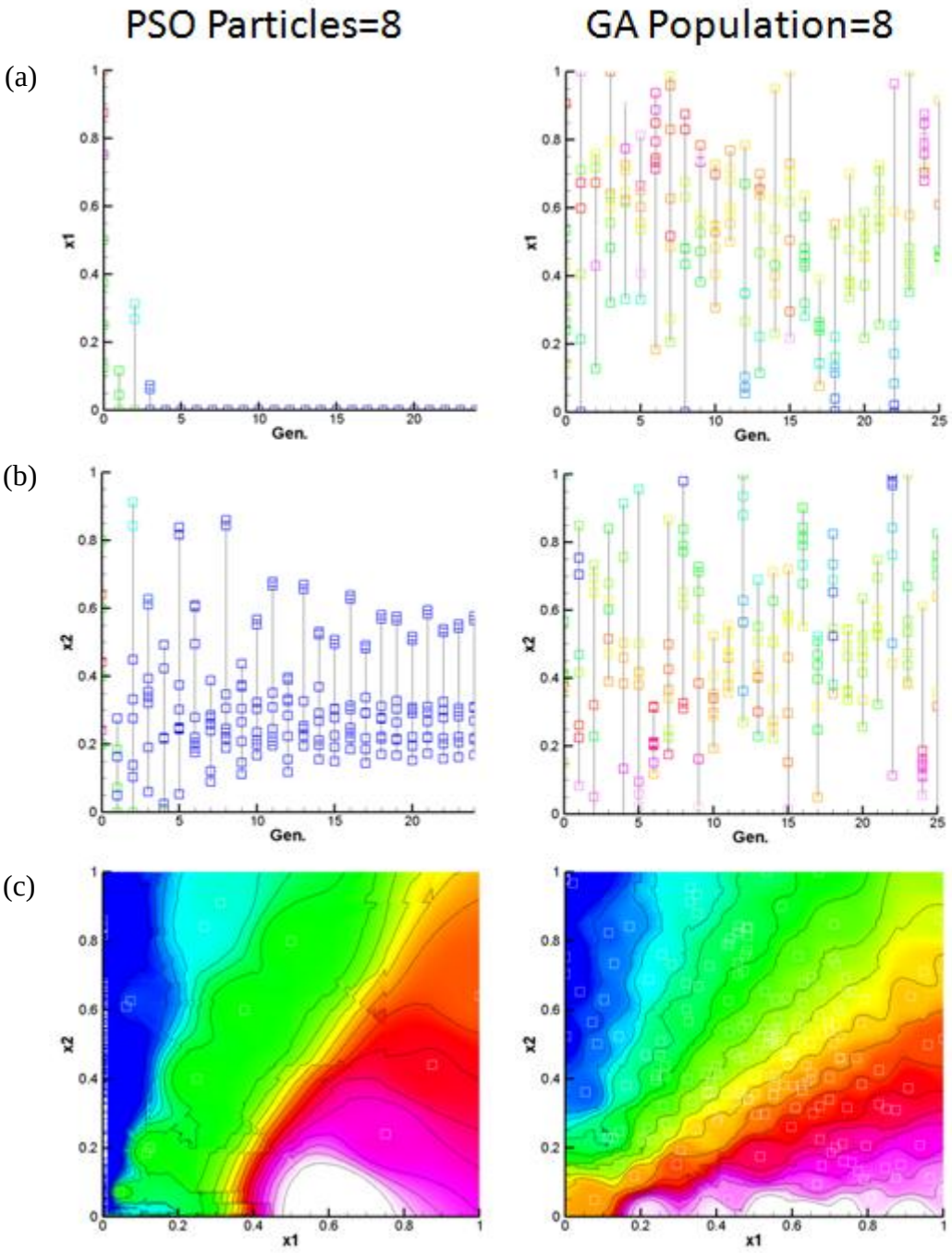


Figure 9-16 Generation history of design variables; (a) generation vs. x1, (b) generation vs. x2, (c) solution topology map by SBD-B and SBD-C

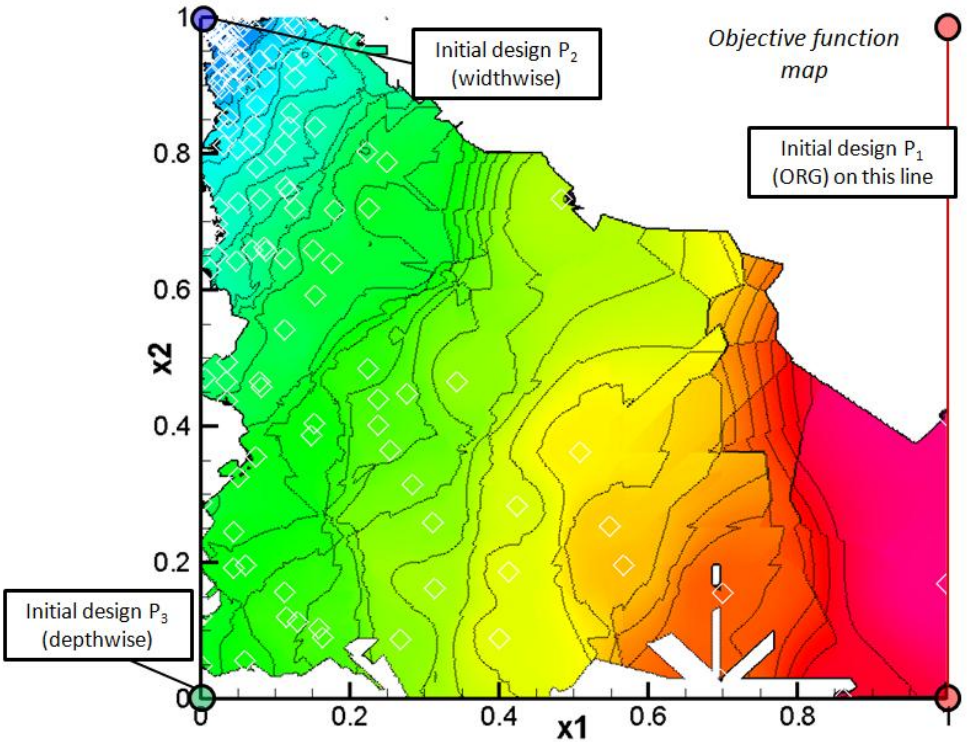


Figure 9-17 Solution topology map for JHSS barehull optimization obtained by SBD-A system

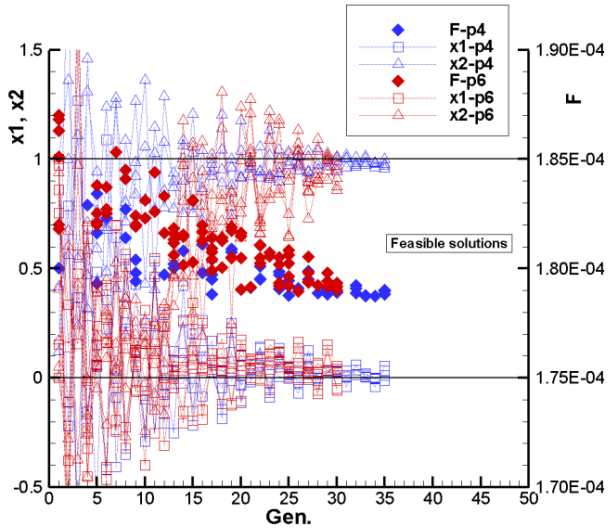


Figure 9-18 Generation history of design variables ($x_1$ and $x_2$) and objective function (F) obtained by SBD-A system with 4 (p4) and 6 particles (p6)

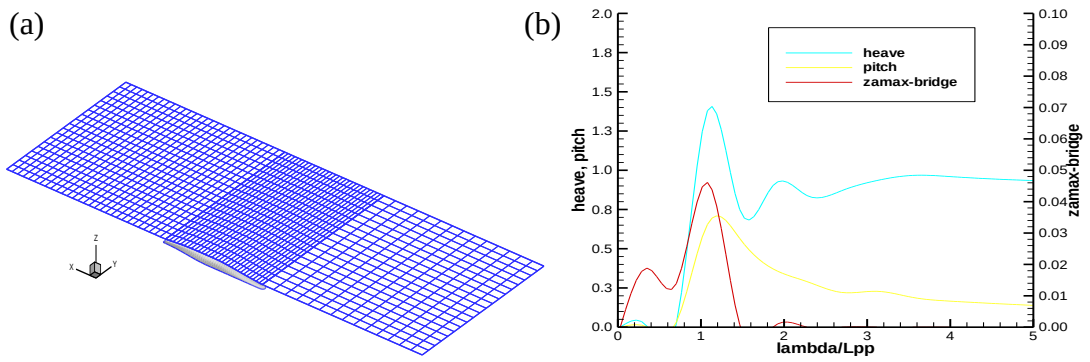


Figure 9-19 Information of frequency domain panel method (FreDOM) for evaluation of seakeeping performance: (a) Panel arrangement, (b) results of RAO for heave, pitch, and $\ddot{z}_B/g$ at bridge for original JHSS ship

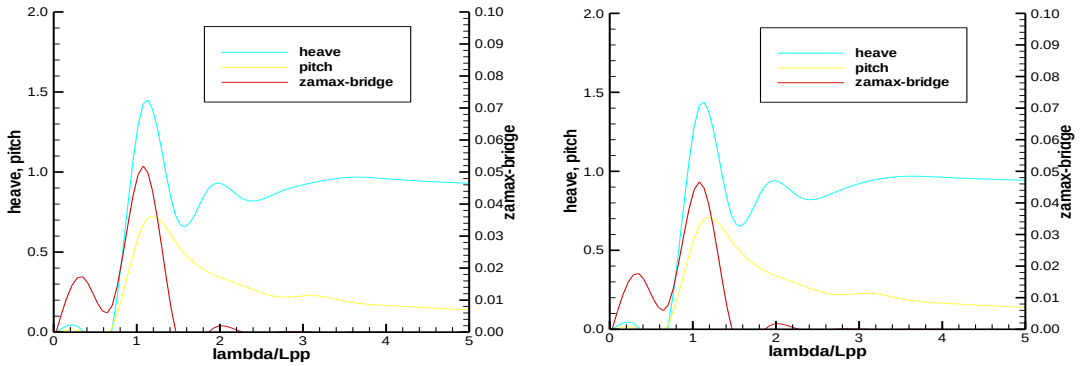


Figure 9-20 Results of RAO for heave, pitch, and $\ddot{z}_B/g$ at bridge for (Left) $P_2$ and (Right) $P_3$

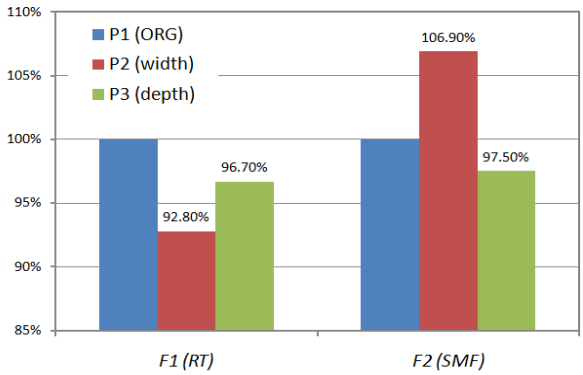


Figure 9-21 Performance analysis of initial designs, $F_1(R_T)$ and $F_2$(SMF) shown in %O

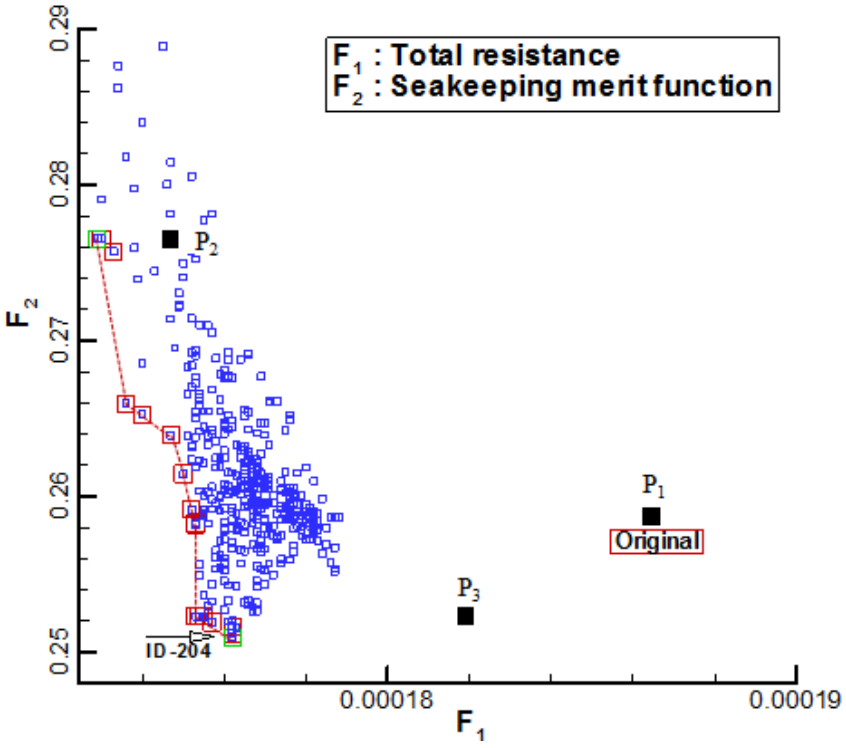


Figure 9-22 Solution distribution for multi-objective optimization by SBD-D system

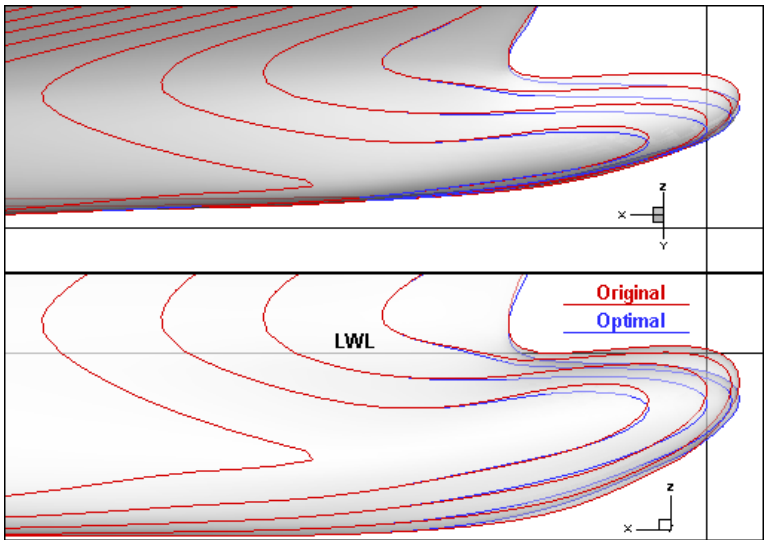


Figure 9-23 Comparison of buttock lines between original and optimal (ID-204) design

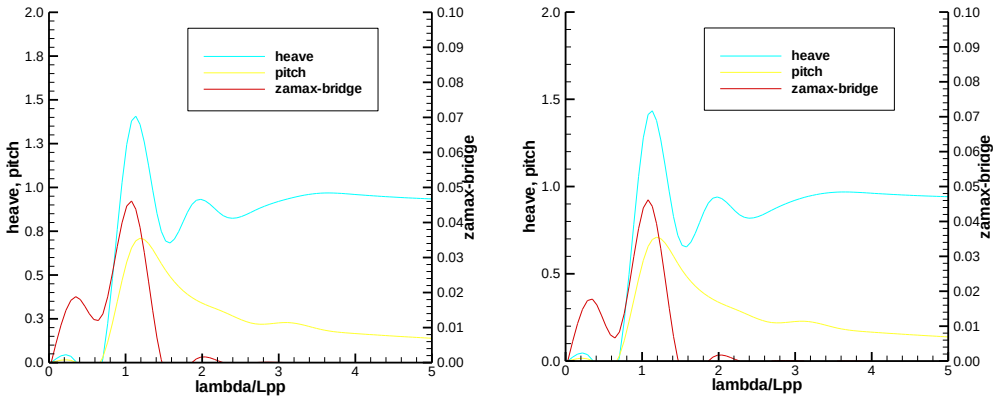


Figure 9-24 Comparison of RAO between (Left) original and (Right) optimal design

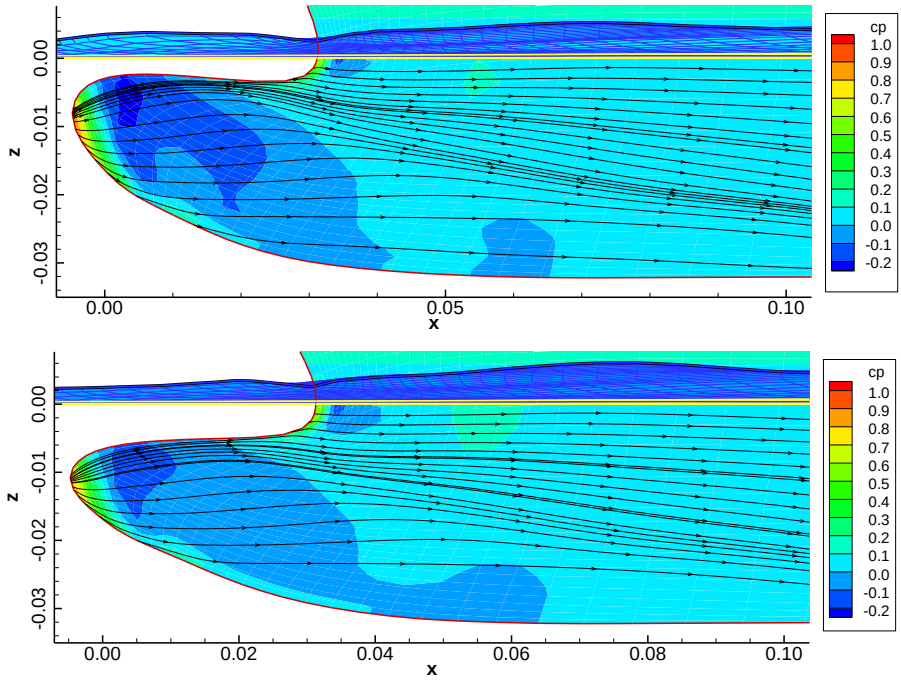


Figure 9-25 Comparison of hull surface pressures shown with limiting streamlines and free surfaces between (Top) original and (Bottom) optimal design

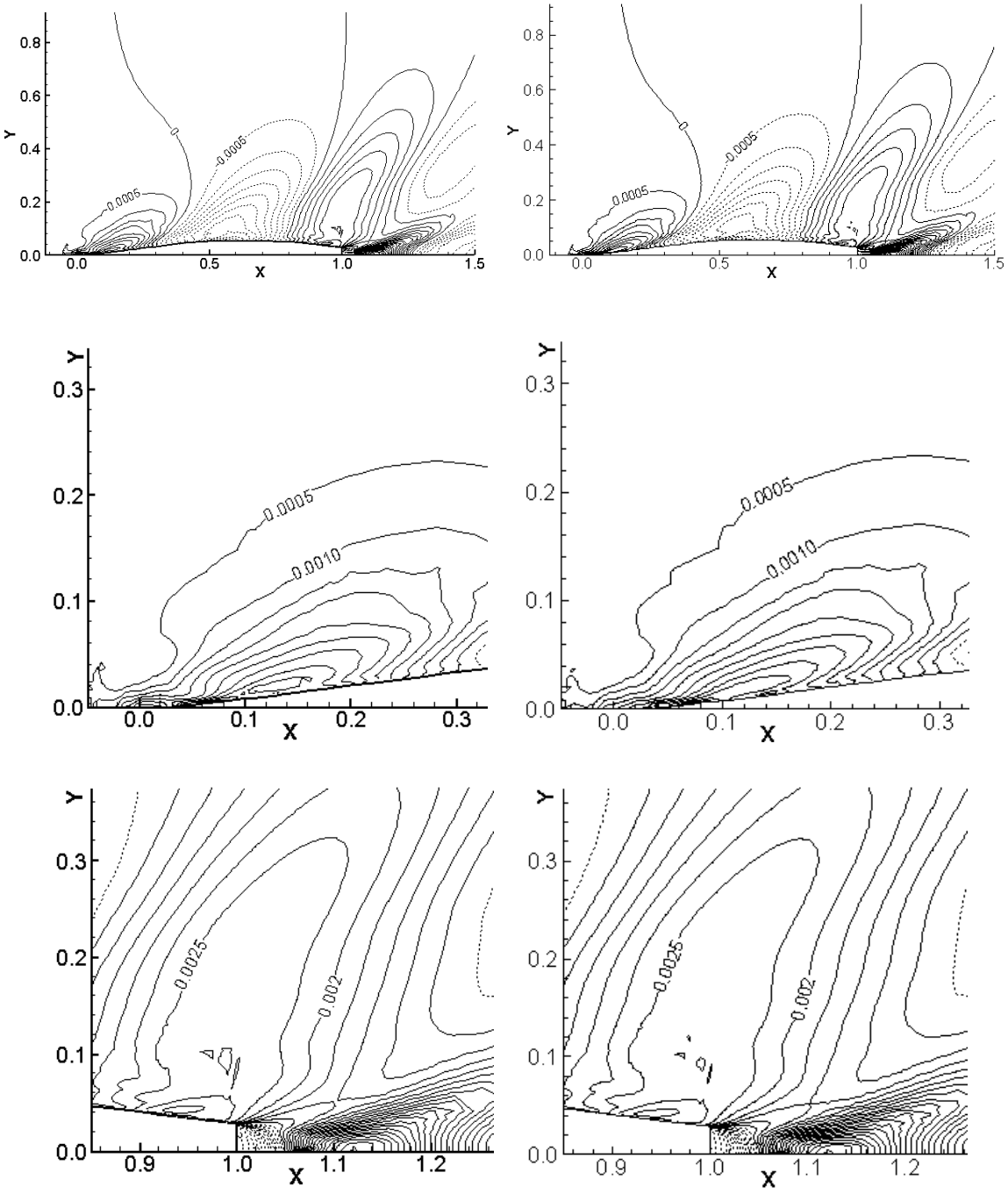


Figure 9-26 Comparison of free surface elevations between (Left) original and (Right) optimal

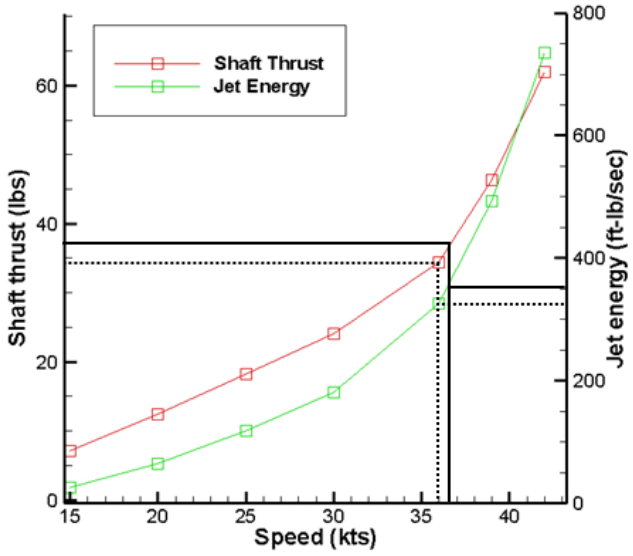


Figure 9-27 Relationship between ship speed and shaft thrust/jet energy from EFD

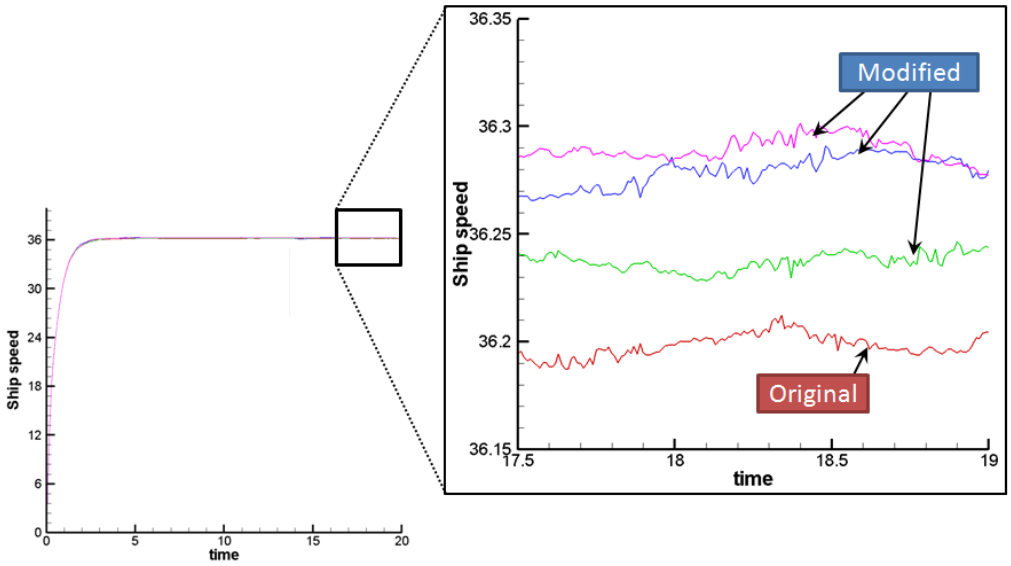


Figure 9-28 Residual history of ship speed (self propulsion point)

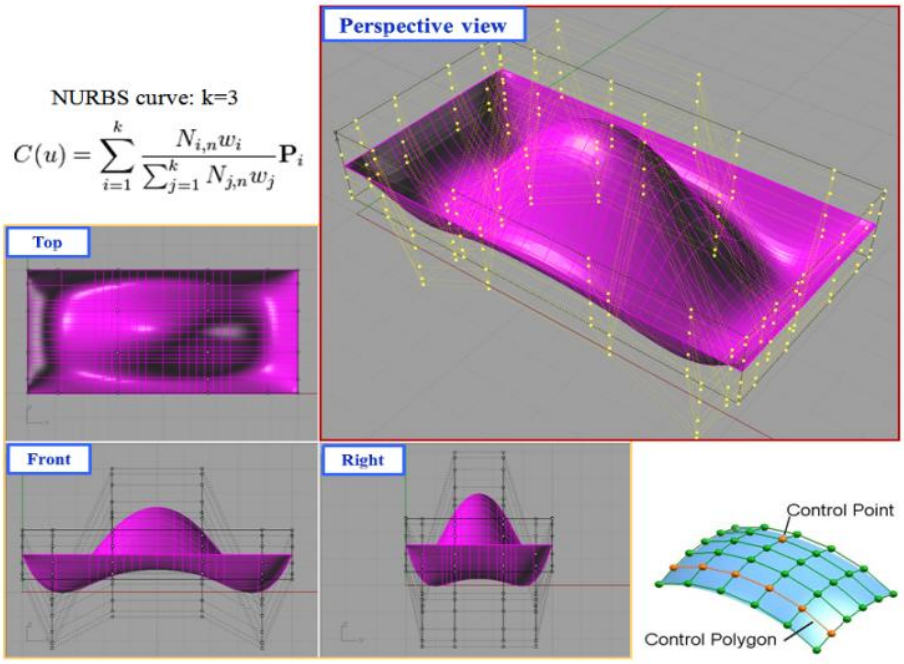


Figure 9-29 Definition of NURBS curve and geometry modeling in Rhino using control points approach

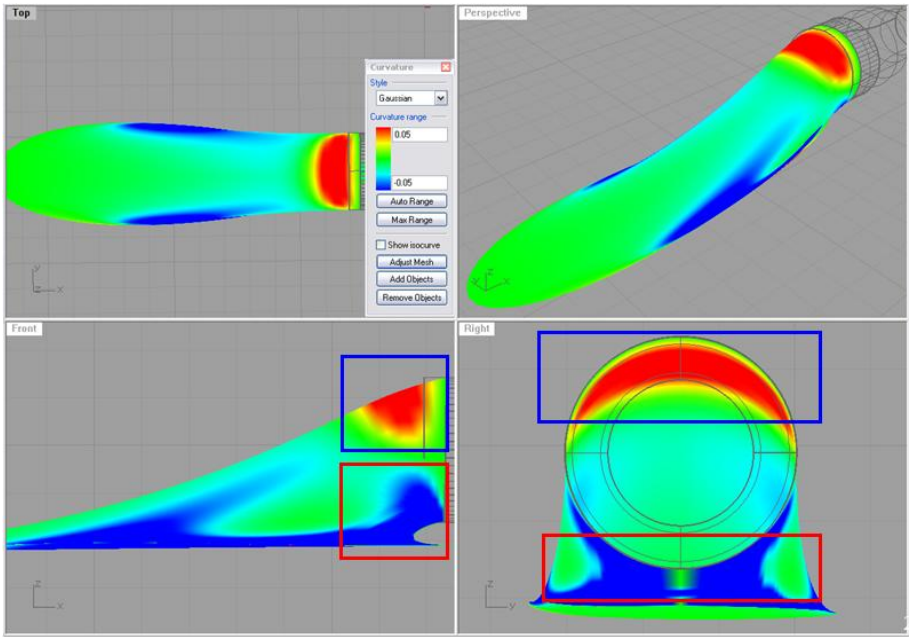


Figure 9-30 Gaussian curvature values plotted on waterjet intake duct

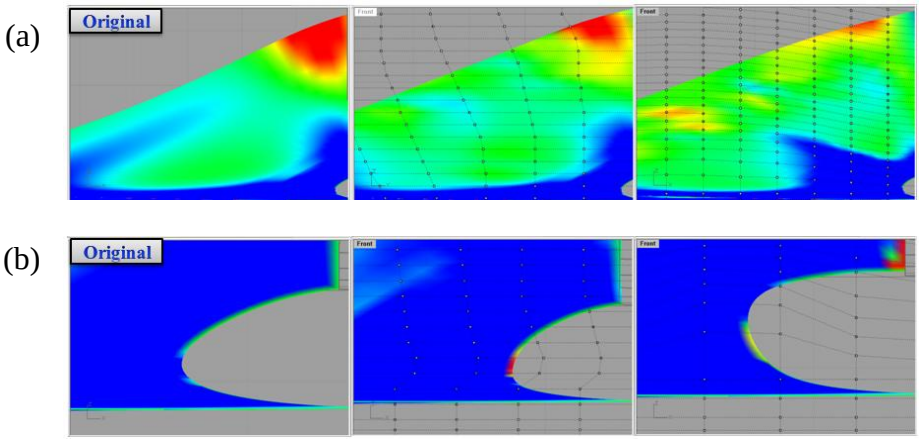


Figure 9-31 Modification results plotted by Gaussian curvature in Rhino: (a) upper curvature, (b) lip shape

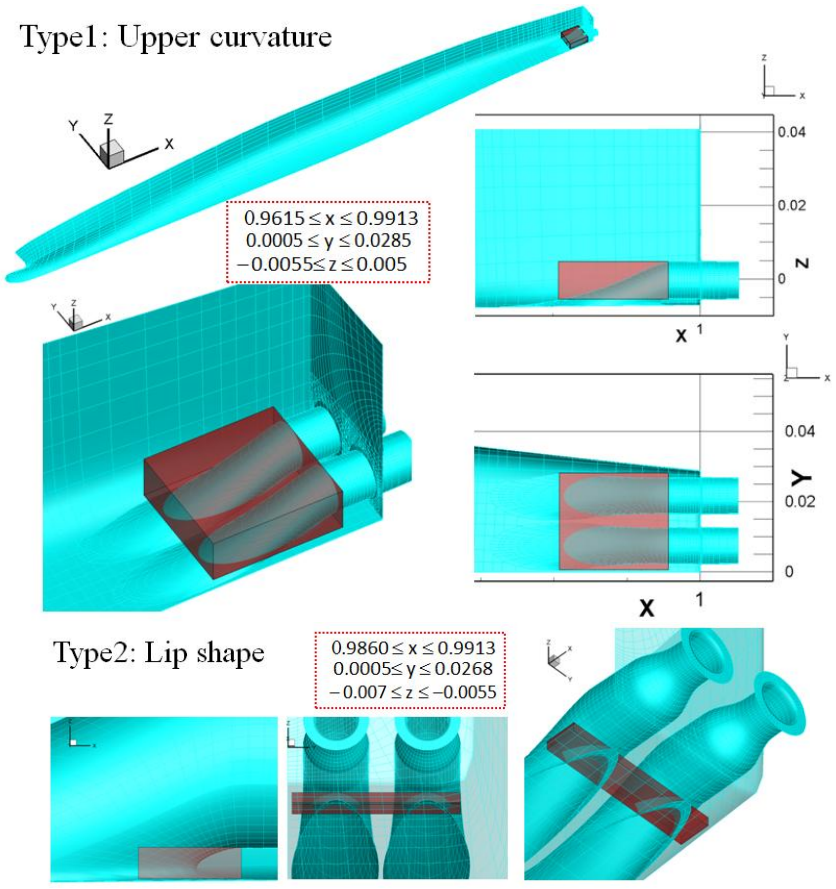


Figure 9-32 Definition of modification region constraint condition for JHSS waterjet inlet shape optimization

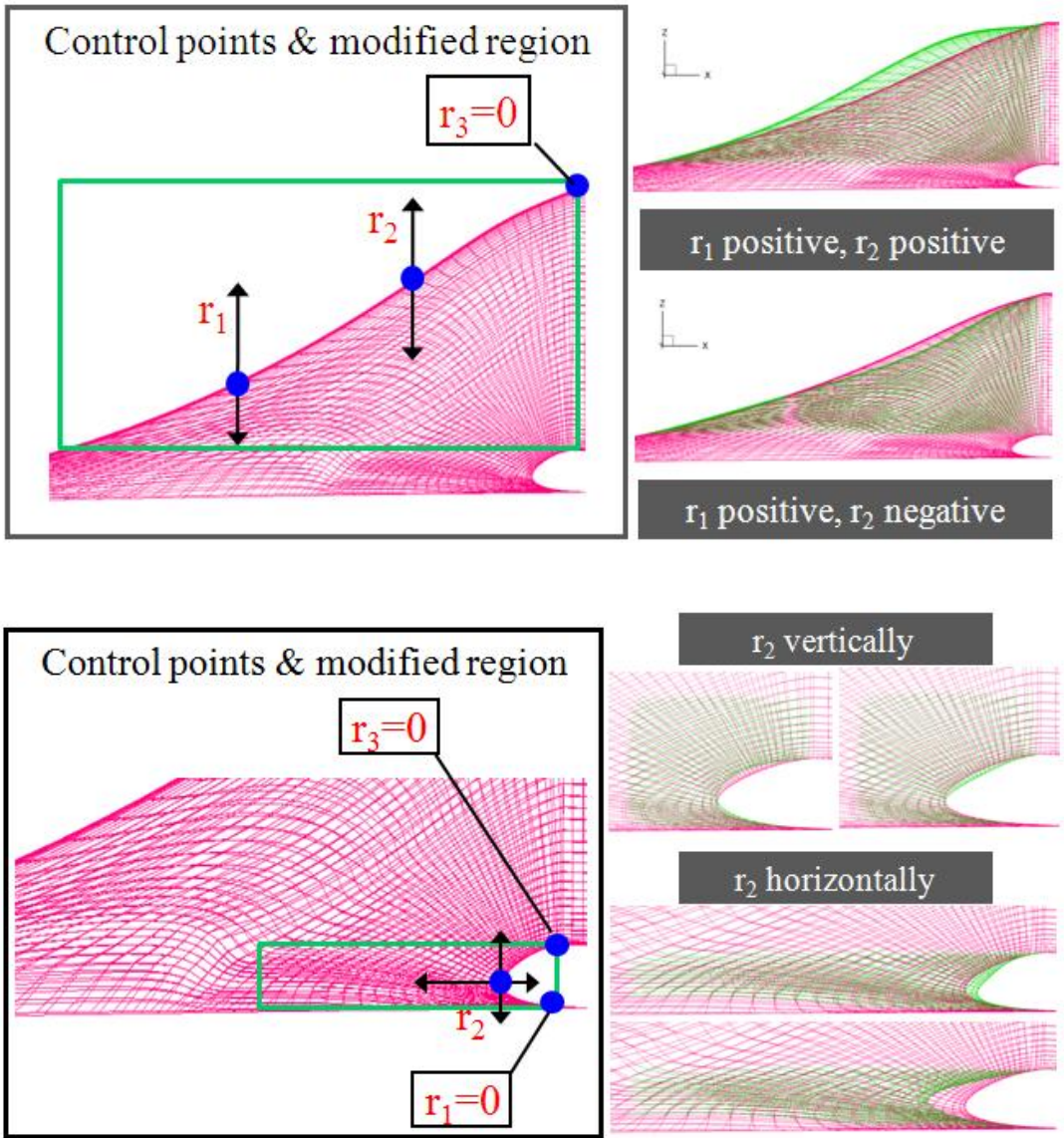


Figure 9-33 Two directions of modification for JHSS waterjet inlet shape sensitivity analysis: (Top: Type1) upper curvature, (Bottom: Type2) lip shape

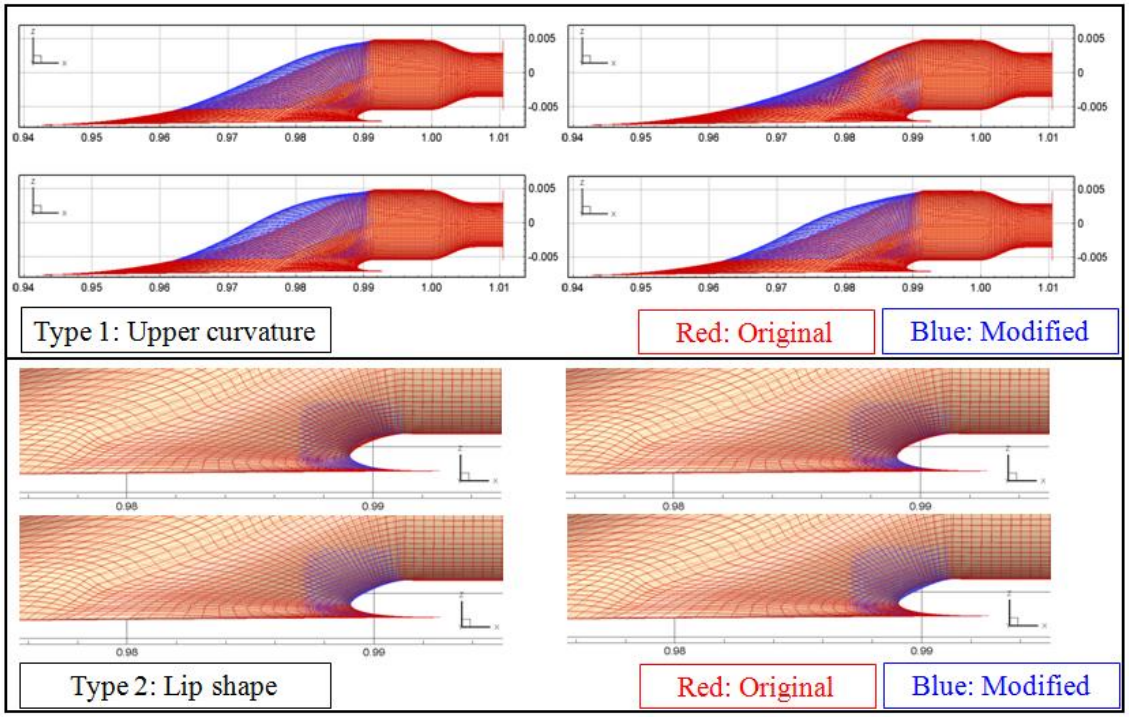


Figure 9-34 Examples of modified shapes compared to original design

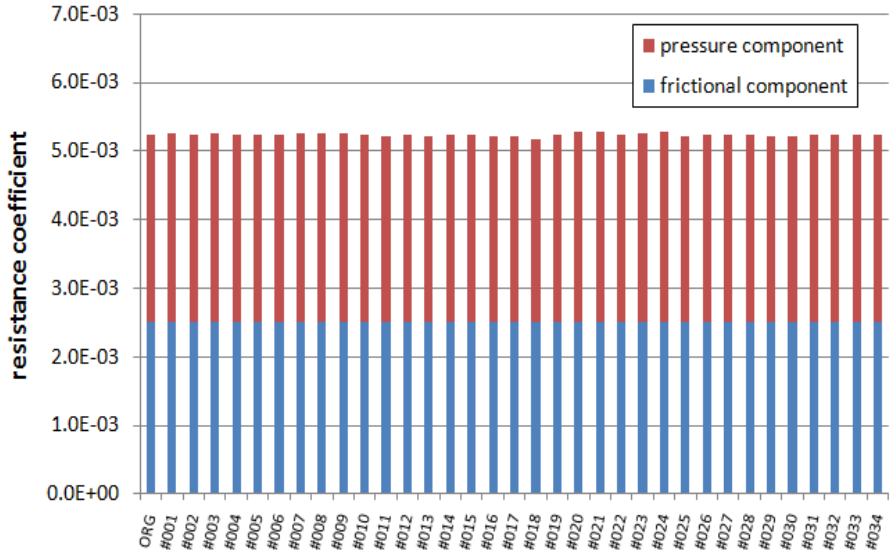


Figure 9-35 Results of resistance (pressure and frictional component) from sensitivity analysis for waterjet inlet shape optimization

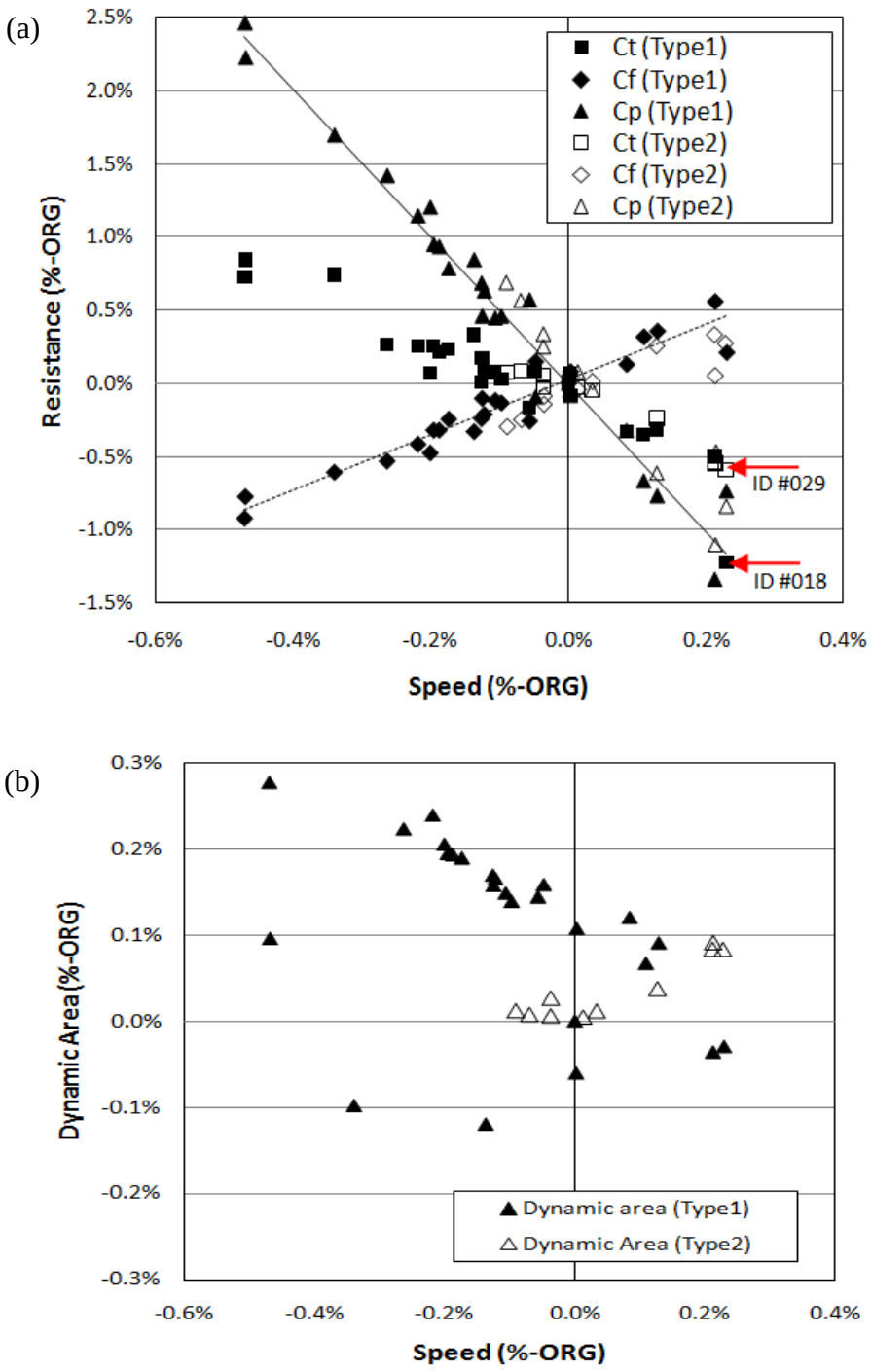


Figure 9-36 Sensitivity results of (a) speed vs. resistance and (b) speed vs. dynamic area for waterjet inlet shape optimization

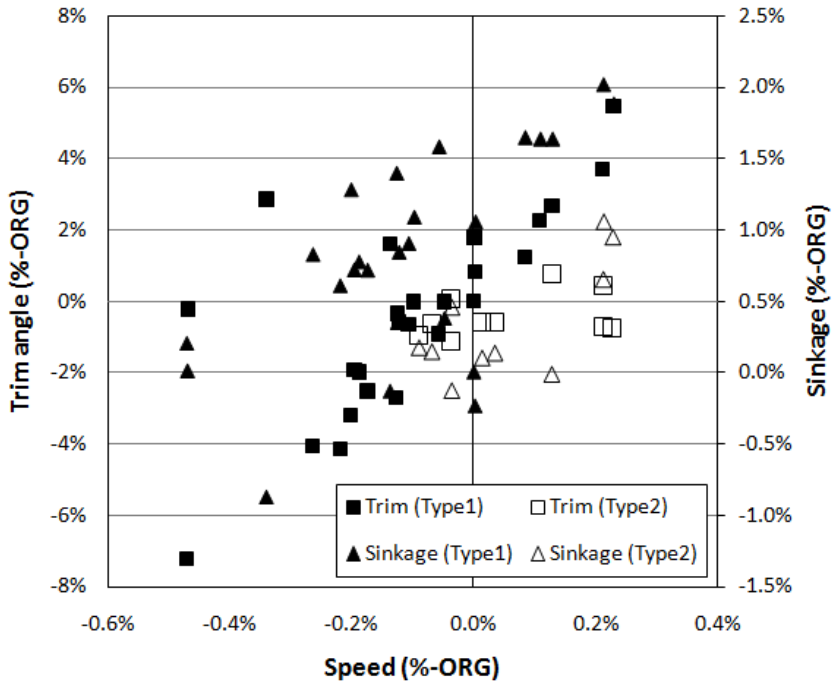


Figure 9-37 Sensitivity results of ship motions for waterjet inlet shape optimization

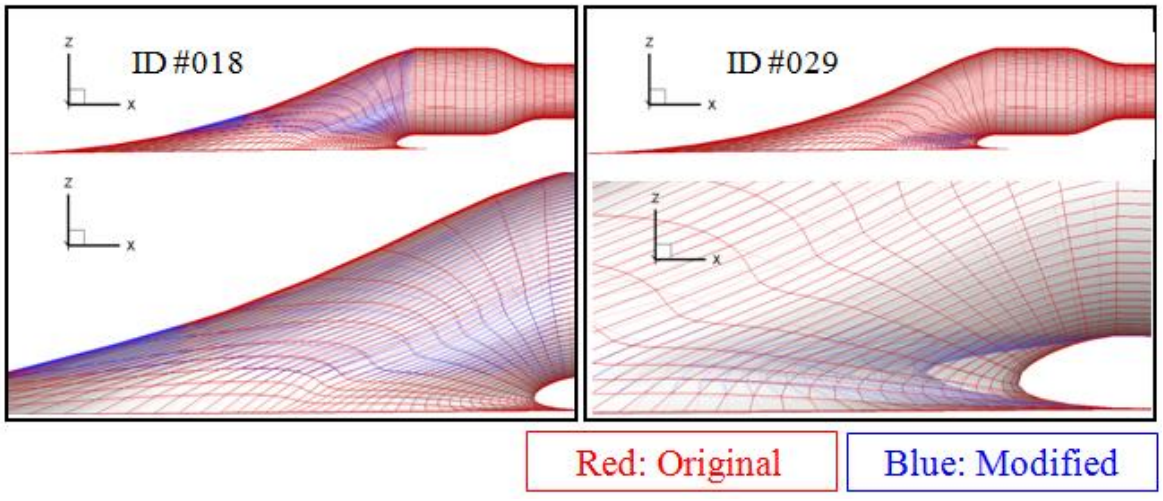


Figure 9-38 Initial designs for JHSS waterjet intake duct shape optimization: (Left) $P_{2W,}$ (Right) $P_{3W}$

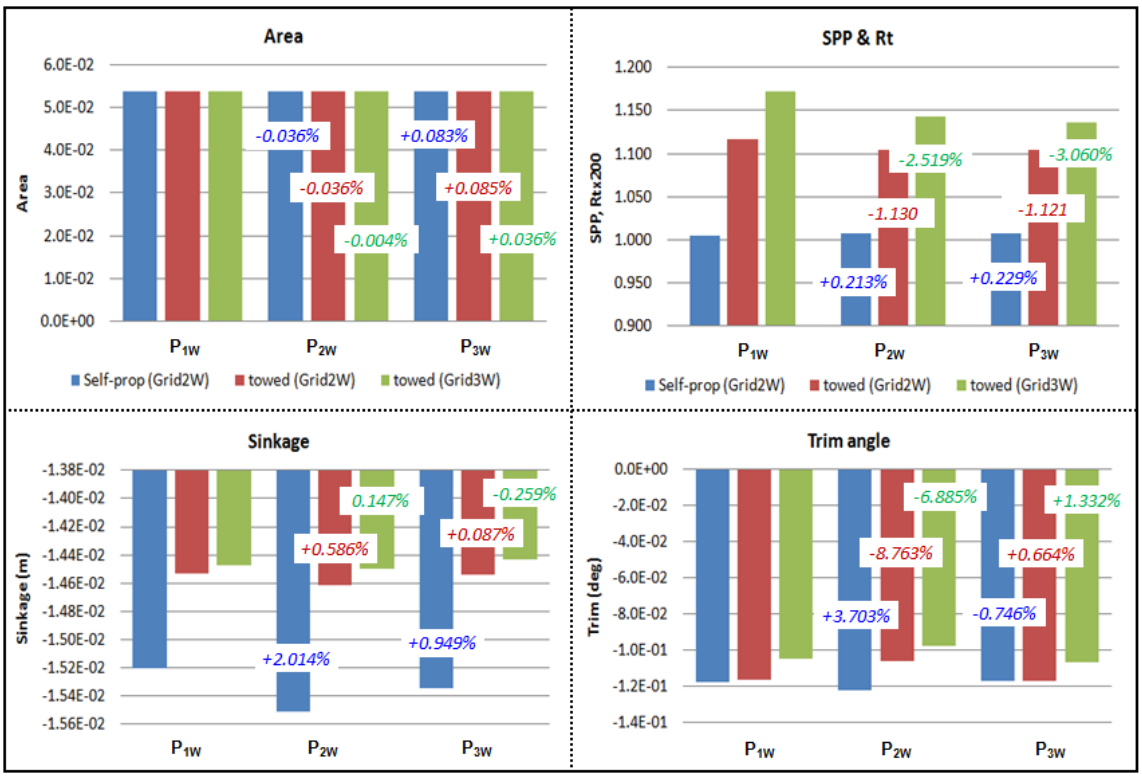


Figure 9-39 Comparison of dynamic area, SPP/Rt, sinkage, and trim among the solutions from Grid 2W and 3W for initial designs with self-propulsion and towed simulation conditions

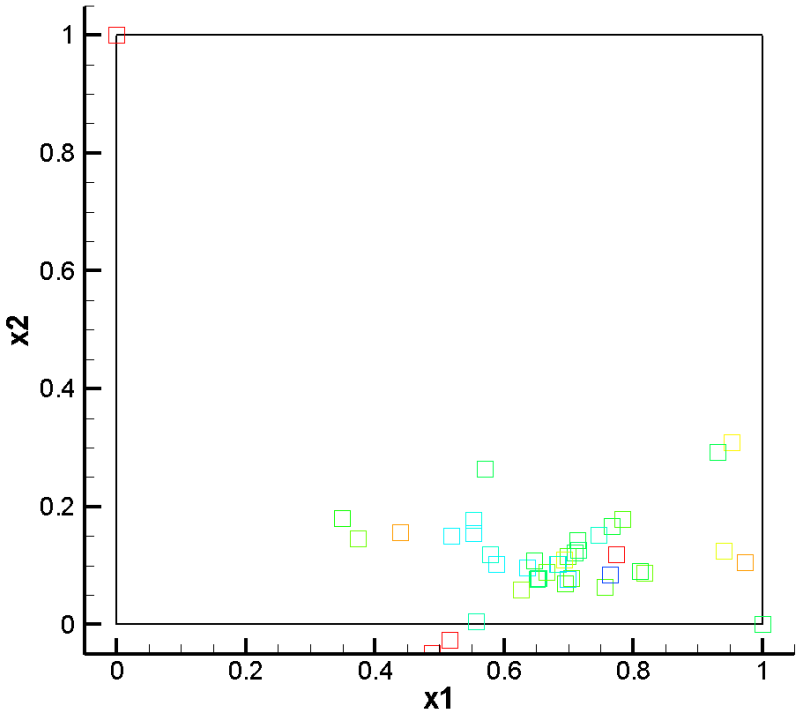


Figure 9-40 Solution distribution on design space ($x_1$ vs. $x_2$) by SBD-A system for waterjet inlet design optimization

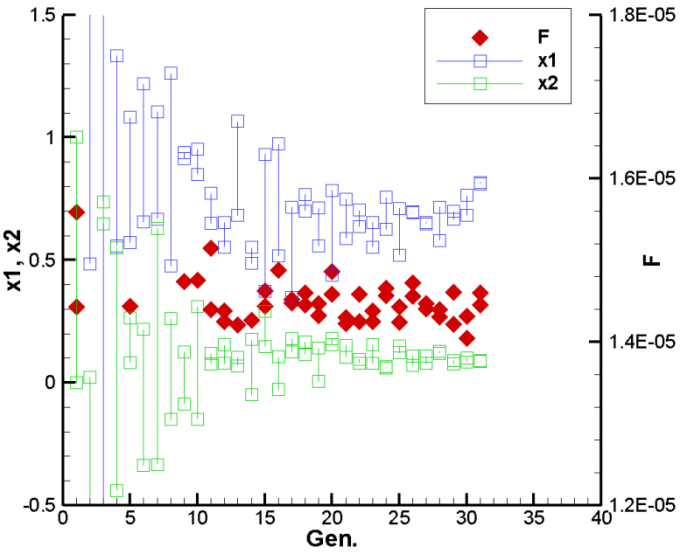


Figure 9-41 Generation history of design variables and objective function for waterjet inlet design optimization

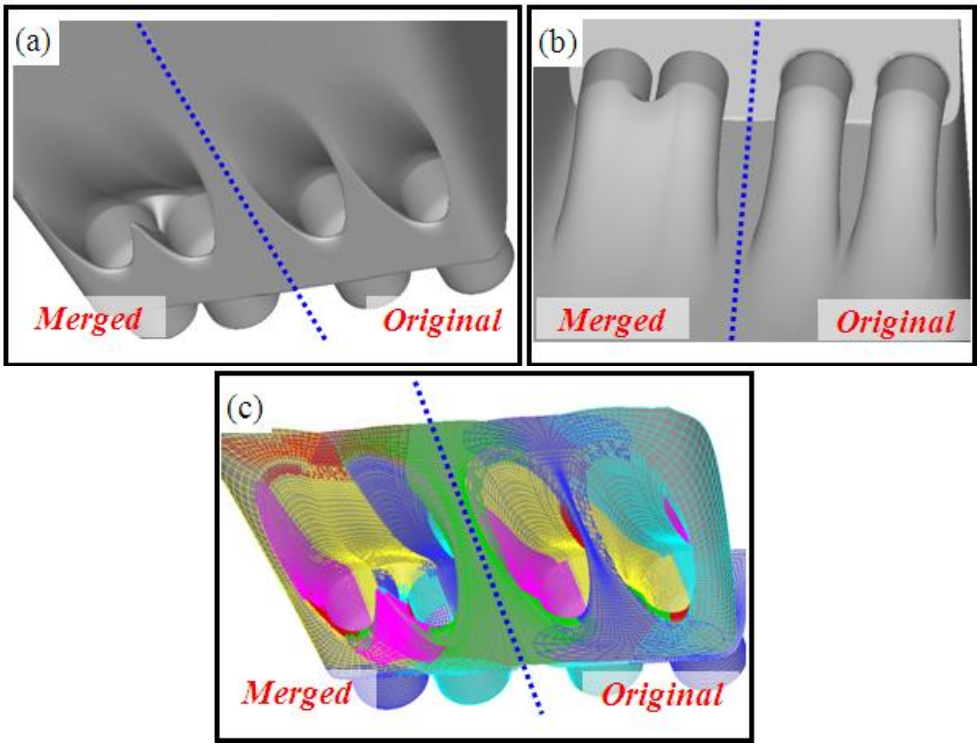


Figure 9-42 Illustrations of JHSS waterjet merged inlet geometry and surface mesh: (a-b) comparison of the intake duct shape between merged and original design, (c) surface meshes for merged and original intake duct

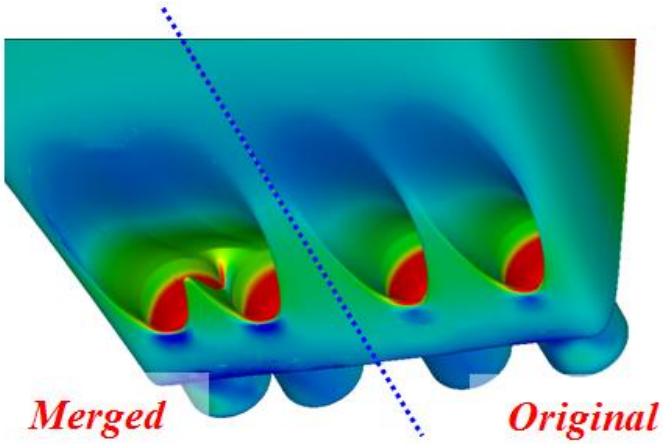


Figure 9-43 Comparison of hull surface pressure between merged and original inlet

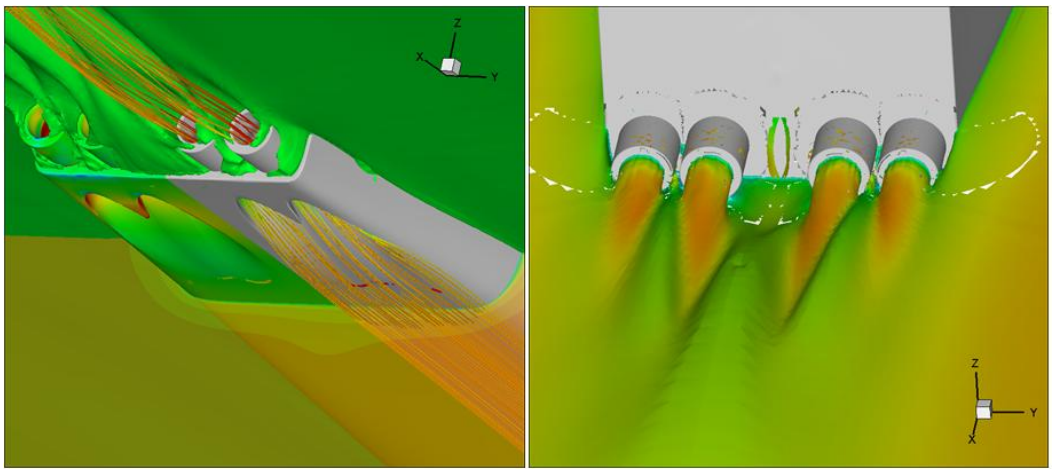


Figure 9-44 Free surface elevation and jet outflow of waterjet merged inlet design

# CHAPTER 10
# CONCLUSION AND FUTURE WORK

## 10.1 Conclusion

The main objective of the present thesis is development and demonstration of Simulation Based Design (SBD) system for ship hydrodynamic design optimization. URANS solver, CFDSHIP-IOWA V.4, is employed as the high-fidelity flow solver, and global optimization algorithms are used in order to seek for the optimal design of both JHSS barehull bow shape and JHSS waterjet intake duct shape. In order to achieve the main objective, mainly three approaches are taken into account; development and validation of the numerical method for waterjet propelled simulation, development of the global optimization algorithm and flexible geometric modeling method for the hydrodynamic design, and demonstration of the capability of SBD method for a practical naval vessel.

The V&V analysis demonstrates the feasibility of using URANS for performance analysis of hull-integrated waterjet propelled ship with free surface and dynamic motions. A verification study is conducted for barehull simulations by four systematically refined grids ranging from $1.2\times10^6$ to $28\times10^6$ grid points, which allows two sets of grid studies; on the other hands, it is done for waterjet case by three systematically refined grids. Uncertainty intervals of iterative/grid size convergences are assessed for both barehull and waterjet case, and the solutions are validated at the design speed (36knots) with corresponding EFD data. Ultimately, total resistance coefficient ($C_t$) for barehull is validated at the average interval of 7.0%D and ship speed for waterjet self-propulsion simulation is validated at the interval of 1.1%D. In addition, predictions of CFD computations capture the general trend of resistance over the speed range of 18-42knots, and show reasonable agreement with EFD within the average errors of 1.8%D and 8.0%D for barehull and waterjet case, respectively. CFD also captures trends of EFD

motions over the speed range with reasonable accuracy. For barehull simulation, the verification of point variables for wave profiles is also performed, and the grid uncertainty shows reasonable intervals (average of 2.3%S). Detailed flow parameters for waterjet propelled simulations are also investigated. Overall, the main performance parameters; namely, net jet thrust, inlet efficiency are predicted reasonably well with an accuracy of ~10%. This work paves way for waterjet inlet optimization opportunity. The main objective of the optimization is identified as reduction of powering requirements by increasing the inlet efficiency, which currently shows significant losses (> 15%) over the speed range. The validation is achieved at reasonable uncertainty and URANS captures the important trends of force and motions properly. Thus, the current V&V work has proved that the present URANS approach is an accurate tool to predict the resistance of both JHSS barehull resistance and waterjet computations.

The comparison study of optimization algorithms is performed in order to investigate the performance of four different methods. SQP is selected as a gradient based algorithm and PSO, RCGA, and BCGA are selected as derivative-free global algorithms. Both single- and multi-objective optimization problems are solved by these four algorithms and the results are discussed. In particular, the solutions for multi-objective problems are evaluated quantitatively. Studies are focused on the following topics; verification of PSO performance, PSO vs. RCGA vs. SQP for single-objective optimization problems, performance analysis of RCGA for single-objective problems, dependency on population size for PSO for single-objective problems, PSO vs. RCGA for multi-objective problems, and BCGA vs. RCGA for multi-objective problems. In consequence, overall results from four algorithms show both advantages and disadvantages. For the single objective optimization problems, PSO shows best performance in terms of speed and accuracy to detect the optimal design with the condition of enough population size. For the multi-objective problems, both RCGA and

PSO have different advantages; thus, they should be used depending on the purpose and demands.

Finally, the hydrodynamic design optimization is demonstrated by developed SBD framework. Four different basic SBD environments are generated and tested in a nonlinear, constrained, single-/multi-objective optimization problems. In the present study, two objective functions to be minimized are considered, i.e., the total resistance and seakeeping merit function. Realistic functional and geometrical constraints for preventing unfeasible results and to get a final meaningful design are enforced. Three optimization demonstrations are carried out using different SBD environments. First test case is focused on JHSS barehull with single-objective function (*Rt*). Both high-fidelity and low-fidelity flow solvers are employed and the solutions are compared. Final optimal design obtained by different SBD system looks similar and shows significant reduction of objective function (~8%O). Second case is for barehull design with multi-objective function. It is found that the present SBD system can detect the so-called Pareto optimal set with improvement of both objective functions. The final demonstration is for JHSS waterjet intake duct design problem. Only initial result is presented in the present thesis due to the huge computational load. It still needs to be improved the optimization approach for this particular problem; however, the initial result shows the promising designs. In the present demonstration case, the final optimal design show 2.7%O reduction in *Rt*; thus, 16%O improvement in inlet efficiency. For all the cases, final optimal designs show significant reduction of objective functions; hence, the optimization demonstrations have proven the capability of the developed SBD system for the practical hydrodynamic design optimization.

## 10.2 Future work

Overall, demonstration results show that present SBD system has basic capability to the design optimization of the complex high-speed sea-lift with waterjet propulsion system. Certain future work should be addressed both on SBD system and waterjet propelled simulation method for further improvement of the system.

***SBD system***

Further development of present SBD system is of great interest, such as introduction of the physics-based variable fidelity URANS/PF approach, implementation of complete interface among the two optimization methods developed in the present work, introduction of Metamodelling (Kriging) technique, integration of design CAD systems, and demonstrations for waterjet/hull optimization problems with more practical multi-objective functions.

Design engineers typically have a suite of different tools to evaluate the performance of a ship, ranging from some simple (i.e., low-fidelity (LF)) model based on some simplified theory to more complex simulation codes. Complex (i.e., high-fidelity (HF)) physical models provide obviously high quality in the prediction, at the expense of large computational costs. Variable fidelity modeling (VFM) techniques reduce the number of expense HF analysis by taking advantage of cheap LF models. The idea of using computational models of varying fidelity has a long history in engineering design: perform most of the computations with LF model and correct these predictions by using indication coming from a HF model. VFM procedures may be obtained by changing the physics, but also by using different grid density or computational accuracy. Occasional recourse to HF models does not ensure the convergence to HF solutions. The ability of the LF model to guide the optimization process has to be monitored and its quality improved when required, while consistency constraints have to be enforced to ensure global convergence to the original HF solutions.

Optimizers also could be improved. As shown in the present study, two global optimization methods (PSO and RCGA) have both advantage and disadvantage each other. It might be possible to combine the advantages from each algorithm in order to reduce the disadvantage. Additionally, metamodel approach should be included. A significant challenge in the applications of evolutionary algorithms based optimization methods to engineering design problem has been the high computational cost due to the large number of simulation (or function) calls required by these methods. One of the promising strategies to reduce the computational effort for such optimization methods is to use metamodeling techniques. Kriging has been widely used in recent years for metamodeling of computationally expensive deterministic simulations. Kriging predicts the response of unobserved points, i.e., those whose response has not been obtained by the simulation based on all of the observed points.

Generally, ship designers use design CAD system such as NAPA, Pro-Engineering, CATIA, and so on, to design the new ships or revise the existing ones in the industry; thus, it would be proper that one of these popular CAD software is integrated into the SBD system. Perhaps, designers are more familiar with the commercial software to modify the geometry than using numerical methods introduced in the present study, such as B-Spline approach or FFD.

Finally, for the waterjet design optimization, more practical objective functions need to be applied, such as cavitation condition. Also, CFDSHIP-IOWA can handle to predict the dynamic motions in time-domain; hence, the URANS solver could be used to estimate the seakeeping merit function more accurately than potential-based solver. Also, currently ongoing transition of SBD system to ship building industry and research institution should be completed in the near future.

***URANS simulation for waterjet propelled ships***

Ultimately, the main performance parameters for waterjet propelled ship; namely, net jet thrust, inlet efficiency are predicted reasonably well with an acceptable accuracy

in the present study. However, certain issues need to be addressed further to improve validation of the detailed flow features within the duct; both the shaft and the downstream rotor induce some swirl at the inlet St. 3 and 6, which has been neglected. In fact, the actuator disk model provides a pressure jump in the axial direction; however, it does not account for the swirl effects due to the blade-rotating. It might cause the increase in error with increase in loading for the shaft thrust. The effects of blades and shafts are needed to be investigated numerically; therefore, it is recommended that future work extends present waterjet simulations by replacing body force propeller model with detailed CFD waterjet modeling including actual blade-rotating to achieve more realistic simulation. It is expected that CFD and EFD agreement will be improved in terms of flux parameters at not only St.3 but also St.6.

## REFERENCES


1. Balay, S., Buschelman, K., Gropp, W., Kaushik, D., Curfman, L., Smith, B., and Zhang, H., 2002, "PETSc User Manual", ANL-95/11- Revision 2.1.5, Argonne National Laboratory

2. Bassanini, P., 1996, "A Boundary Integrodifferential Equation Arising from the Linearized Theory of Water Waves", Meccanica, Kluwer Academic Publishers, No. 31; pp 433-440

3. Bassanini, P., Bulgarelli, U., Campana, E. F., Lalli, F., 1994, "The Wave Resistance Problem in a Boundary Integral Formulation", Surveys on Mathematics for Industries, Vol. 4; pp 151-194

4. Black, S., 1995, "The use of numerical optimization in advanced blade section design", 24th ATTC College Station, TX, USA

5. Boger, DA., and Dreyer, J.J., 2006, "Prediction of hydrodynamic forces and moments for underwater vehicles using overset grids", Proceedings of 44th AIAA(American Institute of Aeronautics and Astronautics) Aerospace Sciences Meeting and Exhibit, Reno, NV

6. Brandner, P. A, and Walker, G. J., 2007, "An Experimental Investigation into the Performance of a Flush Water-Jet Inlet", Journal of Ship Research, Vol. 51(1); pp 1-21

7. Brewer, W. H., Newman, J. C., Burgreen, G. W., Burg, C. O., 2003, "A Design method for investigating cavitation delay", 8th International Conference on Numerical Ship Hydrodynamics, Busan, Korea, September

8. Brewton, S. Gowing, S., and Gorski, J., 2006, "Performance Predictions of a Waterjet Rotor and Rotor/Stator Combination Using RANS Calculations", 26th Symposium on Naval Hydrodynamics, Rome, Italy, September

9. Campana, E. F., Liuzzi, G., Lucidi, S., Peri, D., Piccialli, V., and Pinto, A., 2009a, "New global optimization methods for ship design problems", Optimization and Engineering, Vol. 10(4); pp 533-555

10. Campana, E. F., Fasana, G., and Pinto, A., 2009b, "Dynamic analysis for the selection of parameters and initial population, in particle swarm", Journal of Global Optimization

11. Campana, E. F., Peri, D., Tahara, Y., Kandasamy, M., and Stern, F., 2009c, "Numerical Optimization Methods for Ship Hydrodynamic Design", Trans SNAME

12. Campana, E. F., *et al*., 2008, " ITTC Proceedings: The Resistance Committee", Final Report and Recommendations to the 25th ITTC, Fukuoka, Japan

13. Campana, E., Peri, D., Tahara, Y., Kandasamy, M., Stern, F., Cary, C., Hoffman, R., Gorski, J., and Kennel, C., 2006a, "Simulation Based Design of Fast Multihull Ships", 26th Symposium on Naval Hydrodynamics, Rome, Italy, September

14. Campana, E. F., Fasana, G., Peri, D., and Pinto, A., 2006b, "Particle swarm optimization: Efficient globally convergent modifications", 3rd European Conference on Computational Mechanics Solids, Structures and Coupled Problem in Engineering, Lisbon, Portugal, June

15. Campana, E. F., Fasano, G., and Pinto, A., 2006c, "Dynamic system analysis and initial particles position in particle swarm optimization", Proceeding of IEEE Symposium on swarm intelligence, Indianapolis, IN, USA

16. Campana, E. F., Peri, D., Tahara, Y., Stern, F., 2006d, "Shape optimization in ship hydrodynamics using computational fluid dynamics", Computer Methods in Applied Mechanics and Engineering, Vol. 196; pp 634-651

17. Campana, E. F., Fasano, G., and Pinto, A., 2005, "Particle Swarm Optimization: dynamic system analysis for parameter selection in global optimization frameworks", INSEAN Technical Report, Italy

18. Campana, E. F., Fasano, G., and Pinto, A., 2005, "Issues on Nonlinear Programming for Multidisciplinary Design Optimization (MDO) in Ship Design Framework", 8th Numerical Towing Tank Symposium (NuTTS '05), Varna, Bulgaria, October

19. Carderock Division, Naval Surface Warfare Center, 2008, "SEA FRAME", Carderock Division Publication, Vol. 4, Issue. 1

20. Carrica, P., Huang, J., Noack, R., Kaushik, D., Smith, B., and Stern, F., 2008, "Toward Large-Scale Computations of Ship Motions with Dynamic overset Curvilinear Grids", 27th Symposium on Naval Hydrodynamics, Seoul, Korea, October

21. Carrica, P.M., Wilson, R.V., and Stern, F., 2007a, "An unsteady single-phase level set method for viscous free surface flows", International Journal for Numerical Methods in Fluids, Vol. 53; pp 229-256

22. Carrica, P.M., Wilson, R.V., Noack, R., and Stern, F., 2007b, "Ship motions using single-phase level set with dynamic overset grids", Journal of Computers & Fluids, Vol. 36; pp 1415-1433

23. Carrica, P. M., Wilson, R. V., and Stern, F., 2006, "Unsteady RANS simulation of the ship forward speed diffraction problem", Journal of Computers & Fluids, Vol. 35; pp 545-570

24. Chen, J-H., Shih, Y-S., 2007, "Basic design of a series propeller with vibration consideration by genetic algorithm", Journal of Marine Science and Technology, Vol. 12; pp 119-129

25. Coello, C. A., Pulido, G. R., and Lechuga, M. S., 2004, "Handling Multiple Objectives with Particle Swarm Optimization", IEEE Transactions on evolutionary computation, Vol. 8(3)

26. Dai, C., Kerr, C., Nguyen, P., Wang, H-C., 1995, "A Novel Flush Inlet Design Methodology for Waterjet Propulsion", 3rd International Conference on Fast Sea Transportation, Lubeck-Travemunde, Germany, September

27. Deb, K., 2001, "Multiobjective optimization using evolutionary algorithms", Wiley, New York

28. Delaney, K., Donnelly, M., Ebert, M., and Fry, D., 2009, "Use of RANS for Waterjet Analysis of a High-Speed Sealift Concept Vessel", 1st International Symposium on Marine Propulsors, smp'09, Trondheim, Norway, June

29. Eberhart, R. C., and Shi, Y., 2001, "Particle swarm optimization: developments, applications, and resources", Proceedings of the Congress on Evolutionary Computation, Seoul, Korea

30. Eberhart, R. C., Simpson, P. K., and Dobbins, R. W., 1996, "Computational intelligence PC tools", Academic Press, Boston

31. Eberhart, R. C., and Kennedy, J., 1995, "A new optimizer using particle swarm theory", Proceedings of the 6th international symposium on micro machine and human science, Nagoya, Japan

32. Eca, L., and Hoekstra, M., 2008, "The numerical friction line", Journal of Marine Science and Technology, Vol. 13; pp 328-345

33. Faltinsen, O. M., 2006, "Hydrodynamics of High-Speed Marine Vehicles", Cambridge University Press

34. Fonseca, C. M., Fleming, P. J., 1995, "An Overview of Evolutionary Algorithms in Multiobjective Optimization", Evolutionary Computation, Vol. 3(1); pp 1-16

35. Fourie, P. C., and Groenwold, A. A., 2002, "The particle swarm optimization algorithm in size and shape optimization", Structural and Multidisciplinary Optimization, Vol. 23; pp 259-267

36. Gao, H., Lin, W., Du, Z., 2008, "Numerical flow and performance analysis of a water-jet axial flow pump", Ocean Engineering, Vol. 35; pp 1604-0614

37. Gorski, J., Miller, R., Carrica, P., Kandasamy, M., and Stern, F., 2007, "Powering and Motion Predictions of High Speed Sea Lift (HSSL) Ships", HPCMP User Group Conference 2007

38. Grigson CWB, 1999, "A planar friction algorithm and its use in analysing hull resistance", Trans RINA; pp 76-115

39. Hart, C. G., Vlahopoulos, N., 2009, "An integrated multidisciplinary particle swarm optimization approach to conceptual ship design", Structural and Multidisciplinary Optimization, accepted

40. Hassan, R., Cohanim, B., de Weck, O., and Venter, G., 2005, "46th AIAA/ASME/ASCE/AHS/ASC Structures", Structural Dynamics & Materials Conference, Austin, TX, USA, April

41. Heppner, H., and Grenander, U., 1990, "A stochastic non-linear model for coordinated bird flocks", S. Krasner (Ed.), The Ubiquity of chaos, Washington D.C.: AAAS; pp 233-238

42. Hino, T., and Ohashi, K., 2009, "Numerical Simulation of Flow around a Waterjet Propelled Ship", 1st International Symposium on Marine Propulsors, smp'09, Trondheim, Norway, June

43. Hoyt, J. G., *et al*.,, 1999, " ITTC Proceedings: The Specialist Committee on Waterjets.", Final Report and Recommendations to the 22nd ITTC, Seoul, Korea and Shanghai, China

44. Hsin, C-Y., Lin, B-H., and Lin, C-C., 2008, "The Optimum Design of a Propeller Energy-Saving Device by Computational Fluid Dynamics", Computational Fluid Dynamics

45. Hu, P., and Zangeneh, M., 1999, "A Method for Automatic Optimization of the Intake duct geometry of marine water-jets", Proceedings of the 5th international conference on Fast Sea Transportation, Seattle, WA, USA

46. Ismail, F., Carrica, P. M., Xing, T., and Stern, F., 2009, "Evaluation of linear and nonlinear convection schemes on multidimensional non-orthogonal grids with applications to KVLCC2 tanker", International Journal for Numerical Methods in Fluids

47. Proceeding of the 8th ITTC, 1957, "ITTC Proceedings", Final Report and Recommendations to the 8th ITTC, Madrid, Spain

48. Jacquin, E., Guillerm, P.-E., Drouet, A., Perdon, P., 2006, "Simulation of unsteady ship maneuvering using free-surface RANS solver", 26th Symposium on Naval Hydrodynamics, Rome, Italy, September

49. Jang, J. H., Park, W. G., Boo, J. S., Chun, H. H., & Kim, M. C., 2004, "Numerical Simulations of Waterjet with Rotor-Stator Interaction.", 10th International symposium on transport phenomenon and dynamics of rotating machinery, HI, USA

50. Jessup, S., Donnelly, M., Cusanelli, D., and Wilson, M., 2008, "Performance Analysis of a Four Waterjet Propulsion System for a Large Sealift Ship", 27th Symposium on Naval Hydrodynamics, Seoul, Korea, October

51. Jones, K. O., 2005, "Comparison between genetic algorithm and particle swarm optimization", International Conference on Computer Systems and Technologies

52. Jung, K.H., Kim, C. K., Yoon, S. Y., Kwon, S. H., Chun, H. H., and Kim, M. C., 2006, "Investigation of turbulent flows in a waterjet intake duct using stereoscopic PIV measurements.", Journal of Marine Science and Technology, Vol. 11; pp 270-278

53. Kandasamy, M., Ooi, S. K., Carrica, P., Stern, F., 2010, "Integral Force/Moment Waterjet Model for CFD Simulation", Journal of Fluids Engineering, submitted

54. Kandasamy, M., Takai, T., and Stern, F., 2009a, "Validation of Detailed Waterjet Simulation using URANS for Large High- Speed Sea-Lifts", 10th International Conference on Fast Sea Transportation: FAST2009, Athens, Greece, October

55. Kandasamy, M., Ooi, S. K., Carrica, P., Stern, F., Campana, E. F., Peri, D., Osborne, P., Cote, J., Macdonald, N., and Waal, N. D., 2009b, "URANS based optimization of a high speed foil-assisted semi-planing catamaran for low wake", 10th International Conference on Fast Sea Transportation: FAST2009, Athens, Greece, October

56. Kandasamy, M., Peri, D., Ooi, S. K., Carrica, P., Stern, F., Campana, E. F., Osborne, P., Cote, J., Macdonald, N., and Waal, N. D., 2009c, "Multi-fidelity Optimization of a High-speed Foil-assisted Semi-planing Catamaran for Low wake", Journal of Marine Science and Technology, submitted

57. Kandasamy, M., Ooi, S. K., Carrica, P., Stern, F., Campana, E. F., Peri, D., Osborne, P., Cote, J., Macdonald, N., and Waal, N. D., 2009d, "CFD validation studies for a high-speed foil-assisted semi-planing catamaran", 10th International Conference on Fast Sea Transportation: FAST2009, Athens, Greece, October

58. Katsui, T., Asai, H., Himeno, Y., and Tahara, Y., 2005, "The proposal of a new friction line", 5th Osaka Colloquium on advanced CFD applications to ship flow and hull form design, Osaka, Japan

59. Kennedy, J., and Eberhart, R. C., 1995, "Particle swarm optimization", Proceedings of the IEEE international conference on neural networks, Vol. 4; pp 1942-1948

60. Kerwin, J. E., Michael, T. J., and Neely, S. K., 2006, "Improved Algorithms for the Design/Analysis of Multi-Component Complex Propulsors", 11st Propellers/Shafting Symposium, Williamsburg, Virginia, USA

61. Kim, H. J., Chun, H. H., Peri, D., Campana, E. F., 2008, "Optimizing Parametric Modification Functions and Global Optimization Methods", 27th Symposium on Naval Hydrodynamics, Seoul, Korea, October

62. Kim, K. H., *et al*., 2008, " ITTC Proceedings: The Propulsion Committee", Final Report and Recommendations to the 25th ITTC, Fukuoka, Japan

63. Kim, M-C., Chun, H-H., Kim, H. Y., Park, W. K., Jung, U. H., 2009, "Comparison of waterjet performance in tracked vehicles by impeller diameter", Ocean Engineering, Vol. 36; pp 1438-1445

64. Kruppa, I. C., *et al*., 1996, " ITTC Proceedings: Waterjets Group", Final Report and Recommendations to the 21st ITTC, Trondheim, Norway

65. Lavis, D. R., Forstell, B. G., Purnell, J. G., 2006a, "Compact Waterjets for High-Speed Ships", 5th International Conference on High Performance Marine Vehicles, Australia, November

66. Lavis, D. R., Forstell, B. G., Purnell, J. G., 2006b, "Advanced Compact Waterjet Propulsion for High-Speed Ships", 9th International Marine Design Conference (IMDC), Ann Arbor, MI, USA, May

67. Lee, S., Almen, P., Fink, W., Petropoulos, A. E., and Temile, R. J., 2005, "Comparison of Multi-Objective Genetic Algorithms in Optimizing Q-Law Low-Thrust Orbit Transfers", GECCO '05, Washington D.C., USA, June

68. Levy, T., Degani, D., and Seginer, A., 1990, "Graphical visualization of vortical Flows by means of helicity", AIAA Journal, Vol. 28 (8), pp.1347-1352

69. Mentor, F., 2009, "Review of the shear-stress transport turbulence model experience from an industrial perspective", International Journal of Computational Fluid Dynamics, Vol. 23(4); pp 305-316

70. Mentor, F., 1994, "Two-equation eddy viscosity turbulence models for engineering applications", AIAA journal, Vol. 32(8)

71. Miettinen, K. M., 1999, "Nonlinear Multiobjective Optimization", Kluwer Academic Publisher

72. Mishima, S., 1996, "Design of Cavitating Propeller Blades in Non-Uniform Flow by Numerical Optimization", Ph D. thesis, Massachusetts Institute of Technology, Cambridge, MA, USA

73. Mousaviraad, S. M., Carrica, P. M., Huang, J., and Stern, F., 2008, "CFD Prediction of Ship Response to Severe Ocean Waves and Wind", 26th Symposium on Naval Hydrodynamics, Rome, Italy, September

74. N.W.H. Bulten, 2008, "A Breakthrough in Waterjet Propulsion Systems", Doha International Maritime Defense Exhibition and Conference (DIMDEX), Qatar, March

75. N.W.H. Bulten, and B. P. M. van Esch, 2007, "Fully Transit CFD Analyses of Waterjet Pumps", Marine Technology, Vol.44, No.3; pp 185-193

76. N.W.H. Bulten, 2006, "Numerical Analysis of Waterjet Propulsion System", PhD thesis, Technical University of Eindhoven, ISBN-10: 90-386-2988-5. Library Eindhoven University of Technology

77. N.W.H. Bulten, and R. Verbeek, 2004, "CFD simulations of the flow through a waterjet Installation", International Conference on Waterjet Propulsion 4, RINA, London, UK; pp 11-19

78. Nakos, D., and Sclavounos, P., 1990, "Ship Motions by a Three-Dimensional Rankine Panel Method", 18th Symposium on Naval Hydrodynamics, Ann Arbor, MI, USA

79. Newman, J. N., 1977, "Marine hydrodynamics", MIT Press, Cambridge

80. Noack, R., 2005, "SUGGAR: a General capability for moving body overset grid assemble", Proc. 17th AIAA Computational Fluid Dynamics Conference, Toronto, Ontario, Canada

81. Obayashi, S., Sasaki, D., Oyama, A., 2004, "Finding Tradeoffs by Using Multiobjective Optimization Algorithms", Trans JSASS, Vol. 47(155); pp 51-58

82. Ono, I., Kobayashi, S., 1997, "A real-coded genetic algorithm for function optimization using unimodel normal distribution crossover", The 7th International Conference on Genetic Algorithms; pp 246-253

83. Pareto, V., 1906, "Manual of Political Economy", A.M, Kelly, New York (1971) Originally in French

84. Park, W.-G., *et al*., 2005a, "Numerical flow simulation of flush type intake duct of waterjet", Ocean Engineering, Vol. 32; pp 2107-2120

85. Park, W.-G., *et al*., 2005a, "Numerical flow and performance analysis of waterjet propulsion system", Ocean Engineering, Vol. 32; pp 1740-1761

86. Parsopoulos, K. E., and Vrahatis, M. N., 2002, "Particle Swarm Optimization Method in Multiobjective Problems", Proceedings of 2002 ACM symposium on Applied Computing, Madrid, Spain

87. Paterson, E. G., Wilson, R. V., and Stern, F., 2003, "General-purpose parallel unsteady RANS ship hydrodynamics code: CFDSHIP-IOWA", IIHR Technical Report, No.432, The University of Iowa, Iowa City, IA, USA

88. Peri, D., Campana, E. F., Tahara, Y., Kandasamy, M., and Stern, F., 2010, "New developments in Simulation-Based Design with application to High Speed Waterjet Ship Design", 28th Symposium on Naval Hydrodynamics, Pasadena, CA, USA, September

89. Peri, D., Campana, E. F., Kandasamy, M., Ooi, S-K., Carrica, P. M., Stern, F., Osborne, P., Macdonald, N., Waal, N., 2009, "Potential flow based optimization of a high speed, foil-assisted, semi-planning catamaran for low wake", 10th International Conference on Fast Sea Transportation: FAST2009, Athens, Greece, October

90. Peri, D., and Campana, E. F., 2005, "High-Fidelity Models in Global Optimization", COCS 2003, LNCS 3478; pp 112-126

91. Peri, D., and Campana, E. F., 2003, "Multidisciplinary Design Optimization of a Naval Surface Combatant", Journal of Ship Research, Vol. 47; pp 1-12

92. Peri, D., Rossetti, M., and Campana, E. F., 2001, "Design Optimization of ship hulls via CFD techniques", Journal of Ship Research, Vol. 45(2); pp 140-149

93. Pinto, A., Peri, D., and Campana, E. F., 2007, "Multiobjective Optimization of a Containership Using Deterministic Particle Swarm Optimization", Journal of Ship Research, Vol. 51(3); pp 217-228

94. Pinto, A., Peri, D., and Campana, E. F., 2004, "Global optimization algorithms in naval hydrodynamics", Ship Technology Research, Vol. 51(3); pp 123-133

95. Poli, R., Kennedy, J., and Blackwell, T., 2007, "Particle swarm optimization -An overview-", Swarm Intelligence, Vol. 1; pp 33-57

96. Sakamoto, N., 2009, "URANS simulations of static and dynamic maneuvering for surface combatant", Ph.D. thesis, The University of Iowa, Iowa City, Iowa, USA

97. Sakamoto, N., Wilson, R. V., and Stern, F., 2007, "Reynolds-Averaged Navier-Stokes Simulations for High-Speed Wigley Hull in Deep and Shallow Water", Journal of Ship Research, Vol. 51(3); pp 187-203

98. Samareh, J. A., 2005, "Geometry and Grid/Mesh Generation Issues for CFD and CSM Shape Optimization", Optimization and Engineering, Vol. 6; pp 21-32

99. Schoenherr, K. E., 1932, "Resistance of flat surfaces", Trans SNAME, Vol. 40; pp 279-313

100. Sederberg, T. W., and Parry, S. R., 1986, "Free-Form Deformation of Solid Geometric Models", SIGGRAPH '86, Vol. 20(4); pp 269-278

101. Stantnikov, R.B., and Matusov, J.B., 1995, "Multicriteria Optimization and Engineering", Chapman & Hall, New York

102. Steen, S., *et al*., 2008, " ITTC Proceedings: The Specialist Committee on Powering Performance Prediction", Final Report and Recommendations to the 25th ITTC, Fukuoka, Japan

103. Stern, F., Wilson, R. and Shao, J., 2006a, "Quantitative V&V of CFD simulations and certification of CFD code", International Journal for Numerical Methods in Fluids, Vol. 50; pp 1335-1355

104. Stern, F., Carrica, P., Kandasamy, M., Gorski, J., O'Dea, J., Hughes, M., Miler, R., Hendrix, D., Kring, D., Milewski, W., Hoffman, R., Cary, C., 2006b, "Computational Hydrodynamic Tools for High-Speed Sealift", Trans SNAME, Vol. 114

105. Stern, F., Wilson, R. Hugh, W. C., Eric G, P., 2001a, "Comprehensive Approach to Verification and Validation of CFD Simulations - Part1: Methodology and Procedures", Journal of Fluids Engineering, Vol.123; pp 793-801

106. Stern, F., Wilson, R. Hugh, W. C., Eric G, P., 2001b, "Comprehensive Approach to Verification and Validation of CFD Simulations -Part2: Application for RANS Simulation of a Cargo/Container Ship", Journal of Fluids Engineering, Vol.123; pp 803-809

107. Stern, F., Wilson, R. V., Coleman, W., Paterson, E. G., 1999, "Verification and Validation of CFD simulations", IIHR Technical Report, No.407, The University of Iowa, Iowa City, IA, USA

108. Stern, F., Peterson, E. G., and Tahara, Y., 1996, "CFDSHIP-IOWA: Computational Fluid Dynamics Method for Surface-Ship Boundary Layers, Wakes, and Wave Fields", IIHR Technical Report, No. 381, September

109. Stern, F., Toda, Y., and Kim, H. T., 1991, "Computation of Viscous Flow around Propeller-Body Configurations: Iowa Axisymmetric Body", Journal of Ship Research, Vol. 35(2); pp 151-161

110. Tahara, Y., Norisada, K., Yamane, M., and Takai, T., 2008a, "Development and Demonstration of CAD/CFD/Optimizer Integrated Simulation-Based Design Framework by Using High-Fidelity Viscous Free-Surface RaNS Equation Solver", Journal of Japan Society of Naval Architects and Ocean Engineers, Vol. 7; pp 171-184

111. Tahara, Y., Peri, D., Campana, E. F., and Stern, F., 2008b, "Single- and Multi-objective Design Optimization of a Fast Multihull Ship: numerical and experimental results", 27th Symposium on Naval Hydrodynamics, Seoul, Korea, October

112. Tahara, Y., Peri, D., Campana, E. F., and Stern, F., 2008c, "Computational fluid dynamics-based multiobjective optimization of a surface combatant using a global optimization method", Journal of Marine Science and Technology, Vol. 13; pp 95-116

113. Tahara, Y., Campana, D. F., Peri, D., Pinto, A., Kandasamy, M., Stern, F., 2007, "Global Optimization and Variable Fidelity Strategies in the Single and Multiobjective Optimal Design of Fast Multihull Ships", 9th International Conference on Numerical Ship Hydrodynamics, Ann Arbor, MI, August

114. Tahara, Y., Tohyama, S., and Katsui, T., 2006a, "CFD-based multiobjective optimization method for ship design", International Journal for Numerical Methods in Fluids, Vol. 52; pp 449-527

115. Tahara, Y., Wilson, R., Carrica, P. M., and Stern, F., 2006b, "RANS simulation of a container ship using a single-phase level set method with overset grids and prognosis for extension to self-propulsion simulator", Journal of Marine Science and Technology, Vol. 11; pp 209-228.

116. Tahara, Y., Peri, D., Campana, E. F., and Stern, F., 2005, "CFD-based multiobjective optimization method for a surface combatant", 5th Osaka Col. On Advanced Research on Ship Viscous Flow and Hull Form Design by EFD and CFD Approach, Osaka, Japan, March

117. Tahara, Y., Stern, F., and Himeno, Y., 2004, "Computational Fluid Dynamics-Based Optimization of a Surface Combatant", Journal of Ship Research, Vol. 28(4); pp 273-287.

118. Tahara, Y., Sugimoto, S., Murayama, S., Katsui, T., 2003, "Development of CAD/CFD/optimizer-integrated hull-form design system", Journal of the Kansai Society of Naval Architects, Vol. 240; pp 29-36

119. Takai, T., Kandasamy, M., and Stern, F., 2010, "Verification and Validation study of URANS simulations for axial waterjet propelled large high-speed ship", Journal of Marine Science and Technology, submitted

120. Takekoshi, Y., Kawamura, T., Yamaguchi, H., Maeda, M., Ishii, N., Kimura, K., Taketani, T., and Fujii, A., 2005, "Study on the design of propeller blade sections using the optimization algorithm", Journal of Marine Science and Technology, Vol. 10; pp 70-81

121. Van Terwisga, T., *et al*., 2005, " ITTC Proceedings-Volume 2: The Specialist Committee on Validation of Waterjet Test Procedures", Final Report and Recommendations to the 24th ITTC, Edinburgh, UK

122. Van Terwisga, T., *et al*., 2002, " ITTC Proceedings-Volume 2: The Specialist Committee on Validation of Waterjet Test Procedures", Final Report and Recommendations to the 23rd ITTC, Venice, Italy

123. Veelo, B. N., 2004, "Shape Modification of Ship Hulls in H-rep", Ship Technology Research, Vol.55; pp 162-172

124. Venter, G., Haftka, R. T., 2010, "Constrained particle swarm optimization using a bi-objective formulation", Structural and Multidisciplinary Optimization, Vol.40; pp 65-76

125. Venter, G., and Sobieszczanski-Sobieski, J., 2003, "Particle swarm optimization", AIAA Journal, Vol. 41(8); pp 1583-1589

126. Wilson, W., Gorski, J., Kandasamy, M., Takai, T., He, W., Stern, F., Tahara, T., 2010, "Hydrodynamic Shape Optimization for Naval Vehicles", Proceeding of the HPCMP User Group Conference 2010

127. Wilson, W., Gorski, J., Kandasamy, M., Takai, T., Stern, F., Tahara, T., 2009, "Hydrodynamic Shape Optimization for Naval Vehicles", Proceeding of the HPCMP User Group Conference 2009

128. Wilson, R. V., Carrica, P. M., and Stern, F., 2006, "Unsteady RANS method for ship motions with application to roll for a surface combatant", Journal of Computers & Fluids, Vol.35; pp 501-524

129. Wilson, R., and Stern, F., 2001, "Verification and Validation for RANS Simulation of a Naval Surface Combatant", AIAA Journal

130. Xing, T. and Stern, F., 2010, "Factor of safety for Richardson extrapolation", Journal of Fluids Engineering

131. Xing, T. and Stern, F., 2009, "Factor of safety for Richardson extrapolation for industrial applications", IIHR Technical Report, No.469, The University of Iowa, Iowa City, IA, USA

132. Xing, T. and Stern, F., 2008a, "Factor of safety for Richardson extrapolation for industrial applications", IIHR Technical Report, No.466, The University of Iowa, Iowa City, IA, USA

133. Xing, T., Carrica, P., and Stern, F., 2008b, "Computational Towing Tank Procedures for Single Run Curves of Resistance and Propulsion", Journal of Fluids Engineering, Vol.130

134. Xu, G., Wang, G.-Z., and Chen, X.-D., 2008, "Free-Form Deformation with Rational DMS-Spline Volumes", Journal of Computer Science and Technology, Vol. 23(5); pp 862-873

135. Yang, J., Bhushan, S., Suh, J.S., Wang, Z., Koo, B., Sakamoto, N., Xing, T., and Stern, F., 2008, "Large-Eddy Simulation of Ship Flows with Wall-Layer Models on Cartesian Grids", 27th Symposium on Naval Hydrodynamics, Seoul, Korea, October

136. Yang, J., Sakamoto, N., Wang, Z., Carrica, P., and Stern, F., 2007, "Two Phase Level-Set/Immerged-Boundary Cartesian Grid Method for Ship Hydrodynamics", 9th International Conference on Numerical Ship Hydrodynamics, Ann Arbor, MI, USA, August